

Ministry of Science and Higher Education of the Russian Federation
ITMO University

ISSN 2220-8054

NANOSYSTEMS:
PHYSICS, CHEMISTRY, MATHEMATICS

2024, volume 15 (3)

Наносистемы: физика, химия, математика

2024, том 15, № 3



NANOSYSTEMS:

PHYSICS, CHEMISTRY, MATHEMATICS

ADVISORY BOARD MEMBERS

Chairman: V.N. Vasiliev (*St. Petersburg, Russia*),
V.M. Buznik (*Moscow, Russia*); V.M. Ievlev (*Voronezh, Russia*), P.S. Kop'ev (*St. Petersburg, Russia*), N.F. Morozov (*St. Petersburg, Russia*), V.N. Parmon (*Novosibirsk, Russia*),
A.I. Rusanov (*St. Petersburg, Russia*),

EDITORIAL BOARD

Editor-in-Chief: I.Yu. Popov (*St. Petersburg, Russia*)

Section Co-Editors:

Physics – V.M. Uzdin (*St. Petersburg, Russia*),

Material science – V.V. Gusarov (*St. Petersburg, Russia*); O.V. Al'myasheva (*St. Petersburg, Russia*);

Chemistry – V.K. Ivanov (*Moscow, Russia*),

Mathematics – I.Yu. Popov (*St. Petersburg, Russia*).

Editorial Board Members:

V.M. Adamyan (*Odessa, Ukraine*); A.P. Alodjants (*St. Petersburg, Russia*); S. Bechta (*Stockholm, Sweden*); J. Behrndt (*Graz, Austria*); A. Chatterjee (*Hyderabad, India*); A.V. Chizhov (*Dubna, Russia*); A.N. Enyashin (*Ekaterinburg, Russia*), P.P. Fedorov (*Moscow, Russia*); E.A. Gudilin (*Moscow, Russia*); H. Jónsson (*Reykjavik, Iceland*); A.A. Kiselev (*Durham, USA*); Yu.S. Kivshar (*Canberra, Australia*); S.A. Kozlov (*St. Petersburg, Russia*); P.A. Kurasov (*Stockholm, Sweden*); A.V. Lukashin (*Moscow, Russia*); I.V. Melikhov (*Moscow, Russia*); G.P. Miroshnichenko (*St. Petersburg, Russia*); I.Ya. Mittova (*Voronezh, Russia*); H. Najjar (*Monastir, Tunisia*), Nguyen Anh Tien (*Ho Chi Minh, Vietnam*); V.V. Pankov (*Minsk, Belarus*); K. Pankrashkin (*Orsay, France*); A.V. Ragulya (*Kiev, Ukraine*); V. Rajendran (*Tamil Nadu, India*); A.A. Rempel (*Ekaterinburg, Russia*); A.A. Rogachev (*Minsk, Belarus*); V.Ya. Rudyak (*Novosibirsk, Russia*); H.M. Sedighi (*Ahvaz, Iran*); D Shoikhet (*Karmiel, Israel*); M.N. Smirnova (*Moscow, Russia*); P. Stovicek (*Prague, Czech Republic*); V.M. Talanov (*Novocherkassk, Russia*); A.Ya. Vul' (*St. Petersburg, Russia*); A.V. Yakimansky (*St. Petersburg, Russia*), V.A. Zagrebnov (*Marseille, France*).

Editors:

I.V. Blinova; A.I. Popov; A.I. Trifanov; E.S. Trifanova (*St. Petersburg, Russia*),
R. Simoneaux (*Philadelphia, Pennsylvania, USA*).

Address: ITMO University, Kronverkskiy pr., 49, St. Petersburg 197101, Russia.

Phone: +7(812)607-02-54, **Journal site:** <http://nanojournal.ifmo.ru/>,

E-mail: nanojournal.ifmo@gmail.com

AIM AND SCOPE

The scope of the journal includes all areas of nano-sciences. Papers devoted to basic problems of physics, chemistry, material science and mathematics inspired by nanosystems investigations are welcomed. Both theoretical and experimental works concerning the properties and behavior of nanosystems, problems of its creation and application, mathematical methods of nanosystem studies are considered.

The journal publishes scientific reviews (up to 30 journal pages), research papers (up to 15 pages) and letters (up to 5 pages). All manuscripts are peer-reviewed. Authors are informed about the referee opinion and the Editorial decision.

CONTENT

MATHEMATICS

Shashwath S. Shetty, K. Arathi Bhat

Energy and spectral radius of Zagreb matrix of graph with applications 315

PHYSICS

G.P. Miroshnichenko, A.N. Arzhanenkova, M.Yu. Plotnikov

Errors of in-phase and quadrature demodulation method created by low-pass filter 325

K.A. Chichay, I.S. Lobanov, V.M. Uzdin

Stability and transformations of domain walls in cylindrical wires 332

R.V. Shalayev, V.N. Varyukhin, A.I. Linnik,

V.V. Syrotkin, S.A. Kostyrya

Low temperature magnetron deposition of Ni-C nanostructural films: synthesis, structure and magnetic properties 340

I.V. Pleshakov, A.A. Alekseev, E.E. Bibik,

I.V. Ilichev, A.V. Prokof'ev

Effect of laser radiation on magnetite nanoparticles in deposited ferrofluid 346

CHEMISTRY AND MATERIAL SCIENCE

D.D. Kolmanovich, N.N. Chukavin, N.A. Pivovarov,

S.A. Khaustov, V.K. Ivanov, A.L. Popov

Cellular uptake of FITC-labeled $Ce_{0.8}Gd_{0.2}O_{2-x}$ nanoparticles in 2D and 3D mesenchymal stem cell systems 352

D.P. Elovikov, A.A. Osminina

The role of pH of the reaction medium in the formation of nanocrystalline phases in the Bi_2O_3 - P_2O_5 - H_2O system 361

O.V. Proskurina, K.I. Babich, S.M. Tikhanova, K.D. Martinson,

V.N. Nevedomskiy, V.G. Semenov, R.Sh. Abiev, V.V. Gusarov

Magnetic and photocatalytic properties of $BiFeO_3$ nanoparticles formed during the heat treatment of hydroxides coprecipitated in a microreactor with intense swirling flows 369

E.N. Gatina, T.P. Maslennikova

Formation of chrysotile nanotubes with titania in the internal channel 380

S.N. Kharina, A.Yu. Kurenkova, A.A. Saraev, E.Yu. Gerasimov, E.A. Kozlova Copper-modified g-C₃N₄/TiO₂ nanostructured photocatalysts for H₂ evolution from glucose aqueous solution	388
M.M. Kamble, B. R. Bade, A. V. Rokade, V. S. Waman, S.V. Bangale, S.R. Jadkar Synthesis and study of nickel sulfide nanostructures for energy storage device applications	398
Q. Berdinazarov, E. Khakberdiev, N. Ashurov The effect of layered silicates on the morphological, rheological and mechanical properties of PA and PP blends	410
Shazia Showket, Khurshed A. Shah, G.N. Dar Investigating the sensing performance of silicene nanoribbon towards methanol and ethanol molecules: A computational study	418
Information for authors	429

Energy and spectral radius of Zagreb matrix of graph with applications

Shashwath S. Shetty^{1,a}, K. Arathi Bhat^{1,b}¹Manipal Institute of Technology, Manipal Academy of Higher Education, Manipal, Karnataka, India^ashashwathshetty01334@gmail.com, ^barathi.bhat@manipal.edu

Corresponding author: K. Arathi Bhat, arathi.bhat@manipal.edu

ABSTRACT The \mathcal{Z} -matrix of a simple graph Γ is a square symmetric matrix, whose rows and columns correspond to the vertices of the graph and the i_j^{th} entry is equal to the sum of the degrees of i^{th} and j^{th} vertex, if the corresponding vertices are adjacent in Γ , and zero otherwise. The Zagreb eigenvalues of Γ are the eigenvalues of its \mathcal{Z} -matrix and the Zagreb energy of Γ is the sum of absolute values of its Zagreb eigenvalues. We study the change in Zagreb energy of a graph when the edges of the graph are deleted or rotated. Suppose Γ is a graph obtained by identifying $u \in \mathcal{V}(\Gamma_1)$ and $v \in \mathcal{V}(\Gamma_2)$ or adding an edge between u and v , then it is important to study the relation between Zagreb energies of Γ_1 , Γ_2 and Γ . The highlight of the paper is that, the acentric factor of n -alkanes appear to have a strong positive correlation (where the correlation coefficient is 0.9989) with energy of the \mathcal{Z} -matrix. Also, the novel correlation of the density and refractive index of n -alkanes with spectral radius of the \mathcal{Z} -matrix has been observed.

KEYWORDS spectral radius, energy, Zagreb matrix, acentric factor, density, refractive index

ACKNOWLEDGEMENTS We acknowledge the Institution for overall support. The authors sincerely appreciate the reviewers for all the valuable comments and suggestions, which helped to improve the quality of the manuscript.

FOR CITATION Shashwath S. Shetty, K. Arathi Bhat Energy and spectral radius of Zagreb matrix of graph with applications. *Nanosystems: Phys. Chem. Math.*, 2024, **15** (3), 315–324.

1. Introduction

In mathematical chemistry, graph energies have received considerable attention because of their immense applications [1]. Recently, various types of matrices and the corresponding energies of graphs have been studied. In 1978, Gutman defined the energy [2] of a simple graph as the sum of the absolute values of eigenvalues of the adjacency matrix of the corresponding graph.

Let $\Gamma = (\mathcal{V}, E)$ be an undirected graph on a finite non-empty set of vertices \mathcal{V} and the prescribed collection E of an unordered pair of vertices called edges. Two vertices are said to be adjacent, if they share an edge. We use $i \sim j$ to denote that vertices i and j are adjacent. The neighborhood of vertex i in graph Γ is a collection of all vertices that are adjacent to i in Γ . The adjacency matrix of a graph Γ denoted by \mathcal{A}^Γ is $n \times n$ matrix whose rows and columns correspond to the vertices of the graphs and the i_j^{th} entry is one if vertex i is adjacent to vertex j , and zero otherwise. The energy of a graph is defined as the sum of absolute values of eigenvalues of adjacency matrix of the graph. The singular values of a real matrix \mathcal{A} is the square root of the eigenvalues of $\mathcal{A}^T \mathcal{A}$, where \mathcal{A}^T is the transpose of the matrix \mathcal{A} . For a real symmetric positive definite matrix, the singular values of the matrix coincide with the eigenvalues of the matrix. Let \mathcal{A}_{TI}^Γ is an extended adjacency matrix of the graph Γ corresponding to the degree based symmetric topological index TI , and $\mathcal{A}_{TI}^\Gamma[u]$ be a matrix obtained from \mathcal{A}_{TI}^Γ by deleting the row and column corresponding to the vertex u , where u is a vertex of the graph Γ .

The first extended adjacency matrix corresponding to a degree based topological index defined was the Randić matrix [3], and the energy of the corresponding matrix was defined in a similar manner and termed as the Randić energy. The first Zagreb index, $M_1(\Gamma)$ of a graph Γ is defined [4] as the sum of the squares of the degrees over all vertices of the graph. Interesting facts concerned with the first Zagreb index are available in the literature [5, 6] and recently it has been considered for graphs with self-loops [7].

The first Zagreb matrix (\mathcal{Z} -matrix) [8] of a graph Γ denoted by \mathcal{Z}^Γ is an $n \times n$ matrix whose rows and columns correspond to the vertices of the graph and its i_j^{th} entry, z_{ij} is given by

$$z_{ij} = \begin{cases} d_i + d_j, & \text{if } i \sim j; \\ 0, & \text{otherwise,} \end{cases}$$

where d_i is the degree of vertex $i \in \mathcal{V}(\Gamma)$. The Zagreb energy of a simple graph Γ is defined as the sum of the absolute values of the Zagreb matrix eigenvalues of the graph. Let $\zeta_1 \geq \zeta_2 \geq \dots \geq \zeta_n$ be the eigenvalues and ζ_1 be the \mathcal{Z} -spectral radius corresponding to the \mathcal{Z} -matrix of the graph Γ . If x is the principal eigenvector of the \mathcal{Z} -matrix then the Rayleigh

quotient of \mathcal{Z} is a scalar, $\frac{x^\top \mathcal{Z} x}{x^\top x}$ and, the supremum value of this quotient over all the vectors x gives one the spectral radius of \mathcal{Z} , i.e.,

$$\zeta_1 = \sup_x \frac{x^\top \mathcal{Z} x}{x^\top x}.$$

For all other undefined terminologies of graph theory reader can refer [9].

A few bounds for \mathcal{Z} -spectral radius and its variation during deletion and the rotation of an edge is discussed in Section 2. In Section 3, the relation between Zagreb energies of Γ_1, Γ_2 and Γ is discussed, where Γ is a graph obtained by identifying $u \in \mathcal{V}(\Gamma_1)$ and $v \in \mathcal{V}(\Gamma_2)$ or adding an edge between u and v . Chemical applications of \mathcal{Z} -spectral radius and Zagreb energy is discussed in the last section.

2. \mathcal{Z} -spectral Radius

An edge rotation of $e = xy \in E(\Gamma)$ around $x \in \mathcal{V}(\Gamma)$, replaces xy by an edge xw where $xw \notin E(\Gamma)$. The variation of \mathcal{Z} -spectral radius during the deletion and rotation of an edge is discussed in this section along with few bounds.

Theorem 1. *Let Γ be a connected graph of order n , maximum degree Δ and \mathcal{Z} -spectral radius ζ_1 . If $M_1(\Gamma)$ denotes the first Zagreb index of the graph Γ , then*

$$\frac{M_1(\Gamma) + \sum_{u \in \mathcal{V}} d_{2,u}}{n} \leq \zeta_1 \leq 2\Delta^2,$$

where $d_{2,u}$ is the sum of degrees of all the vertices which are adjacent to u in Γ . Equality holds in both if and only if Γ is regular.

Proof. Now,

$$\zeta_1 \geq \frac{\mathbf{J}^\top \mathcal{Z} \mathbf{J}}{\mathbf{J}^\top \mathbf{J}} = \frac{\sum_{u \in \mathcal{V}(\Gamma)} (d_u^2 + d_{2,u})}{n} = \frac{M_1(\Gamma) + \sum_{u \in \mathcal{V}(\Gamma)} d_{2,u}}{n},$$

where $d_{2,u}$ is the sum of degrees of all the vertices which are adjacent to u in Γ . Since, the all one vector \mathbf{J} is the eigenvector corresponding to the regular graph Γ , equality holds in the above if and only if Γ is a regular graph.

Let x_u is the maximum component of the principal eigenvector x . The eigenvalue equation for the \mathcal{Z} -matrix of the simple graph is given by,

$$\zeta_1 x_u = \sum_{v \in N(u)} (d_u + d_v) x_v.$$

Therefore,

$$\begin{aligned} \zeta_1 x_u &= \sum_{v \in N(u)} (d_u + d_v) x_v \leq \sum_{v \in N(u)} (d_u + d_v) x_u \\ &\leq 2\Delta \sum_{v \in N(u)} x_u \\ &\leq 2\Delta^2 x_u. \end{aligned}$$

Equality holds in the above if and only if $d_u = d_v = \Delta$, i.e., Γ is regular. □

Theorem 2. [10] *Suppose that $\mathcal{A} = (a_{ij})$ and $\mathcal{B} = (b_{ij})$ are two $n \times n$ non-negative symmetric matrices. If $\mathcal{A} \leq \mathcal{B}$, i.e., $a_{ij} \leq b_{ij}$ for all i, j , then $\zeta_1(\mathcal{A}) \leq \zeta_1(\mathcal{B})$. Furthermore, if \mathcal{B} is irreducible and $\mathcal{A} \neq \mathcal{B}$, then $\zeta_1(\mathcal{A}) < \zeta_1(\mathcal{B})$.*

Theorem 3. *Let Γ be a forest of order n and size m with $n \leq 2m$. Then*

$$2 \leq \zeta_1(\Gamma) \leq n\sqrt{2m - n + 1},$$

with equality in the lower bound holds if and only if $\Gamma \cong \frac{n}{2}K_2$ and equality in the upper bound holds if and only if Γ isomorphic to the star S_n .

Furthermore for $n > 2$, if Γ is connected, then

$$6 \cos \frac{\pi}{n+1} \leq \zeta_1(P_n) \leq \zeta_1(\Gamma)$$

with equality if and only if $\Gamma \cong P_3$

Proof. Since Γ is a forest, we have $d_i + d_j \leq n$ for every i, j in $\mathcal{V}(\Gamma)$. Hence,

$$\mathcal{Z}^\Gamma \leq n\mathcal{A}^\Gamma, \tag{1}$$

where \mathcal{A}^Γ is the adjacency matrix of the graph Γ . Here, the equality in (1) holds if and only if Γ is a star graph. Now by using Theorem 2, $\zeta_1 \leq n\rho$, where ρ is the adjacency spectral radius of the graph. But, we have [11] $\rho \leq \sqrt{2m - n + 1}$ and the equality follows if and only if the graph is a star graph or a complete graph on n vertices.

As $n \leq 2m$, we have

$$2\mathcal{A}^\Gamma \leq \mathcal{Z}^\Gamma$$

with equality if and only if $\Gamma \cong \frac{n}{2}K_2$.

Furthermore, when Γ is connected and $n \geq 3$, we have

$$3\mathcal{A}^\Gamma \leq \mathcal{Z}^\Gamma$$

with equality if and only if Γ is a path graph on 3 vertices. We know that,

$$\rho(P_n) = 2 \cos \frac{\pi}{n+1},$$

from which the result follows. □

Theorem 4. Let Γ be a connected graph with the \mathcal{Z} -spectral radius ζ_1 and the corresponding principal eigenvector x . If $e = uv$ is not an edge in Γ , then

$$\zeta_1(\Gamma + e) > \zeta_1(\Gamma).$$

Proof. Let x_u denote the u^{th} component of the eigenvector x , corresponding to the spectral radius of Γ . By using Rayleigh quotient

$$\zeta_1(\Gamma + e) \geq \frac{x^\top \mathcal{Z}^{\Gamma+e} x}{x^\top x} = \frac{x^\top \mathcal{Z}^\Gamma x}{x^\top x} + \frac{x^\top \mathcal{C}_1 x}{x^\top x},$$

where

$$\mathcal{C}_1 = \begin{bmatrix} \mathbf{0}_{n-2 \times n-2} & \mathbf{J}_u & \mathbf{J}_v \\ \mathbf{J}_u^\top & \mathbf{0} & d_u + d_v + 2 \\ \mathbf{J}_v^\top & d_u + d_v + 2 & \mathbf{0} \end{bmatrix},$$

and d_u and d_v are the degrees of the vertices u and v respectively, in the graph Γ . \mathbf{J}_u is the column vector of size $(n-2)$ corresponding to the vertex u , whose entries are 0 or 1, accordingly the corresponding vertex is adjacent to u or not. Similarly, the column vector \mathbf{J}_v corresponds to the vertex v . Therefore

$$\frac{x^\top \mathcal{C}_1 x}{x^\top x} = \frac{M}{x^\top x},$$

where $M = 2(d_u + d_v + 2)x_u x_v + 2 \sum_{w \sim u} x_u x_w + 2 \sum_{y \sim v} x_v x_y$.

Here M is strictly greater than zero, since x is a positive eigenvector [12]. □

Theorem 5. Let p, q, r be the vertices of a connected graph Γ such that rp is an edge in Γ , where as rq is not an edge in Γ . Then

$$\zeta_1(\Gamma - rp + rq) \geq \zeta_1(\Gamma), \text{ if } N \geq 0$$

and the inequality is strict if $N > 0$,

where $N = d_r(x_q - x_p)x_r + (d_q x_q + x_q - d_p x_p)x_r + \sum_{y \sim q, y \neq r} x_q x_y - \sum_{w \sim p, w \neq r} x_p x_w$.

Proof. Let x be the eigenvector corresponding to $\zeta_1(\Gamma)$. Then, we have

$$\zeta_1(\Gamma - rp + rq) \geq \frac{x^\top \mathcal{Z}^{(\Gamma-rp+rq)} x}{x^\top x} = \frac{x^\top \mathcal{Z}^\Gamma x}{x^\top x} + \frac{x^\top \mathcal{C}_2 x}{x^\top x},$$

where

$$\mathcal{C}_2 = \begin{bmatrix} \mathbf{0}_{n-3 \times n-3} & \mathbf{0}_{n-3 \times 1} & -\mathbf{J}_p & \mathbf{J}_q \\ \mathbf{0}_{1 \times n-3} & \mathbf{0} & -(d_r + d_p) & d_r + d_q + 1 \\ -\mathbf{J}_p^\top & -(d_r + d_p) & \mathbf{0} & \mathbf{0} \\ \mathbf{J}_q^\top & d_r + d_q + 1 & \mathbf{0} & \mathbf{0} \end{bmatrix},$$

where d_p, d_q and d_r are the degrees of the vertices p, q and r respectively, in the graph Γ . \mathbf{J}_p is the column vector of size $(n-3)$ corresponding to the vertex p , whose entries are 0 or 1, accordingly the corresponding vertex is adjacent to p or not. Similarly, the column vector \mathbf{J}_q corresponds to the vertex q . Hence

$$\frac{x^\top \mathcal{C}_2 x}{x^\top x} = \frac{2N}{x^\top x},$$

where $2N = 2(d_r + d_q + 1)x_r x_q - 2(d_r + d_p)x_r x_p + 2 \sum_{y \sim q, y \neq r} x_q x_y - 2 \sum_{w \sim p, w \neq r} x_p x_w$. □

3. Zagreb energy

The coalescence of two graphs Γ_1 and Γ_2 denoted by $\Gamma_1 \circ \Gamma_2$ is obtained by identifying two arbitrary vertices, $u \in \mathcal{V}(\Gamma_1)$ and $v \in \mathcal{V}(\Gamma_2)$. The change in adjacency energy during the coalescence of two graphs was studied in [13]. Similar type result is discussed below for the Zagreb energy.

Theorem 6. *Let $\Gamma_1 \circ \Gamma_2$ be coalescence of two graphs Γ_1 and Γ_2 obtained by identifying the vertices $u \in \mathcal{V}(\Gamma_1)$ and $v \in \mathcal{V}(\Gamma_2)$. Then*

$$\mathcal{ZE}(\Gamma_1 \circ \Gamma_2) \leq \mathcal{ZE}(\Gamma_1) + \mathcal{ZE}(\Gamma_2) + 2d_u\sqrt{d_v} + 2d_v\sqrt{d_u}$$

with equality if and only if u is an isolated vertex in Γ_1 and / or v is an isolated vertex in Γ_2 .

Proof. It is direct that

$$\mathcal{Z}^{\Gamma_1 \circ \Gamma_2} = \begin{bmatrix} \mathcal{Z}^{\Gamma_1}[u] & [x_1 + x_2] & \mathbf{0} \\ [x_1 + x_2]^\top & \mathbf{0} & [y_1 + y_2]^\top \\ \mathbf{0} & [y_1 + y_2] & \mathcal{Z}^{\Gamma_2}[v] \end{bmatrix},$$

where x_1 is the deleted column of \mathcal{Z}^{Γ_1} corresponding to the vertex u and x_2 is the column vector obtained by replacing all the non-zero entries of x_1 by d_u . Similarly, y_2 is the deleted column of \mathcal{Z}^{Γ_2} corresponding to the vertex v and y_1 is the column vector obtained by replacing all the non-zero entries of y_2 by d_u . Now,

$$\mathcal{Z}^{\Gamma_1 \circ \Gamma_2} = \mathcal{A}_1 + \mathcal{A}_2,$$

where

$$\mathcal{A}_1 = \begin{bmatrix} \mathcal{Z}^{\Gamma_1}[u] & [x_1 + x_2] & \mathbf{0} \\ [x_1 + x_2]^\top & \mathbf{0} & \mathbf{0} \\ \mathbf{0} & \mathbf{0} & \mathbf{0} \end{bmatrix} \text{ and}$$

$$\mathcal{A}_2 = \begin{bmatrix} \mathbf{0} & \mathbf{0} & \mathbf{0} \\ \mathbf{0} & \mathbf{0} & [y_1 + y_2]^\top \\ \mathbf{0} & [y_1 + y_2] & \mathcal{Z}^{\Gamma_2}[v] \end{bmatrix}.$$

For a symmetric matrix singular values are nothing but the absolute values of the eigenvalues and hence by using the Ky Fan's inequality [13] for singular values of the matrix, we have

$$\mathcal{E}(\mathcal{Z}^{\Gamma_1 \circ \Gamma_2}) \leq \mathcal{E}(\mathcal{A}_1) + \mathcal{E}(\mathcal{A}_2) \tag{2}$$

and the equality holds if and only if there exists an orthogonal matrix \mathcal{Q} such that both $\mathcal{Q}\mathcal{A}_1$ and $\mathcal{Q}\mathcal{A}_2$ are positive semi-definite. Since \mathcal{Q} is orthogonal,

$$\mathcal{Q}^\top \mathcal{Q} = \begin{bmatrix} \mathbf{Q}_{11}^\top & \mathbf{Q}_{21}^\top & \mathbf{Q}_{31}^\top \\ \mathbf{Q}_{12}^\top & \mathbf{Q}_{22}^\top & \mathbf{Q}_{32}^\top \\ \mathbf{Q}_{13}^\top & \mathbf{Q}_{23}^\top & \mathbf{Q}_{33}^\top \end{bmatrix} \begin{bmatrix} \mathbf{Q}_{11} & \mathbf{Q}_{12} & \mathbf{Q}_{13} \\ \mathbf{Q}_{21} & \mathbf{Q}_{22} & \mathbf{Q}_{23} \\ \mathbf{Q}_{31} & \mathbf{Q}_{32} & \mathbf{Q}_{33} \end{bmatrix} = \mathbf{I},$$

where the blocks \mathbf{Q}_{ij} 's are of appropriate size. Therefore

$$\begin{aligned} \mathbf{Q}_{11}^\top \mathbf{Q}_{11} + \mathbf{Q}_{21}^\top \mathbf{Q}_{21} + \mathbf{Q}_{31}^\top \mathbf{Q}_{31} &= \mathbf{I}, \\ \mathbf{Q}_{13}^\top \mathbf{Q}_{13} + \mathbf{Q}_{23}^\top \mathbf{Q}_{23} + \mathbf{Q}_{33}^\top \mathbf{Q}_{33} &= \mathbf{I}, \\ \mathbf{Q}_{11}^\top \mathbf{Q}_{13} + \mathbf{Q}_{21}^\top \mathbf{Q}_{23} + \mathbf{Q}_{31}^\top \mathbf{Q}_{33} &= \mathbf{0}. \end{aligned}$$

Consider,

$$\mathcal{Q}\mathcal{A}_1 = \begin{bmatrix} \mathbf{Q}_{11} \mathcal{Z}^{\Gamma_1}[u] + \mathbf{Q}_{12}[x_1 + x_2]^\top & \mathbf{Q}_{11}[x_1 + x_2] & \mathbf{0} \\ \mathbf{Q}_{21} \mathcal{Z}^{\Gamma_1}[u] + \mathbf{Q}_{22}[x_1 + x_2]^\top & \mathbf{Q}_{21}[x_1 + x_2] & \mathbf{0} \\ \mathbf{Q}_{31} \mathcal{Z}^{\Gamma_1}[u] + \mathbf{Q}_{32}[x_1 + x_2]^\top & \mathbf{Q}_{31}[x_1 + x_2] & \mathbf{0} \end{bmatrix},$$

which implies $\mathbf{Q}_{31}[x_1 + x_2] = \mathbf{0}$. Also,

$$\mathcal{Q}\mathcal{A}_2 = \begin{bmatrix} \mathbf{0} & \mathbf{Q}_{13}[y_1 + y_2] & \mathbf{Q}_{12}[y_1 + y_2]^\top + \mathbf{Q}_{13} \mathcal{Z}^{\Gamma_2}[v] \\ \mathbf{0} & \mathbf{Q}_{23}[y_1 + y_2] & \mathbf{Q}_{22}[y_1 + y_2]^\top + \mathbf{Q}_{23} \mathcal{Z}^{\Gamma_2}[v] \\ \mathbf{0} & \mathbf{Q}_{33}[y_1 + y_2] & \mathbf{Q}_{32}[y_1 + y_2]^\top + \mathbf{Q}_{33} \mathcal{Z}^{\Gamma_2}[v] \end{bmatrix},$$

which implies $\mathbf{Q}_{13}[y_1 + y_2] = 0$. Hence,

$$[\mathbf{Q}_{11}[x_1 + x_2]]^T \mathbf{Q}_{13}[y_1 + y_2] + [\mathbf{Q}_{21}[x_1 + x_2]]^T \mathbf{Q}_{23}[y_1 + y_2] + [\mathbf{Q}_{31}[x_1 + x_2]]^T \mathbf{Q}_{33}[y_1 + y_2] = \mathbf{0}$$

implies

$$[\mathbf{Q}_{21}[x_1 + x_2]]^T \mathbf{Q}_{23}[y_1 + y_2] = 0,$$

and here both $\mathbf{Q}_{21}[x_1 + x_2]$ or $\mathbf{Q}_{23}[y_1 + y_2]$ are scalars.

Now if $\mathbf{Q}_{21}[x_1 + x_2] = 0$, and since $\mathcal{Q}\mathcal{A}$ is diagonally dominant we arrive at $[x_1 + x_2] = 0$, which implies that u is an isolated vertex in Γ_1 . Similarly if $\mathbf{Q}_{23}[y_1 + y_2] = 0$, we arrive at $[y_1 + y_2] = 0$, which implies that v is an isolated vertex in Γ_2 . Let

$$\mathcal{A}_1 = \mathcal{A}_3 + \mathcal{A}_4 \text{ and } \mathcal{A}_2 = \mathcal{A}_5 + \mathcal{A}_6,$$

where

$$\mathcal{A}_3 = \begin{bmatrix} \mathcal{Z}^{\Gamma_1}[u] & x_1 & \mathbf{0} \\ x_1^T & \mathbf{0} & \mathbf{0} \\ \mathbf{0} & \mathbf{0} & \mathbf{0} \end{bmatrix}, \mathcal{A}_4 = \begin{bmatrix} \mathbf{0} & x_2 & \mathbf{0} \\ x_2^T & \mathbf{0} & \mathbf{0} \\ \mathbf{0} & \mathbf{0} & \mathbf{0} \end{bmatrix},$$

$$\mathcal{A}_5 = \begin{bmatrix} \mathbf{0} & \mathbf{0} & \mathbf{0} \\ \mathbf{0} & \mathbf{0} & y_2^T \\ \mathbf{0} & y_2 & \mathcal{Z}^{\Gamma_2}[v] \end{bmatrix} \text{ and } \mathcal{A}_6 = \begin{bmatrix} \mathbf{0} & \mathbf{0} & \mathbf{0} \\ \mathbf{0} & \mathbf{0} & y_1^T \\ \mathbf{0} & y_1 & \mathbf{0} \end{bmatrix}.$$

Again by using the same inequality,

$$\begin{aligned} \mathcal{E}(\mathcal{A}_1) &\leq \mathcal{E}(\mathcal{A}_3) + \mathcal{E}(\mathcal{A}_4) \\ &= \mathcal{Z}\mathcal{E}(\Gamma_1) + 2\sqrt{x_2^T x_2} = \mathcal{Z}\mathcal{E}(\Gamma_1) + 2\sqrt{d_u d_v^2} \end{aligned}$$

and the equality holds if and only if either u is an isolated vertex in Γ_1 or v is an isolated vertex in Γ_2 .

Similarly,

$$\begin{aligned} \mathcal{E}(\mathcal{A}_2) &\leq \mathcal{E}(\mathcal{A}_5) + \mathcal{E}(\mathcal{A}_6) \\ &= \mathcal{Z}\mathcal{E}(\Gamma_2) + 2\sqrt{y_1^T y_1} = \mathcal{Z}\mathcal{E}(\Gamma_2) + 2\sqrt{d_v d_u^2} \end{aligned}$$

with equality condition as stated above. □

The change in Zagreb energy by adding an edge between the two vertices of two different graphs is given below.

Theorem 7. Let Γ be a graph obtained by adding a bridge $e = uv$ between the vertices $u \in \mathcal{V}(\Gamma_1)$ and $v \in \mathcal{V}(\Gamma_2)$ and let d'_u and d'_v be the degrees of the vertices u and v in the original graphs Γ_1 and Γ_2 respectively. Then

$$\mathcal{Z}\mathcal{E}(\Gamma) \leq \mathcal{Z}\mathcal{E}(\Gamma_1) + \mathcal{Z}\mathcal{E}(\Gamma_2) + 2(\sqrt{d'_u} + \sqrt{d'_v} + d'_u + d'_v + 2)$$

and the equality holds if and only if u and v are isolated vertices in Γ .

Proof. The \mathcal{Z} -matrix corresponding to the above mentioned graph Γ is,

$$\mathcal{Z}^\Gamma = \begin{bmatrix} \mathcal{Z}^{\Gamma_1}[u] & [x_1 + \mathbf{J}_u] & \mathbf{0} & \mathbf{0} \\ [x_1 + \mathbf{J}_u]^T & \mathbf{0} & d'_u + d'_v + 2 & \mathbf{0} \\ \mathbf{0} & d'_u + d'_v + 2 & \mathbf{0} & [y_1 + \mathbf{J}_v]^T \\ \mathbf{0} & \mathbf{0} & [y_1 + \mathbf{J}_v] & \mathcal{Z}^{\Gamma_2}[v] \end{bmatrix}.$$

Here x_1 (and y_1) represents the column vector of \mathcal{Z}^{Γ_1} (and \mathcal{Z}^{Γ_2}) corresponding to the vertex u (and v) in the respective graph. The column vector \mathbf{J}_u is obtained by replacing all the non-zero entries of x_1 by 1 and, the column vector \mathbf{J}_v is obtained by replacing all the non-zero entries of y_1 by 1.

$$\mathcal{Z}^\Gamma = \mathcal{B}_1 + \mathcal{B}_2$$

where

$$\mathcal{B}_1 = \begin{bmatrix} \mathcal{Z}^{\Gamma_1}[u] & x_1 & \mathbf{0} & \mathbf{0} \\ x_1^\top & \mathbf{0} & \mathbf{0} & \mathbf{0} \\ \mathbf{0} & \mathbf{0} & \mathbf{0} & y_1^\top \\ \mathbf{0} & \mathbf{0} & y_1 & \mathcal{Z}^{\Gamma_2}[v] \end{bmatrix}$$

and

$$\mathcal{B}_2 = \begin{bmatrix} \mathbf{0} & \mathbf{J}_u & \mathbf{0} & \mathbf{0} \\ \mathbf{J}_u^\top & \mathbf{0} & d'_u + d'_v + 2 & \mathbf{0} \\ \mathbf{0} & d'_u + d'_v + 2 & \mathbf{0} & \mathbf{J}_v^\top \\ \mathbf{0} & \mathbf{0} & \mathbf{J}_v & \mathbf{0} \end{bmatrix}.$$

Hence by using the singular values inequality,

$$\mathcal{Z}\mathcal{E}(\Gamma) \leq \mathcal{E}(\mathcal{B}_1) + \mathcal{E}(\mathcal{B}_2). \quad (3)$$

Now, it is easy to observe that

$$\mathcal{E}(\mathcal{B}_1) = \mathcal{Z}\mathcal{E}(\Gamma_1) + \mathcal{Z}\mathcal{E}(\Gamma_2).$$

Let

$$\mathcal{B}_2 = \mathcal{B}_3 + \mathcal{B}_4,$$

where

$$\mathcal{B}_3 = \begin{bmatrix} \mathbf{0} & \mathbf{J}_u & \mathbf{0} & \mathbf{0} \\ \mathbf{J}_u^\top & \mathbf{0} & \mathbf{0} & \mathbf{0} \\ \mathbf{0} & \mathbf{0} & \mathbf{0} & \mathbf{J}_v^\top \\ \mathbf{0} & \mathbf{0} & \mathbf{J}_v & \mathbf{0} \end{bmatrix}$$

and

$$\mathcal{B}_4 = \begin{bmatrix} \mathbf{0} & \mathbf{0} & \mathbf{0} & \mathbf{0} \\ \mathbf{0} & \mathbf{0} & d'_u + d'_v + 2 & \mathbf{0} \\ \mathbf{0} & d'_u + d'_v + 2 & \mathbf{0} & \mathbf{0} \\ \mathbf{0} & \mathbf{0} & \mathbf{0} & \mathbf{0} \end{bmatrix}.$$

Therefore by applying the same inequality again, we get

$$\mathcal{E}(\mathcal{B}_2) \leq \mathcal{E}(\mathcal{B}_3) + \mathcal{E}(\mathcal{B}_4) = 2\sqrt{d'_u} + 2\sqrt{d'_v} + 2(d'_u + d'_v + 2). \quad (4)$$

Equality holds in the inequality (4), if and only if there exists an orthogonal matrix \mathcal{Q} , such that both $\mathcal{Q}\mathcal{B}_3$ and $\mathcal{Q}\mathcal{B}_4$ are positive semi-definite. If we assume the existence of such an orthogonal matrix \mathcal{Q} , we have

$$\begin{aligned} \mathcal{Q}^\top \mathcal{Q} &= \\ &= \begin{bmatrix} \mathbf{Q}_{11}^\top & \mathbf{Q}_{21}^\top & \mathbf{Q}_{31}^\top & \mathbf{Q}_{41}^\top \\ \mathbf{Q}_{12}^\top & \mathbf{Q}_{22}^\top & \mathbf{Q}_{32}^\top & \mathbf{Q}_{42}^\top \\ \mathbf{Q}_{13}^\top & \mathbf{Q}_{23}^\top & \mathbf{Q}_{33}^\top & \mathbf{Q}_{43}^\top \\ \mathbf{Q}_{14}^\top & \mathbf{Q}_{24}^\top & \mathbf{Q}_{34}^\top & \mathbf{Q}_{44}^\top \end{bmatrix} \begin{bmatrix} \mathbf{Q}_{11} & \mathbf{Q}_{12} & \mathbf{Q}_{13} & \mathbf{Q}_{14} \\ \mathbf{Q}_{21} & \mathbf{Q}_{22} & \mathbf{Q}_{23} & \mathbf{Q}_{24} \\ \mathbf{Q}_{31} & \mathbf{Q}_{32} & \mathbf{Q}_{33} & \mathbf{Q}_{34} \\ \mathbf{Q}_{41} & \mathbf{Q}_{42} & \mathbf{Q}_{43} & \mathbf{Q}_{44} \end{bmatrix} \\ &= \mathbf{I}, \end{aligned}$$

where \mathbf{Q}_{ij} , $1 \leq i, j \leq 4$, are assumed to have the appropriate size. Hence,

$$\begin{aligned} \mathbf{Q}_{12}^\top \mathbf{Q}_{12} + \mathbf{Q}_{22}^\top \mathbf{Q}_{22} + \mathbf{Q}_{32}^\top \mathbf{Q}_{32} + \mathbf{Q}_{42}^\top \mathbf{Q}_{42} &= \mathbf{I}, \\ \mathbf{Q}_{13}^\top \mathbf{Q}_{13} + \mathbf{Q}_{23}^\top \mathbf{Q}_{23} + \mathbf{Q}_{33}^\top \mathbf{Q}_{33} + \mathbf{Q}_{43}^\top \mathbf{Q}_{43} &= \mathbf{I}, \end{aligned} \quad (5)$$

$$\mathcal{Q}\mathcal{B}_4 = \begin{bmatrix} \mathbf{0} & \mathbf{Q}_{13}(d'_u + d'_v + 2) & \mathbf{Q}_{12}(d'_u + d'_v + 2) & \mathbf{0} \\ \mathbf{0} & \mathbf{Q}_{23}(d'_u + d'_v + 2) & \mathbf{Q}_{22}(d'_u + d'_v + 2) & \mathbf{0} \\ \mathbf{0} & \mathbf{Q}_{33}(d'_u + d'_v + 2) & \mathbf{Q}_{32}(d'_u + d'_v + 2) & \mathbf{0} \\ \mathbf{0} & \mathbf{Q}_{43}(d'_u + d'_v + 2) & \mathbf{Q}_{42}(d'_u + d'_v + 2) & \mathbf{0} \end{bmatrix}.$$

Since QB_4 is diagonally dominant, we have $Q_{13} = Q_{12} = Q_{43} = Q_{42} = 0$, as $d'_u + d'_v + 2$ can not be equal to zero. So Equation (5) reduces to

$$\begin{aligned} Q_{22}^T Q_{22} + Q_{32}^T Q_{32} &= I, \\ Q_{23}^T Q_{23} + Q_{33}^T Q_{33} &= I. \end{aligned} \quad (6)$$

Also,

$$\begin{aligned} QB_3 &= \begin{bmatrix} Q_{12}J_u^T & Q_{11}J_u & Q_{14}J_v & Q_{13}J_u^T \\ Q_{22}J_u^T & Q_{21}J_u & Q_{24}J_v & Q_{23}J_u^T \\ Q_{32}J_u^T & Q_{31}J_u & Q_{34}J_v & Q_{33}J_u^T \\ Q_{42}J_u^T & Q_{41}J_u & Q_{44}J_v & Q_{43}J_u^T \end{bmatrix} \\ &= \begin{bmatrix} 0 & Q_{11}J_u & Q_{14}J_v & 0 \\ Q_{22}J_u^T & Q_{21}J_u & Q_{24}J_v & Q_{23}J_u^T \\ Q_{32}J_u^T & Q_{31}J_u & Q_{34}J_v & Q_{33}J_u^T \\ 0 & Q_{41}J_u & Q_{44}J_v & 0 \end{bmatrix}, \end{aligned}$$

Again, $Q_{11}J_u = Q_{14}J_v = Q_{22}J_u^T = Q_{32}J_u^T = Q_{41}J_u = Q_{44}J_v = Q_{33}J_u^T = Q_{23}J_u^T = 0$, as QB_3 is also diagonally dominant.

Now, from Equation (6),

$$\begin{aligned} J_u &= J_u Q_{22}^T Q_{22} + J_u Q_{32}^T Q_{32} \\ &= [Q_{22}J_u^T]^T Q_{22} + [Q_{32}J_u^T]^T Q_{32} = 0, \\ J_v &= J_v Q_{23}^T Q_{23} + J_v Q_{33}^T Q_{33} \\ &= [Q_{23}J_v^T]^T Q_{23} + [Q_{33}J_v^T]^T Q_{33} = 0, \end{aligned}$$

which implies both u and v are isolated vertices in Γ_1 and Γ_1 respectively.

Now, it is direct that equality in (3) holds only if the equality in (4) holds and it is direct that, the equality in (3) holds when u and v are isolated vertices in Γ_1 and Γ_2 respectively. Hence the result follows. \square

The energy of a graph and a subgraph obtained by deleting an edge is discussed below.

Theorem 8. Let Γ be a graph and $e = uv$ be an edge in Γ and let d_u and d_v be the degrees of the vertices u and v in the resultant graph $\Gamma - e$. Then

$$\mathcal{ZE}(\Gamma - e) \geq \mathcal{ZE}(\Gamma) - 2(\sqrt{d_u} + \sqrt{d_v} + d_u + d_v + 2)$$

with equality if and only if $e = uv$ is an isolated edge in Γ .

Proof. Consider

$$\mathcal{Z}^\Gamma = \begin{bmatrix} \mathcal{Z}^\Gamma[u, v] & [x_1 + x_2] & [y_1 + y_2] \\ [x_1 + x_2]^T & \mathbf{0} & d_u + d_v + 2 \\ [y_1 + y_2]^T & d_u + d_v + 2 & \mathbf{0} \end{bmatrix},$$

where x_1 and y_1 represents the column vector of \mathcal{Z}^Γ corresponding to the vertex u and v . The column vector x_2 is obtained by replacing all the non-zero entries of x_1 by -1 and, the column vector y_2 is obtained by replacing all the non-zero entries of y_1 by -1 .

The proof follows similarly. \square

4. Applications

Pi-electron energy is an important concept in chemistry and material science. It is crucial in describing electron interactions in the *pi*-orbitals of adjacent atoms in conjugated systems such as double bonds and aromatic rings. These *pi*-electrons' energy levels have an impact on the stability, reactivity, and electronic properties of organic compounds and conjugated materials. By using the Hückel molecular orbital (HMO) theory one can get many important properties of the conjugated molecules using the total *pi*-electron energy.

For vinyl compounds specifically, which are organic compounds containing the vinyl functional group ($R-CH=CH_2$), the Total *pi*-electron energy would quantify the energy associated with the *pi*-electrons within the double bond. The Zagreb indices would describe the molecular size and branching patterns of the compound's structure. The *pi*-electron energy of the polyenes and vinyl compounds [14] are compared with the Zagreb energy and also the scatter plot

is shown in Fig. 1, which shows that the Zagreb energy and π -electron energy are highly correlated with the correlation coefficient of 0.9971.

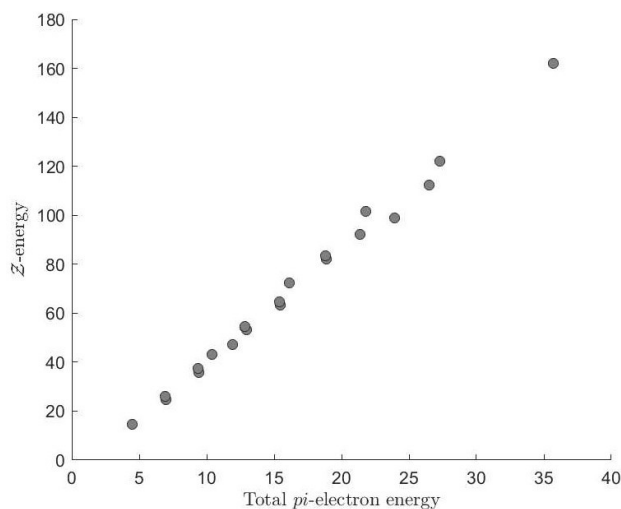


FIG. 1. Scatter plot of total π -electron energy v/s Z -energy of polyenes and vinyl compounds.

The acentric factor is directly related to the critical properties of a substance, such as its critical temperature and critical pressure. R. Zheng et al. [15], have compared the experimental results of entropy and acentric factor of octane isomers (Fig. 2) with the spectral radius of Arithmetic-Geometric (\mathcal{AG}), Atom Bond Connectivity (\mathcal{ABC}) and Sombor (\mathcal{S}) matrix of the molecular graphs of the same. For octane isomers, they found that correlation coefficient of the spectral radius of \mathcal{AG} , \mathcal{ABC} and \mathcal{S} with entropy are -0.917 , -0.906 and -0.912 , respectively, and with acentric factor it is found to be -0.947 – 0.930 and -0.962 , respectively.

The acentric factor depends on molecular shape and size, which are influenced by factors such as molecular weight, branching, and symmetry. Alkanes with higher molecular weight and more branching tend to have higher acentric factors because they deviate more from spherical shape and have greater molecular interactions. Entropy is a measure of the number of microscopic configurations or arrangements that are consistent with the macroscopic state of a system. In general, increasing molecular branching tends to increase entropy. This is because branching increases the number of possible arrangements of the molecules, leading to a greater number of microstates accessible to the system. Contrary to this, the spectral radius of graphs (in general) decreases if they deviate more from spherical shape. That is, star graph has the maximum spectral radius ($\sqrt{n-1}$) and path graph has the minimum ($2 \cos \frac{\pi}{n+1}$). The correlation study of thermodynamic properties of aromatic compounds with the various topological indices obtained from the eigenvalues of the adjacency matrix has been carried out in [16]. The present study shows that, Z -spectral radius and the acentric factor (entropy) of the octane isomers are negatively correlated with the correlation coefficient of -0.974 (-0.9168). The experimental values of the entropy and acentric factor of octane isomers were taken from [15].

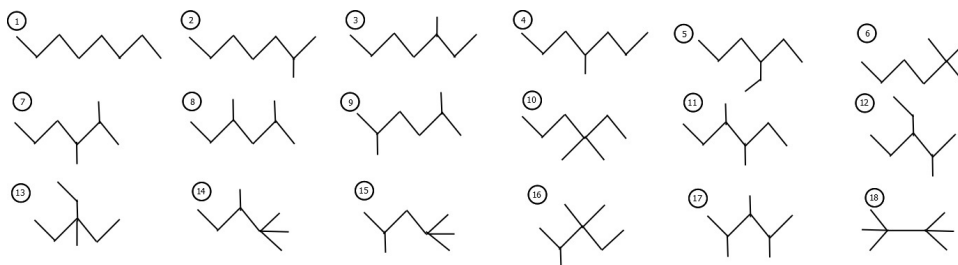


FIG. 2. Octane isomers

Since these factors are well correlated, we can predict the acentric factor and entropy of the octane isomers. Now, from Figs. 6 and 7 we have

$$\begin{aligned} \text{acnfac} &= -0.02172 \times \zeta_1 + 0.5597, \\ \text{entropy} &= -2.606 \times \zeta_1 + 132.3. \end{aligned}$$

The experimental values of density (in g/cm^3), refractive index and acentric factors of the n -alkanes from C_2 to C_{30} are taken from [17] and from [18–20] and also the Z -spectral radius and Z -energy of the molecular graph of the same has

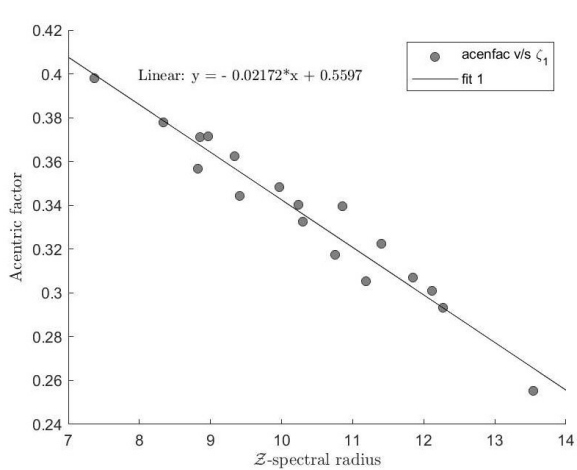


FIG. 3. Linear fit for the scatter plot of acenfac v/s \mathcal{Z} -spectral radius.

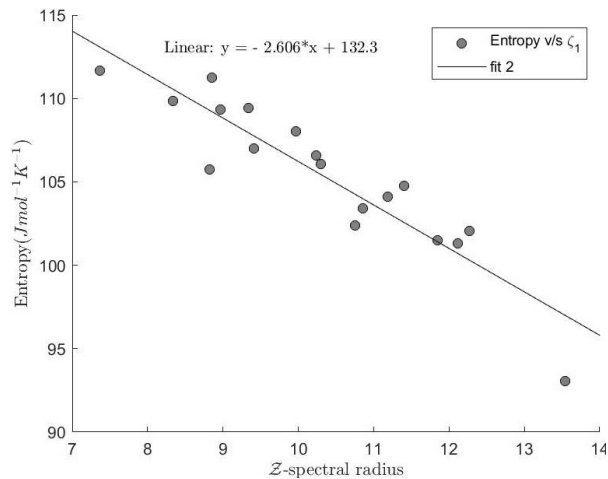


FIG. 4. Linear fit for the scatter plot of entropy v/s \mathcal{Z} -spectral radius.

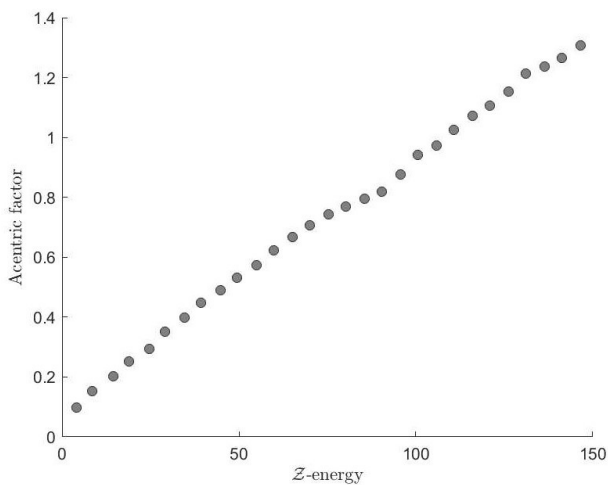


FIG. 5. Scatter plot of acentric factor against Zagreb energy.

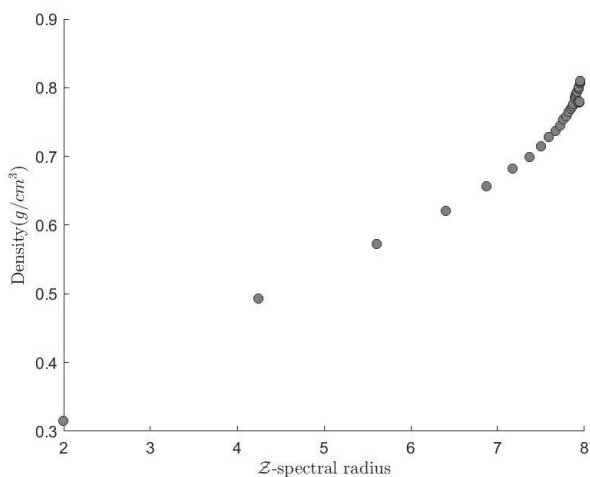


FIG. 6. Scatter plot of density (in gcm^{-3}) against Zagreb spectral radius.

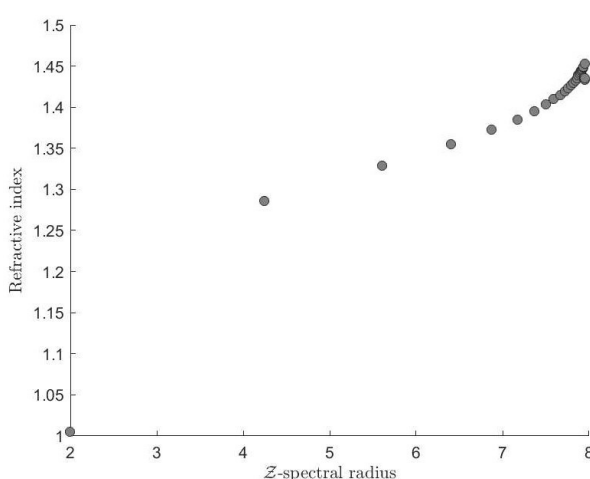


FIG. 7. Scatter plot of refractive index against Zagreb spectral radius.

been computed. Previously, it is observed that the acentric factors of octane isomers are negatively correlated to the \mathcal{Z} -spectral radius. Now, a very high positive correlation between the \mathcal{Z} -energy and the acentric factor of n -alkanes has been observed, where the correlation coefficient is found to be 0.9989. Even though the branching is similar, the number of carbon atoms are different and more the number of carbon atoms higher the Zagreb energy (of its graphical representation) and also the acentric factor. This increase in acentric factor is because, longer the carbon chain in n -alkanes (i.e., as n increases), more will be the deviation from the spherical shape.

When a molecule is highly branched, it tends to have a lower density compared to a molecule with a linear or less-branched structure. This lower density can lead to a decrease in the refractive index of the material. Hence as expected, it is found that, density and refractive index of the n -alkanes are positively correlated to \mathcal{Z} -spectral radius, with respective correlation coefficient of 0.9821 and 0.9693. Figs.5,6 and 7 show that one can predict the acentric factor (and hence the critical properties), density and refractive index of n -alkanes, just by computing the \mathcal{Z} -spectral radius and \mathcal{Z} -energy.

Conclusion

In this paper, we found some bounds for the spectral radius of the Zagreb matrix of graphs and also we study how it changes during the deletion and rotation of an edge. Also, the change in Zagreb energy of a graph, which is obtained by deleting an edge or identifying the end vertices of an edge, are studied. Mainly, the excellent correlation between the acentric factor (density, refractive index) of n -alkanes and the Zagreb energy (and spectral radius) of the molecular graph of the same has been observed.

References

- [1] Gutman I. and Furtula B. *Graph energies and their applications*. Bulletin (Académie serbe des sciences et des arts. Classe des sciences mathématiques et naturelles. Sciences mathématiques), 2019, **44**, P. 29–45.
- [2] Gutman I. The energy of a graph. *Ber. Math. Stat. Sect. Forschungsz. Graz.*, 1978, **103**, P. 1–22.
- [3] Bozkurt S.B., A. Dilek G., Gutman I. and Cevik A.S. Randic matrix and Randic energy. *MATCH Commun. Math. Comput. Chem.*, 2010, **64**(1), P. 239–250.
- [4] Gutman I. and Trinajstić N. Graph theory and molecular orbitals. Total ϕ -electron energy of alternant hydrocarbons. *Chem. phys. lett.*, 1972, **17**(4), P. 535–538.
- [5] Gutman I. and Das K.C. The first Zagreb index 30 years after. *MATCH Commun. Math. Comput. Chem.*, 2004, **50**(1), P. 83–92.
- [6] Nikolić S., Kovačević G., Miličević A. and Trinajstić N. The Zagreb indices 30 years after. *Croatica Chemica Acta*, 2003, **76**(2), P. 113–124.
- [7] Shetty S.S. and Bhat K.A. On the first Zagreb index of graphs with self-loops. *AKCE Inter. J. Graphs Comb.*, 2023, **20**(3), P. 326–331.
- [8] Rad N.J., Jahanbani A., and Gutman I. Zagreb energy and Zagreb estrada index of graphs. *MATCH Commun. Math. Comput. Chem.*, 2018, **79**, P. 371–386.
- [9] West D.B. *Introduction to graph theory*, **2**. Prentice Hall Upper Saddle River, 2001.
- [10] Johnson C.R. and Horn R.A. *Matrix analysis*, Cambridge university press, Cambridge, 1985.
- [11] Yuan H. A bound on the spectral radius of graphs. *Linear Algebra Appl.* 1988, **108**, P. 135–139.
- [12] Stevanovic D. *Spectral radius of graphs*, Birkhäuser, 2014.
- [13] So W., Robbiano M., N.M.M. de Abreu and Gutman I. Applications of theorem by Ky Fan in the theory of graph energy. *Linear Algebra Appl.*, 2010, **432**(9), P. 2163–2169.
- [14] Coulson C.A. and Streitwieser A. *Dictionary of π -electron calculations*. Pergamon Press, 1965.
- [15] Zheng R., Su P. and Jin X. Arithmetic-geometric matrix of graphs and its applications. *Applied Math. Comput.*, 2023, **442**, P. 371–386.
- [16] Hayat S., Mahadi H., Alanazi S. and Wang S. Predictive potential of eigenvalues-based graphical indices for determining thermodynamic properties of polycyclic aromatic hydrocarbons with applications to polyacenes. *Computat. Materials Sci.*, 2024, **238**, P. 112944.
- [17] <https://www.nist.gov/srd>
- [18] Ohse R.W. and Tippelskirch H.V. The critical constants of the elements and of some refractory materials with high critical temperatures. *High Temperatures-High Pressures*, 1977, **9**(4), P. 367–385.
- [19] Wang Q., Jia Q. and Ma P. Prediction of the acentric factor of organic compounds with the positional distributive contribution method. *Journal of Chemical & Engineering Data*, 2012, **57**(1), P. 169–189.
- [20] Yaws C.L. *The yaws handbook of physical properties for hydrocarbons and chemicals: physical properties for more than 54,000 organic and inorganic chemical compounds, Coverage for C1 to C100 Organics and Ac to Zr Inorganics*. Gulf Professional Publishing, 2015.

Submitted 23 January 2024; revised 30 April 2024; accepted 11 May 2024

Information about the authors:

Shashwath S. Shetty – Department of Mathematics, Manipal Institute of Technology, Manipal Academy of Higher Education, Manipal, Karnataka, 576104, India; ORCID 0009-0004-0324-1835; shashwathshetty01334@gmail.com

K. Arathi Bhat – Department of Mathematics, Manipal Institute of Technology, Manipal Academy of Higher Education, Manipal, Karnataka, 576104, India; ORCID 0000-0002-1526-5760; arathi.bhat@manipal.edu

Conflict of interest: the authors declare no conflict of interest.

Errors of In-Phase and Quadrature demodulation method created by low-pass filter

George P. Miroshnichenko^a, Alina N. Arzhanenkova^b, Michail Yu. Plotnikov^c

ITMO University, St. Petersburg, Russia

^agpmirosh@gmail.com, ^b11arzh11@gmail.com, ^cplotnikov-michael@yandex.ru

Corresponding author: George P. Miroshnichenko, gpmirosh@gmail.com

ABSTRACT This article explores phase errors created by low-pass filter in interferometric signals which are processed by In-Phase and quadrature demodulation algorithm (IQ-demodulation). These errors were calculated using the analytical method and were compared with mathematical modeling, which uses pre-calculated parameters: phase, sampling period, infinitesimal parameters. In this paper, we show that phase errors calculated with analytical method clearly correlate with mathematical modeling errors. This work made it possible to calculate corrections to the demodulated phase, which, in turn, made it possible to refine the phase calculation step in IQ demodulation algorithm using the arctangent function. The resulting formulas describing the correction to the demodulated phase will increase the accuracy of the quadrature method, which is used to process signals from interferometric devices of various types, such as: reflectometers, geophysical seismic systems, interferometric radiometry, etc.

KEYWORDS demodulation, IQ demodulation, interferometry, measurement errors, sawtooth modulation

ACKNOWLEDGEMENTS The research was carried out within the state assignment of Ministry of Science and Higher Education of the Russian Federation (project No. FSER-2024-0006)

FOR CITATION Miroshnichenko G.P., Arzhanenkova A.N., Plotnikov M.Yu. Errors of In-Phase and Quadrature demodulation method created by low-pass filter. *Nanosystems: Phys. Chem. Math.*, 2024, **15** (3), 325–331.

1. Introduction

Fiber-optical interferometric sensors based on phase difference measurement in signal and control interferometer arms, which is created by the interaction of the fiber and environment. Mach–Zehnder, Michelson, Sagnac and Fabry–Perot interferometers are often used as sensors. It can also be “moving” interferometers, where interfering beams are Rayleigh scattering waves which were excited by a light pulse propagating in the fiber, as it happens, for example, in coherent reflectometry schemes. Optical circuits, which are used to measure phase shifts, implement three classical phase demodulation methods: Phase Generated Carrier (PGC) demodulation method, 3×3 coupler demodulation method, and In-phase and Quadrature (IQ) demodulation method [1]. Phase demodulation is used in many interferometric devices such as temperature and pressure sensors, fiber accelerometers and hydrophones, which are used in seismoacoustic streamers [2, 3].

Signal $S_{in}(t)$ taken from detector, value of the intensity of interfering waves, consists of two terms:

$$S_{in}(t) = F + G \cdot \cos(\omega t + \varphi(t)). \quad (1)$$

The first term, F , is the total intensity of the interfering waves, the second term is the interfering term which changes periodically with the modulation frequency ω and depends on the signal (measured) phase $\varphi(t)$. Parameter G determines so-called interference fringes visibility G/F .

Variable signal changed at high frequency ω and depends on slow-changed phase, which contains environment information. This method use two local oscillator signals which changed at frequency ω and shifted related to each other at $\pi/2$ radians in phase:

$$L_1(t) = I \cdot \cos(\omega t), \quad L_2(t) = I \cdot \sin(\omega t),$$

where I is the local oscillator intensity value.

Signals of local oscillators are multiplied with processed signal (1). As a result of applying low-frequency filters in this method, two low-frequency signals generate two quadratures: changing in phase (In-phase signal) and shifted by (Quadrature signal) signals

$$C(t) = G \cdot I \cdot \cos(\varphi(t)), \quad S(t) = G \cdot I \cdot \sin(\varphi(t)).$$

Subsequent processing of quadrature allows one to determine the phase and the amplitude of measured signal.

$$G \cdot I = \sqrt{S(t)^2 + C(t)^2}, \quad \varphi(t) = \arctan\left(\frac{S(t)}{C(t)}\right).$$

2. Previous researches

IQ demodulation scheme is the part, for example, of schemes for coherent phase-sensitive optical reflectometry of fiber optic channels in the time domain (Φ -OTDR). Phase demodulation of the backscattered light interference signal provides unique local information about the state of the optical fiber at distances of hundreds of kilometers. A balanced photodetector measures the temporal speckle of the interference. By monitoring the change in the speckle for successive injected pulses, one can detect a local change in the refractive index of the fiber under test. In a heterodyne detection system, an intermediate frequency signal, on the order of 200 MHz, at the output of a photon balanced detector, is acquired by a data acquisition system at a sampling rate several times that of the intermediate frequency, and digital In-phase/Quadrature (IQ) demodulation is performed to obtain phase information [2, 4–19]. In articles [2, 4, 5, 10], an optical IQ demodulation scheme instead of digital RF demodulation is presented. Here, a 90-degree optical hybrid is used to obtain the IQ components of the Rayleigh backscatter signal, which can significantly reduce computational costs. In [2], a heterodyne polling system for an array of interferometric fiber optic sensors with time multiplexing is used to demodulate the phase shift using the IQ demodulation method. The interference signal is generated in unbalanced Michelson interferometers. The method showed a high degree of linearity and a low level of noise. Heterodyne reception transfers the 1550.12 nm signal to the 200 MHz intermediate frequency region, where IQ method is used to extract the phase. Quadrature signal processing has a unique advantage in demodulating fiber Bragg grating interferometer sensors [2, 11, 15], which convert strain-induced changes in the Bragg wavelength into changes in intensity.

The quality of phase and amplitude reproduction depends on the noise level of the installation, among which, the main ones are: shot noise (depending on the dark current of the detector and on the receiver bandwidth), thermal noise (depending on the absolute temperature and load resistor) [10]. The articles [2, 4, 6–8, 11] analyze a possible drawback of the IQ demodulation method associated with inevitable hardware defects. This is an imbalance of quadrature amplitudes, which can manifest itself in both the DC and AC components of the received signals. An IQ imbalance can lead to signal distortion and reduced signal-to-noise ratio. In the listed works, a method for compensating for the imbalance was developed. As shown in [2], after compensation for the amplitude imbalance in the demodulated signals, there are still some internal distortions that arise due to the time skew and phase mismatch of the IQ signals. This article proposes a new method that takes into account the effects of high frequency cable length differences, fiber length differences, and non-orthogonality between IQ signals, providing a basis for accurate real-time compensation.

In this work, we neglect the noise characteristics in the signal $S_{in}(t)$, so signal $S_{in}(t)$ is written as follows:

$$S_{in}(t) = F + G \cdot \cos(\text{Saw}(t) + \varphi(t)). \quad (2)$$

After that, we explore corrections to quadrature signals $S(t)$, $C(t)$ from LPF. Here we used sawtooth phase modulation $\text{Saw}(t)$, which depends on time, with “saw” tilt Ω and period T_c .

3. LPF-moving average filter

Main characteristics of any non-recursive low-pass filter are frequency response, impulse response, and impulse response width [20]. Discrete moving average filter, which used in ADC (analog-to-digital converters), has the following impulse response:

$$y_n = \frac{1}{P} \cdot \sum_{j=n}^{n+P-1} x_j. \quad (3)$$

Here, P is the averaging interval (filter order), ω_d is the sampling frequency, ω_c is the modulation frequency.

$$P = \frac{\omega_d}{\omega_c} = \frac{T_c}{T_d}.$$

It should be remembered, that ω_c is always less than Nyquist frequency $\omega_d/2$. This condition means that $P > 2$. Here T_c is the modulation period, T_d is the sampling period. With this choice of filter order, we obtain the important relation

$$\sum_{j=n}^{n+P-1} \exp(i \cdot r \cdot \omega_c \cdot j \cdot T_d) = 0, \quad (4)$$

where r is an integer. Let's write formula (3) in continuous form, assuming that

$$y(t) = \frac{1}{T_c} \cdot \int_t^{t+T_c} x(t') dt'. \quad (5)$$

Feature (4) is true in continuous form:

$$\int_t^{t+T_c} \exp(i \cdot r \cdot \omega_c \cdot t') dt' = 0.$$

Apply formula (5) to function

$$x(t') = \cos(\omega_c t' + \varphi(t')) \cdot \cos(\omega_c t'). \quad (6)$$

Suppose that function $\varphi(t')$ can be expanded in a Taylor series near point $t' = t$. Let us take two terms of this series on the segment $t + T_c \geq t' \geq t$

$$\varphi(t') \approx \varphi(t) + \dot{\varphi}(t) \cdot (t' - t),$$

where $\dot{\varphi}(t)$ denotes the derivative.

The function slowly changes over this interval. Integral (5) is approximately calculated

$$\begin{aligned} y(t) &= \frac{1}{T_c} \cdot \int_t^{t+T_c} \cos(\omega_c \cdot t' + \varphi(t')) \cdot \cos(\omega_c \cdot t') dt' \\ &\approx \frac{1}{T_c} \cdot \int_t^{t+T_c} \cos((\omega_c + \dot{\varphi}(t)) \cdot t' + \varphi(t) - \dot{\varphi}(t) \cdot t) \cdot \cos(\omega_c \cdot t') dt'. \end{aligned}$$

The integral is as follows

$$y(t) = \frac{1}{T_c} \sin\left(\dot{\varphi}(t) \frac{T_c}{2}\right) \left(\frac{\cos\left(\varphi(t) + \dot{\varphi}(t) \frac{T_c}{2}\right)}{\dot{\varphi}(t)} + \frac{\cos\left((2\omega_c t + \varphi(t) + \dot{\varphi}(t) \frac{T_c}{2})\right)}{2\omega_c + \dot{\varphi}(t)} \right). \quad (7)$$

Assuming that $\dot{\varphi}(t) T_c/2 \ll 1$, we obtain the approximate solution

$$y(t) \approx \frac{1}{2} \cos\left(\varphi(t) + \dot{\varphi}(t) \frac{T_c}{2}\right) + \frac{\dot{\varphi}(t)}{4\omega_c} \cos\left(2\omega_c t + \varphi(t) + \dot{\varphi}(t) \frac{T_c}{2}\right). \quad (8)$$

Formula (8) provides a first-order correction for the rate of phase change $\varphi(t)$ to the result of averaging the function (6), obtained using formula (5). It is easy to show that the discrete version of the moving average filter formula (3) gives a similar formula for the averaging correction. Therefore, further corrections to the signals will be calculated using simple formula (5).

4. Signals correction

Let's find corrections to signals $S(t)$, $C(t)$ with using formula of moving average filter in continuous form. By definition, signals $S(t)$, $C(t)$ are calculated by formulas (with using LP moving average filter)

$$\begin{aligned} C(t) &= \frac{1}{T_c} \cdot \int_t^{t+T_c} \frac{S_{in}(t')}{G} \cdot \cos(\omega_c t') dt', \\ S(t) &= \frac{1}{T_c} \cdot \int_t^{t+T_c} \frac{S_{in}(t')}{G} \cdot \sin(\omega_c t') dt'. \end{aligned}$$

After substitution of (2), one obtains

$$\begin{aligned} C(t) &= \frac{1}{T_c} \cdot \int_t^{t+T_c} \cos(\text{Saw}(t') + \varphi(t')) \cdot \cos(\omega_c t') dt', \\ S(t) &= \frac{1}{T_c} \cdot \int_t^{t+T_c} \cos(\text{Saw}(t') + \varphi(t')) \cdot \sin(\omega_c t') dt'. \end{aligned}$$

The time axis is divided into intervals of width T_c . Let's say that selected random moment of time t' belongs to interval with number k , so that moment t' is located in interval $kT_c \leq t' \leq (k+1)T_c$. Moment $t' + T_c$ is located in interval $(k+1)T_c < t' \leq (k+2)T_c$. Sawtooth curve $\text{Saw}(t')$ is as follows:

$$\text{Saw}(t') = \begin{cases} \Omega \cdot (t' - kT_c), & kT_c \leq t' \leq (k+1)T_c; \\ \Omega \cdot (t' - (k+1)T_c), & (k+1)T_c < t' \leq (k+2)T_c. \end{cases} \quad (9)$$

Substitution of (9) into integrals for $S(t)$, $C(t)$ gives one the following expressions:

$$\begin{aligned} C(t) &= \frac{1}{T_c} \cdot \int_t^{(k+1)T_c} \cos(\Omega \cdot (t' - kT_c) + \varphi(t')) \cdot \cos(\omega_c t') dt' \\ &+ \frac{1}{T_c} \cdot \int_{(k+1)T_c}^{t+T_c} \cos(\Omega \cdot (t' - kT_c) + \varphi(t')) \cdot \cos(\omega_c t') dt', \\ S(t) &= \frac{1}{T_c} \cdot \int_t^{(k+1)T_c} \cos(\Omega \cdot (t' - kT_c) + \varphi(t')) \cdot \sin(\omega_c t') dt' \\ &+ \frac{1}{T_c} \cdot \int_{(k+1)T_c}^{t+T_c} \cos(\Omega \cdot (t' - kT_c) + \varphi(t')) \cdot \sin(\omega_c t') dt'. \end{aligned}$$

Suppose that angle of “saw” differs little from ω_c

$$\Omega = \omega_c - \Delta, \quad |\Delta| \ll \omega_c.$$

Phase $\varphi(t')$ changes slowly enough (doesn't exceed dynamic range), so $\dot{\varphi}(t) \ll \omega_c$. Let's introduce infinitesimal order:

$$\zeta = \frac{\Delta}{\omega_c}, \quad \xi = \frac{\dot{\varphi}(t)}{\omega_c}.$$

Let us find functions $S(t)$, $C(t)$ with first order accuracy in parameters ζ , ξ . One can write

$$\begin{aligned} S(t) &= S^{(0)}(t) + \delta_s(t), \\ C(t) &= C^{(0)}(t) + \delta_c(t) \end{aligned}$$

and obtain

$$\begin{aligned} S^{(0)}(t) &= -\frac{1}{2} \sin(\varphi(t)), \\ C^{(0)}(t) &= \frac{1}{2} \cos(\varphi(t)), \\ \delta_s(t) &= -\frac{1}{4} \zeta \cdot \sin(\varphi(t)) + \frac{\pi}{2} (\zeta - \xi) \cdot \cos(\varphi(t)) + \frac{1}{4} \xi \cdot \sin(2\omega_c t + \varphi(t)), \\ \delta_c(t) &= -\frac{1}{4} \zeta \cdot \cos(\varphi(t)) + \frac{\pi}{2} (\zeta - \xi) \cdot \sin(\varphi(t)) + \frac{1}{4} \xi \cdot \cos(2\omega_c t + \varphi(t)). \end{aligned}$$

5. ATAN-method of phase calculation $\varphi(t)$ and results

Phase $\varphi(t)$ calculation is made with arctangent function in the IQ protocol. Due to the filtering error, the calculated phase $\tilde{\varphi}(t)$ will be distorted. Let's find excited phase within the first order of ξ , ζ parameters:

$$\begin{aligned} \tilde{\varphi}(t) &= \arctan\left(\frac{-S(t)}{C(t)}\right) = \arctan\left(\frac{\sin(\varphi(t))}{\cos(\varphi(t))} (1 - \gamma(t))\right), \\ \gamma(t) &= 2 \frac{\delta_c(t)}{\cos(\varphi(t))} + 2 \frac{\delta_s(t)}{\sin(\varphi(t))}. \end{aligned}$$

Finally, phase with LPF errors is calculated as follows:

$$\tilde{\varphi}(t) = \varphi(t) - \pi(\zeta - \xi) + \frac{1}{2} \zeta \cdot \sin(2\varphi(t)) - \frac{1}{2} \xi \cdot \sin(2\omega_c t + 2\varphi(t)). \quad (10)$$

Let's determine the theoretical correction to the calculated phase

$$\Delta\Phi_{\text{teor}}(t) = \tilde{\varphi}(t) - \varphi(t). \quad (11)$$

Now we need to perform mathematical modeling of the IQ demodulation algorithm. Let us choose the phase change function as follows:

$$\begin{aligned} \varphi(t) &= \pi(\cos(0.05 \cdot \nu_c \cdot t) - 1), \\ \nu_c &= \frac{\omega_c}{2\pi} = 2 \cdot 10^4, \text{ s}^{-1}. \end{aligned} \quad (12)$$

Select the sampling step Δt , which is equal to the sampling period:

$$\Delta t = T_d = 5 \cdot 10^{-7}, \text{ s.}$$

Modelling steps are as follows:

1. Input signal (2) is multiplied by two harmonics: $\cos(\omega_c t)$ and $\sin(\omega_c t)$, which gives one the following functions:

$$\begin{aligned} FC(t) &= \cos(\text{Saw}(t) + \varphi(t)) \cdot \cos(\omega_c t), \\ FS(t) &= \cos(\text{Saw}(t) + \varphi(t)) \cdot \sin(\omega_c t). \end{aligned}$$

2. These functions are discretized:

$$\begin{aligned} FC_p &= FC(\Delta t \cdot p), \\ FS_p &= FS(\Delta t \cdot p). \end{aligned}$$

3. The resulting vectors are filtered using the moving average method:

$$\begin{aligned} C_n &= \frac{1}{P} \cdot \sum_{j=n}^{n+P-1} FC_j, \\ S_n &= \frac{1}{P} \cdot \sum_{j=n}^{n+P-1} FS_j. \end{aligned}$$

4. Next, we applied the ATAN procedure allowing us phase calculation, which values are continuously extended from the range of arctangent function to the whole axis. The result is the distorted phase $\tilde{\varphi}_n$, found in discretization points:

$$\tilde{\varphi}_n = \arctan\left(-\frac{S_n}{C_n}\right).$$

5. Let us introduce the notation for the experimental correction

$$\Delta\Phi_{\text{exp}}(t) = \tilde{\varphi}_n - \varphi(\Delta t \cdot n). \quad (13)$$

and compare graphically $\Delta\Phi_{\text{teor}}(t)$ and $\Delta\Phi_{\text{exp}}(t)$.

Figure 1 shows ‘‘saw’’ graph with taking into account the form error ζ , $\zeta = 0.1$. A study of the thermal modulation process of VCSEL wavelength is presented in paper [21] for the case of periodic sinusoidal modulation.

For chosen $\varphi(t)$ (12) the maximum parameter ξ is

$$\xi_{\text{max}} = 0.025.$$

Figure 2 demonstrates error in phase determining found by the method of mathematical modeling and the error in phase determining, calculated using formula (10). One can see that the result of mathematical modelling of phase errors and the result of analytical phase errors calculation is almost identical.

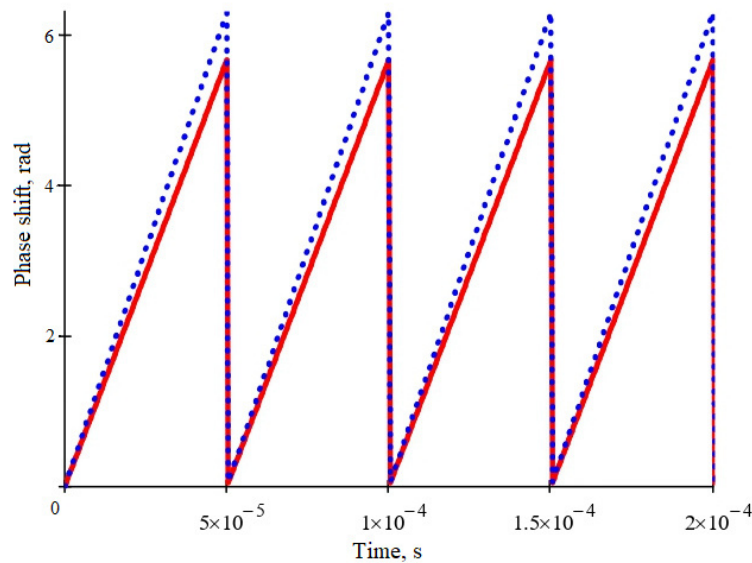


FIG. 1. VCSEL sawtooth phase modulation. Solid line – distorted saw with incline Ω (9), dotted line – ideal saw with incline ω_c .

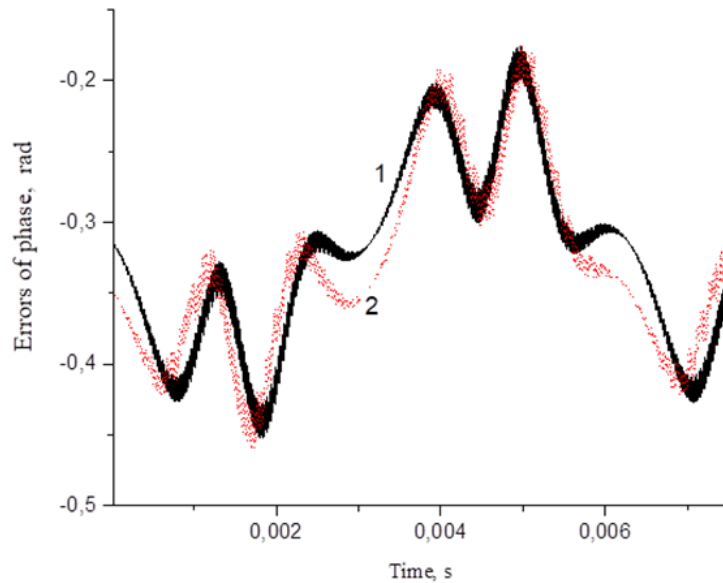


FIG. 2. Phase errors, 1 – analytically calculated error $\Delta\Phi_{\text{teor}}(t)$ (11), 2 – experimentally calculated error $\Delta\Phi_{\text{exp}}(t)$ (13)

6. Conclusion

This article is devoted to the study of errors that arise in the demodulated phase due to the passage of the processed signal through a low-pass filter in the IQ algorithm. In this work, we considered a signal with sawtooth wavelength modulation, which has its own form errors which further distorts the signal supplied to the demodulation circuit. Taking into account the saw shape error, as well as taking into account the calculated phase corrections due to the influence of the moving average filter, an adjusted formula for the signal was obtained, which is fed to the IQ processing circuit. To confirm the calculations, mathematical modeling was carried out using experimentally obtained parameters. It is shown that the results of modeling and analytical solutions correlate well with each other. This work will improve the quadrature demodulation method, which will allow better processing of data from interferometric sensors using VCSEL as a source.

References

- [1] Li Y., et al. Phase Demodulation Methods for Optical Fiber Vibration Sensing System: A Review. *IEEE Sensors J.*, 2022, **22** (3), P. 1842–1866.
- [2] Guojie Tu, Benli Yu, Mengmeng Zhao, Jiping Lin. A phase-sensitive optical time-domain reflectometry system with an electrical IQ demodulator. *Proceedings of the SPIE 10821, Advanced Sensor Systems and Applications VIII*, 2018, 1082123.
- [3] Hartog A., Frignet B., Mackie D., Clark M. Vertical seismic optical profiling on wireline logging cable. *Geophysical Prospecting*, 2014, **62**, P. 693–701.
- [4] He X., et al. Multi-event waveform-retrieved distributed optical fiber acoustic sensor using dual-pulse heterodyne phase-sensitive OTDR. *Optics Letters*, 2017, **42**, P. 442–445.
- [5] Yu M., Liu M., Chang T., Lang J., Chen J., Cui H.-L. Phase-sensitive optical time-domain reflectometric system based on a single-source dual heterodyne detection scheme. *Applied Optics*, 2017, **56**, P. 4058–4064.
- [6] Lu Y., Zhu T., Chen L., Bao X. Distributed vibration sensor based on coherent detection of phase-OTDR. *J. of Lightwave Technology*, 2010, **28** (22), P. 3243–3249.
- [7] Pan Z., Liang K., Ye Q., Cai H., Qu R., Fang Z. Phase-sensitive OTDR system based on digital coherent detection. *Optical Sensors and Biophotonics, Proceedings of the SPIE 8311 (Optical Society of America)*, 2011, 83110S.
- [8] Yuelan Lu, Tao Zhu, Liang Chen, Xiaoyi Bao. Distributed Vibration Sensor Based on Coherent Detection of Phase-OTDR. *J. of Lightwave Technology*, 2010, **28** (22), 3243.
- [9] Yongkang Dong, Xi Chen, Erhu Liu, Cheng Fu, Hongying Zhang, Zhiwei Lu. Quantitative measurement of dynamic nanostrain based on a phase-sensitive optical time domain Reflectometer. *Applied Optics*, 2016, **55** (28), P. 7810–7815.
- [10] Qin M., He X., Liu F., Zheng X., Zhang M. Real-time phase demodulation and data administration of distributed optical fiber vibration sensing system. *Proceedings of the SPIE*, 2017, **10208**, P. 1020810–1020818.
- [11] Zinan Wang, Li Zhang, Song Wang, Naitian Xue, Fei Peng, Mengqiu Fan, Wei Sun, Xianyang Qian, Jiarui Rao, Yunjiang Rao. Coherent Φ -OTDR based on IQ demodulation and homodyne detection. *Optics Express*, 2016, **24** (2), P. 853–858.
- [12] Martins H.F., Shi K., Thomsen B.C., Martin-Lopez S., Gonzalez-Herraez M., Savory S.J. Real time dynamic strain monitoring of optical links using the backreflection of live PSK data. *Optics Express*, 2016, **24** (19), P. 22303–22318.
- [13] Yan Q., Tian M., Li X., Yang Q., Xu Y. Coherent Φ -OTDR based on polarization-diversity integrated coherent receiver and heterodyne detection. *Proceedings of the SPIE*, 2017, **10323**, P. 1032383–1032386.
- [14] Fang G., Xu T., Li F. Heterodyne interrogation system for TDM interferometric fiber optic sensors array. *Optics Communications*, 2015, **341**, P. 74–78.
- [15] Song M., Yin S., Ruffin P.B. Fiber Bragg grating strain sensor demodulation with quadrature sampling of a Mach–Zehnder interferometer. *Applied Optics*, 2000, **39** (7), P. 1106–1111.

- [16] Fu Y., Xue N., Wang Z., Zhang B., Xiong J., Rao Y. Impact of I/Q amplitude imbalance on coherent – OTDR. *J. of Lightwave Technology*, 2018, **36** (4), P. 1069–1075.
- [17] Faruk M.S., Kikuchi K. Compensation for In-Phase/Quadrature imbalance in coherent-receiver front end for optical quadrature amplitude modulation. *IEEE Photonics J.*, 2013, **5** (2), 7800110.
- [18] Chang S.H., Chung H.S., Kim K. Impact of quadrature imbalance in optical coherent QPSK receiver. *IEEE Photonics Technology Letters*, 2009, **21** (11), P. 709–711.
- [19] Naitian Xue, Yun Fu, Chongyu Lu, Ji Xiong, Le Yang, Zinan Wang. Characterization and Compensation of Phase Offset in Φ -OTDR with Heterodyne Detection. *J. of Lightwave Technology*, 2018, **36** (23), P. 5481–5487.
- [20] Miroshnichenko G.P., Arzhanenkova A.N., Plotnikov M.Y. Errors in the demodulation algorithm with a generated carrier phase introduced by the low-pass filter. *Scientific and Technical J. of Information Technologies, Mechanics and Optics*, 2023, **23** (4), P. 795–802 (in Russian).
- [21] Miroshnichenko G.P., Arzhanenkova A.N., Plotnikov M.Y. Investigation of the method of current thermal modulation of the wavelength VCSEL. *Nanosystems: Physics, Chemistry, Mathematics*, 2022, **13** (6), P. 615–620.

Submitted 15 April 2024; revised 20 April 2024; accepted 19 May 2024

Information about the authors:

George P. Miroshnichenko – Research Center of light guide photonics, ITMO University, Kronverksky pr. 49, St. Petersburg, 197101, Russia; ORCID 0000-0002-4265-8818; gpmirosh@gmail.com

Alina N. Arzhanenkova – Research Center of light guide photonics, ITMO University, Kronverksky pr. 49, St. Petersburg, 197101, Russia; ORCID 0000-0003-4869-2838; 11arzh11@gmail.com

Michail Yu. Plotnikov – Research Center of light guide photonics, ITMO University, Kronverksky pr. 49, St. Petersburg, 197101, Russia; ORCID 0000-0003-2506-0379; plotnikov-michael@yandex.ru

Conflict of interest: the authors declare no conflict of interest.

Stability and transformations of domain walls in cylindrical wires

Ksenia A. Chichay^{1,a}, Igor S. Lobanov^{1,b}, Valery M. Uzdin^{1,c}

¹Department of Physics, ITMO University, St. Petersburg, Russia

^aks.chichay@gmail.com, ^blobanov.igor@gmail.com, ^cv.uzdin@mail.ru

Corresponding author: K. A. Chichay, ks.chichay@gmail.com

PACS 75.60.Ch, 75.30.Gw

ABSTRACT For magnetic wires and other systems with cylindrical symmetry, algorithms have been proposed for constructing a multidimensional energy surface, searching for minimal energy paths between locally stable states and the activation energies of transitions between such states. The mechanisms of nucleation and transformation of domain walls of various types in amorphous ferromagnetic nanowires with a nonuniform anisotropy distribution have been studied. The stability of the domain walls structure with respect to thermal fluctuations and random external perturbations has been assessed.

KEYWORDS Domain wall, cylindrical systems, amorphous ferromagnetic microwires, micromagnetics, domain wall transformation, transition state theory.

ACKNOWLEDGEMENTS This work was funded by the Russian Science Foundation (project No. 23-72-10028, <https://rscf.ru/en/project/23-72-10028/>). K.A.Ch. acknowledges the support of ITMO Fellowship Program.

FOR CITATION Chichay K.A., Lobanov I.S., Uzdin V.M. Stability and transformations of domain walls in cylindrical wires. *Nanosystems: Phys. Chem. Math.*, 2024, **15** (3), 332–339.

1. Introduction

Magnetic wires are among the most suitable and promising systems where creation and controlled movement individual domain walls (DWs) can be used for technological applications such as high-density memory and energy-efficient logic devices [1–3]. A large number of investigations have been devoted to the study of the dynamics of DWs in flat and cylindrical wires. This was stimulated in particular by the concept of a magnetic racetrack memory [2, 4, 5] which requires high speed and high stability of the DW. From this point of view, cylindrical wires as hosts of DW-magnetic bits have a number of significant advantages. DW velocities that have been reported for cylindrical wires reach several kilometers per second [6–9]. Also, due to cylindrical symmetry, there is no preferred direction in the wire perpendicular to the direction of DW movement, and therefore the DW can be oriented at any angle while moving without changing the internal structure, which gives it more stability comparing to DW in planar wires [10, 11].

Very high values of the DW velocity were reported in glass coated amorphous ferromagnetic wires of micron and submicron thickness [8, 12]. Due to the peculiarities of the production process, this type of cylindrical wires have a complex anisotropy distribution induced by internal mechanical stresses [13, 14]. The presence of induced anisotropy in amorphous ferromagnetic wire makes it possible to change their magnetic properties and characteristics of the DW dynamics in a wide range by changing the thickness of the glass shell, fabrication conditions and using various post-processing methods, such as annealing [12, 15]. This makes amorphous ferromagnetic wires in glass shell unique systems with remarkable properties important for applications.

Most of the experimental data are related to the study of the dynamics of the DW and methods for tuning it. However, there is not much information about the type and internal structure of the DWs. The study and description of the local magnetic structure (internal structure of the DW) in microwires is a complex task, which is the flip side of their uniqueness and outstanding properties due to the presence of a complex stress distribution, glass shell, amorphous state and their micrometer size [16]. Previously, we discovered two types of DWs in cylindrical wires with inhomogeneous anisotropy: transverse and radial DWs [17]. But the existence of various types of DWs poses new challenges, since the trend towards miniaturization of the functional elements of devices leads to the problem of their stability with respect to thermal fluctuations and random external disturbances [18, 19]. The presence of inhomogeneous anisotropy can affect the stability of the DWs.

In this work, we examine spontaneous transitions between different type of DWs. We are constructing the energy surface of the system and find on it the minimal energy path between states corresponding to different types of DWs, which allows us to find the activation energy for transitions between them. Also we consider the nucleation process of the radial DW from the homogenous ferromagnetic state.

2. Model

The total energy of the system includes exchange energy, anisotropy and Zeeman term:

$$E = E_A + E_K + E_B. \quad (1)$$

The exchange energy is given by the integral

$$E_A = \frac{A}{2} \int_{\Omega} [\nabla \mathbf{S}(\mathbf{r})]^2 d\mathbf{r},$$

where \mathbf{S} is unit magnetization vector, A is the exchange stiffness, and the integral is taken over the cylinder representing the cylindrical wire:

$$\Omega = \{0 \leq z \leq L, 0 \leq \rho \leq R, 0 \leq \phi < 2\pi\},$$

where ρ, ϕ and z are the cylindrical coordinates, with the basic vector \mathbf{e}_z oriented along the cylinder axis. Energy of anisotropy with constant K_i and the anisotropy axis \mathbf{e}_i is given by:

$$E_{K,i} = - \int_{\Omega} K_i(\mathbf{r})(\mathbf{S}(\mathbf{r}) \cdot \mathbf{e}_i)^2 d\mathbf{r}.$$

In cylindrical wire \mathbf{e}_i may not be constant, but assuming symmetry with respect to rotations around the cylinder axis, the anisotropy can be decomposed over the easy axis/easy plane anisotropies with axes $\mathbf{e}_\rho, \mathbf{e}_\phi$ and \mathbf{e}_z oriented along the cylindrical coordinates axes:

$$E_K = E_{K,\rho} + E_{K,\phi} + E_{K,z}.$$

Below, we consider only symmetric case, where anisotropy constants depend only on ρ .

Zeeman energy for the magnetic field \mathbf{B} oriented along the cylinder axis has the following form:

$$E_B = -B \int_{\Omega} (\mathbf{S}(\mathbf{r}) \cdot \mathbf{e}_z) d\mathbf{r}.$$

In the simulation we consider the cylinder of finite length L , hence all energies are bounded, and energy of the homogeneous ferromagnetic state

$$E_{FM} = -(K + B)\pi LR^2.$$

The geometry of the wire plays an important role, for example. in a cylindrical wire, there is no energy barrier for moving the transverse domain wall, while in a rectangular wire, the barrier is non-zero. Commonly used discretization with cubic grid, e.g. in the popular MuMAX3 code, [20] does not allow boundary conditions to be properly taken into account. Codes based on finite element methods, such as [21,22], can correctly work with complex geometry, but the codes are not in public domain and are tricky to implement. For the study we derived discretized energy for the cylindrical domains, which explicitly takes into account the symmetry of the problem and gives precise value for the preferred FM state and error of order h^2 for every smooth magnetization field, where h is the discretization lattice constant (see Appendix).

In the article we used uniform lattice in the cylindrical coordinates with grid steps:

$$h_\rho = \frac{R}{N_\rho}, \quad h_\phi = \frac{2\pi}{N_\phi}, \quad h_z = \frac{L}{N_z - 1},$$

where $N_\rho \times N_\phi \times N_z$ is size of the grid. Then the magnetization is defined by array n of its values at the grid points:

$$\mathbf{S} = \mathbf{S}(\rho, \phi, z), \quad \mathbf{n}_{ijk} = \mathbf{S}(h_\rho(i + 1/2), h_\phi j, h_z k). \quad (2)$$

We use central finite differences to approximate the partial derivatives, which result in staggered grids. To find values of the integrals, we use midpoint and trapezoidal rule, which is appropriated for each term. As the result, we obtain the following discrete forms of the energy contributions. The exchange energy is split into three parts $E_A = I_\rho + I_\phi + I_z$, each corresponds to the partial derivatives along the respective coordinate according to the exchange energy integral in the cylindrical coordinates:

$$E_A = \int_{\Omega} \frac{A}{2} \left[\left(\frac{\partial \mathbf{S}}{\partial \rho} \right)^2 + \frac{1}{\rho^2} \left(\frac{\partial \mathbf{S}}{\partial \phi} \right)^2 + \left(\frac{\partial \mathbf{S}}{\partial z} \right)^2 \right] \rho \cdot d\rho \cdot d\phi \cdot dz$$

The first discretized term can be thought of as the standard Heisenberg interspin exchange, but the exchange parameter in this case is not constant even if the exchange stiffness and magnetization do not change, since the discrete parameter includes non-constant volumes associated with the magnetic element:

$$I_\rho = -h_z h_\phi A \sum_{k=0}^{N_z-1} \sum_{j=0}^{N_\phi-1} \sum_{i=0}^{N_\rho-2} (i+1) \xi_{i+1} \zeta_k \mathbf{n}_{i+1,j,k} \cdot \mathbf{n}_{i,j,k}. \quad (3)$$

It is worth noting that grid points lying on the boundary of the domain have smaller associated volumes, which is taken into account by introducing corrections:

$$\zeta_k = 1, \quad 0 < k < N_z - 1, \quad \zeta_0 = \zeta_{N_z-1} = \frac{1}{2}, \quad (4)$$

and another one for the volume element $\rho d\rho$:

$$\xi_i = 1 + \frac{1}{8}\delta_{i,1} + \frac{4R - h_\rho}{8(R - h_\rho)}\delta_{i,N_\rho-1}, \quad i = 1 \dots N_\rho - 1. \quad (5)$$

The two remaining terms has similar forms, but describes interaction with different neighbours:

$$I_\phi = -\frac{h_z}{h_\phi} A \sum_{k=0}^{N_z-1} \sum_{j=0}^{N_\phi-1} \sum_{i=0}^{N_\rho-1} \frac{\zeta_k}{i + 1/2} \mathbf{n}_{i,j,k} \cdot \mathbf{n}_{i,j+1,k}. \quad (6)$$

Here arithmetic with respect to j is done modulo N_ϕ , since period boundary conditions in ϕ are assumed:

$$I_z = -\frac{h_\phi h_\rho^2}{h_z} A \sum_{i=0}^{N_\rho-1} \sum_{j=0}^{N_\phi-1} \sum_{k=0}^{N_z-2} (i + 1/2) \mathbf{n}_{i,j,k} \cdot \mathbf{n}_{i,j,k+1}. \quad (7)$$

The discretized anisotropy energy and the Zeeman energy are written as

$$E_{K,i} = K_i h_\rho^2 h_\phi h_z \sum_{l=0}^{N_\rho-1} \sum_{j=0}^{N_\phi-1} \sum_{k=0}^{N_z-1} (l + 1/2) \zeta_k (\mathbf{n}_{ljk} \cdot \mathbf{e}_i)^2, \quad (8)$$

and

$$E_B = B h_\rho^2 h_\phi h_z \sum_{i=0}^{N_\rho-1} \sum_{j=0}^{N_\phi-1} \sum_{k=0}^{N_z-1} (i + 1/2) \zeta_k (\mathbf{n}_{ijk} \cdot \mathbf{e}_z). \quad (9)$$

In what follows the exchange stiffness $A = 2 \cdot 10^{-11}$ J/m, saturation magnetization $M_s = 500$ kA/m and anisotropy constants K_i are taken for Fe-based amorphous ferromagnetic wires in glass shell. The sign of $K_i(\rho)$ defines easy-axis/easy-plane anisotropy, which is non-uniform along the radius ρ of the wire. The anisotropy axis \mathbf{e}_i is assumed to be different in the center of the wire, where it coincides with the z axis \mathbf{e}_z , and near the surface, where it is assumed to be radial. This partition corresponds to a simplified form of the stress-induced anisotropy distribution in amorphous ferromagnetic microwires in a glass shell, given in Ref. [13, 23]. Thus, starting from the center of the wire to $0.9R$, we used the average value of the axial anisotropy $K_{ax} = 3 \cdot 10^4$ J/m³ (easy axis). On the periphery, the radial type of anisotropy, $K_\rho = 2 \cdot 10^4$ J/m³, prevails (easy axis). Besides the stress-induced anisotropy, the system contains the effective shape anisotropy for cylinder $K_{eff} = \mu_0 M_s^2 / 4$ due to the demagnetization fields.

We performed the micromagnetic simulations using own original code, which implements the finite-difference discretization scheme described above. For calculations we used the cylindrical coordinates, taking into account the different volume of units cells to calculate the magnetic moment. The simulated wire was of radius $R = 1 \cdot 10^{-7}$ m and length $L = 3.5 \cdot 10^{-7}$ m in case of DW transformation modeling and $L = 7.5 \cdot 10^{-7}$ m for investigation of nucleation process. Periodic boundary conditions were used in the z direction. The number of nodes along the each axis was: $N_\rho = 30$ (from the center of wire to the periphery), $N_\phi = 100$, $N_z = 140$ or $N_z = 300$ when considering the transformation or nucleation processes, respectively.

3. Domain wall transformation and nucleation

The stability of magnetic domain walls of various types can be studied within the framework of the transition state theory for magnetic degrees of freedom. For this purpose, the energy of the system is considered as a functional of all variables that uniquely determine the magnetic state. This defines the multidimensional energy surface of the system. If a micromagnetic model with a continuous magnetization distribution is used, then the system is divided into cells, each of which has its own size and effective exchange and anisotropy parameters. Local minima on the energy surface are correspond to the ground and metastable magnetic states of the system.

In the cylindrical wires under consideration, the ground state corresponds to a magnetization distribution that does not change along the wire axis. Domain boundaries of various types are metastable states. To find the energy barrier between states corresponding to domain boundaries of different types, a minimum energy path (MEP) between states is constructed. The difference between maximal energy along the MEP and, in the initial equilibrium state, determines the activation energy of the corresponding transition. The path itself corresponds to the most likely transition scenario among nearby paths. In the harmonic approximation, for the dependence of energy on all degrees of freedom at the minimum and saddle point, one can obtain the transition frequencies. The lifetime of the magnetic state at arbitrary temperature can be found if transition in all possible metastable states as well as to the ground state will be taken into account. However, the main role is usually played by the transition with minimal activation energy.

A schematic representation of a cylindrical wire in the cylindrical coordinates is shown in Fig. 1a. In this study, we consider two types of domain walls that are stabilized in a cylindrical wire with inhomogeneous anisotropy, namely radial and transverse domain walls. We described these types of domain walls in more detail in [17].

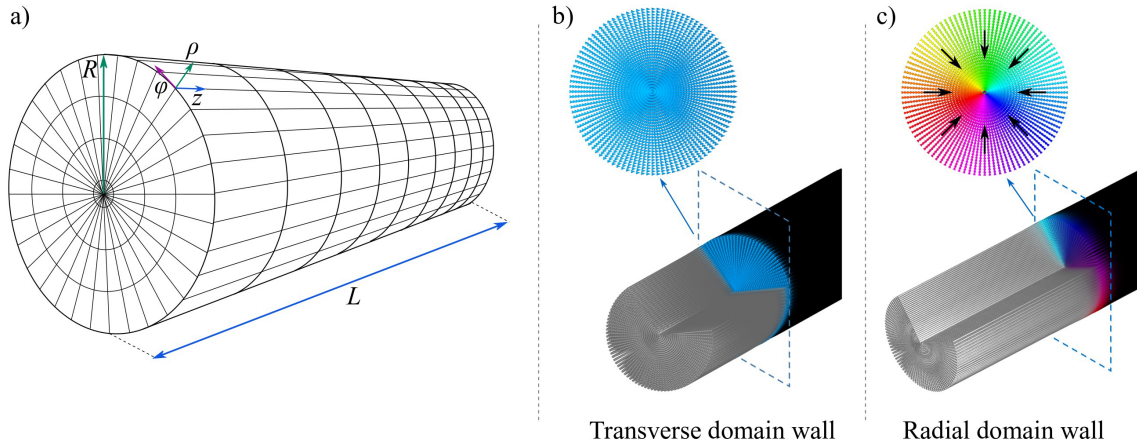


FIG. 1. a) Schematic representation of a wire in the cylindrical coordinate system. R is the wire radius, L is the length of the wire. b) and c) 3D view and cross section of the cylindrical wire representing magnetic configuration of transverse DW (b), radial DW (c).

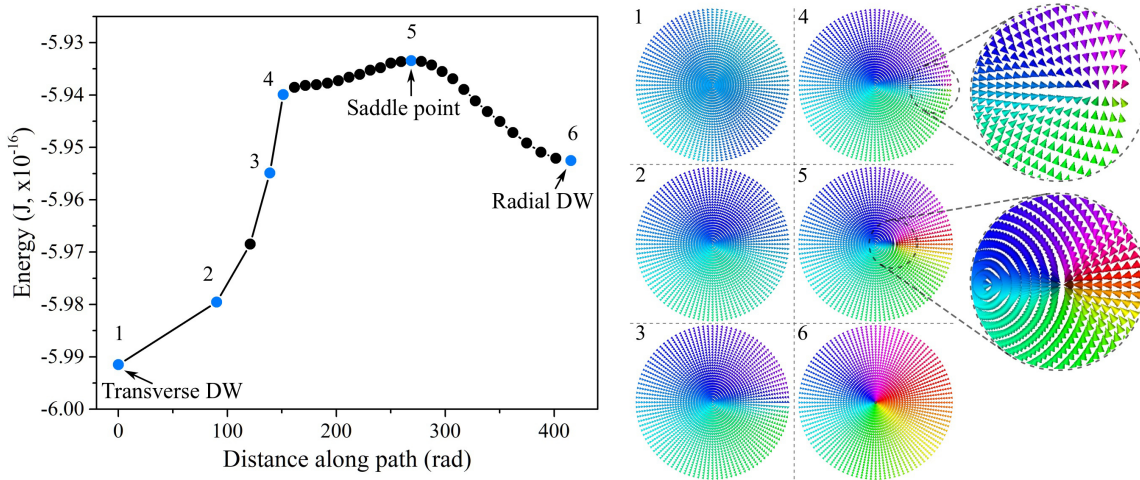


FIG. 2. MEP for the transformation of transverse DW into radial DW in cylindrical wire with inhomogeneous anisotropy. The numbered points on the graph correspond to the magnetic configurations presented on the right side of the figure. Scaled-up parts of magnetic states numbered 4 and 5 correspond to the appearance and propagation of the Bloch point.

Within the framework of the transition state theory, the MEP was calculated for the transformation of a transverse domain wall (designated by number 1 in Fig. 2) into a radial domain wall (designated by number 6 in Fig. 2). It corresponds to the most likely transition scenario among nearby paths and sets the value of the energy barrier shown in Fig. 2. The maximum energy along the path is achieved at the saddle point of the energy surface (configuration number 5 in Fig. 2), and the value of the energy barrier is determined as the difference in energy at the saddle point and the initial equilibrium state corresponding to the chosen structure of the domain wall. The energy barrier value is $E_{tr} = 5.8 \cdot 10^{-18} J$ for the transition of the transverse DS to the radial one. It can be seen that the transition from a transverse domain wall to a radial one occurs due to the formation of a Bloch point in the peripheral part of the wire and its gradual movement towards the center of the wire. The saddle point in this case (which has the highest energy along the MEP), is the state in which the Bloch point approaches the middle of the wire.

In addition to DW transformation, we also studied nucleation processes of the transverse DW. Magnetization reversal by the rapid DW movement in amorphous ferromagnetic wires in glass shell is characteristic of magnetically bistable wires (which is manifested in a rectangular hysteresis loop). This means that when a new domain nucleates in the middle of the wire, a pair of DW arise, which then immediately propagate in different directions along the axis of the wire.

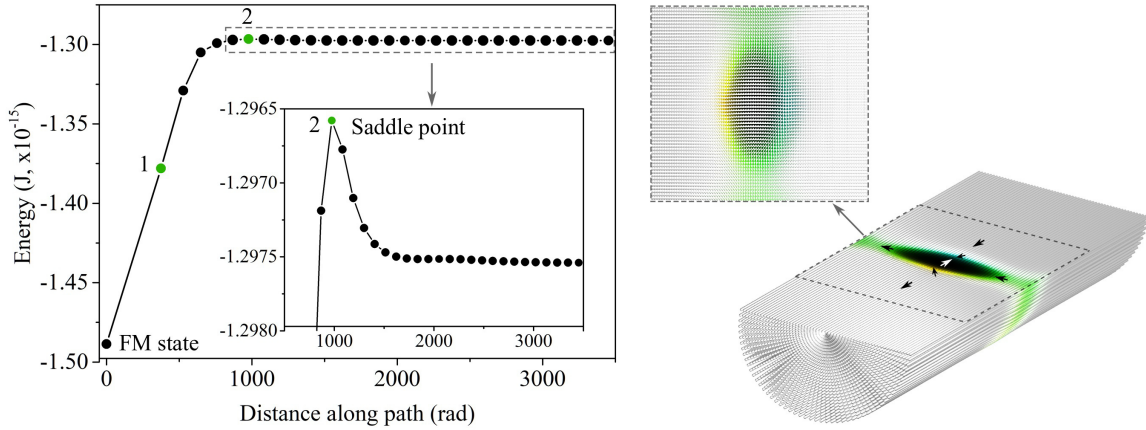


FIG. 3. MEP for nucleation of transverse DWs pair from ferromagnetic state. The right side of the figure depicts the magnetic state corresponding to point 1 on the graph. Point 2 is the saddle point. White and black colors correspond to magnetization along the wire axis.

Therefore, to study nucleation processes, we considered the appearance of two DWs in the middle of the wire and their gradual propagation. Fig. 3 shows the energy barrier for the nucleation of a pair of transverse DWs from the ferromagnetic state. The right side of Fig. 3 corresponds to point 1 on the graph. From this figure, it can be seen that a domain with opposite magnetization begins to nucleate in the center of the wire (indicated in black); thus the DWs are separated in the middle part and merged in the peripheral part of the wire. Subsequently, the formed domain walls separate and move in opposite directions. The value of the energy barrier for nucleation of a pair of transverse DWs is $E_n = 1.92 \cdot 10^{-16}$ J for a wire with the considered geometric parameters.

4. Conclusion

Construction of the energy surface of magnetic systems and the MEPs between states makes it possible to assess the stability of magnetic states with respect to thermal fluctuations and random external perturbations. The MEP determines the most likely scenario for the transition between different types of DWs and the energy barrier for the activation of such processes. When going from microwires to nanowires, the barrier decreases, which makes transitions between different types of DWs possible at room temperature. The barrier to DW formation and collapse remains sufficiently large, which allows the use of DW to store information in magnetic memory technologies.

5. Appendix

We use a cylindrical grid with grid points located at the intersection of the coordinate surfaces

$$\rho_i = h_\rho(i + 1/2), \quad \phi_j = h_\phi j, \quad z_k = h_z k,$$

where

$$i = 0 \dots, N_\rho - 1, \quad j = 0 \dots, N_\phi - 1, \quad k = 0 \dots, N_z - 1.$$

The values of \mathbf{S} at the grid points are given by the array \mathbf{n} defined by (2). The boundary conditions with respect to the polar angle ϕ are naturally periodic, hence

$$\mathbf{n}_{i,0,k} = \mathbf{n}_{i,N_\phi,k}.$$

The boundary conditions on the surfaces $z = 0$ and $z = L$ are fixed, since we consider single DW inside the simulation domain, and the deviation of the DW from the FM state is rapidly vanishing:

$$\mathbf{n}_{i,j,0} = \mathbf{e}_z, \quad \mathbf{n}_{i,j,N_z-1} = -\mathbf{e}_z.$$

Due to the continuity of \mathbf{S} , the value \mathbf{S} does not depend on ϕ for $\rho = 0$, therefore it does not carry a lot of information. Hence the set of grid points ρ_i do not contain extreme values for the integration domain, while grid points for other degrees of freedom ϕ and z do.

Partial derivatives are approximated by central finite difference quotients resulting in a staggered grid, that is the field \mathbf{S} and its derivatives are defined at different points. The derivative with respect to z is defined only at the centers $z_{k+1/2}$ of the segments $[z_k, z_{k+1}]$:

$$\frac{\partial \mathbf{S}}{\partial z}(\rho_i, \phi_j, z_{k+1/2}) = h_\rho^{-1}(\mathbf{n}_{i,j,k+1} - \mathbf{n}_{i,j,k}) + O(h_z^2).$$

Due to periodic boundary condition with respect to ϕ , the corresponding derivative is defined at N_ϕ points shifted to half lattice constant: $\phi_j = \phi_j + h_\phi/2$:

$$\frac{\partial \mathbf{S}}{\partial \phi}(\rho_{i+1/2}, \phi_{j+1/2}, z_k) = h_\rho^{-1}(\mathbf{n}_{i,j+1,k} - \mathbf{n}_{i,j,k}) + O(h_\phi^2).$$

The central finite quotient are readily gives the derivative with respect to ρ at points $\rho_{i+1/2} = (i+1)h_\rho$:

$$\frac{\partial \mathbf{S}}{\partial \rho}(\rho_{i+1/2}, \phi_j, z_k) = h_\rho^{-1}(\mathbf{n}_{i+1,j,k} - \mathbf{n}_{i,j,k}) + O(h_\rho^2).$$

The derivative is not defined at the surface $\rho = R$ corresponding to $i = N_\rho$, but it can be extrapolated to the points using linear extrapolation with the nodes $\rho_{N_\rho-1}, \rho_{N_\rho-2}$, which introduce the error term $O(h_\rho)$.

The integrals for all the contributions to energy can be written as iterated integrals with respect to the variables $\rho \in [0, R]$, $\phi \in [0, 2\pi]$ and $z \in [0, L]$. We approximate each of the integrals by a numerical quadrature. Namely, we use the trapezoidal rule, if the integrand is given at the ends of the intervals $[x_k, x_{k+1}]$:

$$\int_a^b f(x)dx = \sum_{n=0}^N f(x_k)h_x \zeta_n + O(h_x^3),$$

where ζ_k is defined by (4), and the rectangle rule, if the integrand is given at the centers of the intervals:

$$\int_a^b f(x)dx = \sum_{n=0}^{N-1} f(x_{k+1/2})h_x + O(h_x^3),$$

where x is either ρ , ϕ or z . The factors σ_k indicate which fraction of the volume surrounding the point x_k in the computation grid belongs to the integration domain. Although trapezoid rule is based on linear interpolation of the integrand, while rectangle rule uses only constant interpolation, both rules give the same precision since the term x is canceled out after integration over any symmetric interval.

To compute integral

$$I_\rho = \frac{J}{2} \int_0^L dz \int_0^{2\pi} d\phi \int_0^R \left(\frac{\partial S}{\partial \rho} \right)^2 \rho d\rho,$$

we use trapezoid rule for the variables ϕ and z , where the integral with respect to ϕ is taken over the segment $[0, 2\pi]$ and its ends coincide due to periodic boundary conditions, and rectangle rule for ρ in the interval $[\rho_0, \rho_{N-1}]$. To approximate the integral in the remaining segments $[0, \rho_0]$ and $[\rho_{N-1}, R]$, we assume that the derivative $\partial \mathbf{S}/\partial \rho$ is constant in the intervals and equal to its values in ρ_0 and ρ_{N-1} , respectively. This gives us correction terms ξ_i (see (5)) to the rectangle rule for the first and the last segments. Thus, the expression (3) is obtained.

The quadrature for the exchange integral

$$I_\phi = \frac{J}{2} \int_0^L dz \int_0^R \frac{d\rho}{\rho} \int_0^{2\pi} \left(\frac{\partial S}{\partial \phi} \right)^2 d\phi,$$

is obtained using the rectangle rule for the integral with respect to ϕ with points $\phi_{j+1/2}$ (taking into account periodic boundary conditions), the trapezoid rule for z and the rectangle rule for ρ with grid points ρ_i . It is worth noting that we consider only smooth magnetization fields, therefore the derivative under the integral is zero at the origin and the integral does not have singularities. The final quadrature is given by (6).

The third exchange integral

$$I_z = \frac{J}{2} \int_0^R \rho d\rho \int_0^{2\pi} d\phi \int_0^L \left(\frac{\partial S}{\partial z} \right)^2 dz$$

is obtained using the same rule for ρ as in I_ϕ , the same rule for ϕ as in I_ρ , and rectangle rule for the integral over z with grid points $z_{k+1/2}$. The quadrature formula obtained is given by (7).

The anisotropy energy contributions

$$E_K = \sum_l K_l \int_0^R \rho d\rho \int_0^{2\pi} d\phi \int_0^L (\mathbf{S} \cdot \mathbf{e}_l)^2 dz,$$

and the Zeeman energy contributions

$$E_B = B \int_0^R \rho d\rho \int_0^{2\pi} d\phi \int_0^L (\mathbf{S} \cdot \mathbf{e}_z) dz,$$

are approximated by using the trapezoid rule for integrals with respect to ϕ and z (with periodic BC for ϕ), and the rectangle rule for the integral with respect to ρ . The corresponding quadratures are (8), (9).

The proposed discretization scheme gives an exact answer for linear functions \mathbf{S} in precise arithmetic. Among the functions only constant ones satisfy the constraint on the length of the magnetization, hence the exact answer is obtained only on the ferromagnetic state. In all other magnetization fields, the error of the provided quadrature formulas for the contributions to energy equals $O(h^2)$, which is originated from extrapolation of $\partial S/\partial \rho$ to the ends of integration interval in computation I_ρ .

We benchmarked the convergence of the discrete model to the micromagnetic one using domain wall ansatz

$$\mathbf{S} = (\sin \theta \cos \phi, \sin \theta \sin \phi, \cos \theta),$$

where ϕ is an arbitrary fixed angle, and

$$\theta(z) = 2 \arctan \exp \frac{z}{\Delta},$$

with DW width $\Delta = 1.36 \cdot 10^{-8}$ m. The magnetic wire geometry and parameters were the same as in the main part of the article. The sparsest grid has size $N_\rho = 2$, $N_\phi = 2$, $N_z = 8$. The step sizes for all the dimensions were scaled with the same factor, gradually increasing resolution of the boundary. The total exchange energy error compared to the micromagnetic one scales as $O(h^2)$ as expected. Anisotropy energy error decreases even faster as step size decreases, since the term does not suffer from the extrapolating procedure. For comparison, we computed energy of the same ansatz using Mumax3 [20] (Fig. 4). The cubic grid used in Mumax3 can not approximate surface of the cylinder reasonable well, resulting in highly nonmonotonic convergence and 6 orders of magnitude larger errors for the anisotropy energy and 1 order for the exchange energy.

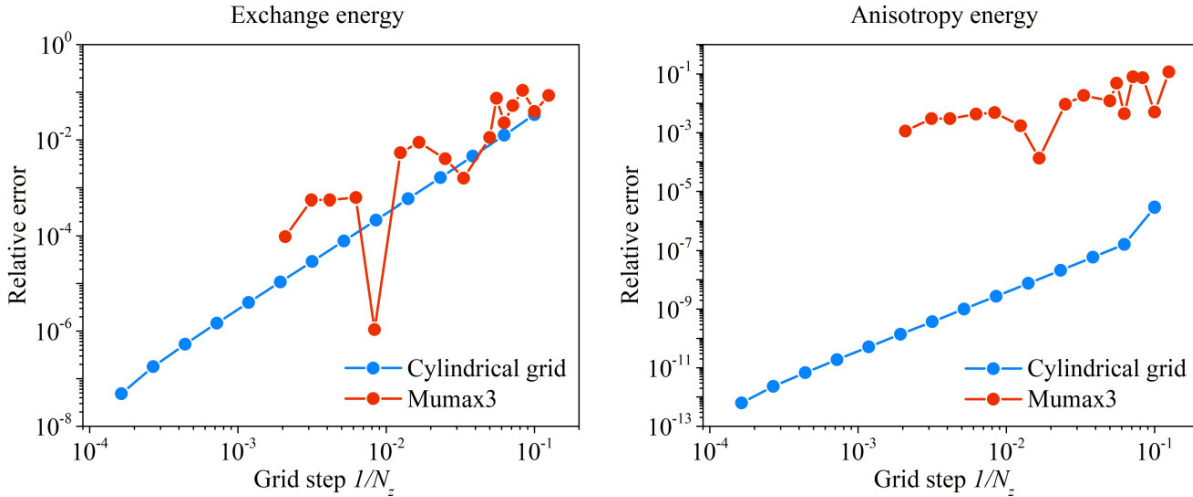


FIG. 4. Relative error for exchange and anisotropy energies for transverse DW computed in discrete models as a function of the grid step h_z . (Blue line) Energy estimated by (3), (6), (7) and (8). (Red line) Energy computed using Mumax3.

References

- [1] Foerster M., Boule O., Esefelder S., Mattheis R., Kläui M. *Domain Wall Memory Device*. In: Xu, Y., Awschalom, D., Nitta, J. (eds) Handbook of Spintronics. Springer, Dordrecht, 2016
- [2] Parkin S.S.P., Hayashi M. and Thomas L. Magnetic Domain-Wall Racetrack Memory. *Science*, 2008, **320**(5873), P. 190–194.
- [3] Venkat G., Allwood D.A., Hayward T.J. Magnetic domain walls: types, processes and applications. *J. Phys. D: Appl. Phys.*, 2024, **57**, P. 1688.
- [4] Parkin S., Yang S.H. Memory on the racetrack. *Nature nanotechnology*, 2015, 10(3), P. 195–198.
- [5] Blasing R. et al. Magnetic Racetrack Memory: From Physics to the Cusp of Applications Within a Decade. *Proc. IEEE* 2020, **108**, P. 1303–1321.
- [6] Hertel R. Ultrafast domain wall dynamics in magnetic nanotubes and nanowires. *J. Phys.: Condens. Matter*, 2016, **28**, P. 483002.
- [7] Yan M., Andreas C., Kakay A., Garcia-Sanchez F., Hertel R. Fast domain wall dynamics in magnetic nanotubes: Suppression of Walker breakdown and Cherenkov-like spin wave emission. *Appl. Phys. Lett.*, 2011, **99**, P. 122505.
- [8] Corte-León P., Gonzalez-Legarreta L., Zhukova V., Ipatov M., Blanco J.M., Churyukanova M., Taskaev S. and Zhukov A. Controlling the domain wall dynamics in Fe-, Ni- and Co-based magnetic microwires. *J. Alloys Compound.*, 2020, **834**, P. 155170.
- [9] Tejo F., Fernandez-Roldan J.A.F., Guslienko K., Otxoa R.M. and Chubykalo-Fesenko O. Giant supermagnonic Bloch point velocities in cylindrical ferromagnetic nanowires. *Nanoscale*, 2024, Advance Article
- [10] Alam J., et.al. Cylindrical micro and nanowires: Fabrication, properties and applications. *J. Magn. Magn. Mater.*, 2020, **513**, P. 167074.
- [11] Yan M. Beating the Walker limit with massless domain walls in cylindrical nanowires. *Phys. Rev. Lett.*, 2010, **104**, P. 057201.
- [12] Zhukova V., Corte-Leon P., González-Legarreta, L., Talaat, A., Blanco, J.M., Ipatov, M., Olivera, J. and Zhukov, A. Review of domain wall dynamics engineering in magnetic microwires. *Nanomaterials*, 2020, **10**(12), P. 2407.
- [13] Chiriac H., Ovari T., Zhukov A. Magnetoelastic anisotropy of amorphous microwires. *J. Magn. Magn. Mater.*, 2003, **496**, P. 254–255.

- [14] Zhukova V., Blanco J.M., Ipatov M., Zhukov A. Magnetoelastic contribution in domain wall dynamics of amorphous microwires. *Physica B*, 2012, **407**, P. 1450–1454.
- [15] Chichay K., et. al. Tunable domain wall dynamics in amorphous ferromagnetic microwires. *J. Alloys Compound.*, 2020, **835**, P. 154843.
- [16] Gudoshnikov S.A., Grebenshchikov Yu.B., Ljubimov B.Ya., Palvanov P.S., Usov N.A., Ipatov M., Zhukov A., Gonzalez J. Ground state magnetization distribution and characteristic width of head to head domain wall in Fe-rich amorphous microwire. *Phys. Stat. Sol. A*, 2009, **206**(4), P. 613–617.
- [17] Chichay K.A., Lobanov I.S., Uzdin V.M. The structure of magnetic domain walls in cylindrical nano- and microwires with in- homogeneous anisotropy. *Nanosystems: Phys. Chem. Math.*, 2023, **15**, P. 55–59.
- [18] Lobanov I.S., Potkina M.N., Uzdin V.M. Stability and Lifetimes of Magnetic States of Nano- and Microstructures (Brief Review). *JETP Letters*, 2021, **113**, **12**, P. 801–813.
- [19] Lobanov I.S., Uzdin V.M. The lifetime of micron scale topological chiral magnetic states with atomic resolution. *Comp. Phys. Commun.*, 2021, **269**, P. 108136.
- [20] Vansteenkiste A., Leliaert J., Dvornik M., Helsen M., Garsia-Sanchez F., B. Van Waeyenberge F. The design and verification of MuMax3. *AIP Advances*, 2014, **4**, P. 107133.
- [21] Fischbacher T., Franchin M., Bordignon G., and Fangohr H. A Systematic Approach to Multiphysics Extensions of Finite-Element-Based Micromagnetic Simulations: Nmag, *IEEE Transactions on Magnetics*, 2007, **43**(6), P. 2896–2898.
- [22] Abert C., Exl L., Bruckner F., Drews A., Suess D. magnum. fe: A micromagnetic finite-element simulation code based on FEniCS. *Journal of Magnetism and Magnetic Materials*, 2013, **345**, P. 29–35.
- [23] Chiriac H., Ovari T.A., Pop Gh. Internal stress distribution in glass-covered amorphous magnetic wires. *Phys. Rev. B.*, 1995, **52**(14), P. 10104.

Submitted 10 April 2024; revised 8 May 2024; accepted 11 May 2024

Information about the authors:

Ksenia A. Chichay – Department of Physics, ITMO University, St. Petersburg, 197101, Russia; ORCID 0000-0002-6921-6075; ks.chichay@gmail.com

Igor S. Lobanov – Department of Physics, ITMO University, St. Petersburg, 197101, Russia; ORCID ORCID 0000-0001-8789-3267; lobanov.igor@gmail.com

Valery M. Uzdin – Department of Physics, ITMO University, St. Petersburg, 197101, Russia; ORCID 0000-0002-9505-0996; v.uzdin@mail.ru

Conflict of interest: the authors declare no conflict of interest.

Preparation, structure and magnetic properties of the nanostructural Ni@C films obtained by magnetron deposition

Rostyslav V. Shalayev^{1,a}, Victor N. Varyukhin^{1,b}, A. I. Linnik, Vladimir V. Syrotkin^{1,c}, S. A. Kostyrya

¹Galkin Donetsk Institute for Physics and Engineering, Donetsk, Russia

^asharos@donfti.ru, ^bdirector@donfti.ru, ^cvladir.52@mail.ru

Corresponding author: Rostyslav V. Shalayev, sharos@donfti.ru

PACS 81.15.Gh, 52.40.Hf, 81.07.-b

ABSTRACT Three series of films were obtained by magnetron sputtering of the composite C-Ni target with different ratios C/Ni (vol.%) = 60/40; 40/60; 30/70. The effect of the substrate temperature on the structure and the size of film-forming nickel nanocrystallites with a carbon shell was studied with using X-ray diffraction analysis. The cluster nature of film deposition on the growth surface was established by using atomic force microscopy. The saturation magnetization of nickel nanoparticles $4\pi MS$ was measured by the inductive-frequency method and the substrate temperature dependence was studied. It has been shown that the films with a high carbon content exhibit magnetism only when deposited on hot substrates. The films with the minimum carbon concentration exhibit ferromagnetic behavior even when deposited on a relatively cold substrate.

KEYWORDS magnetron deposition, nucleation processes, nanoclusters, saturation magnetization

FOR CITATION Shalayev R.V., Varyukhin V.N., Linnik A.I., Syrotkin V.V., Kostyrya S.A. Preparation, structure and magnetic properties of the nanostructural Ni@C films obtained by magnetron deposition. *Nanosystems: Phys. Chem. Math.*, 2024, **15** (3), 340–345.

1. Introduction

After the discovery of carbon nanostructured materials (nanotubes, nanofibers, etc.), a significant part of the research is aimed at studying the mechanisms of their growth [1–3]. From the point of view of applications, nanotubes are the objects of particular interest when they are filled with various materials like special magnetic metals. In this case, the nanotube plays the role of a kind of shell for a metal nanowire/nanorod, which is in a magnetically ordered state.

The classical methods [4, 5] for producing carbon nanotubes filled with transition metal atoms usually require the use of metal-catalysts, fairly high (600 – 800 °C) growth temperatures, and technologically complex processing of the resulting structures. At the same time, the necessary activation of carbon and nitrogen during the growth of such materials is also possible in low-temperature plasma. This fact allows combination of these materials with polymers and other objects characterized by low operating temperatures in order to expand the application area.

Around 2010s, we developed a low-temperature technology for producing columnar nanostructures of the C–N system that grow perpendicular to the substrate surface and do not require the use of a metal catalysts. This technology is based on magnetron sputtering of carbon in low-temperature plasma at substrate temperatures of $\sim 150 - 200$ °C. We established that columnar carbon nanostructures were formed at low substrate temperatures and nitrogen concentrations up to 10 at.% [6, 7]. Hybrid nanocolumn structures consisting of core-shell nanoclusters (magnetic metals (Ni, Fe, Co) coated with carbon) were of special interest. The structure and the properties were intensively studied due to their promising potential applications. So, further studies showed the possibility of obtaining metal-containing nanocolumn structures of the Ni–C–N system in low-temperature plasma [2, 8, 9]. However, it should be noted that the structural and phase composition of “metal core-carbon shell” nanoobjects has not been enough studied. The main reason is the diversity of synthesis processes affecting the structure of these composites.

The present work contains some materials not included in our earlier published work [10] and is aimed at studying structure and magnetic properties of hybrid nickel-carbon films synthesized at low temperature magnetron deposition of Ni-C clusters.

2. Experimental technique

Nanostructural Ni@C films were obtained by the method of magnetron sputtering of a nickel-carbon target in argon atmosphere with small nitrogen admixture onto quartz glass substrates. The target-substrate distance was 2.0 cm, the substrate holder was grounded. The planar DC magnetron with a flat cathode and a ring anode was used. Magnetron discharge power did not exceed 20 W. Working gas pressure was 26 Pa. The pressure was almost an order of magnitude

higher than that typically used in magnetron sputtering experiments at low magnetron plasma power [11]. The substrate temperature varied in the range 100 – 350 °C. The films growth time varied in the range 10 s up to 10 min.

A double disk structure was used as a target: a nickel disk with apertures was imposed onto a solid graphite disk. Three series of films were grown in the following C/Ni-ratios (vol.%): 30/70 – A group; 40/60 – B group; 60/40 – C group. The film thickness was up to 100 nm.

The surface morphology of the films was analyzed with the atomic force microscope (AFM). The relative content of atoms in the samples was registered by the energy dispersive X-ray (EDX) spectroscopy with using INCA Penta FETx3 (Oxford Instruments) attachment. The structure of samples was studied with the X-ray diffraction (XRD) on a DRON-3 instrument using $\text{CoK}\alpha$ radiation. The saturation magnetization of the film material was studied with using an inductive-frequency device, in which a change in the resonance frequency $\Delta F \propto \Delta M = f(H)$ was measured for an oscillatory circuit with a sample placed into the induction coil [12].

3. Main results and discussion

Nucleation processes and growth dynamics of nanostructural nickel-carbon films on a substrate were studied with AFM. Polished quartz glass substrates with small roughness were used, so the control the complicated morphology of sample surfaces with accuracy ~ 1 nm was allowed.

Fig. 1 shows the AFM-images of the Ni-C nanostructures surface after 30 and 300 s growth. After 30 s growth the whole surface of the substrate is covered with cluster elements of about 10 nm in size.

Thus, we can talk about the cluster nature of the films deposition. As a result, the formed clusters of the sputtered material are deposited on the substrate surface. Formation of clusters in plasma is presumably caused by sufficiently high buffer gas pressure (let's remember that we used pressure of 26 Pa). So, a small plasma area has a high concentration of sputtered atoms. This fact is the reason of starting self-organizing processes: formation of clusters from the atoms of target material and buffer gas in plasma at rather low temperature. The speed of buffer gas flow is small as compared to thermal speeds of the target atoms and the atoms of buffer gas. It has no influence on the concentration and distribution of the sputtered atoms. Also, the presence of carbon in the structure of films indicates existence of a carbon cover around of nickel nanocrystallites/nanoclusters as it is shown in works [1,2].

Such results require reconsideration of the processes of nanostructure deposition with using magnetron sputtering and the development of new nucleation models, in particular the growth of nanotubes/nanofibres from small charged clusters in the gas phase [13].

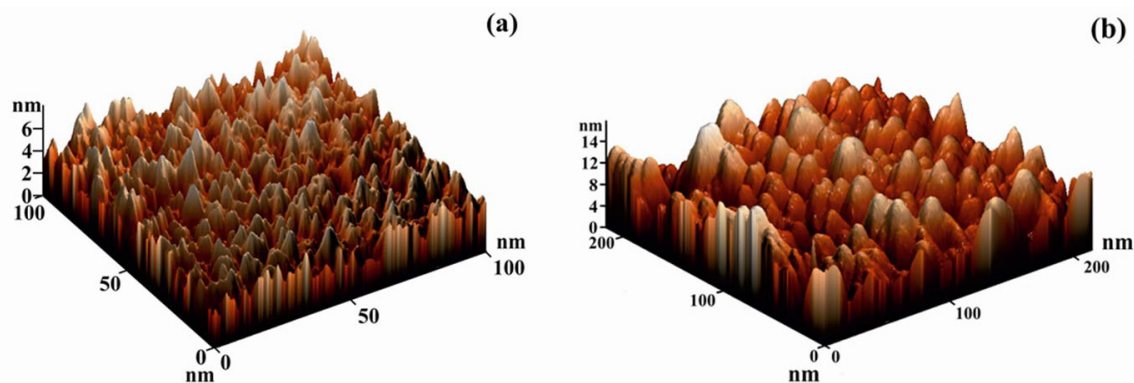


FIG. 1. AFM-images of hybrid Ni-C nanostructures surfaces at growth time, s: (a) - 30 s, (b) - 300 s

The rest of the studies except nucleation processes were performed on the films of three series (A, B, and C) with the growth time above 10 min.

The X-ray diffraction patterns of A group films (Fig. 2) show the reflexes corresponding to the FCC-lattice of nickel only. The lattice constant has appeared to be 3,53 Å that is close to the value for bulk nickel (3,56 Å). At the same time, some line broadening is observed in the X-ray reflexes that indicates rather small size of Ni-crystallites making the films up.

Being estimated by broadening of X-ray reflexes, the size of the Ni-nanocrystallites of the films of group A smoothly increases with substrate temperature T_S increase. The values for reflexes (111) and (200) are different. It should be noted that the distinction is not present at low temperatures. Hence, the clusters deposited on a substrate at low temperatures have a spherical form.

The B-group films (C/Ni=40/60 vol.%) demonstrate nickel FCC-phase at average and high substrate temperatures (see X-ray diffraction patterns in Fig. 3a). At the same time, the reflexes of the NiO phase are registered at substrate temperatures < 160 °C (see Fig. 3a, too).

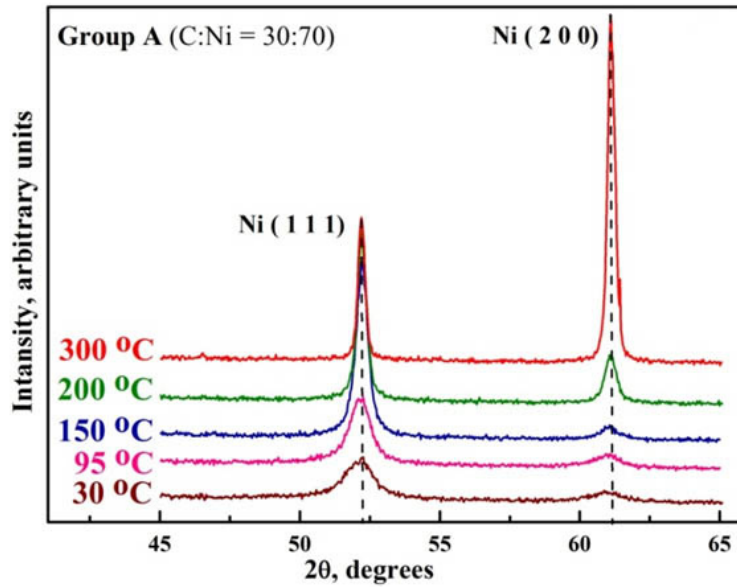


FIG. 2. Influence of substrate temperature T_S on X-ray diffraction of the A-group films

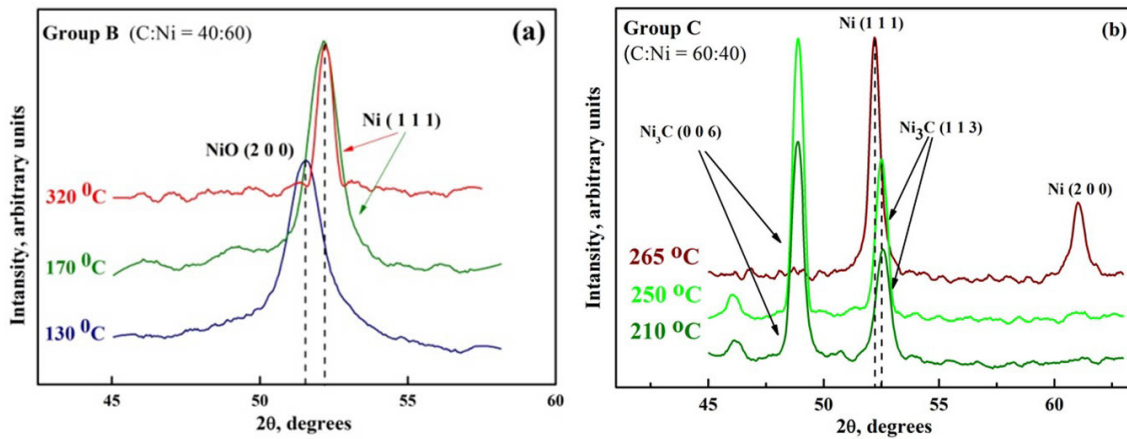


FIG. 3. Influence of substrate temperature T_S on X-ray diffraction of B (a) and C (b) groups films

It is possible to assume, that the increase in concentration of carbon in the films results in a change of carbon structure covering the nickel nanocrystallites. At low carbon concentrations in the Ni-C nanoclusters, the carbon shells around the metal nanocrystallites are mostly unclosed and composed by imperfect curved fragments with pores. It is obvious that nickel oxidation takes place under the interaction of the nanoclusters with atmosphere. At the same time, an increase in the substrate temperature results in a sharp increase of ordering of curved carbon fragments and provides protection of the Ni-crystallites against oxidation.

The C-group films (C/Ni=60/40 vol.%) demonstrate the nickel carbide Ni_3C HCP phase at the substrate temperature below 250 °C (see X-ray diffraction patterns in Fig. 3b). However, the reflexes corresponding to the FCC-lattice of nickel (111) and (200) are registered only at increasing temperature.

Fig. 4 shows substrate temperature T_S dependences of Ni-nanocrystallites size D of the B-group films. With T_S increase, the Ni-crystallites size increases, too. There is some critical temperature of the substrate T_{cr} nearby 80 °C, below which the nickel particles size tends to zero. This fact is the proof of amorphous nature of nanoclusters deposited onto a substrate.

In Fig. 4, there are also substrate temperature dependences of the nickel carbide Ni_3C nanocrystallites size D of the C-group films in direction (113). With T_S increase from 170 to 250 °C, the crystallites size sharply increases. The nickel carbide particles size tends to zero below the critical temperature of the substrate T_{cr} nearby 150 °C.

Application of the inductive-frequency method allows measuring directly the saturation magnetization of ferromagnetic samples $4\pi M_S$ [8, 12]. The presence of nonmagnetic impurities (for example, carbon) does not distort the result of measurements. Saturation magnetization of all samples was measured at room temperature. Fig. 5 shows the effect

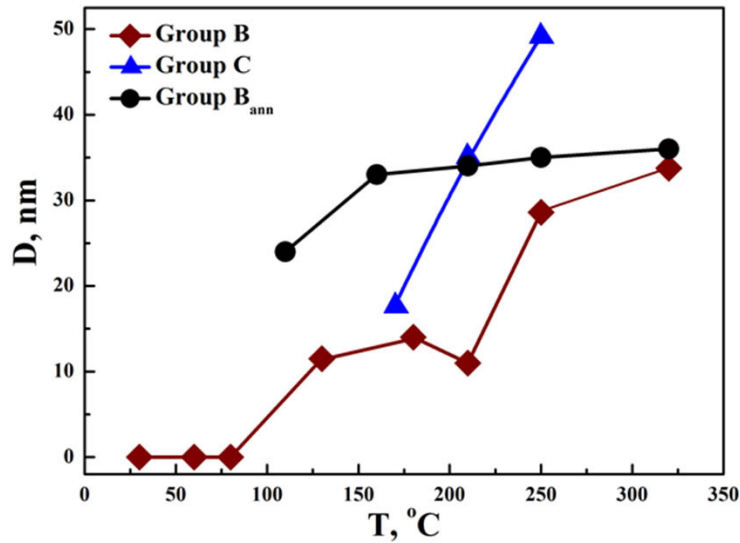


FIG. 4. Substrate temperature T_S dependence of size D of Ni- and Ni_3C -nanocrystallites of B- and C-groups films. B_{ann} – B-group films after annealing

of substrate temperature T_S on saturation magnetization $4\pi M_S$ of the ferromagnetic component for nickel-carbon films during growth. It is shown that the films of A-group characterized by the minimal content of carbon demonstrate ferromagnetism even at deposition onto a cold substrate. This result confirms the data of X-ray diffraction presented above in Fig. 2, where the Ni phase is fixed already for the lowest substrate temperatures. An increase of $4\pi M_S$ with the rising substrate temperature T_S can be explained by dimensional effect [8] due to increasing crystallite size D . These data are in good agreement with the conclusion that the deposited clusters have the structure of the “Ni core/C shell” type at low carbon concentration. They are formed directly in the magnetron plasma by crystallization of nickel atoms inside the nickel-carbon cluster. As the substrate temperature rises, the size of a cluster’s nickel-core grows due to diffusive processes and saturation magnetization of such crystallites $4\pi M_S$ is increased, too. We can see in Fig. 5 that $4\pi M_S$ comes nearer to magnetization of bulk nickel when the Ni crystallite size reaches macroscopic values at the substrate temperature $T_S \approx 300^\circ\text{C}$.

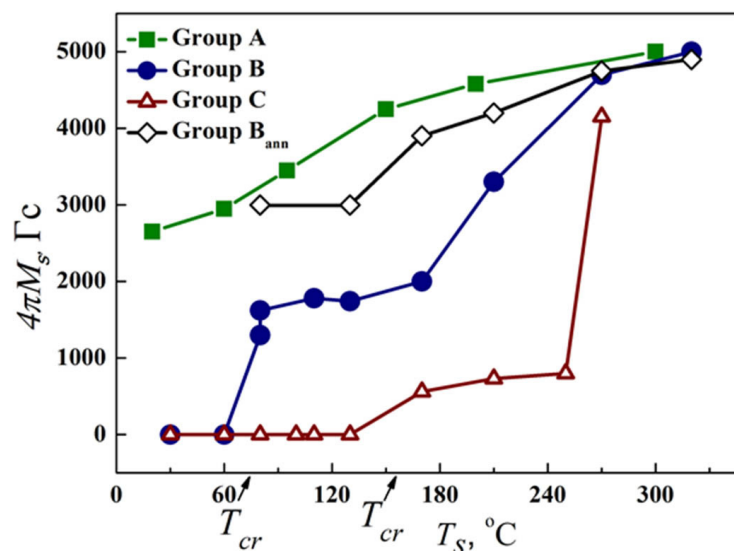


FIG. 5. Dependences of saturation magnetization $4\pi M_S$ on substrate temperature T_S for A-, B-, C-groups films of Ni-C system. B_{ann} – B-group films after annealing

At the same time, the films of B- and C-groups characterized by a larger content of carbon appear nonmagnetic in the case of deposition onto a cold substrate. They demonstrate ferromagnetism when deposited directly onto hot substrates. The critical temperature T_{cr} of ferromagnetism occurrence rises with an increase of the carbon – nickel ratio: for C/Ni = 40/60 vol.% $T_{cr} \approx 80^\circ\text{C}$, for C/Ni = 60/40 vol.% $T_{cr} \approx 150^\circ\text{C}$. At a higher substrate temperature,

magnetization of deposited clusters grows quickly until it approaches magnetization of bulk nickel at ~ 300 °C. This behavior of ferromagnetism in the films of B- and C-groups may be explained by the dissolution of carbon atoms in the nickel crystallites of deposited clusters. As a result, weakly magnetic solid solution of carbon in nickel can be formed and nonmagnetic carbide phase can be registered at large concentration of carbon.

It should be noted that we have observed a similar behavior of the ferromagnetic moment in the nickel-nitrogen films [14]. Besides, the magnetization depends on the crystallite size of nickel phase in the center of the deposited cluster. It is shown in Fig. 5 that increasing carbon concentration is accompanied by the increased substrate temperature at which the mentioned critical size is reached. In Fig. 5, we can see that the magnetization is decreased with increasing carbon concentration. This fact agrees with the model assuming the formation of an increasingly saturated solid solution of carbon in nickel. Further, with increase in substrate temperature, there is a crystallization of a nickel phase in separate clusters at first. When the carbon concentration in cluster becomes higher, the magnetization of nickel crystallite and its size is less [14]. The same process obviously takes place in the range of substrate temperatures T_S 80...180 °C for B-group films and 150...250 °C for C-group films. At higher T_S , there is an increase of the magnetization and confluence of separate clusters with increased nickel core and with general carbon shell, due to diffusive processes on a substrate and extraction of carbon from nickel phase.

To verify the model, we have carried out annealing of the B-group samples. The experiment was carried out on air at the temperature about 370 °C during 10 min. We can see increasing magnetization after annealing for the samples obtained at low substrate temperatures (see Fig. 5, B_{ann} curve). This fact confirms the diffusive mechanism of nickel crystallites growth at high substrate temperatures. The X-ray data also give evidences of an increase in Ni-crystallites size for the samples of B-group subjected to annealing (see Fig. 4, B_{ann} curve).

The results of the study allow us to make the following conclusions. At high C/Ni ratios, the nickel-carbon clusters formed in the plasma are amorphous formations in the form of a mixture of Ni and C atoms. Being deposited on a cold substrate, the clusters compose nonmagnetic films. Forming of nickel ferromagnetic crystallites starts for the substrate temperatures above T_{cr} . The higher the C/Ni ratio, the higher the value T_{cr} . It should be noted that if the carbon concentration is not high enough (imperfect carbon shell around the nickel core), oxidation of some of the Ni-crystallites and the appearance of the NiO phase is possible in the case of exposing samples to air. Similar situation is observed in the B-group films at the substrate temperature 130 °C (Fig. 3). In the films of C-group, clusters containing the hexagonal phase of nickel carbide Ni_3C are formed basically at the substrate temperature within the range of 170 – 250 °C due to the high content of carbon in magnetron plasma. The ferromagnetic crystallites of nickel phase are of small size and well protected by carbon shell. Nickel carbide is decomposed at the substrate temperature above 250 °C and deposited clusters have ordinary structure, namely “a crystal Ni-core/carbon shell”.

4. Conclusion

Three series of Ni@C films were grown with different ratios C/Ni (vol.%) = 30/70 (group A); 40/60 (group B); 60/40 (group C). Using atomic force microscopy, it is shown that Ni-C clusters with a characteristic dimension about ~ 10 nm are formed in the plasma and deposited onto the growth surface of the film. Thus, magnetron deposition of the films is of predominant cluster's nature. For the samples of A-group, X-ray diffraction analysis reveals the nickel phase and the increase in the size of its crystallites with increasing substrate temperature. For the samples of B- and C-groups, the nickel phase is observed only at relatively high substrate temperature, while the films with nanocrystalline nickel carbide Ni_3C are formed on relatively cold substrates. The research results show that the samples of A-group (low carbon content) exhibit ferromagnetic properties even when deposited on a cold substrate, while for B- and C-groups (average and high carbon content), ferromagnetism occurs only under conditions of sample growth at temperatures higher than certain critical substrate temperatures: 80 and 150 °C, respectively.

References

- [1] Sunny V., Kumar D., Yoshida Ya., Makarewicz M., Tabis W., Anantharaman M. Synthesis and properties of highly stable nickel/carbon core/shell nanostructures. *Carbon*, 2010, **48**(5), P. 1643–1651.
- [2] El Mel A., Gautron E., Angleraud B., Granier A., Tessier P. Synthesis of nickel-filled carbon nanotubes at 350°C. *Carbon*, 2011, **49**(13), P. 4595–4598.
- [3] Kumar M., Ando Y. Chemical vapor deposition of carbon nanotubes: a review on growth mechanism and mass production. *J. Nanosci. Nanotechnol.*, 2010, **10**(6), P. 3739–3758.
- [4] He Z., Lee Ch.S., Maurice Jean-L., Pribat D., Haghi-Ashtiani P., Cojocaru C.S. Vertically oriented nickel nanorod/carbon nanofiber core/shell structures synthesized by plasma-enhanced chemical vapor deposition. *Carbon*, 2011, **49**(14), P. 4710–4718.
- [5] Hayashi Y., Tokunaga T., Toh S., Moon W.J., Kaneko K. Synthesis and characterization of metal-filled carbon nanotubes by microwave plasma chemical vapor deposition. *Diamond and Related Materials*, 2005, **14**(3-7), P. 790–793.
- [6] Shalae R.V., Ulyanov A.N., Prudnikov A.M., Shin G.M., Yoo S.I., Varyukhin V.N. Noncatalytic synthesis of carbon nitride nanocolumns by DC magnetron sputtering. *Phys. Status Solidi A.*, 2010, **207**(10), P. 2300–2302.
- [7] Shalae R.V., Prudnikov A.M., Ulyanov A.N., Shin G.M. et al. Effect of in situ ultraviolet irradiation on the formation of nanostructural carbon nitride films. *Phys. Status Solidi A.*, 2012, **209**(7), P. 1287–1290.
- [8] Novikov S.I., Konev A.S., Uymin M.A., Ermakov A.E., Privalova D.V., Maykov V.V. Magnetic properties of Ni@C nanocomposites. *International journal of applied and fundamental research*, 2017, **12**, P. 247–251.

- [9] Uymin M.A., Novikov S.I., Konev A.S., Byzov I.V., Ermakov A.E. et al. Evolution of structure and magnetic properties composite nanoparticles Ni@C during annealing. *Physics of metals and metal science*, 2019, **120**(3), P. 245–250.
- [10] Shalayev R.V., Varyukhin V.N., Prudnikov A.M., Linnik A.I., Syrotkin V.V. Role of carbon in the formation of the structure and magnetic properties of Ni@CN_x nanoclusters under reactive magnetron deposition. *Nanosystems: Phys. Chem. Math.*, 2017, **8**(6), P. 804–808.
- [11] Kashtanov P.V., Smirnov B.M., Hippler R. Magnetron plasma and nanotechnology. *Phys. Usp.*, 2007, **50**, P. 455–488.
- [12] Dovgii V.T., Linnik A.I., Pashchenko V.P., Derkachenko V.N., Prokopenko V.K., Turchenko V.A., Davydeiko N.V. Anomalous magnetic hysteresis in La_{0.6}Sr_{0.2}Mn_{1.2}O_{3- δ} manganites with a perovskite structure. *Technical Physics Letters*, 2003, **29**(7), P. 610–612.
- [13] Liechtenstein I.Ya., Schemchenko E.I., Varyukhin V.N. Mechanism of formation of the internal structure in multi-walled carbon nanotubes produced by a DC-magnetron. *PHPT*, 2021, **31**(4), P. 42–47.
- [14] Linnik A.I., Prudnikov A.M., Shalaev R.V., Linnik T.A., Varyukhin V.N., Kostyrya S.A., Burkhovetskii V.V. Magnetic properties and thermal modification of nanostructured films of nickel nitrides. *Technical Physics Letters*, 2013, **39**(2), P. 143–146.

Submitted 15 May 2024; revised 24 May 2024; second revision 14 June 2024; accepted 15 June 2024

Information about the authors:

Rostyslav V. Shalayev – Galkin Donetsk Institute for Physics and Engineering, R. Luxembourg str. 72, 283048, Donetsk, Russia; ORCID 0000-0003-1258-2434; sharos@donfti.ru

Victor N. Varyukhin – Galkin Donetsk Institute for Physics and Engineering, R. Luxembourg str. 72, 283048, Donetsk, Russia; ORCID 0000-0001-7717-8745; director@donfti.ru

A. I. Linnik

Vladimir V. Syrotkin – Galkin Donetsk Institute for Physics and Engineering, R. Luxembourg str. 72, 283048, Donetsk, Russia; vladir.52@mail.ru

S. A. Kostyrya

Conflict of interest: the authors declare no conflict of interest.

Effect of laser radiation on magnetite nanoparticles in deposited ferrofluid

Ivan V. Pleshakov^{1,a}, Arseniy A. Alekseev^{2,b}, Efim E. Bibik^{3,c}, Igor V. Ilichev^{1,d}, Andrey V. Prokof'ev^{1,e}

¹Ioffe Institute, St. Petersburg, Russia

²Peter the Great St. Petersburg Polytechnic University, St. Petersburg, Russia

³St. Petersburg State Institute of Technology (Technical University), St. Petersburg, Russia

^aivanple@yandex.ru, ^barseniy.alekseev98@gmail.com, ^ceefimovich@yandex.ru,

^diiv@mail.ioffe.ru, ^eAndrey.prokofyev@algo-spb.com

Corresponding author: Ivan V. Pleshakov, ivanple@yandex.ru

PACS 42.50.Wk, 75.50.Mm

ABSTRACT The processes in a system of nanoparticles of a concentrated colloidal solution of magnetite induced by laser light with a wavelength of 650 μm have been studied. It was found that radiation focused on a drying drop of this substance, under certain conditions, leads to the formation of large accumulations of particles, in some cases strongly protruding above the surface of the sediment or, on the contrary, to their displacement from the illuminated area. A qualitative discussion of possible mechanisms of the observed phenomena is carried out.

KEYWORDS laser beam, optical force, magnetic fluid, ferrofluid.

ACKNOWLEDGEMENTS The authors are grateful to A. V. Tronev for his help in the experiments.

FOR CITATION Pleshakov I.V., Alekseev A.A., Bibik E.E., Ilichev I.V., Prokof'ev A.V. Effect of laser radiation on magnetite nanoparticles in deposited ferrofluid. *Nanosystems: Phys. Chem. Math.*, 2024, **15** (3), 346–351.

1. Introduction

The study of magnetic liquids or ferrofluids (FFs) has recently become particularly relevant due to their possible application in biomedicine [1, 2], as well as because of their unique optical properties that are promising for creating various photonics devices [3]. It has been proposed, for example, to use such materials in sensors [4–6], modulators [7], Bragg gratings [8] and many other optoelectronic instruments [9]. In all cases, an important fact was the sensitivity of these substances to the magnetic field, which leads to the formation of aggregates of nanoparticles composing ferrofluid [10, 11], and, as a consequence, a change in its characteristics. The latter, however, can also occur under the influence of light itself. It is known, for instance, that it can induce the clusters [12].

In general, as has been shown in many works, the effect of light on FF turns out to be different depending on the conditions, since the optical forces acting on particles can be attractive or repulsive [13–19]. It was found that in solid polymer composites, even at relatively low radiation power densities, nanoparticles are electrically polarized [20]; it is natural to extend this effect to liquids as well. Herewith, it should be borne in mind that polarized particles can both be drawn into the light beam and pushed out of it [13, 16]. The results of the always present heating are similar, determined by the sign of the thermal diffusion coefficient [17]. The competition of polarization and thermal phenomena creates a complex and not always unambiguous picture of the light effect on FF.

Undoubtedly, the information about the specificity of the processes in illuminated colloids is important for analyzing the operation of any optical device where such a substance is used. Since it is not complete enough at the moment, further studies of the behavior of nanoparticles in the light field are required. In this work, we investigated the structures formed by magnetic nanoparticles when they are deposited on a substrate in a laser beam focused on a drying drop of highly concentrated FF.

2. Samples and experiment

Ferrofluids are colloidal solutions of magnetically ordered compounds suspended in an appropriate carrier. As a solid phase ferrites are often used, although there are many other options. Liquid media are diverse, with water (this is essential for biological applications) and hydrocarbons (e.g. kerosene) being very common. The properties of these materials depend on the method of their stabilization, that is, on how the particles are prevented from sticking together. This is usually done by applying the surfactant onto the surface of nanoparticles; sometimes the structure of such a layer can be quite complex. In aqueous solutions, for this purpose, a coating by electric charge is widely created (ion stabilization). In some cases, additional stabilizing admixtures are added to the carrier composition (more details on the principles of obtaining and using of FFs can be found, for example, in the review [21]).

In this work, we used aqueous and kerosene-based solutions of magnetite Fe_3O_4 , both commercial and self-synthesized, with different types of stabilization. Basic information about the samples is given in the Table 1 (the compositions of the stabilizer and additives for samples No. 1 and No. 2 were not specified by the manufacturer in more detail than indicated). The approaches used in the synthesis of materials are described in [22]. In all cases, magnetite nanoparticles had a characteristic size of about 10 nm. Solution No. 3 was prepared from the centrifuged sediment of the ion-stabilized fluid by diluting it in water. Solution No. 4 was obtained by dilution in kerosene of a paste-like precursor, obtained during the reaction of an ammonia water precipitation of solution of FeCl_3 and FeSO_4 with subsequent condensation with oleic acid (the same sample was used in [23]). In this case, a small uncontrollable amount of the latter substance passes into the liquid phase.

TABLE 1. The main characteristics of the samples used

No	Liquid carrier	Coating	Additives, vol. %	Initial concentration of solid phase, vol. %	Origin
1	Water	Organic stabilizer	Organic oil, 18	27	Commercial
2	Kerosene	Polymer stabilizer	Organic oil, 22	18	
3	Water	Ionic	–	20	Self-synthesized
4	Kerosene	Monomolecular (nominally) layer of oleic acid	Impurity of oleic acid, < 5 %	20	

To obtain different concentrations n , the samples were diluted with the appropriate carrier liquid from the initial concentration indicated in Table 1 to 5 vol. % (further, the volume percentages of the solid phase content are given everywhere). The solutions were treated in an ultrasonic bath for one hour.

The experiments were performed as follows. The liquid was applied in several drops onto a glass plate and distributed over it so that the resulting layer had a thickness of about 1 mm. Then, using a mirror, a laser beam was directed at the liquid, focused in such a way that the focus was inside it. A semiconductor CW laser with a wavelength of $650 \mu\text{m}$ and a power of 40 mW was used. The estimated power density in the focal spot was approximately 10 kW/cm^2 . After drying for several hours at continuous radiation exposure, the trace of light was formed on the surface of the sediment. Its appearance depended on the sample, and this was the subject of the investigation.

The traces were studied by microscopes. One of them (Micro 200T-01), having a short focal length, made it possible to obtain images of a sample illuminated from above or below, and also, by adjusting the depth of field, to estimate the height of the object's protrusion above the surface h (since this method gives one only qualitative results, in the graphs below errors are not indicated). The other (Altami SM0745-T) had a larger focal length, which made it possible to rotate the sample at an angle convenient for recording its lateral image.

The shape of the object formed near the focus was influenced by the composition of nanoparticle coating, additives, and the concentration of the deposited material. In certain cases significant accumulations of matter could be observed on the surface of the sediment, but even at low n , the trace of the laser radiation was visible. The criterion for its linear size was taken to be $D = 2\sqrt{S/\pi}$, where S is its area (it should be noted that, despite the fact that the shape of the laser trace was not ideal, it was almost always close to a circle).

3. Results and discussion

The micrographs shown in Fig. 1 illustrate the effect of light on aqueous solutions obtained by dilution of composition No. 1 (see Table 1). In these cases, a pronounced effect of nanoparticles being drawn into the laser beam is observed. The images are obtained with a short-focus microscope as the top views. On Figs. 1a,c,d, the surface of the sediment is illuminated from above, in Fig. 1b, the illumination is made from below to emphasize the boundary of the spot. It can be seen that a dense (opaque) clot appears near the area of focused radiation, the size of which correlates with the concentration of the colloid. In Fig. 1b, there is certain heterogeneity of the sediment outside the light-induced trace, but it is obvious that on average, it is much thinner than in the trace.

Lateral images obtained for the same samples using a long-focus microscope show that at large n , light-induced aggregates can noticeably protrude above the surface. As an example, Fig. 2 demonstrates the type of laser trace for the sample with $n = 20 \%$ at two viewing angles. In Fig. 2a, the cone-shaped formation, elongated in the direction of the laser beam, is clearly visible. Its height h was estimated as $230 \mu\text{m}$. It should be noted that this value, as well as the dimension of the "base" of this structure, is significantly smaller than the average diameter D , measured by Fig. 1b. However, it

should be borne in mind that the darkened area that practically does not rise above the surface is several times larger than the protruding object – this is somewhat better detected by another rotation of the sample (Fig. 2b).

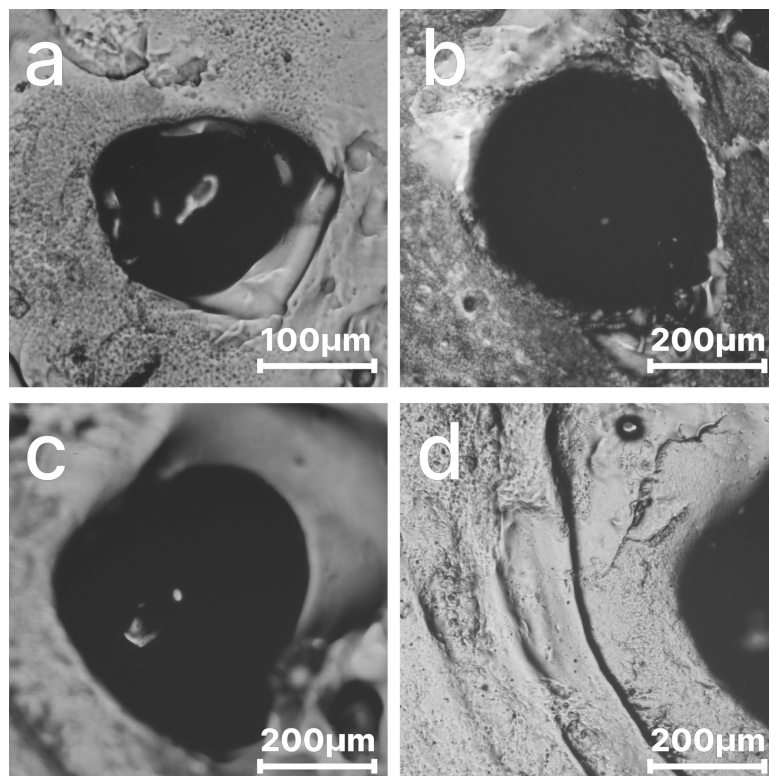


FIG. 1. Structures formed on the surface of the sediment of aqueous ferrofluids obtained from solution No. 1 (top view). a – $n = 12\%$; b – $n = 20\%$ (bottom illumination); c – $n = 27\%$; d – edge of the laser trace in FF with $n = 27\%$

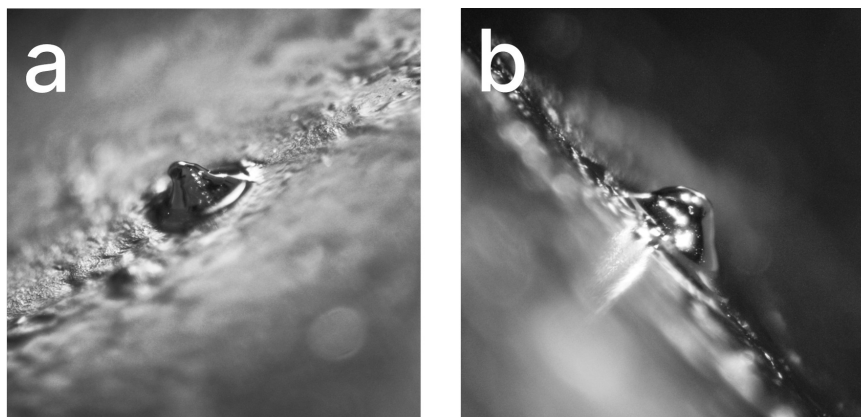


FIG. 2. Trace formed by laser radiation in precipitated aqueous solution of FF with $n = 20\%$ (lateral view). Figures a and b refer to different orientations of the sample

The action of light on kerosene-based materials with another type of stabilization (initial solution No. 2, Table 1) turns out to be opposite. As can be seen from Fig. 3, in this case, the laser radiation leads to an outward movement of nanoparticles from irradiated area. Herewith, a ring-shaped object appears with a solid phase substance completely displaced from the central region. The opening has approximately the same size as the size of the dark spot for aqueous material with the same n (Fig. 3a, micrograph obtained with illumination from below). Such phenomena were observed at concentrations from 18 to 10%.

Aqueous samples based on solution No. 3 displayed the effect of particles being drawn into the beam, but the appearance of a strongly protruding object was not registered. It should be noted that these substances are the “cleanest” of the used ones, i.e. its nominally do not contain any organic additives, unlike for other substances, where a certain “gluing effect” was manifested during precipitation that promotes the formation of a relatively smooth surface. In contrast, the

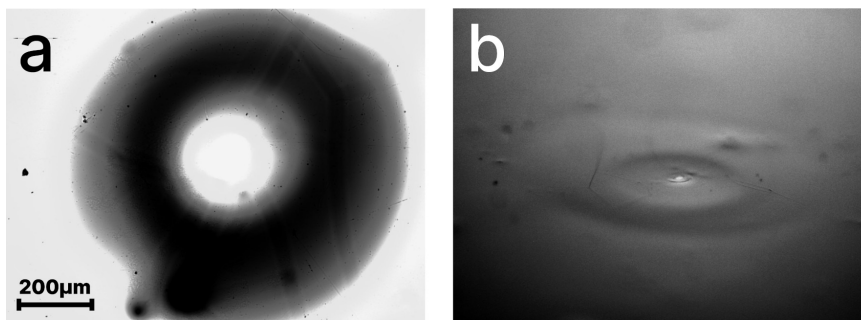


FIG. 3. Trace formed by laser radiation in a precipitated solution of FF based on kerosene (No. 2) with $n = 10\%$. a – top view, bottom illumination; b – lateral view

precipitates of solutions No. 3 were strongly cracked, which made it difficult to measure the aggregate height h , although the size of the spot D was easily determined.

The dependences of the geometric characteristics of laser traces on the concentration are shown in Fig. 4. Their increase with the growth of n can be remarked as a trend (though for large n this is apparently violated). Let's add that at $n < 5\%$, the traces usually were also observed, but less pronounced and not protruding above the surface.

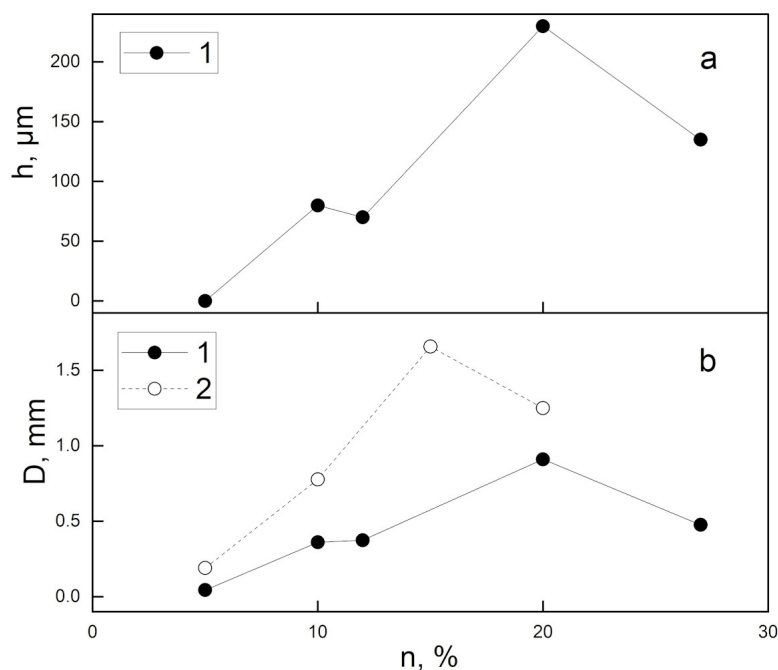


FIG. 4. Dependence of the geometric characteristics of the aggregates formed in aqueous solutions on the solid phase content, 1 – samples with organic stabilization (dilution from the initial substance No. 1); 2 – samples with ionic stabilization (dilution from initial substance No. 3). a – the height of the unit protrusion above the sediment surface; b – the size of the spot in the sediment plane. (The lines on the graph are drawn for ease of perception)

To some extent, solutions based on kerosene colloid No. 4 are of a special case. As it is seen from Fig. 5, which shows micrographs related to samples with $n = 10\%$ (Fig. 5a) and $n = 20\%$ (Fig. 5b), a height occurs in the area of irradiation, but near it one observes the formation of a deepening – the image resembles a crater. Also it should be noted that at a fairly large distance from the center of this object, a certain wave-like structure can be noticed (a similar sometimes was observed for other samples, see the edge of the laser-induced spot in Fig. 1d).

The results presented above cannot be strictly analyzed at this time; however, it is obvious that qualitatively one can come to some general ideas concerning to the behavior of nanoparticles in a laser beam. The most significant thing is the fundamentally different nature of the optical force acting on nanoparticles of the same composition (i.e., the material of the magnetic core) but with different solvents – from pronounced retraction into the light field to equally well-observed expulsion from it (Figs. 1 and 3). Of course, this is in agreement with the works mentioned above, since (even under

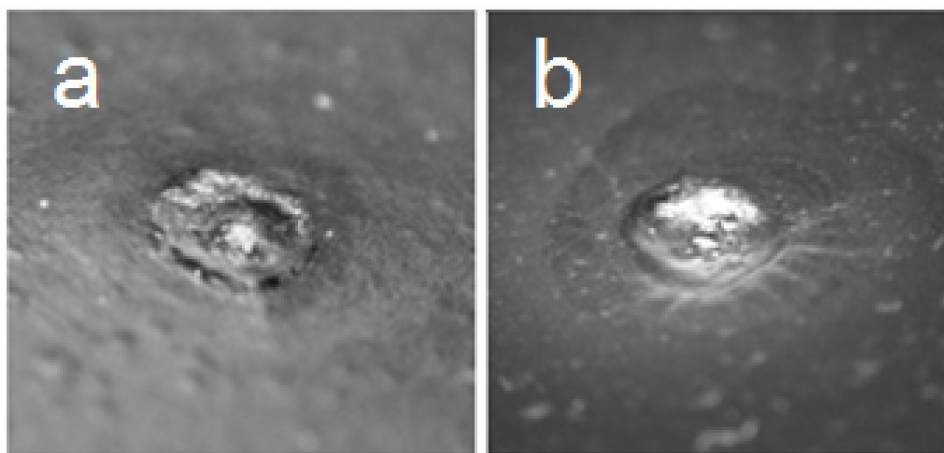


FIG. 5. Lateral view of the laser trace in precipitated FF based on paste and kerosene. a – $n = 10\%$; b – $n = 20\%$

the assumption that the laser radiation creates the same polarizations in particles) optical-induced movement can occur in different ways owing to the fact that it is determined by many mechanisms.

Polarization effects, which by themselves can lead to the appearance of forces of different signs [12, 13], are complemented by thermodiffusion, which depends on the sign of the Soret coefficient [17, 24]. (It should be noted that there may also be a time dependence here [17, 18], however, we believe that in our case, we are dealing with a steady-state process, since the time of the experiment significantly exceeds the characteristic times of the evolution of optical responses mentioned in literature). An important fact should be pointed out that there are two cases with opposite results for polar and nonpolar solvents (Figs. 1 and 3). Apparently, the optical polarization of the medium should indeed be taken into account, but attention should also be paid to the fact that samples from solutions No. 3 and 4, being made on the basis of water and kerosene, give one similar results (results shown in Fig. 5 may not be interpreted quite unambiguously, but nevertheless, here, in the center of the laser trace, an accumulation of substance is clearly visible). A significant role for the optical radiation action on FFs must be played by the thermal parameters of solvents responsible for the appearance of temperature gradients. They differ not only for different carrier liquids (the thermal conductivity of water is several times higher than that of kerosene), but perhaps also for the same liquids with different additives (see Table 1).

Finally, it should be taken into consideration that in all the materials studied, the coatings of nanoparticles are different. The interaction of the surfactant with the adjacent layers of material leads to the formation of the layer of non-magnetic substance. If its thickness is one or two lattice constants, the volume of the shell turns out to be approximately 50 % of the total volume of the particle. Since the electromagnetic field of a light wave can cause polarization in such a substance too, it should be assumed that with the same magnetic cores, the total polarizations of nanoparticles of FFs with different types of stabilization differ.

To summarize, we can say that the interaction of the laser beam with polarization induced in the materials of the core and shell of the particle, the type and thermal characteristics of the liquid medium, as well as the direction of thermal diffusion produce a combination of factors leading to the appearance of optical force acting on the particle. Depending on their sign and magnitude, this force can be directed inward or outward in relation to the beam, thus forming condensations or rarefactions of nanoparticles in the FF thickness, which, when deposited, create structures observed in our experiments.

4. Conclusion

In this work, the phenomena associated with the laser beam action on nanoparticles of various ferrofluids lead to the formation of distinct patterns on the surface of their sediment were discovered. It has been established that the optically induced force responsible for their appearance depends on the properties of the liquid, creating an areas with a substance suppressed from it, or, oppositely, with its accumulation, sometimes in the form of large objects strongly protruding in the direction of the beam.

This information may be useful in further studying the behavior of ferrofluid nanoparticles in a light wave.

References

- [1] Socoliuc V., Avdeev M., Kuncser V., Turcu R., Tombácz E., Vekas L. Ferrofluids and bio-ferrofluids: looking back and stepping forward. *Nanoscale*, 2022, **14**, P. 4786–4886.
- [2] Imran M., Alam M.M., Khan A. Advanced biomedical applications of iron oxide nanostructures based ferrofluids. *Nanotechnology*, 2021, **32**(42), P. 422001.
- [3] Philip J., Laskar J.M. Optical properties and applications of ferrofluids – a review. *J. Nanofluids*, 2012, **1**, P. 3-20.

- [4] Zhengyong Li, Changrui Liao, Jun Song, Ying Wang, Feng Zhu, Yiping Wang, Xiaopeng Dong. Ultrasensitive magnetic field sensor based on an in-fiber Mach–Zehnder interferometer with a magnetic fluid component. *Photonics Res.*, 2016, **4**(5), P. 197–201.
- [5] Taghizadeh M., Bozorgzadeh F., Ghorbani M. Designing magnetic field sensor based on tapered photonic crystal fibre assisted by a ferrofluid. *Sci. Rep.*, 2021, **11**(1), P. 14325.
- [6] Alberto N., Domingues M.F., Marques, C. André P., Antunes P. Optical fiber magnetic field sensors based on magnetic fluid: a review. *Sensors*, 2018, **18**(12), P. 4325.
- [7] Agruzov P.M., Pleshakov I.V., Bibik E.E., Shamray A.V. Magneto-optic effects in silica core microstructured fibers with a ferrofluidic cladding. *Appl. Phys. Lett.*, 2014, **104**(7), P. 071108.
- [8] Candiani A., Margulis W., Sterner C., Konstantaki M., Pissadakis S. Phase-shifted Bragg microstructured optical fiber gratings utilizing infiltrated ferrofluids. *Opt. Lett.*, 2011, **36**(13), P. 2548–2550.
- [9] Yong Zhao, Yuyan Zhang, Lu R.-Q., Qi Wang. Novel optical devices based on the tunable refractive index of magnetic fluid and their characteristics. *J. Magn. Magn. Mat.*, 2011, **323**(23), P. 2987–2996.
- [10] Pleshakov I.V., Prokof'ev A.V., Bibik E.E., Kuz'min Yu.I. Investigation of structures formed by magnetic fluid nanoparticles in polymer matrices by static light scattering. *Nanosystems: physics, chemistry, mathematics*, 2022, **13**(3), P. 285–289.
- [11] Pleshakov I.V., Ryzhov V.A., Marchenko Ya.Yu., Alekseev A.A., Karseeva E.K., Nevedomskiy V.N., Prokof'ev A.V. Agglomeration of magnetite nanoparticles with citrate shell in an aqueous magnetic fluid. *Nanosystems: physics, chemistry, mathematics*, 2023, **14**(3), P. 334–341.
- [12] Xiangpeng Yang, Qian Li, Xiangshen Meng, Decai Li. Evolution of nonlinear optical characteristics of magnetic nanoparticle colloidal suspensions after laser-induced clusters. *ACS Omega*, 2020, **5**(26), P. 15821–15827.
- [13] Tianjun Yao, Shengli Pu, Jie Rao, Jianming Zhang. Investigation of optical force on magnetic nanoparticles with magnetic-fluid-filled Fabry-Perot interferometer. *Sci. Rep.*, 2018, **8**(1), P. 12352.
- [14] Bacia M., Masajada J., Drobczycki S. Observation of magnetic nanoparticles ring formation and dynamics with a fast video camera. *Photonics Lett. Pol.*, 2013, **5**(4), P. 137–139.
- [15] Masajada J., Bacia M., Drobczycki S. Cluster formation in ferrofluids induced by holographic optical tweezers. *Opt. Lett.*, 2013, **38**(19), P. 3910–3913.
- [16] Zi-Ming Meng, Hai-Ying Liu, Wei-Ren Zhao, Wei Zhang, Hai-Dong Deng, Qiao-Feng Dai, Li-Jun Wu, Sheng Lan, Achanta Venu Gopal. Effects of optical forces on the transmission of magnetic fluids investigated by Z-scan technique. *J. Appl. Phys.*, 2009, **106**(4), P. 044905.
- [17] Alvès S., Demouchy G., Bee A., Talbot D., Bourdon A., Figueiredo Neto A.M. Investigation of the sign of the Soret coefficient in different ionic and surfactant magnetic colloids using forced Rayleigh scattering and single-beam Z-scan techniques. *Philos. Mag.*, 2003, **83**(17-18), P. 2059–2066.
- [18] Hoffmann B., Köhler W., Krekhova M. On the mechanism of transient bleaching of the optical absorption of ferrofluids and dyed liquids. *J. Chem. Physics.*, 2003, **118**(7), P. 3237–3242.
- [19] Hoffmann B., Köhler W. Reversible light-induced cluster formation of magnetic colloids. *J. Magn. Magn. Mat.*, 2003, **262**(2), P. 289–293.
- [20] Milichko V.A., Nechaev A.I., Valtisfer V.A., Strelnikov V.N., Kulchin Yu.N., Dzyuba V.P. Photo-induced electric polarizability of Fe₃O₄ nanoparticles in weak optical fields. *Nanoscale Res. Lett.*, 2013, **8**, P. 317.
- [21] Scherer C., Figueiredo Neto A.M. Ferrofluids: properties and applications. *Braz. J. Phys.*, 2005, **35**(3A), P. 718–727.
- [22] Griбанov N.M., Bibik E.E., Buzunov O.V., Naumov V.N. Physico-chemical regularities of obtaining of highly dispersed magnetite by the method of chemical condensation. *J. Magn. Magn. Mater.*, 1990, **85**(1-3), P. 7–10.
- [23] Mazur A.S., Pleshakov I.V., Khudyakov A.V., Kuzmin Y.I. NMR investigation of iron-containing magnetically ordered nanomaterial used for preparing of magnetic fluid. *J. Phys.: Conf. Ser.*, 2019, **1326**(1), P. 012009.
- [24] Alvès S.I., Bourdon A., Figueiredo Neto A.M. Investigation of the Soret coefficient in magnetic fluids using the Z-scan technique. *J. Magn. Magn. Mater.*, 2005, **289**, P. 285–288.

Submitted 15 May 2024; revised 30 May 2024; accepted 31 May 2024

Information about the authors:

Ivan V. Pleshakov – Ioffe Institute, Politechnicheskaya 26, St. Petersburg, 194021, Russia; ORCID 0000-0002-6707-6216; inanple@yandex.ru

Arseniy A. Alekseev – Peter the Great St. Petersburg Polytechnic University, Politechnicheskaya 29, St. Petersburg, 195251, Russia; ORCID 0009-0000-5368-6788; arseniy.alekseev98@gmail.com

Efim E. Bibik – St. Petersburg State Institute of Technology (Technical University), Moskovsky Ave., 26, St. Petersburg, 190013, Russia; ORCID 0000-0003-4063-2697; eefimovich@yandex.ru

Igor V. Ilichev – Ioffe Institute, Politechnicheskaya 26, St. Petersburg, 194021, Russia; ORCID 0000-0001-7809-0630; iiv@mail.ioffe.ru

Andrey V. Prokof'ev – Ioffe Institute, Politechnicheskaya 26, St. Petersburg, 194021, Russia; ORCID 0009-0009-7894-1947; Andrey.prokofyev@algo-spb.com

Conflict of interest: the authors declare no conflict of interest.

Cellular uptake of FITC-labeled Ce_{0.8}Gd_{0.2}O_{2-x} nanoparticles in 2D and 3D mesenchymal stem cell systems

Danil D. Kolmanovich^{1,a}, Nikita N. Chukavin^{1,2,b}, Nikita A. Pivovarov^{1,c}, Sergey A. Khaustov^{2,d}, Vladimir K. Ivanov^{3,e}, Anton L. Popov^{1,2,f}

¹Institute of Theoretical and Experimental Biophysics of the Russian Academy of Sciences, Pushchino, Russia

²Scientific and Educational Center, State University of Education, Moscow, Russia

³Kurnakov Institute of General and Inorganic Chemistry of the Russian Academy of Sciences, Moscow, Russia

^akdd100996@mail.ru, ^bchukavinnik@gmail.com, ^cnikitapivovarov.workmail@gmail.com,

^dsergeykhaustov@gmail.com, ^evan@igic.ras.ru, ^fantonpopovleonid@gmail.com

Corresponding author: Anton L. Popov, antonpopovleonid@gmail.com

ABSTRACT Cerium-containing nanoparticles have recently been identified as promising nanozymes for advanced biomedical applications. Additional modification of the core or the surface of CeO₂ nanoparticles (CeO₂ NPs) provides them with new functionalities, making them a unique theranostic agent. In this study, dextran-stabilized CeO₂ NPs doped with Gd (Ce_{0.8}Gd_{0.2}O_{2-x}) were synthesized and further functionalized with fluorescein isothiocyanate (FITC). The synthesized nanoparticles have a high degree of biocompatibility at concentrations up to 5 mg/mL and are readily internalized by human mesenchymal stem cells cultured both in monolayers (2D system) and cellular spheroids (3D system). The functionalization of CeO₂ NPs with Gd and FITC dye allows for monitoring their accumulation within organs and tissues using both magnetic resonance imaging (MRI) and fluorescence spectroscopy techniques.

KEYWORDS nanoparticles, 3D cell spheroid, cerium, gadolinium

ACKNOWLEDGEMENTS The work was supported by the Russian Science Foundation (project No. 22-73-10231, <https://rscf.ru/project/22-73-10231/>)

FOR CITATION Kolmanovich D.D., Chukavin N.N., Pivovarov N.A., Khaustov S.A., Ivanov V.K., Popov A.L. Cellular uptake of FITC-labeled Ce_{0.8}Gd_{0.2}O_{2-x} nanoparticles in 2D and 3D mesenchymal stem cell systems. *Nanosystems: Phys. Chem. Math.*, 2024, **15** (3), 352–360.

1. Introduction

Currently, cerium dioxide is considered one of the most promising biomedical nanomaterials (CeO₂ NPs) [1–5]. CeO₂ nanoparticles show pronounced antioxidant activity, which allows to suppress the intracellular oxidative stress and inflammation [6]. The antioxidant property of CeO₂ NPs is based on their ability to mimic the activity of various endogenous enzymes, such as SOD [7], catalase [8, 9], phosphatase [10], DNase [11], phospholipoperoxidase [12] and others [13]. It is generally accepted that this process is based on the redox cycling of Ce³⁺ and Ce⁴⁺, and it is attributed to the rapid self-repairing cycle of Ce³⁺/Ce⁴⁺ after the inactivation of reactive oxygen species (ROS) [14–18]. Interestingly, the enzyme-like activity of CeO₂ NPs can be modulated by adjusting the size, shape, core composition and surface stabilizer of the particles [19–21]. The use of various biocompatible stabilizers and surfactants not only ensures increased colloidal stability, but also enhances the efficiency of nanoparticle endocytosis and, consequently, provides them with selective cytotoxicity [22]. It has previously been demonstrated that CeO₂ NPs can be internalized by various cell types, such as mesenchymal stem cells [23]. At the same time, the uptake process of CeO₂ NPs by human MSCs is quite complex, as this type of cells does not have a specific function for phagocytosis [24]. In particular, it has been shown that CeO₂ NPs are able to stimulate the proliferation of mouse embryonic fibroblasts [25] and human MSCs, isolated from human tooth pulp [26, 27] and human Wharton's jelly [28]. Surface modification of polymer scaffolds with CeO₂ NPs enhances stem cell proliferation and osteogenesis. Particularly, it has been shown earlier that porous polylactic acid (PLA) scaffolds prepared by 3D printing and decorated with CeO₂ NPs enhanced human mesenchymal stem cell growth, reduced oxidative stress levels in the cells and showed enhanced antibacterial activity against both Gram-negative and Gram-positive bacterial strains [29]. CeO₂ NPs-functionalized poly(ϵ -caprolactone) (PCL)-gelatin electrospun fibers showed superoxide dismutase (SOD)-mimetic activity and enhanced fibroblast proliferation up to ~ 48 % in comparison to the control [30]. Human umbilical cord-derived mesenchymal stem cells, containing CeO₂ NPs, counter oxidative damage and promote tendon regeneration [31].

Mesenchymal stem cells (MSCs) are a promising resource for various biomedical applications, including those associated with tissue regeneration and cancer treatment. The ability of MSCs to migrate to areas of injury and inflammation

makes them an effective delivery vehicle for various functionalized nanomaterials to the sites of injury [32], inflammation [33] or into tumor growth area [34, 35], providing a pronounced therapeutic effect. MSCs fully exhibit their immunomodulatory properties only when they are in a specific microenvironment, which forms their tissue niche *in vivo* [36]. The most promising approach to ensure their optimal characteristics is through three-dimensional cell cultivation in cellular spheroids, as opposed to two-dimensional cultures [37–40]. In 3D structures, MSCs are able to form contacts and exchange regulatory signals with each other, as well as to produce an extracellular matrix that contributes to their function. However, the presence of the extracellular matrix can affect the efficiency of nanoparticles penetration into these structures [41–44]. Earlier, it was shown in a model of cellular spheroids formed from human umbilical vein endothelial cells (HUVEC) and MSCs, that nanoceria-decorated graphene oxide (CeGO) could be used for the treatment of critical limb ischemia [45]. CeGO uptake enhanced the survival rate and anti-apoptotic capacity of cellular spheroids, upregulated expression of angiogenic markers, ensuring high cell survival rate. Thus, the use of cerium-containing nanoparticles shows high promise in maintaining normal functioning of cell spheroids formed from mesenchymal stem cells [31, 46–48].

Additional functionalization of CeO_2 NPs makes it possible to develop effective therapeutic agents exhibiting new functional properties that ensure their tracking both inside cells and in tissues. In particular, it has previously been shown that doping of CeO_2 NPs with gadolinium ions allows for their visualization using magnetic resonance imaging [27]. McDonagh et al. developed a single-pot synthesis of CeO_2 NPs modified with zirconium-89 isotope allowing detailed PET imaging and *ex vivo* biodistribution visualization of CeO_2 NPs [49]. The potential of modifying nanoparticles with carbon dots has also been demonstrated [50]. Zhang et al. synthesized a new type of carbon material doped with cerium (Ce–Cd), using a simple hydrothermal process. This material exhibited pronounced luminescent properties and high photostability. It also possessed biological activity, as demonstrated by its antibacterial and wound-healing properties.

In this study, we performed additional functionalization of gadolinium-doped ceria NPs with a fluorescent tag and conducted a comprehensive assessment of their cytotoxic effects. We further analyzed the specific features of internalization of these multifunctional NPs into mesenchymal stem cells cultured in monolayers (2D system) and cellular spheroids (3D system).

2. Materials and methods

2.1. Synthesis procedure

$Ce_{0.8}Gd_{0.2}O_{2-x}$ NPs were synthesized according to a recently reported procedure [51]. Briefly, a mixed solution of cerium(III) and gadolinium(III) nitrates (0.18 and 0.02 M, respectively) and dextran ($M_r \approx 6000$) was prepared, with the $(Ce(NO_3)_3 \cdot 6H_2O + Gd(NO_3)_3 \cdot 6H_2O)$:dextran ratio being 1:2 (wt). To the continuously stirred solution, 1 M aqueous ammonia was added dropwise for 3 h, maintaining the pH at 7.5–8.0. When pH became constant, the mixture was stirred again, for 2 h, and then aqueous ammonia was added to achieve pH = 12, followed by additional stirring for 8 h. To the sol obtained, an excess of isopropanol was added and the mixture was refluxed to form a white precipitate. The precipitate was further washed with hot isopropanol several times and dried in air at 60 °C. Gadolinium-doped ceria sol was prepared by dispersing the powder in deionized water. $Ce_{0.8}Gd_{0.2}O_{2-x}$ NPs were functionalized using fluorescein isothiocyanate (FITC) to make it possible to study their intracellular localization. The dry powder of dextran-stabilized $Ce_{0.8}Gd_{0.2}O_{2-x}$ nanoparticles (3 g) was added to 20 mL of anhydrous dimethyl sulfoxide (DMSO) and 0.5 mL of pyridine. The mixture was then stirred for four hours at 95 °C until it was completely dissolved. Afterwards, 100 mg of FITC were added to the solution and the mixture was allowed to continue to mix for 2 hours in the dark. Following this, 50 mL of isopropanol was added to the resultant solution. The resulting mixture was then centrifuged at 10,000 g for 10 minutes. The precipitate that formed was repeatedly washed until the color in the supernatant had disappeared, and then it was dried at 60 °C in the dark to a constant mass. The dry powder of FITC- $Ce_{0.8}Gd_{0.2}O_{2-x}$ NPs was stored at 4 °C.

2.2. Characterization of FITC- $Ce_{0.8}Gd_{0.2}O_{2-x}$ NPs

The size and shape of FITC- $Ce_{0.8}Gd_{0.2}O_{2-x}$ NPs were analysed by transmission electron microscopy (TEM) using a Leo912 AB Omega electron microscope equipped with an electron energy loss spectrometer (EELS) operating at an accelerating voltage of 100 kV. The study of the chemical composition of the obtained materials was carried out using energy dispersive X-ray spectroscopy (EDX) using a Tescan Amber GMH microscope equipped with an Ultim MAX detector with 100 mm² active area (Oxford Instruments) at an accelerating voltage of 20 kV. EDX data were processed using the AZtec software (5.0). The concentration of the $Ce_{0.8}Gd_{0.2}O_{2-x}$ NPs (without FITC) sols was measured gravimetrically. The corundum crucibles, pre-annealed at 900 °C for 2 hours, were weighed on analytical scales to establish their initial weight. Then 3 mL of sol was placed in each crucible and heated in a muffle furnace at 900 °C for 2 hours with slow heating (~ 3 °/min). After cooling to room temperature, the crucibles were weighed. The weight of the dry residue of the annealing product was determined and the concentration of the initial sols was calculated. A DS-11+ spectrophotometer (DeNOVIX, USA) was used to measure FITC- $Ce_{0.8}Gd_{0.2}O_{2-x}$ sols absorbance in the UV-visible range. Measurements were carried out in the wavelength range from 200 to 500 nm in 0.1 nm increments. The hydrodynamic size, PDI and ζ -potential of the nanoparticles were determined by dynamic and electrophoretic light scattering at 25 °C using a BeNano analyzer (BetterSize, Dandong, China).

2.3. Cell culture

The experiments were performed using human mesenchymal stem cells (hMSCs). hMSCs were isolated from the pulp of a third molar extracted for orthodontic reasons from a healthy 12-year-old patient (with his written consent). All the experiments were carried out in agreement with good clinical practice and the ethical principles stated in the current edition of the Declaration of Helsinki. Cells were cultured in DMEM/F12 medium (1:1) (PanEko, Moscow, Russia) supplemented with L-glutamine (146 mg per 450 mL of medium) (PanEko, Moscow, Russia), penicillin, streptomycin (PanEko, Moscow, Russia), and 10 % fetal bovine serum (Biosera, Cholet, France). Cultivation was carried out in culture flasks with filter caps with a cultivation area of 25 and 75 cm² (TPP, Trasadingen, Switzerland) in a CO₂ incubator with a CO₂ concentration of 5 % at a temperature of 37 °C.

2.4. MTT assay

Cell metabolic activity was assessed using MTT assay which is based on the reduction of a yellow tetrazolium salt (3-[4,5-dimethylthiazole-2-yl]-2,5-diphenyl tetrazolium bromide, MTT) with the formation of insoluble purple formazan. After 48 hours of cultivation, 0.5 mg/mL MTT reagent solution, dissolved in culture medium without FBS, was added to the wells. The optical density of the formed formazan was measured at $\lambda = 570$ nm using an INNO-S plate reader (LTEK, Korea).

2.5. Measuring of mitochondrial membrane potential

The mitochondrial membrane potential (MMP) was measured by staining cells with TMRE (tetramethylrhodamine, ethyl ester, ThermoFisher, Carlsbad, CA, USA) fluorescent dye followed by fluorescence microscopy analysis. After 24, 48, and 72 hours of incubation with nanoparticles, the culture medium was replaced with TMRE solution in Hanks' buffer (PanEko, Moscow, Russia). After 15 min of incubation with dye, the cells were washed three times with Hanks' buffer solution. Then the cells were photographed using a ZOE fluorescent imager (Bio-Rad, USA). TMRE fluorescence intensity, which directly correlates with the MMP of cells, was measured using the ImageJ software. For statistics, three different areas in three different microphotographs were analyzed. Quantitative analysis results were presented as mean \pm SD.

2.6. Cell proliferation analysis

The analysis of proliferative activity was carried out by examining the confluence of cell culture during 72 hours of coincubation with FITC-Ce_{0.8}Gd_{0.2}O_{2-x} NPs. The cells were monitored in real time using JULI-stage live cell imaging system (NanoEntek, Korea). Confluence growth curves were plotted using the GraphPad Prism 8 software.

2.7. Spheroid formation

Cellular spheroids were prepared using the "hanging drop" technique. hMSCs were removed from the substrate by using a trypsin-EDTA solution (0.05 %) and then washed three times by centrifugation at 1,000 RPM for 5 minutes. Next, DMEM/F12 growth medium with 10 % fetal bovine serum (FBS) was added to the cells. Subsequently, methylcellulose (1 % in DMEM/F12 medium) was added to the cell suspension to ensure that the total concentration of methyl cellulose did not exceed 0.25 %. The concentration of hMSCs used was 125,000 cells/mL. The cells were seeded to form spheroid onto the lid of a 60-mm plastic Petri dish in drops of 20 μ l volume. To prevent desiccation of the drops, a 10-ml Hanks buffer was positioned at the bottom of the dish. Afterwards, the lid of the dish was carefully positioned on top and incubated for 72 hours in a CO₂ incubator. After 24 hours of incubation, the cells had aggregated in the center of the drop, forming a spherical structure.

2.8. Uptake analysis of FITC-Ce_{0.8}Gd_{0.2}O_{2-x} NPs

The cell uptake analysis of FITC-Ce_{0.8}Gd_{0.2}O_{2-x} NPs in the hMSCs' 2D and 3D systems was carried out using fluorescence microscopy with a Celena S cell imager (Logos, Korea) and a Zoe cell imager (Bio RAD, USA). The cells were seeded at a density of 104 cells per cm² into a 35 mm Petri dish with a central hole. After that, FITC-Ce_{0.8}Gd_{0.2}O_{2-x} NPs and the cells were added and cultivated for 0.5 – 16 hours.

2.9. Statistical analysis

The data were analyzed using the GraphPad Prism 8 software. The statistical significance of the deviations between the test sets and the control was confirmed using the Welch t-test. Images were processed using ImageJ and Adobe Photoshop software.

3. Results and discussion

Previously reported procedure of the $Ce_{0.8}Gd_{0.2}O_{2-x}$ NPs synthesis [52] was modified: FITC was used as an additional fluorescent label. Fig. 1a shows the appearance of nanoparticles in the form of dried powder (left) and in the form of colloidal solution (right). TEM image (Fig. 1b) confirms the formation of the individual nanoparticles with a mean size of 3 nm. According to full-profile analysis of the diffraction pattern, the crystal lattice parameter of the FITC- $Ce_{0.8}Gd_{0.2}O_{2-x}$ NPs is equal to 5.425(1) Å. This value differs significantly from ceria lattice parameter, 5.411 Å (PDF2 #00-034-394) indicating the formation of a nanocrystalline solid solution; the calculated value corresponds well with the previous experimental data on the dependence of the NPs lattice parameter on gadolinium content [53]. The chemical composition of the nanoparticles was additionally confirmed by EDX analysis (Fig. 1c). ζ -potential of the FITC- $Ce_{0.8}Gd_{0.2}O_{2-x}$ NPs in deionized water was 11.3 ± 1.2 mV (Fig. 1d). UV/visible spectrum is presented in Fig. 1e. FITC- $Ce_{0.8}Gd_{0.2}O_{2-x}$ NPs exhibited excellent colloidal stability in aqueous media: the hydrodynamic size of the FITC- $Ce_{0.8}Gd_{0.2}O_{2-x}$ NPs is 6.18 nm with polydispersity index (PDI) = 0.44 (Fig. 1f).

CeO_2 NPs have a high degree of biocompatibility [54–56]. In turn, one of the challenges associated with the biomedical use of gadolinium-containing nanoparticles is the potential for uncontrolled release of gadolinium ions into the cell during the dissolution of the nanoparticles. This can lead to a pronounced cytotoxic effect [57–60]. We have previously demonstrated that Gd-doped CeO_2 NPs did not release toxic gadolinium ions due to the extremely low solubility of ceria matrix [52]. FITC- $Ce_{0.8}Gd_{0.2}O_{2-x}$ NPs also show a high degree of biocompatibility towards hMSCs in a wide range of

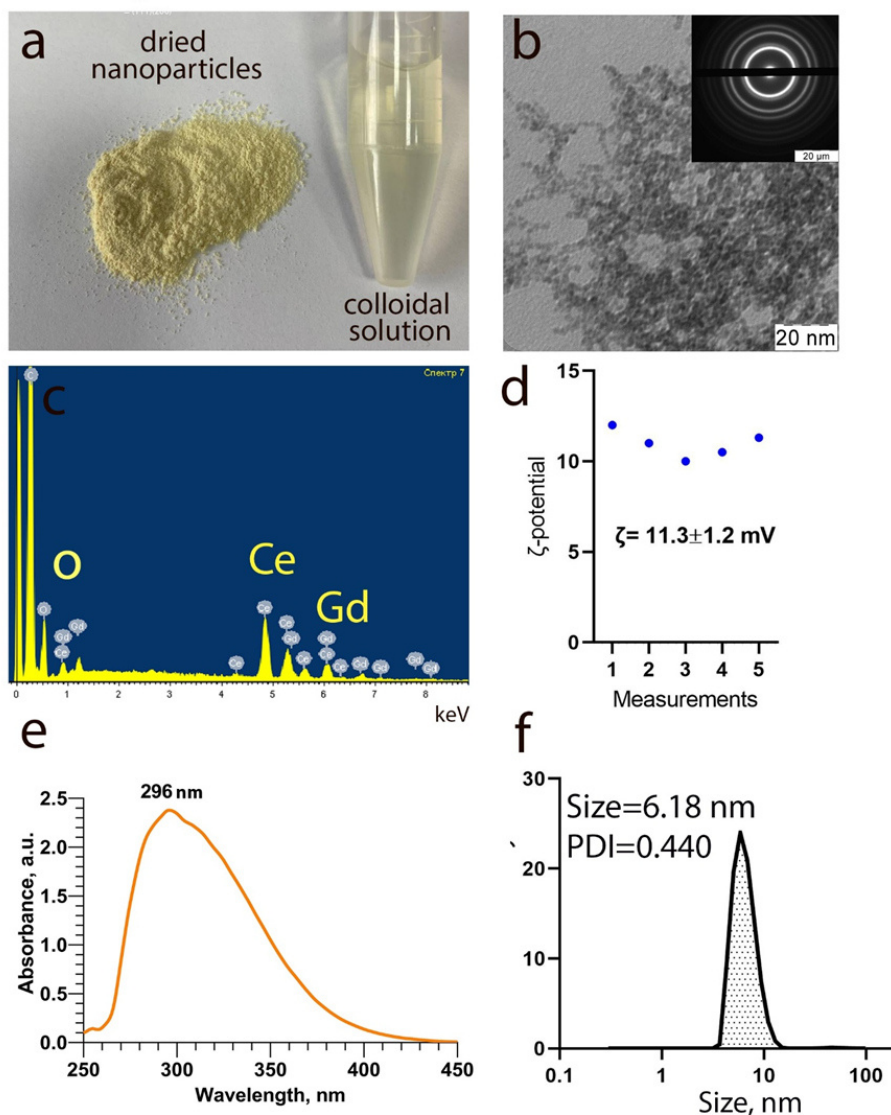


FIG. 1. Visual appearance of dried FITC- $Ce_{0.8}Gd_{0.2}O_{2-x}$ NPs and the corresponding colloidal solution (a), transmission electron microscopy and selected area electron diffraction (in the inset) (b), EDX analysis (c), ζ -potential distribution in MQ water (d), UV-visible absorbance spectrum (e) hydrodynamic size distribution and PDI (f) of the NPs

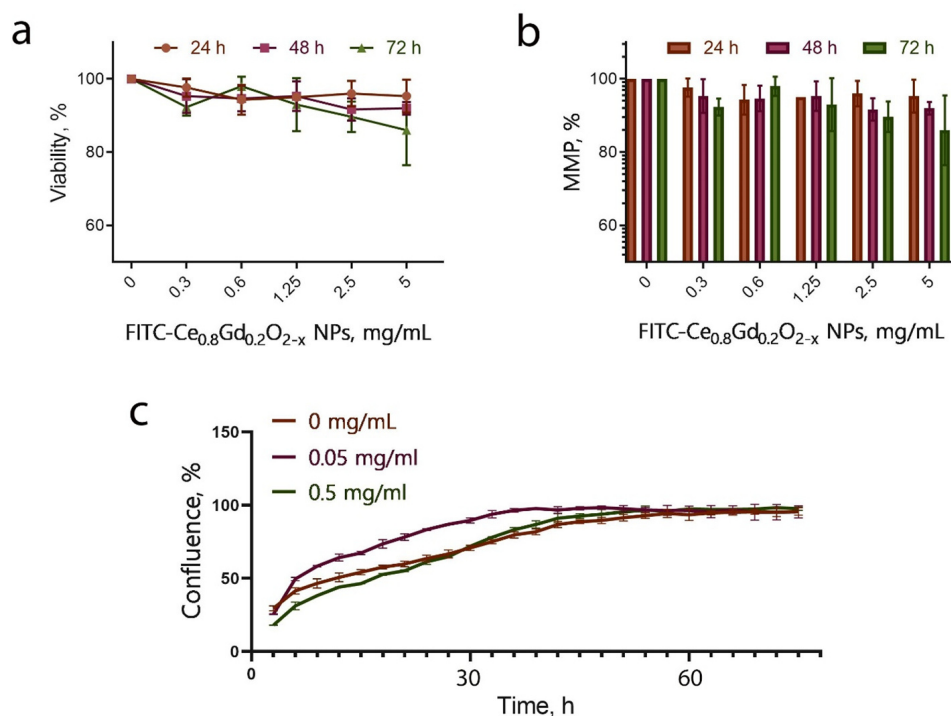


FIG. 2. Cell viability (MTT assay), membrane mitochondrial potential analysis (TMRE staining) and analysis of cell proliferation (JuliStage imaging) of hMSCs after incubation with FITC-Ce_{0.8}Gd_{0.2}O_{2-x} NPs in a wide range of concentrations (0 – 5 mg/mL)

concentrations, up to 5 mg/mL (Fig. 2). Preincubation of the cells with these nanoparticles does not result in a decrease of their metabolic activity (via MTT assay) even at high concentrations (2.5 – 5 mg/mL) after 24, 48, and 72 hours of incubation (Fig. 2a). Analysis of the effect of FITC-Ce_{0.8}Gd_{0.2}O_{2-x} NPs on MMP revealed no decrease in hMSCs' membrane potential in the same concentration range, confirming the high degree of nanoparticles biocompatibility (Fig. 2b). hMSCs proliferation was also assessed after incubation with nanoparticles at concentrations of 0.05 and 0.5 mg/mL, with no statistically significant decrease in cell proliferation rate observed for these concentrations of nanoparticles (Fig. 2c). Therefore, FITC-Ce_{0.8}Gd_{0.2}O_{2-x} NPs do not exhibit any observable cytotoxic effects on hMSCs *in vitro*.

Earlier, CeO₂ NPs were shown to possess brilliant antioxidant properties in various biomedical applications. However, the interaction peculiarities of CeO₂ NPs with cells and their intracellular localization are still poorly understood. It has previously been demonstrated that the efficiency of the cellular uptake and accumulation of CeO₂ NPs depends strongly on their size, charge, shape and concentration [23, 61, 62]. In particular, CeO₂ NPs with a positive or neutral charge are internalized into normal and cancer cells, while CeO₂ NPs with a negative charge are internalized mainly by cancer cell lines [63–65]. This fact was also confirmed in a study by Zhou et al. which showed that negatively charged CeO₂ NPs were predominantly absorbed by lung adenocarcinoma cells (A549) [66]. They attributed this observation to the different efficiencies of protein absorption on the surface of nanoparticles and the formation of different protein coronas [67, 68]. Moreover, when entering cells, CeO₂ NPs are localized in different cellular compartments (for example, in the cytoplasm and in lysosomes), depending on the surface charge of the nanoparticle. The internalization and sub-cellular localization of CeO₂ NPs play a key role in the cytotoxic profile of nanoparticles, with significant toxicity shown when they are located in lysosomes [63]. Here, we have studied the accumulation process of FITC-Ce_{0.8}Gd_{0.2}O_{2-x} NPs in the 2D cell culture of hMSCs (Fig. 3). For this purpose, cell nuclei were stained with a fluorescent dye, Hoechst 33342 (blue fluorescence), to counterstain and to visualize the accumulation of FITC-Ce_{0.8}Gd_{0.2}O_{2-x} NPs (green fluorescence) in the cell cytoplasm. Fig. 3a shows the images of hMSCs 0.5 – 16 hours after treatment with FITC-Ce_{0.8}Gd_{0.2}O_{2-x} NPs. It is clearly seen that the nanoparticles are predominantly localized in the cytoplasm and partially in lysosomes after 16 hours of incubation. The lysosomal localization is confirmed by the presence of bright green zones in the cells cytoplasm. The quantitative assessment of FITC-Ce_{0.8}Gd_{0.2}O_{2-x} NPs internalization is presented in Fig. 3b.

The analysis of the internalization of nanoparticles into cellular spheroids is more interesting, as the more developed intercellular contacts and three-dimensional cell arrangement play a special role in this process [41]. Consequently, a 3D cell arrangement is a more adequate model of biological tissue *in vitro* than a 2D cell monolayer. Multicellular spheroids closely mimic the physiological microenvironment of individual cells [69]. The structure of cellular spheroids with a diameter larger than 300 micrometers is usually represented by several distinct zones, including a necrosis zone,

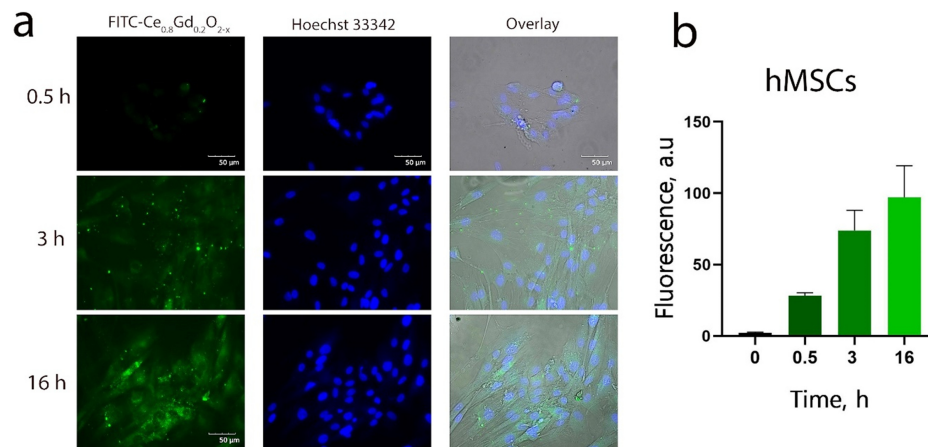


FIG. 3. Cellular uptake analysis of FITC- $Ce_{0.8}Gd_{0.2}O_{2-x}$ NPs in 2D cell cultures of hMSCs. Nanoparticles were introduced at a concentration of $10 \mu\text{g/mL}$ and co-incubated with cells for 3, 6 and 16 hours

hypoxia zone, and proliferation zone [70]. These zones have specific physiological characteristics and vary in pH value, proliferative activity of cells and degree of hypoxia [71].

We have demonstrated that FITC- $Ce_{0.8}Gd_{0.2}O_{2-x}$ NPs are able to internalize cellular spheroids formed from hMSCs effectively (Fig. 4). Within 30 minutes, FITC- $Ce_{0.8}Gd_{0.2}O_{2-x}$ NPs are internalized 20 – 30 micrometers deep into cellular spheroids. This means that the nanoparticles are localized in the proliferation zone. However, after 5 hours, the penetration depth increased up to 120 – 150 micrometers. 12 hours of incubation resulted in the highest uptake of FITC- $Ce_{0.8}Gd_{0.2}O_{2-x}$ NPs into cellular spheroids. Thus, it can be concluded that FITC- $Ce_{0.8}Gd_{0.2}O_{2-x}$ nanoparticles are able to accumulate effectively in cellular spheroids, and remain there for more than 48 hours of co-cultivation.

4. Conclusion

Multi-functional FITC- $Ce_{0.8}Gd_{0.2}O_{2-x}$ NPs were synthesized and characterized in detail by relevant physical techniques. The nanoparticles are not toxic to hMSCs at concentrations up to 5 mg/mL, maintaining a high level of cell viability, metabolic and proliferative activity. In 30 minutes, FITC- $Ce_{0.8}Gd_{0.2}O_{2-x}$ NPs effectively internalize into cellular monolayer of hMSCs and their maximum accumulation occurs after 16 hours. The FITC- $Ce_{0.8}Gd_{0.2}O_{2-x}$ NPs are also effectively internalized into 3D cellular spheroids after 12 hours without causing toxicity or disrupting their structure. The results obtained indicate that the use of cerium-based nanoparticles is a promising approach for the safe and efficient visualization of hMSCs that could be used in tissue engineering and regenerative medicine, such as in 3D bioprinting.

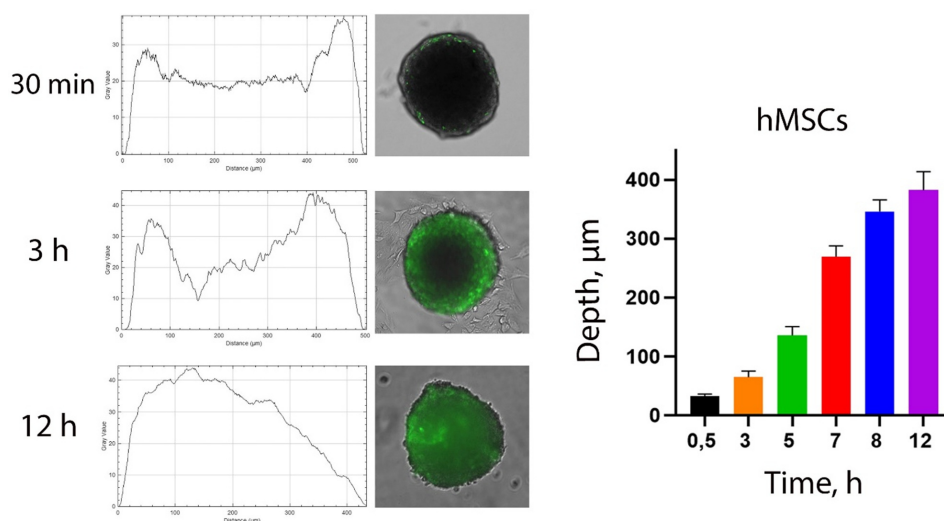


FIG. 4. Accumulation of FITC- $Ce_{0.8}Gd_{0.2}O_{2-x}$ in 3D cellular spheroids formed from hMSCs. Nanoparticles were introduced at a concentration of $10 \mu\text{g/mL}$ and co-incubated with cell spheroids for 12 hours

References

- [1] Feng N., Liu Y., Dai X., Wang Y., Guo Q., Li Q. Advanced Applications of Cerium Oxide Based Nanozymes in Cancer. *RSC Adv.*, 2022, **12**, P. 121486–1493.
- [2] Saifi M.A., Seal S., Godugu C. Nanoceria, the Versatile Nanoparticles: Promising Biomedical Applications. *J. Controlled Release*, 2021, **338**, P. 164–189.
- [3] Tang J.L.Y., Moonshi S.S., Ta H.T. Nanoceria: An Innovative Strategy for Cancer Treatment. *Cell. Mol. Life Sci.*, 2023, **80**, 46.
- [4] Xue Y., Yang F., Wu L., Xia D., Liu Y. CeO₂ Nanoparticles to Promote Wound Healing: A Systematic Review. *Adv. Healthc. Mater.*, 2024, **13** (6), 2302858.
- [5] Shcherbakov A.B., Ivanov V.K., Zholobak N.M., Ivanova O.S., Krysanov E.Yu., Baranchikov A.E., Spivak N.Ya., Tretyakov Yu.D. Nanocrystalline Ceria Based Materials—Perspectives for Biomedical Application. *Biophysics*, 2011, **56**, P. 987–1004.
- [6] Hirst S.M., Karakoti A.S., Tyler R.D., Sriranganathan N., Seal S., Reilly C.M. Anti-Inflammatory Properties of Cerium Oxide Nanoparticles. *Small Weinh. Bergstr. Ger.*, 2009, **5**, P. 2848–2856.
- [7] Heckert E., Karakoti A., Seal S., Self W.T. The Role of Cerium Redox State in the SOD Mimetic Activity of Nanoceria. *Biomaterials*, 2008, **29**, P. 2705–2709.
- [8] Baldim V., Bedioui F., Mignet N., Margail I., Berret J.-F. The Enzyme-like Catalytic Activity of Cerium Oxide Nanoparticles and Its Dependency on Ce³⁺ Surface Area Concentration. *Nanoscale*, 2018, **10**, P. 6971–6980.
- [9] Pirmohamed T., Dowding J.M., Singh S., Wasserman B., Heckert E., Karakoti A.S., King J.E.S., Seal S., Self W.T. Nanoceria Exhibit Redox State-Dependent Catalase Mimetic Activity. *Chem. Commun. Camb. Engl.*, 2010, **46**, P. 2736–2738.
- [10] Dhall A., Burns A., Dowding J., Das S., Seal S., Self W. Characterizing the Phosphatase Mimetic Activity of Cerium Oxide Nanoparticles and Distinguishing Its Active Site from That for Catalase Mimetic Activity Using Anionic Inhibitors. *Environ. Sci. Nano*, 2017, **4**, P. 1742–1749.
- [11] Hu H., Kang X., Shan Z., Yang X., Bing W., Wu L., Ge H., Ji H. A DNase-Mimetic Artificial Enzyme for the Eradication of Drug-Resistant Bacterial Biofilm Infections. *Nanoscale*, 2022, **14**, P. 2676–2685.
- [12] Sozarukova M.M., Proskurnina E.V., Popov A.L., Kalinkin A.L., Ivanov V.K. New Facets of Nanozyme Activity of Ceria: Lipo- and Phospholipoperoxidase-like Behaviour of CeO₂ Nanoparticles. *RSC Adv.*, 2021, **11**, P. 35351–35360.
- [13] Wang G., Zhang J., He X., Zhang Z., Zhao Y. Ceria Nanoparticles as Enzyme Mimetics. *Chin. J. Chem.*, 2017, **35**, P. 791–800.
- [14] Wang Z., Shen X., Gao X., Zhao Y. Simultaneous Enzyme Mimicking and Chemical Reduction Mechanisms for Nanoceria as a Bio-Antioxidant: A Catalytic Model Bridging Computations and Experiments for Nanozymes. *Nanoscale*, 2019, **11**, P. 13289–13299.
- [15] Sozarukova M.M., Chilikina P.A., Novikov D.O., Proskurnina E.V., Baranchikov A.E., Ivanov V.K. Cerium Dioxide Nanoparticles Modulate the Oxidative Metabolism of Neutrophils upon Blood Irradiation with a Pulsed Broadband UV Source. *Nanosyst. Phys. Chem. Math.*, 2023, **14**, P. 644–651.
- [16] Ivanov V.K., Polezhaeva O.S., Tretyakov Yu.D. Nanocrystalline Ceria: Synthesis, Structure-Sensitive Properties, and Promising Applications. *Russ. J. Gen. Chem.*, 2010, **80**, P. 604–617.
- [17] Naganuma T., Traversa E. Stability of the Ce³⁺ Valence State in Cerium Oxide Nanoparticle Layers. *Nanoscale*, 2012, **4**, P. 4950–4953.
- [18] Naganuma T., Traversa E. The Effect of Cerium Valence States at Cerium Oxide Nanoparticle Surfaces on Cell Proliferation. *Biomaterials*, 2014, **35**, P. 4441–4453.
- [19] Popov A.L., Shcherbakov A.B., Zholobak N.M., Baranchikov A.E., Ivanov V.K. Cerium Dioxide Nanoparticles as Third-Generation Enzymes (Nanozymes). *Nanosyst. Phys. Chem. Math.*, 2017, P. 760–781.
- [20] Gao R., Mitra R.N., Zheng M., Wang K., Dahringer J.C., Han Z. Developing Nanoceria-Based pH-Dependent Cancer-Directed Drug Delivery System for Retinoblastoma. *Adv. Funct. Mater.*, 2018, **28**, 1806248.
- [21] Xu C., Lin Y., Wang J., Wu L., Wei W., Ren J., Qu X. Nanoceria-Triggered Synergetic Drug Release Based on CeO₂-Capped Mesoporous Silica Host–Guest Interactions and Switchable Enzymatic Activity and Cellular Effects of CeO₂. *Adv. Healthc. Mater.*, 2013, **2**, P. 1591–1599.
- [22] Zholobak N.M., Ivanov V.K., Shcherbakov A.B. Chapter 12 -0 Interaction of Nanoceria with Microorganisms. In *Nanobiomaterials in Antimicrobial Therapy*, Grumezescu A.M., Ed., William Andrew Publishing, 2016, P. 419–450.
- [23] Singh S., Ly A., Das S., Sakthivel T.S., Barkam S., Seal S. Cerium Oxide Nanoparticles at the Nano-Bio Interface: Size-Dependent Cellular Uptake. *Artif. Cells Nanomedicine Biotechnol.*, 2018, **46**, P. 956–963.
- [24] Lim S., Kim W., Song S., Shim M.K., Yoon H.Y., Kim B.-S., Kwon I.C., Kim K. Intracellular Uptake Mechanism of Bioorthogonally Conjugated Nanoparticles on Metabolically Engineered Mesenchymal Stem Cells. *Bioconjug. Chem.*, 2021, **32**, P. 199–214.
- [25] Popov A.L., Popova N.R., Selezneva I.I., Akkizov A.Y., Ivanov V.K. Cerium Oxide Nanoparticles Stimulate Proliferation of Primary Mouse Embryonic Fibroblasts in Vitro. *Mater. Sci. Eng. C*, 2016, **68**, P. 406–413.
- [26] Mahapatra C., Singh R.K., Lee J.-H., Jung J., Hyun J.K., Kim H.-W. Nano-Shape Varied Cerium Oxide Nanomaterials Rescue Human Dental Stem Cells from Oxidative Insult through Intracellular or Extracellular Actions. *Acta Biomater.*, 2017, **50**, P. 142–153.
- [27] Popov A.L., Savintseva I.V., Kozlova T.O., Ivanova O.S., Zhukov I.V., Baranchikov A.E., Yurkovskaya A.V., Savelov A.A., Ermakov A.M., Popova N.R., et al. Heavily Gd-Doped Non-Toxic Cerium Oxide Nanoparticles for MRI Labelling of Stem Cells. *Molecules*, 2023, **28**, 1165.
- [28] Popov A.L., Ermakov A.M., Savintseva I.V., Selezneva I.I., Poltavtseva R.A., Zaraisky E.I., Poltavtsev A.M., Stepanov A.A., Ivanov V.K., Sukhikh G.T. Citrate-stabilized nanoparticles of CeO₂ stimulate proliferation of human mesenchymal stem cells IN VITRO. *Nanosci. Technol. Int. J.*, 2016, **7**.
- [29] Nilawar S., Chatterjee K. Surface Decoration of Redox-Modulating Nanoceria on 3D-Printed Tissue Scaffolds Promotes Stem Cell Osteogenesis and Attenuates Bacterial Colonization. *Biomacromolecules*, 2022, **23**, P. 226–239.
- [30] Rather H.A., Thakore R., Singh R., Jhala D., Singh S., Vasita R. Antioxidative Study of Cerium Oxide Nanoparticle Functionalised PCL-Gelatin Electrospun Fibers for Wound Healing Application. *Bioact. Mater.*, 2018, **3**, P. 201–211.
- [31] Ren X., Zhuang H., Zhang Y., Zhou P. Cerium Oxide Nanoparticles-Carrying Human Umbilical Cord Mesenchymal Stem Cells Counteract Oxidative Damage and Facilitate Tendon Regeneration. *J. Nanobiotechnology*, 2023, **21**, 359.
- [32] D’Atri D., Zerrillo L., Garcia J., Oieni J., Lupu-Haber Y., Schomann T., Chan A., Cruz L.J., Creemers L.B., Machluf M. Nanoghosts: Mesenchymal Stem Cells Derived Nanoparticles as a Unique Approach for Cartilage Regeneration. *J. Controlled Release*, 2021, **337**, P. 472–481.
- [33] Li X., Wei Z., Zhang W., Lv H., Li J., Wu L., Zhang H., Yang B., Zhu M., Jiang J. Anti-Inflammatory Effects of Magnetically Targeted Mesenchymal Stem Cells on Laser-Induced Skin Injuries in Rats. *Int. J. Nanomedicine*, 2020, **15**, P. 5645–5659.
- [34] Gao Z., Zhang L., Hu J., Sun Y. Mesenchymal Stem Cells: A Potential Targeted-Delivery Vehicle for Anti-Cancer Drug, Loaded Nanoparticles. *Nanomedicine Nanotechnol. Biol. Med.*, 2013, **9**, P. 174–184.
- [35] Roger M., Clavreul A., Venier-Julienne M.-C., Passirani C., Sindji L., Schiller P., Montero-Menei C., Menei P. Mesenchymal Stem Cells as Cellular Vehicles for Delivery of Nanoparticles to Brain Tumors. *Biomaterials*, 2010, **31**, P. 8393–8401.

- [36] Amiri F., Jahanian-Najafabadi A., Roudkenar M.H. In Vitro Augmentation of Mesenchymal Stem Cells Viability in Stressful Microenvironments. *Cell Stress Chaperones*, 2015, **20**, P. 237–251.
- [37] Białkowska K., Komorowski P., Bryszewska M., Miłowska K. Spheroids as a Type of Three-Dimensional Cell Cultures—Examples of Methods of Preparation and the Most Important Application. *Int. J. Mol. Sci.*, 2020, **21**, 6225.
- [38] Zannoni M., Piccinini F., Arienti C., Zamagni A., Santi S., Polico R., Bevilacqua A., Tesei A. 3D Tumor Spheroid Models for in Vitro Therapeutic Screening: A Systematic Approach to Enhance the Biological Relevance of Data Obtained. *Sci. Rep.*, 2016, **6**, 19103.
- [39] Kim W., Gwon Y., Park S., Kim H., Kim J. Therapeutic Strategies of Three-Dimensional Stem Cell Spheroids and Organoids for Tissue Repair and Regeneration. *Bioact. Mater.*, 2023, **19**, P. 50–74.
- [40] Wang W., Itaka K., Ohba S., Nishiyama N., Chung U., Yamasaki Y., Kataoka K. 3D Spheroid Culture System on Micropatterned Substrates for Improved Differentiation Efficiency of Multipotent Mesenchymal Stem Cells. *Biomaterials*, 2009, **30**, P. 2705–2715.
- [41] Tchoryk A., Taresco V., Argent R.H., Ashford M., Gellert P.R., Stolnik S., Grabowska A., Garnett M.C. Penetration and Uptake of Nanoparticles in 3D Tumor Spheroids. *Bioconjug. Chem.*, 2019, **30**, P. 1371–1384.
- [42] Roy S.M., Garg V., Barman S., Ghosh C., Maity A.R., Ghosh S.K. Kinetics of Nanomedicine in Tumor Spheroid as an In Vitro Model System for Efficient Tumor-Targeted Drug Delivery With Insights From Mathematical Models. *Front. Bioeng. Biotechnol.*, 2021, **9**.
- [43] Zhuang J., Zhang J., Wu M., Zhang Y. A Dynamic 3D Tumor Spheroid Chip Enables More Accurate Nanomedicine Uptake Evaluation. *Adv. Sci.*, 2019, **6**, 1901462.
- [44] Sokolova V., Ebel J.-F., Kollenda S., Klein K., Kruse B., Veltkamp C., Lange C.M., Westendorf A.M., Epple M. Uptake of Functional Ultrasmall Gold Nanoparticles in 3D Gut Cell Models. *Small*, 2022, **18**, 2201167.
- [45] Bayarara O., Dashnyam K., Singh R.K., Mandakbayer N., Lee J.H., Park J.-T., Lee J.-H., Kim H.-W. Nanoceria-GO-Intercalated Multicellular Spheroids Revascularize and Salvage Critical Ischemic Limbs through Anti-Apoptotic and pro-Angiogenic Functions. *Biomaterials*, 2023, **292**, 121914.
- [46] Liu D., Lu G., Shi B., Ni H., Wang J., Qiu Y., Yang L., Zhu Z., Yi X., Du X., et al. ROS-Scavenging Hydrogels Synergize with Neural Stem Cells to Enhance Spinal Cord Injury Repair via Regulating Microenvironment and Facilitating Nerve Regeneration. *Adv. Healthc. Mater.*, 2023, **12**, 2300123.
- [47] Liu D.-D., Zhang J.-C., Zhang Q., Wang S.-X., Yang M.-S. TGF- β /BMP Signaling Pathway Is Involved in Cerium-Promoted Osteogenic Differentiation of Mesenchymal Stem Cells. *J. Cell. Biochem.*, 2013, **114**, P. 1105–1114.
- [48] Yin P., Liang W., Han B., Yang Y., Sun D., Qu X., Hai Y., Luo D. Hydrogel and Nanomedicine-Based Multimodal Therapeutic Strategies for Spinal Cord Injury. *Small Methods*, 2024, **8**, 2301173.
- [49] McDonagh P.R., Sundaresan G., Yang L., Sun M., Mikkelsen R., Zweit J. Biodistribution and PET Imaging of 89-Zirconium Labeled Cerium Oxide Nanoparticles Synthesized with Several Surface Coatings. *Nanomedicine Nanotechnol. Biol. Med.*, 2018, **14**, P. 1429–1440.
- [50] Zhang M., Zhai X., Ma T., Huang Y., Yan C., Du Y. Multifunctional Cerium Doped Carbon Dots Nanoplatform and Its Applications for Wound Healing. *Chem. Eng. J.*, 2021, **423**, 130301.
- [51] Shcherbakov A.B., Zholobak N.M., Ivanov V.K., Ivanova O.S., Marchevsky A.V., Baranchikov A.E., Spivak N.Ya., Tretyakov Yu.D. Synthesis and Antioxidant Activity of Biocompatible Maltodextrin-Stabilized Aqueous Sols of Nanocrystalline Ceria. *Russ. J. Inorg. Chem.*, 2012, **57**, P. 1411–1418.
- [52] Popov A.L., Abakumov M.A., Savintseva I.V., Ermakov A.M., Popova N.R., Ivanova O.S., Kolmanovich D.D., Baranchikov A.E., Ivanov V.K. Biocompatible Dextran-Coated Gadolinium-Doped Cerium Oxide Nanoparticles as MRI Contrast Agents with High T1 Relaxivity and Selective Cytotoxicity to Cancer Cells. *J. Mater. Chem. B*, 2021, **9**, P. 6586–6599.
- [53] Dolgoplova E.A., Ivanova O.S., Ivanov V.K., Sharikov F.Yu., Baranchikov A.E., Shcherbakov A.B., Trietyakov Yu.D. Microwave-Hydrothermal Synthesis of Gadolinium-Doped Nanocrystalline Ceria in the Presence of Hexamethylenetetramine. *Russ. J. Inorg. Chem.*, 2012, **57**, P. 1303–1307.
- [54] Aalapati S., Ganapathy S., Manapuram S., Anumolu G., Prakya B.M. Toxicity and Bio-Accumulation of Inhaled Cerium Oxide Nanoparticles in CD1 Mice. *Nanotoxicology*, 2014, **8**, P. 786–798.
- [55] Hirst S.M., Karakoti A., Singh S., Self W., Tyler R., Seal S., Reilly C.M. Bio-Distribution and in Vivo Antioxidant Effects of Cerium Oxide Nanoparticles in Mice. *Environ. Toxicol.*, 2013, **28**, P. 107–118.
- [56] Nosrati H., Heydari M., Khodaei M. Cerium Oxide Nanoparticles: Synthesis Methods and Applications in Wound Healing. *Mater. Today Bio*, 2023, **23**, 100823.
- [57] Akhtar M.J., Ahamed M., Alhadlaq H., Alrokayan S. Toxicity Mechanism of Gadolinium Oxide Nanoparticles and Gadolinium Ions in Human Breast Cancer Cells. *Curr. Drug Metab.*, 2019, **20**, P. 907–917.
- [58] Rogosnitzky M., Branch S. Gadolinium-Based Contrast Agent Toxicity: A Review of Known and Proposed Mechanisms. *BioMetals*, 2016, **29**, P. 365–376.
- [59] Takanezawa Y., Nakamura R., Kusaka T., Ohshiro Y., Uruguchi S., Kiyono M. Significant Contribution of Autophagy in Mitigating Cytotoxicity of Gadolinium Ions. *Biochem. Biophys. Res. Commun.*, 2020, **526**, P. 206–212.
- [60] Friebe B., Godenschweger F., Fatahi M., Speck O., Roggenbuck D., Reinhold D., Reddig A. The Potential Toxic Impact of Different Gadolinium-Based Contrast Agents Combined with 7-T MRI on Isolated Human Lymphocytes. *Eur. Radiol. Exp.*, 2018, **2**, 40.
- [61] Lord M.S., Jung M., Teoh W.Y., Gunawan C., Vassie J.A., Amal R., Whitelock J.M. Cellular Uptake and Reactive Oxygen Species Modulation of Cerium Oxide Nanoparticles in Human Monocyte Cell Line U937. *Biomaterials*, 2012, **33**, P. 7915–7924.
- [62] Ting S.R.S., Whitelock J.M., Tomic R., Gunawan C., Teoh W.Y., Amal R., Lord M.S. Cellular Uptake and Activity of Heparin Functionalised Cerium Oxide Nanoparticles in Monocytes. *Biomaterials*, 2013, **34**, P. 4377–4386.
- [63] Asati A., Santra S., Kaitanis C., Perez J.M. Surface-Charge-Dependent Cell Localization and Cytotoxicity of Cerium Oxide Nanoparticles. *ACS Nano*, 2010, **4**, P. 5321–5331.
- [64] Zamyatina E.A., Kottsov S.Yu., Anikina V.A., Popov A.L., Shevelyova M.P., Popova N.R. Cerium Oxide@silica Core-Shell Nanocomposite as Multimodal Platforms for Drug Release and Synergistic Anticancer Effects. *Nanosyst. Phys. Chem. Math.*, 2023, **14**, P. 560–570.
- [65] Johnson K.K., Koshy P., Kopecky C., Devadason M., Biazik J., Zheng X., Jiang Y., Wang X., Liu Y., Holst J., et al. ROS-Mediated Anticancer Effects of EGFR-Targeted Nanoceria. *J. Biomed. Mater. Res. A*, 2024, **112**, P. 754–769.
- [66] Zhou X., Wang B., Chen Y., Mao Z., Gao C. Uptake of Cerium Oxide Nanoparticles and Their Influences on Functions of A549 Cells. *J. Nanosci. Nanotechnol.*, 2013, **13**, P. 204–215.
- [67] Mazzolini J., Weber R.J.M., Chen H.-S., Khan A., Guggenheim E., Shaw R.K., Chipman J.K., Viant M.R., Rappoport J.Z. Protein Corona Modulates Uptake and Toxicity of Nanoceria via Clathrin-Mediated Endocytosis. *Biol. Bull.*, 2016, **231**, P. 40–60.
- [68] Butterfield A.D., Wang B., Wu P., Hardas S.S., Unrine J.M., Grulke E.A., Cai J., Klein J.B., Pierce W.M., Yokel R.A., et al. Plasma and Serum Proteins Bound to Nanoceria: Insights into Pathways by Which Nanoceria May Exert Its Beneficial and Deleterious Effects In Vivo. *J. Nanomedicine Nanotechnol.*, 2020, **11**, 546.

- [69] Ryu N.-E., Lee S.-H., Park H. Spheroid Culture System Methods and Applications for Mesenchymal Stem Cells. *Cells*, 2019, **8**, 1620.
- [70] Browning A.P., Sharp J.A., Murphy R.J., Gunasingh G., Lawson B., Burrage K., Haass N.K., Simpson M. Quantitative Analysis of Tumour Spheroid Structure. *eLife*, 2021, **10**, e73020.
- [71] Pinto B., Henriques A.C., Silva P.M.A., Bousbaa H. Three-Dimensional Spheroids as In Vitro Preclinical Models for Cancer Research. *Pharmaceutics*, 2020, **12**, 1186.

Submitted 23 January 2024; revised 23 March 2024; accepted 26 April 2024

Information about the authors:

Danil D. Kolmanovich – Institute of Theoretical and Experimental Biophysics of the Russian Academy of Sciences, Pushchino, 142290, Russia; ORCID 0000-0003-3391-7889; kdd100996@mail.ru

Nikita N. Chukavin – Institute of Theoretical and Experimental Biophysics of the Russian Academy of Sciences, Pushchino, 142290, Russia; Scientific and Educational Center, State University of Education, Moscow 105005, Russia; ORCID 0000-0001-8431-4485; chukavinnik@gmail.com

Nikita A. Pivovarov – Institute of Theoretical and Experimental Biophysics of the Russian Academy of Sciences, Pushchino, 142290, Russia; ORCID 0009-0005-1997-0845; nikitapivovarov.workmail@gmail.com

Sergey A. Khaustov – Scientific and Educational Center, State University of Education, Moscow 105005, Russia; ORCID 0000-0001-9286-3644; sergeykhaustov@gmail.com

Vladimir K. Ivanov – Kurnakov Institute of General and Inorganic Chemistry of the Russian Academy of Sciences, Moscow, 119991, Russia; ORCID 0000-0003-2343-2140; van@igic.ras.ru

Anton L. Popov – Institute of Theoretical and Experimental Biophysics of the Russian Academy of Sciences, Pushchino, 142290, Russia; Scientific and Educational Center, State University of Education, Moscow 105005, Russia; ORCID 0000-0003-2643-4846; antonpopovleonid@gmail.com

Conflict of interest: the authors declare no conflict of interest.

The role of the reaction medium pH in the formation of nanocrystalline phases in the $\text{Bi}_2\text{O}_3\text{--P}_2\text{O}_5\text{--H}_2\text{O}$ system

Dmitry P. Elovikov^a, Alena A. Osminina^b

Grebenshchikov Institute of Silicate Chemistry, Russian Academy of Sciences, St. Petersburg, Russia

^asyncdima@mail.ru, ^balenaosminina3001@gmail.com

Corresponding author: Dmitry P. Elovikov, syncdima@mail.ru

ABSTRACT The work is devoted to studying the influence of pH values in an aqueous-salt medium on the formation of compounds in the $\text{Bi}_2\text{O}_3\text{--P}_2\text{O}_5\text{--H}_2\text{O}(\text{OH}^-, \text{H}^+)$ oxide system. It has been shown that in an acidic environment ($\text{pH} = 2$) at a temperature of 298 K, hexagonal BiPO_4 forms, while at pH values of 8 and 12, X-ray amorphous substances are produced. After hydrothermal treatment at 473 K in an aqueous-salt environment, a monoclinic modification of bismuth phosphate forms from hexagonal bismuth phosphate in an acidic environment, and nanometer-sized particles of crystalline compounds $\text{Bi}_3\text{O}(\text{OH})(\text{PO}_4)_2$ (with a crystallite size of about 62 nm) and Bi_2O_3 (with a crystallite size of about 70 nm) form in weakly alkaline and alkaline media. Using the method of thermodynamic calculation, the dependences of the equilibrium molar solubility of these crystalline compounds on the pH value of the aqueous-salt suspension were obtained. Thermodynamic calculations showed that the BiPO_4 compound is stable in the pH range from 0 to 5.8 at temperatures of 298 and 473 K. The pH range from 5.8 to 9.8 is characterized by the formation of the $\text{Bi}_3\text{O}(\text{OH})(\text{PO}_4)_2$ compound at 298 K, and a further increase in the pH value leads to the precipitation of Bi_2O_3 , BiOOH or $\text{Bi}(\text{OH})_3$, which are similar in solubility, at 298 and 473 K. The data obtained from thermodynamic calculations are consistent with experimental data on the stability boundaries of BiPO_4 , $\text{Bi}_3\text{O}(\text{OH})(\text{PO}_4)_2$, and Bi_2O_3 compounds.

KEYWORDS nanocrystals, BiPO_4 , $\text{Bi}_3\text{O}(\text{OH})(\text{PO}_4)_2$, influence of pH value, solubility, thermodynamic calculation, hydrothermal synthesis

ACKNOWLEDGEMENTS The work was supported by state assignment No. 1023032900322-9-1.4.3. Elemental analyses of samples were performed employing the equipment of the Engineering Center of the St. Petersburg State Institute of Technology. The X-ray structural studies of the samples were carried out using the DRON-8 diffractometer at the Ioffe Institute.

FOR CITATION Elovikov D.P., Osminina A.A. The role of the reaction medium pH in the formation of nanocrystalline phases in the $\text{Bi}_2\text{O}_3\text{--P}_2\text{O}_5\text{--H}_2\text{O}$ system. *Nanosystems: Phys. Chem. Math.*, 2024, **15** (3), 361–368.

1. Introduction

Low-temperature chemistry encompasses a wide variety of methods and approaches for synthesizing compounds and producing functional materials based on them [1–6]. Among the widely used and promising methods are precipitation and co-precipitation techniques [7–9], sol-gel methods [10–15], and hydrothermal treatment in various modifications [16–24]. Water and aqueous solutions often serve as the medium for heat and mass transfer during synthesis using these approaches. It is known that the composition of such a medium can significantly influence on the processes of compound formation [25–30], their structure and polymorphic transformations [31–35], the morphology of the resulting particles [36–39], crystallite sizes [40–43], and, consequently, the physicochemical and functional properties of the obtained compounds and materials. In this regard, it is pertinent to study the influence of various factors on the processes of compound formation, such as the composition of the aqueous solution, the concentration of soluble precursors, mineralizing additives, the sequence and conditions of mixing solutions, the presence and state of amorphous precursors [44–49], and the use of specific additional conditions: such as limiting mass transfer [6, 50], various physical impacts [51, 52], and the organization of reagent solution flows [53–55].

One of the important synthesis parameters reflected in this work is the pH value of solutions and suspensions, as well as its influence on the processes of oxide compound formation. For many low-temperature processes involving bismuth cation and phosphate anions, it is characteristic that a stable bismuth phosphate (with a hexagonal structure) precipitates at certain stages [56]. In some cases, associated with the formation of complex oxide compounds based on bismuth and phosphorus, this leads to kinetic hindrances (undesirable limiting factors of mass transfer) and the stable existence of BiPO_4 over a wide pH range [57]. Several studies have focused on the polymorphic transformations of simple compounds in the $\text{Bi}_2\text{O}_3\text{--P}_2\text{O}_5$ system [56, 58, 59] and the targeted synthesis of individual compounds: BiPO_4 or Bi_2O_3 . There are mentions of a new and promising compound for use in photocatalysis, $\text{Bi}_3\text{O}(\text{OH})(\text{PO}_4)_2$, obtained in this system [60, 61].

However, little attention has been paid to the thermodynamic analysis of the formation of complex compounds in the $\text{Bi}_2\text{O}_3\text{-P}_2\text{O}_5\text{-H}_2\text{O}(\text{OH}^-, \text{H}^+)$ system.

Due to the reasons listed above, this work is devoted to studying the influence of the pH value of the solution in the reaction medium on the formation of compounds in the $\text{Bi}_2\text{O}_3\text{-P}_2\text{O}_5\text{-H}_2\text{O}$ system, as well as the stability boundaries of these compounds, particularly, by using the thermodynamic calculations.

2. Experimental

For the synthesis, two solutions were initially prepared. The first solution was an acidic aqueous solution of bismuth nitrate, obtained by dissolving $\text{Bi}(\text{NO}_3)_3 \cdot 5\text{H}_2\text{O}$ (analytical grade) in a 6 M aqueous solution of HNO_3 (analytical grade). The second solution was prepared by dissolving a specified amount of NaOH (analytical grade) in 50 ml of distilled water, followed by the addition of a measured amount of $(\text{NH}_4)_2\text{HPO}_4$ (analytical grade). The mixing of the two solutions was carried out by the dropwise addition of the acidic bismuth nitrate solution into the alkaline ammonium phosphate solution under continuous stirring. The resulting suspensions with pH values of 2, 8, and 12 were stirred for 10 minutes at $T = 298$ K.

The hydrothermal treatment of the suspensions obtained at room temperature was carried out in a stainless steel autoclave with a Teflon liner (filling coefficient 0.8) at $T = 473$ K for 20 hours.

The samples, obtained both by precipitation and after hydrothermal treatment, were decanted by centrifugation (3500 rpm) for 30 minutes, washed with distilled water until $\text{pH} = 7$, dried at $T = 353$ K for 24 hours, and ground in an agate mortar.

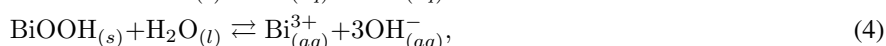
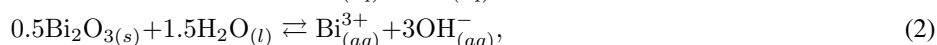
The samples were designated in the work according to the pH of the aqueous-saline suspension during precipitation: those obtained by the precipitation method were labeled as “pH = 2”, etc.; those obtained after hydrothermal treatment were labeled as “pH = 2(HTS)”, etc.

X-ray diffraction studies of the obtained samples were performed using the DRON-8 (8H) X-ray diffractometer (Russia) with CuK_α radiation in the 2θ range of $10 - 80^\circ$, with a step size of 0.0142° and a scanning speed of $3^\circ/\text{min}$. Qualitative analysis of the samples was performed using the ICSD PDF-2 database. The distribution of crystallites by size and the average weighted values of crystallite sizes were determined for the reflections with the maximum intensity.

For X-ray spectral microanalysis of the samples' composition, a scanning electron microscope Tescan Vega 3 SBH (Tescan, Czech Republic) with an Oxford Instruments INCA x-act attachment (United Kingdom) was used. Measurements were conducted in the range up to 20 keV.

3. Calculation

In aqueous-salt solutions saturated with relatively sparingly soluble solids $h\text{-BiPO}_4$, $c\text{-Bi}_2\text{O}_3$, $\text{Bi}(\text{OH})_3$, BiOOH , and $\text{Bi}_3\text{O}(\text{OH})(\text{PO}_4)_2$, the following heterogeneous equilibria are established:



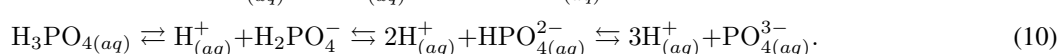
The thermodynamic constants of the specified heterogeneous equilibria are determined by the expressions:

$$K_S^0(1) = [a_{\text{Bi}^{3+}} \cdot X_{\text{Bi}^{3+}} \cdot a_{\text{PO}_4^{3-}} \cdot X_{\text{PO}_4^{3-}}]_T = \text{const}(T),$$

$$K_S^0(2-4) = [a_{\text{Bi}^{3+}} \cdot X_{\text{Bi}^{3+}} \cdot a_{\text{OH}^-}^3]_T = \text{const}(T),$$

$$K_S^0(5) = [a_{\text{Bi}^{3+}}^3 \cdot X_{\text{Bi}^{3+}}^3 \cdot a_{\text{OH}^-}^3 \cdot a_{\text{PO}_4^{3-}}^2 \cdot X_{\text{PO}_4^{3-}}^2]_T = \text{const}(T),$$

where K_S^0 is the thermodynamic solubility constant, $X_{\text{Bi}^{3+}}$ and $X_{\text{PO}_4^{3-}}$ – are the mole fractions of free cations Bi^{3+} and anions PO_4^{3-} , respectively. In an aqueous solution, depending on the pH value, the following homogeneous equilibria of water-soluble weak acids and bases are established:



Equilibria (6) – (9) are described by the corresponding stability constants of mononuclear hydroxo complexes of Bi(III) in an aqueous medium: $\beta_1, \beta_2, \beta_3, \beta_4 = f(T)$.

Equilibria (10) are described by the corresponding constants of the three-step dissociation of phosphoric acid: $K_1, K_2, K_3 = f(T)$.

The necessary values of the Gibbs free energy of formation for compounds were taken from the HSC 6.0 database. The Gibbs free energy of formation of the compound $\text{Bi}_3\text{O}(\text{OH})(\text{PO}_4)_2$ was calculated using the increment method based on data from reference [62]. Using these values, changes in the Gibbs free energy of processes were calculated, and subsequently, equilibrium constants, stability constants of mononuclear hydroxo complexes, and dissociation constants were calculated. By means of mathematical transformations described earlier in reference [63], the equilibrium molar solubility (S , mol/L) of sparingly soluble BiPO_4 , Bi_2O_3 , $\text{Bi}(\text{OH})_3$, BiOOH , and $\text{Bi}_3\text{O}(\text{OH})(\text{PO}_4)_2$ in the aqueous-salt suspension was calculated. The calculation was performed taking into account the mole fractions of water-soluble bound and free ions (equilibria (6) – (10)), the ionic strength of the solution (calculated for each composition point), the temperature dependence of the water autoprotolysis constant, and the temperature dependence of equilibria (1) – (4) and (6) – (10). For the calculation at 473 K, it was assumed that water is only in the liquid state.

4. Results and discussion

The results of X-ray diffraction studies of the obtained samples showed that the pH value and temperature play an important role in the formation processes of compounds in the $\text{Bi}_2\text{O}_3\text{-P}_2\text{O}_5\text{-H}_2\text{O}$ system. Thus, under precipitation conditions at room temperature (298 K) and a pH value of 2 of the aqueous-salt suspension, the appearance of reflections of crystalline BiPO_4 with a hexagonal ximengite-like structure can be observed (Fig. 1). With an increase in pH to 8 and 12, well-defined reflections of the crystalline compound are absent (Fig. 1a). This indicates the X-ray amorphous state of the obtained samples. Hydrothermal treatment at 473 K for 20 h of the aqueous-salt suspensions obtained at room temperature leads to the formation of new crystalline compounds (Fig. 1b). The results of elemental analysis of the obtained samples (Table 1) satisfy the stoichiometry of the crystalline compounds within the error of determination of Bi and P atoms.

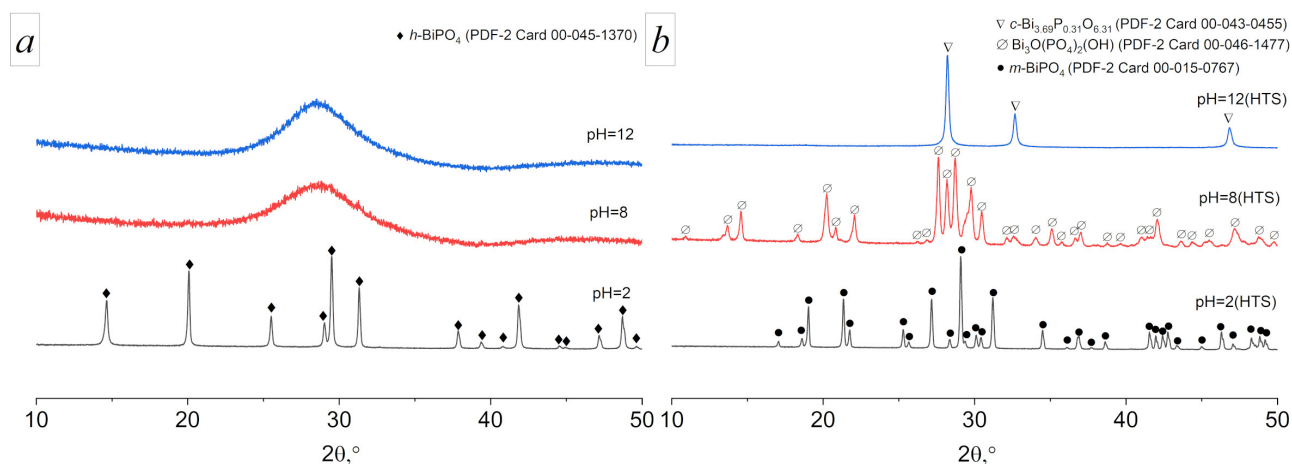


FIG. 1. Diffraction patterns obtained under different conditions (pH, T) of samples. a – 298 K, b – 473 K

During isothermal treatment under hydrothermal conditions of the aqueous-salt suspension with a pH of 2, containing particles of sparingly soluble crystalline BiPO_4 , a restructuring of the structure from hexagonal to a low-temperature monoclinic modification is observed, which is reflected in the change in the topology of the reflections (Fig. 1).

It is worth noting that the average crystallite sizes (weighted average) increase from 75 to 200 nm, while the average sizes of aggregated particles (length) increase from 1 to 1.5 μm . This indicates that even at room temperature under these conditions, there is active crystallite growth and the formation of large aggregates, the treatment of which under hydrothermal conditions leads to further growth in crystallite sizes. The similarity in morphology and particle sizes (on average 0.3 and 0.4 μm in width) may indicate that the polymorphic transformation $h\text{-BiPO}_4 \rightarrow m\text{-BiPO}_4$ occurs via a martensitic mechanism. The subsequent prolonged particle growth (on average 0.03 $\mu\text{m}/\text{h}$, Fig. 2) primarily affects the change in particle length and may be due to mass transfer processes limited in speed by the low ion concentration in the solution. This polymorphic transition was also noted in paper [59].

Hydrothermal treatment of aqueous-salt suspensions containing amorphous substances, obtained at room temperature under precipitation conditions at pH 8 and 12, leads to the formation of nanocrystalline compounds $\text{Bi}_3\text{O}(\text{OH})(\text{PO}_4)_2$ with a petitjeanite-like structure and $c\text{-Bi}_2\text{O}_3$ doped with phosphorus, respectively (Fig. 1). The weighted average particle sizes for the $\text{Bi}_3\text{O}(\text{OH})(\text{PO}_4)_2$ compound are approximately 200 nm for particles and approximately 62 nm for crystallites

TABLE 1. Results of X-ray diffraction studies and elemental analysis

Designation of samples	Crystalline phase / Chemical formula in oxide form	Elemental analysis		Chemical formula in oxide form according to elemental analysis
		Bi	P	
pH = 2	<i>h</i> -BiPO ₄ (Ximengite-like structure) 0.5[Bi ₂ O ₃ -P ₂ O ₅]	50±1	50±2	0.5[Bi ₂ O ₃ -P ₂ O ₅]
pH = 8	X-ray amorphous	70±1	30±2	0.7Bi ₂ O ₃ -0.3P ₂ O ₅
pH = 12	X-ray amorphous	88±1	12±2	0.9Bi ₂ O ₃ -0.1P ₂ O ₅
pH = 2(HTS)	<i>m</i> -BiPO ₄ 0.5[Bi ₂ O ₃ -P ₂ O ₅]	51±1	49±2	0.5[Bi ₂ O ₃ -P ₂ O ₅]
pH = 8(HTS)	Bi ₃ O(OH)(PO ₄) ₂ (Petitjeanite-like structure) 1.5[Bi ₂ O ₃ -0.7P ₂ O ₅ -0.3H ₂ O]	63±1	37±2	1.5[Bi ₂ O ₃ -0.6P ₂ O ₅]
pH = 12(HTS)	<i>c</i> -Bi _{3.69} P _{0.31} O _{6.31} 1.8[Bi ₂ O ₃ -0.09P ₂ O ₅]	87±1	13±2	1.8[Bi ₂ O ₃ -0.3P ₂ O ₅]

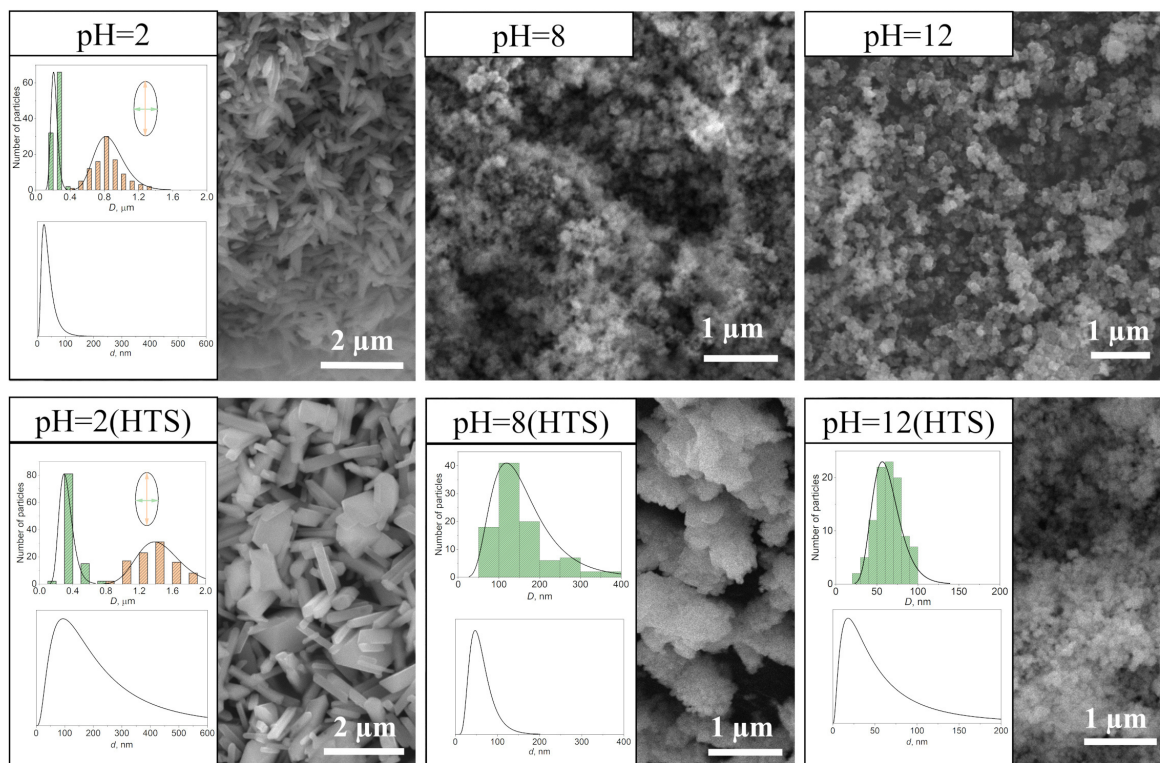


FIG. 2. Microphotographs of particles and lognormal dependences of the size distribution of particles and crystallites

(Fig. 2), indicating that the vast majority of particles are aggregates consisting of 30 – 40 interconnected crystallites. Spherical particles of the $c\text{-Bi}_2\text{O}_3$ compound, obtained by hydrothermal treatment of the X-ray amorphous precursor (Fig. 1b), are comparable in size to the crystallite sizes (weighted average is about 70 nm).

Thermodynamic calculations (Fig. 3) show that the compound BiPO_4 is formed and stable in the oxide system $\text{Bi}_2\text{O}_3\text{-P}_2\text{O}_5\text{-H}_2\text{O}(\text{OH}^-, \text{H}^+)$ within the pH range of 0 – 5.8 at temperatures of 298 and 473 K. This is consistent with the results obtained at pH = 2 in this study and with the results of obtaining BiPO_4 in acidic environments in several other studies [56,57,64,65]. It also aligns with the findings of study [66] where the formation of BiPO_4 was considered in the pH range of 0.5 – 4.0 at 298 K (mention of a white homogeneous mass) and 433 K. From pH 5.8 to 9.8, the most stable compound at 298 K is $\text{Bi}_3\text{O}(\text{OH})(\text{PO}_4)_2$. In this study, the compound $\text{Bi}_3\text{O}(\text{OH})(\text{PO}_4)_2$ was obtained by isothermal treatment under hydrothermal conditions of an amorphous substance with the following composition: $0.7\text{Bi}_2\text{O}_3\text{-}0.3\text{P}_2\text{O}_5$ in an aqueous-salt environment with a pH of 8. In the work of other authors, this compound was obtained at pH = 10, and in another study [61], the authors mention that they obtained it at a pH greater than 10. In this case, the calculation agrees with the data obtained in this study and satisfactorily agrees with the data from the works [60,61] within the error of calculating the Gibbs free energy of formation of $\text{Bi}_3\text{O}(\text{OH})(\text{PO}_4)_2$. The dashed line in Fig. 3 shows the region where freshly precipitated amorphous bismuth hydroxide, which is thermodynamically unstable, forms. At pH values greater than 10, bismuth oxides, hydroxides, and oxyhydroxides are approximately equally stable. However, according to the calculation, the lowest solubility is characteristic of bismuth hydroxide. In this study, at pH = 12, bismuth oxide doped with phosphorus of the composition $1.8\text{Bi}_2\text{O}_3\text{-}0.5\text{P}_2\text{O}_5$ was obtained. Apparently, this compound forms because in these conditions, the solution is dominated by water-soluble unbound phosphate anions. This fact may facilitate the incorporation of phosphorus into the structure. It is worth noting that the amorphous precursors also contain phosphorus atoms (Table 1).

5. Conclusions

It has been shown that the pH value of the medium significantly influences the formation of compounds in the aqueous-salt oxide system $\text{Bi}_2\text{O}_3\text{-P}_2\text{O}_5\text{-H}_2\text{O}(\text{OH}^-, \text{H}^+)$. Thus, at low pH values (pH = 2) and room temperature, hexagonal BiPO_4 is formed, while weakly alkaline and alkaline conditions promote the formation of X-ray amorphous substances. Hydrothermal treatment at 473 K leads to the polymorphic transformation of bismuth phosphate from hexagonal to monoclinic modification, as well as the formation of nanosized particles of crystalline compounds $\text{Bi}_3\text{O}(\text{OH})(\text{PO}_4)_2$ (with a crystal size of about 62 nm) and Bi_2O_3 (with a crystal size of about 70 nm) from amorphous precursors. Elemental analysis confirmed the correspondence of the chemical composition of the obtained crystalline compounds. By thermodynamic calculation, dependencies of the equilibrium molar solubility of identified compounds on the pH value of the aqueous-salt suspension were obtained, and for the compound $\text{Bi}_3\text{O}(\text{OH})(\text{PO}_4)_2$, such a dependence was obtained for the first time. Thermodynamic calculation showed that the compound BiPO_4 is stable in the pH range from 0 to 5.8 at temperatures of 298 and 473 K. The pH range from 5.8 to 9.8 is characterized by the stability of the compound $\text{Bi}_3\text{O}(\text{OH})(\text{PO}_4)_2$ at 298 K, while further increasing the pH leads to the precipitation of compounds with similar solubility, such as Bi_2O_3 , BiOOH , or $\text{Bi}(\text{OH})_3$ at 298 and 473 K. Overall, the thermodynamic calculation is in satisfactory agreement with the experimental data obtained.

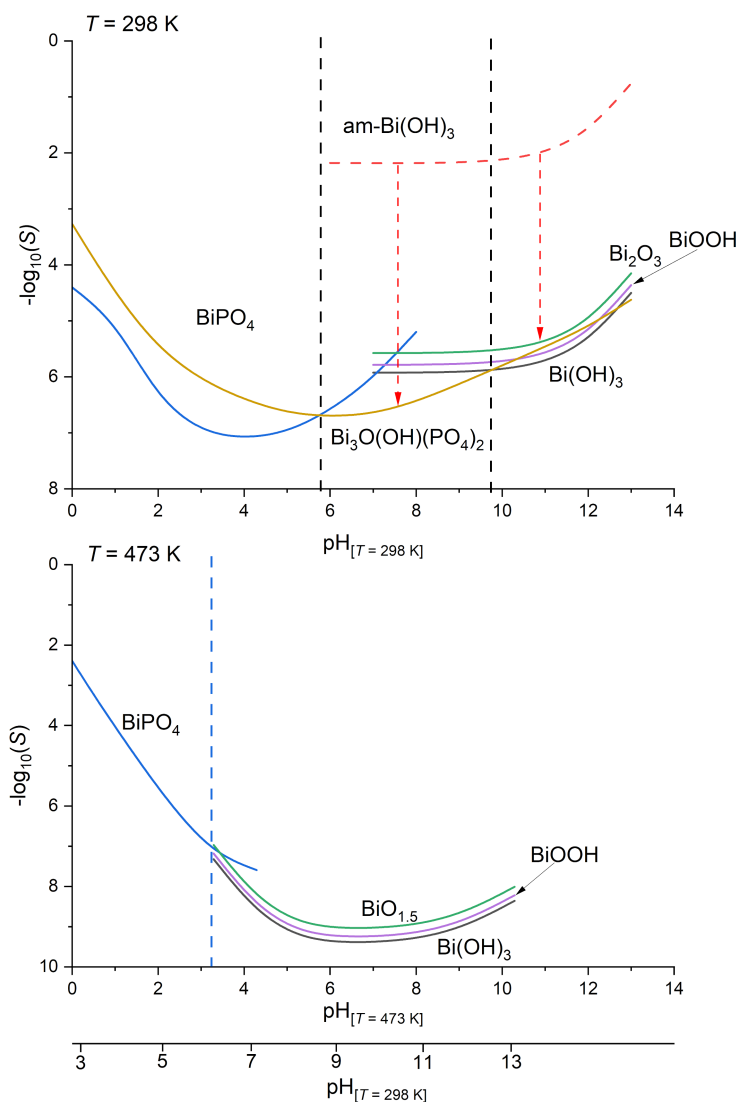


FIG. 3. Dependence of the equilibrium molar solubility (S , mol/L) of solid BiPO_4 , Bi(OH)_3 , $\text{BiO}_{1.5}$, BiOOH and $\text{Bi}_3\text{O(OH)(PO}_4)_2$ in a aqueous-salt suspension on pH at temperatures 298 and 473 K

References

- [1] Diodati S., Walton R.I., Mascotto S., Gross S. Low-temperature wet chemistry synthetic approaches towards ferrites. *Inorganic Chemistry Frontiers*, 2020, **7** (18), P. 3282–3314.
- [2] Bretos I., Jimenez R., Ricote J., Calzada M.L. Low-temperature crystallization of solution-derived metal oxide thin films assisted by chemical processes. *Chemical Society Reviews*, 2018, **47** (2), P. 291–308.
- [3] Diodati S., Dolcet P., Casarin M., Gross S. Pursuing the Crystallization of Mono- and Polymetallic Nanosized Crystalline Inorganic Compounds by Low-Temperature Wet-Chemistry and Colloidal Routes. *Chemical Reviews*, 2015, **115** (20), P. 11449–11502.
- [4] Gusarov V.V. Fast Solid-Phase Chemical Reactions. *Russ. J. Gen. Chem.*, 1997, **67** (12), P. 1846–1851.
- [5] Abiev R.S., Proskurina, O.V., Enikeeva, M.O., Gusarov V.V. Effect of Hydrodynamic Conditions in an Impinging-Jet Microreactor on the Formation of Nanoparticles Based on Complex Oxides. *Theor. Found. Chem. Eng.*, 2021, **55** (1), P. 12–29.
- [6] Almjasheva O.V., Popkov V.I., Proskurina O.V., Gusarov V.V. Phase formation under conditions of self-organization of particle growth restrictions in the reaction system. *Nanosystems: Phys. Chem. Math.*, 2022, **13** (2), P. 164–180.
- [7] Ghanizadeh S., Bao X., Vaidhyanathan B., Binner J. Synthesis of nano α -alumina powders using hydrothermal and precipitation routes: a comparative study. *Ceramics Int.*, 2014, **40** (1), P. 1311–1319.
- [8] Jesus A.C.B., Jesus J.R., Lima R.J.S., Moura K.O., Almeida J.M.A., Duque J.G.S., Meneses C.T. Synthesis and magnetic interaction on concentrated Fe_3O_4 nanoparticles obtained by the co-precipitation and hydrothermal chemical methods. *Ceramics Int.*, 2020, **46** (8), P. 11149–11153.
- [9] Gahrouei Z.E., Imani M., Soltani M., Shafyei A. Synthesis of iron oxide nanoparticles for hyperthermia application: Effect of ultrasonic irradiation assisted co-precipitation route. *Adv. Nat. Sci.: Nanosci. Nanotechnol.*, 2020, **11** (2), 025001.
- [10] Dehghanhadikolaei A., Ansary J., Ghoreishi R. Sol-gel process applications: A mini-review. *Proc. Nat. Res. Soc.*, 2018, **2** (1), P. 02008–02029.
- [11] Danks A.E., Hall S.R., Schnepf Z. The evolution of ‘sol-gel’ chemistry as a technique for materials synthesis. *Materials Horizons*, 2015 **3** (2), P. 91–112.

- [12] Verma S., Rani S., Kumar S. Crystal structure, morphology and optical behaviour of sol-gel derived pyrochlore rare earth titanates $\text{RE}_2\text{Ti}_2\text{O}_7$ (RE= Dy, Sm). *J. of Alloys and Compounds*, 2018, **750**, P. 902–910.
- [13] Bokov D., Jalil A.T., Chupradit S., Suksatan W., Ansari M.J., Shewael I.H., Valiev G.H., Kianfar E. Nanomaterial by sol-gel method: synthesis and application. *Advances in Materials Science and Engineering*, 2021, **2021**.
- [14] Ivanets A.I., Kuznetsova T.F., Prozorovich V.G. Sol-gel synthesis and adsorption properties of mesoporous manganese oxide. *Russian J. of Physical Chemistry A*, 2015, **89**, P. 481–486.
- [15] Berezhnaya M.V., Al'myasheva O.V., Mittova V.O., Nguen A.T., Mittova I.Y. Sol-gel synthesis and properties of $\text{Y}_{1-x}\text{Ba}_x\text{FeO}_3$ nanocrystals. *Russian J. of General Chemistry*, 2018, **88**, P. 626–631.
- [16] Filippova A.D., Rumyantsev A.A., Baranchikov A.E., Kolesnik I.V., Ivanova O.S., Efimov N.N., Khoroshilov A.V., Ivanov V.K. Hydrothermal Synthesis of $\gamma\text{-WO}_3$ and $h\text{-WO}_3$ Powders in the Presence of Citric Acid and Their Photoprotective Properties. *Russ. J. Inorg. Chem.*, 2022, **67** (6), P. 780–789.
- [17] Enikeeva M.O., Proskurina O.V., Gerasimov E.Yu., Nevedomskiy V.N., Gusarov V.V. Synthesis under hydrothermal conditions and structural transformations of nanocrystals in the $\text{LaPO}_4\text{-YPO}_4\text{-(H}_2\text{O)}$ system. *Nanosystems: Phys. Chem. Math.*, 2023, **14** (6), P. 660–671.
- [18] Lomakin M.S., Proskurina O.V., Gusarov V.V. Pyrochlore phase in the $\text{Bi}_2\text{O}_3\text{-Fe}_2\text{O}_3\text{-WO}_3\text{-(H}_2\text{O)}$ system: its formation by hydrothermal synthesis in the low-temperature region of the phase diagram. *Nanosystems: Phys. Chem. Math.*, 2023, **14** (2), P. 242–253.
- [19] Bachina A.K., Almjasheva O.V., Popkov V.I. Formation of ZrTiO_4 under Hydrothermal Conditions. *Russ. J. Inorg. Chem.*, 2022, **67**, P. 830–838.
- [20] Prabhakaran T., Mangalaraja R.V., Denardin J.C. Controlling the Size and Magnetic Properties of Nano CoFe_2O_4 by Microwave Assisted Co-Precipitation Method. *Materials Research Express*, 2018, **5** (2), 026102.
- [21] Ivanov V.K., Baranchikov A.E., Vanetsev A.S., Shaporev A.S., Polezhaeva O.S., Tretyakov Yu.D., Fedorov P.P., Osiko V.V. Effect of Hydrothermal and Ultrasonic/Hydrothermal Treatment on the Phase Composition and Micromorphology of Yttrium Hydroxocarbonate. *Russ. J. Inorg. Chem.*, 2007, **52** (9), P. 1321–1327.
- [22] Khrapova E.K., Kozlov, D.A., Krasilin A.A. Hydrothermal Synthesis of Hydrosilicate Nanoscrolls $(\text{Mg}_{1-x}\text{Co}_x)_3\text{Si}_2\text{O}_5(\text{OH})_4$ in a Na_2SO_3 Solution. *Russian J. of Inorganic Chemistry*, 2022, **67** (6), P. 839–849.
- [23] Enikeeva M.O., Proskurina O.V., Danilovich D.P., Gusarov V.V. Formation of nanocrystals based on equimolar mixture of lanthanum and yttrium orthophosphates under microwave-assisted hydrothermal synthesis. *Nanosystems: Phys. Chem. Math.*, 2020, **11** (6), P. 705–715.
- [24] Meskin P.E., Gavrilov A.I., Maksimov V.D., Ivanov V.K., Churagulov B.P. Hydrothermal/microwave and hydrothermal/ultrasonic synthesis of nanocrystalline titania, zirconia, and hafnia. *Russian J. of Inorganic Chemistry*, 2007, **52**, P. 1648–1656.
- [25] Amin G., Asif M.H., Zainelabdin A., Zaman S., Nur O., Willander M. Influence of pH, Precursor Concentration, Growth Time, and Temperature on the Morphology of ZnO Nanostructures Grown by the Hydrothermal Method. *J. of Nanomaterials*, 2011, **2011**, 269692.
- [26] Zhang A., Zhang J., Cui N., Tie X., An Y., Li L. Effects of pH on Hydrothermal Synthesis and Characterization of Visible-Light-Driven BiVO_4 Photocatalyst. *J. Mol. Catal. A: Chem.*, 2009, **304** (1–2), P. 28–32.
- [27] Shojaei N., Ebadzadeh T., Aghaei A. Effect of Concentration and Heating Conditions on Microwave-Assisted Hydrothermal Synthesis of ZnO Nanorods. *Mater. Charact.*, 2010, **61** (12), P. 1418–1423.
- [28] Solomatin S.V., Bronich T.K., Bargar T.W., Eisenberg A., Kabanov V.A., Kabanov A.V. Environmentally responsive nanoparticles from block ionomer complexes: effects of pH and ionic strength. *Langmuir*, 2003, **19** (19), P. 8069–8076.
- [29] Belous A.G., Pashkova E.V., Elshanskii V.A., Ivanitskii V.P. Effect of precipitation conditions on the phase composition, particle morphology, and properties of iron (III, II) hydroxide precipitates. *Inorganic Materials*, 2000, **36**, P. 343–351.
- [30] Lomakin M.S., Proskurina O.V., Gusarov V.V. Influence of hydrothermal synthesis conditions on the composition of the pyrochlore phase in the $\text{Bi}_2\text{O}_3\text{-Fe}_2\text{O}_3\text{-WO}_3$ system. *Nanosystems: Phys. Chem. Math.*, 2020, **11** (2), P. 246–251.
- [31] Du X., Wang Y., Su X., Li, J. Influences of pH value on the microstructure and phase transformation of aluminum hydroxide. *Powder Technology*, 2009, **192** (1), P. 40–46.
- [32] Alam M.A., Bishwas R.K., Mostofa S., Jahan S.A. Crystallographic phase stability of nanocrystalline polymorphs TiO_2 by tailoring hydrolysis pH. *South African J. of Chemical Engineering*, 2024, **49**, P. 73–85.
- [33] Zhang H., Zhang X., Graham T.R., Pearce C.I., Hlushko H., LaVerne J.A., Liu L., Wang S., Zheng S., Clark S.B., Li P., Wang Z., Rosso K.M. Crystallization and phase transformations of aluminum (oxy) hydroxide polymorphs in caustic aqueous solution. *Inorganic Chemistry*, 2021, **60** (13), P. 9820–9832.
- [34] Kozerozhets I.V., Semenov E.A., Avdeeva V.V. Ivakin Y.D., Kuprenko S.Y., Egorov A.V., Kholodkova A.A., Vasil'ev M.G., Kozlova L.O., Panasyuk G.P. State and forms of water in dispersed aluminum oxides and hydroxides. *Ceramics Int.*, 2023, **49** (18), P. 30381–30394.
- [35] Enikeeva M.O., Kenges K.M., Proskurina O.V., Danilovich D. P., Gusarov V.V. Influence of hydrothermal treatment conditions on the formation of lanthanum orthophosphate nanoparticles of monazite structure. *Russian J. of Applied Chemistry*, 2020, **93**, P. 540–548.
- [36] Li N., Yanagisawa K. Controlling the Morphology of Yttrium Oxide through Different Precursors Synthesized by Hydrothermal Method. *J. Solid State Chem.*, 2008, **181** (8), P. 1738–1743.
- [37] Lu C.H., Yeh C.H. Influence of hydrothermal conditions on the morphology and particle size of zinc oxide powder. *Ceramics Int.*, 2000, **26** (4), P. 351–357.
- [38] Khrapova E.K., Kozlov D., Krasilin A.A. Hydrothermal Synthesis of Hydrosilicate Nanoscrolls $(\text{Mg}_{1-x}\text{Co}_x)_3\text{Si}_2\text{O}_5(\text{OH})_4$ in a Na_2SO_3 Solution. *Russ. J. Inorg. Chem.*, 2022, **67**, P. 839–849.
- [39] Skachkov V.M., Pasechnik L. A., Medyankina I.S. Hydrothermal Synthesis of Calcium Silicates on the Recovery of Phosphorus from Phosphorite. *Russian J. of Inorganic Chemistry*, 2023, **68** (11), P. 1532–1536.
- [40] Chithra M.J., Sathya M., Pushpanathan K. Effect of pH on crystal size and photoluminescence property of ZnO nanoparticles prepared by chemical precipitation method. *Acta Metallurgica Sinica (English Letters)*, 2015, **28**, P. 394–404.
- [41] Syukkalova E.A., Sadetskaya A.V., Demidova N.D., Bobrysheva N.P., Osmolowsky M.G., Voznesenskiy M.A., Osmolovskaya O.M. The effect of reaction medium and hydrothermal synthesis conditions on morphological parameters and thermal behavior of calcium phosphate nanoparticles. *Ceramics Int.*, 2021, **47** (2), P. 2809–2821.
- [42] Obolenskaya L.N., Kuz'micheva G.M., Savinkina E.V., Sadvovskaya N.V., Zhilkina A.V., Prokudina N.A., Chernyshev V.V. Influence of the conditions of the sulfate method on the characteristics of nanosized anatase-type samples. *Russian Chemical Bulletin*, 2012, **61**, P. 2049–2055.
- [43] Proskurina O.V., Sokolova A.N., Sirotkin A.A., Abiev R.S., Gusarov V.V. Role of hydroxide precipitation conditions in the formation of nanocrystalline BiFeO_3 . *Russian J. of Inorganic Chemistry*, 2021, **66**, P. 163–169.
- [44] Uskoković V. Disordering the disorder as the route to a higher order: incoherent crystallization of calcium phosphate through amorphous precursors. *Crystal Growth & Design*, 2019, **19** (8), P. 4340–4357.
- [45] Gómez L.R., Vega, D.A. Amorphous precursors of crystallization during spinodal decomposition. *Physical Review E*, 2011, **83** (2), 021501.

- [46] Vallina B., Rodriguez-Blanco J.D., Brown A.P., Blanco J.A., Benning L.G. The role of amorphous precursors in the crystallization of La and Nd carbonates. *Nanoscale*, 2015, **7** (28), P. 12166–12179.
- [47] Krasilin A.A., Almjasheva O.V., Gusarov V.V. Effect of the structure of precursors on the formation of nanotubular magnesium hydrosilicate. *Inorg. Mater.*, 2011, **47** (10), 1111.
- [48] Popkov V.I., Almjasheva O.V., Schmidt M.P., Gusarov V.V. Formation mechanism of nanocrystalline yttrium orthoferrite under heat treatment of the coprecipitated hydroxides. *Russ. J. Gen. Chem.*, 2015, **85** (6), P. 1370–1375.
- [49] Galanov S.I., Sidorova O.I. Effect of a precursor on the phase composition and particle size of the active component of Ni-ZrO₂ catalytic systems for the oxidation of methane into syngas. *Russian J. of Physical Chemistry A*, 2014, **88**, P. 1629–1636.
- [50] Almjasheva O.V., Krasilin A.A., Gusarov V.V. Formation mechanism of core-shell nanocrystals obtained via dehydration of coprecipitated hydroxides at hydrothermal conditions. *Nanosystems: Phys. Chem. Math.*, 2018, **9** (4), P. 568–572.
- [51] Yang G., Park S.J. Conventional and microwave hydrothermal synthesis and application of functional materials: A review. *Materials*, 2019, **12** (7), 1177.
- [52] Almjasheva O.V., Gusarov V.V. Prenucleation Formations in Control over Synthesis of CoFe₂O₄ Nanocrystalline Powders. *Russian J. of Applied Chemistry*, 2016, **89** (6), P. 851–856.
- [53] Abiev R.Sh. Impinging-Jets Micromixers and Microreactors: State of the Art and Prospects for Use in the Chemical Technology of Nanomaterials (Review). *Theor. Found. Chem. Eng.*, 2020, **54**, P. 1131–1147.
- [54] Abiev R.S., Nikolaev A.M., Kovalenko A.S., Tsvigun N.V., Baranchikov A.E., Kopitsa G.P., Shilova O.A. One step synthesis of FeO_x magnetic nanoparticles in the microreactor with intensively swirling flows. *Chemical Engineering Research and Design*, 2024, **205**, P. 335–342.
- [55] Abiev R.S., Almjasheva O.V., Popkov V.I., Proskurina O.V. Microreactor synthesis of nanosized particles: The role of micromixing, aggregation, and separation processes in heterogeneous nucleation. *Chemical Engineering Research and Design*, 2022, **178**, P. 73–94.
- [56] Wang Y., Guan X., Li L., Li G. pH-driven hydrothermal synthesis and formation mechanism of all BiPO₄ polymorphs. *Cryst. Eng. Comm.*, 2012, **14** (23), P. 7907–7914.
- [57] Elovikov D.P., Nikiforova K.O., Tomkovich M.V., Proskurina O.V., Gusarov V.V. The pH value influence on the waylandite-structured BiAl₃(PO₄)₂(OH)₆ compound formation under hydrothermal conditions. *Inorganica Chimica Acta*, 2024, **561**, 121856.
- [58] Achary S.N., Errandonea D., Muñoz A., Rodríguez-Hernández P., Manjón F.J., Krishna P.S.R., Patwe S.J., Grover V., Tyagi A.K. Experimental and theoretical investigations on the polymorphism and metastability of BiPO₄. *Dalton Transactions*, 2013, **42** (42), P. 14999–15015.
- [59] Zhao M., Li G., Zheng J., Li L., Wang H., Yang L. Preparation and polymorph-sensitive luminescence properties of BiPO₄: Eu, Part I: room-temperature reaction followed by a heat treatment. *Cryst. Eng. Comm.*, 2011, **13** (20), P. 6251–6257.
- [60] Sahu S.P., Qanbarzadeh M., Ateia M., Torkzadeh H., Maroli A.S., Cates E.L. Rapid degradation and mineralization of perfluorooctanoic acid by a new petitjeanite Bi₃O(OH)(PO₄)₂ microparticle ultraviolet photocatalyst. *Environmental Science & Technology Letters*, 2018, **5** (8), P. 533–538.
- [61] Bentel M.J., Mason M.M., Cates E.L. Synthesis of Petitjeanite Bi₃O(OH)(PO₄)₂ Photocatalytic Microparticles: Effect of Synthetic Conditions on the Crystal Structure and Activity toward Degradation of Aqueous Perfluorooctanoic Acid (PFOA). *ACS Applied Materials & Interfaces*, 2023, **15** (17), P. 20854–20864.
- [62] Eremin O.V., Yurgenson G.A., Solodukhina M.A., Epova E.S. Hypergene minerals of antimony and bismuth: a method for estimating their standard Gibbs potentials. *Mineralogy of technogenesis*, 2018, **19**, P. 103–131.
- [63] Shkol'nikov E.V., Elovikov D.P. Thermodynamic calculation of the effect of polymorphism and pH value on the solubility of aluminium oxide and its hydrates in aqueous media. *Izvestiya SPbLTA*, **231**, 2020, P. 209–221 (in Russian).
- [64] Tuan A.D. Low-temperature hydrothermal synthesis of BiPO₄ for Rhodamine B removal. *Vietnam J. of Catalysis and Adsorption*, 2022, **11** (3), P. 33–36.
- [65] Cheng L.W., Tsai J.C., Huang T.Y., Huang C.W., Unnikrishnan B., Lin Y.W. Controlled synthesis, characterization and photocatalytic activity of BiPO₄ nanostructures with different morphologies. *Materials Research Express*, 2014, **1** (2), 025023.
- [66] Shi X., Liu Y., Zhang J., Zhang K., Li P., Zuo H., Li J. Effects of pH and Sm³⁺ doping on the structure, morphology and luminescence properties of BiPO₄: Sm³⁺ phosphors prepared by hydrothermal method. *Ceramics Int.*, 2015, **41** (2), P. 3162–3168.

Submitted 29 April 2024; revised 30 May 2024; accepted 3 June 2024

Information about the authors:

Dmitry P. Elovikov – Grebenshchikov Institute of Silicate Chemistry, Russian Academy of Sciences, St. Petersburg, Russia, 197022, St. Petersburg, Russia; ORCID 0000-0003-4345-6086; syncdima@mail.ru

Alena A. Osminina – Grebenshchikov Institute of Silicate Chemistry, Russian Academy of Sciences, St. Petersburg, Russia, 197022, St. Petersburg, Russia; ORCID 0009-0008-8804-4732; alenaosminina3001@gmail.com

Conflict of interest: the authors declare no conflict of interest.

Magnetic and photocatalytic properties of BiFeO₃ nanoparticles formed during the heat treatment of hydroxides coprecipitated in a microreactor with intense swirling flows

Olga V. Proskurina^{1,2,a}, Ksenia I. Babich^{1,2,b}, Sofia M. Tikhanova^{1,2,c}, Kirill D. Martinson^{1,2,d}, Vladimir N. Nevedomskiy^{1,e}, Valentin G. Semenov^{3,f}, Rufat Sh. Abiev^{1,2,g}, Victor V. Gusarov^{1,h}

¹Ioffe Institute, St. Petersburg, Russia

²St. Petersburg State Institute of Technology, St. Petersburg, Russia

³St. Petersburg State University, St. Petersburg, Russia

^aproskurinaov@mail.ru, ^bbabich3111@gmail.com, ^ctikhanova.sof@gmail.com, ^dmartinsonkirill@mail.ru,

^enevedom@mail.ioffe.ru, ^fval_sem@mail.ru, ^gabiev.rufat@gmail.com, ^hvictor.v.gusarov@gmail.com

Corresponding author: O. V. Proskurina, proskurinaov@mail.ru

ABSTRACT In this work, hydroxide deposition in a microreactor with intensively swirling flows was used to obtain BiFeO₃, followed by heat treatment of co-precipitated bismuth and iron hydroxides. The study of the formation of nanocrystalline bismuth orthoferrite was carried out using a set of methods: EDXMA, TEM, XRD, ⁵⁷Fe Mössbauer spectroscopy, DRS, etc. The photocatalytic activity and magnetic characteristics of the material were determined. It is shown that during heat treatment of hydroxide precipitation for 1 minute at a temperature of 530 °C, BiFeO₃ nanocrystals with an average crystallite size of 14±7 nm are formed. It was found that the resulting BiFeO₃ nanopowder is represented by agglomerates of individual nanoparticles. The saturation magnetization and residual magnetization values of these bismuth orthoferrite nanoparticles are 2.31 and 0.48 emu/g, respectively. According to the DRS results, band gap energy for the samples calculated at 530, 515, and 500 °C were 1.82, 1.86, and 1.91 eV, respectively, which ensures strong absorption of visible light by the samples. The sample showed higher photocatalytic activity in the X-ray amorphous state compared with nanocrystalline BiFeO₃ in the process of Fenton-like discoloration of methyl violet under the action of visible light with reaction rate constants of the pseudo-first order 0.0256 and 0.0072 min⁻¹, respectively.

KEYWORDS microreactor with intensively swirling flows, nanocrystals, nanoparticles, bismuth ferrite, photocatalysis, Fenton-like reactions.

ACKNOWLEDGEMENTS EDXMA and X-ray diffraction studies were performed employing the equipment of the Engineering Center of the St. Petersburg State Institute of Technology. TEM characterization was performed using equipment owned by the Federal Joint Research Center “Material science and characterization in advanced technology”. The work was financially supported by the Russian Science Foundation (Project No. 20-63-47016).

FOR CITATION Proskurina O.V., Babich K.I., Tikhanova S.M., Martinson K.D., Nevedomskiy V.N., Semenov V.G., Abiev R.Sh., Gusarov V.V. Magnetic and photocatalytic properties of BiFeO₃ nanoparticles formed during the heat treatment of hydroxides coprecipitated in a microreactor with intense swirling flows. *Nanosystems: Phys. Chem. Math.*, 2024, **15** (3), 369–379.

1. Introduction

Bismuth orthoferrite BiFeO₃ is a well-known multiferroic and continues to attract the attention of researchers due to the promising functional properties of the materials obtained from it [1–3]. Magnetic [4–6], electrophysical [7, 8], optical [9, 10], photocatalytic properties [11–14], photovoltaic [15], and the use of bismuth orthoferrite as a sensor material are actively investigated [16–19].

The morphology, sizes and structure of bismuth orthoferrite nanoparticles, the presence and amount of impurity phases can significantly affect the functional properties of the materials obtained from them [20–23].

Methods for the synthesis of bismuth orthoferrite nanopowders are constantly being developed in order to provide the characteristics required to obtain materials with certain functional properties. Bismuth orthoferrite is obtained by various methods, in particular, the solution combustion method [24–26], hydrothermal synthesis [27–29], hydrothermal microwave [30], solid-phase synthesis [31–33], the method of mechanical activation [34] is used. Nevertheless, the problem of obtaining phase-pure nanocrystalline bismuth orthoferrite powders remains relevant [35–37].

A promising direction for the production of oxide nanoparticles is the use of microreactor technology [38]. Free impinging-jets microreactor have been successfully used to obtain nanocrystals of complex oxides [39, 40]. In such microreactors, self-organizing spatially separated reaction zones with dimensions of about hundreds of nanometers are formed, in which nanoparticles with certain size parameters are formed [41, 42]. When producing nanocrystalline bismuth orthoferrite using a free impinging-jets microreactor, no impurity phases are detected [43].

Swirling-flow microreactors have found wide application for the production of various oxide nanoparticles. In such microreactors, a high level of specific energy dissipation rate is created (on the order of 2–35 kW/kg), which, in turn, contributes to the intensification of the micro-mixing process [44, 45].

In [46, 47], various types of microreactors were used to obtain nanocrystalline bismuth orthoferrite, but studies of the functional properties of bismuth orthoferrite were not carried out. The purpose of this work was to determine the magnetic and photocatalytic properties of nanocrystalline bismuth orthoferrite obtained by heat treatment of bismuth and iron hydroxides co-deposited in a microreactor with intensively swirling flows.

2. Experimental

To obtain bismuth orthoferrite, bismuth and iron nitrates $\text{Bi}(\text{NO}_3)_3 \cdot 5\text{H}_2\text{O}$ and $\text{Fe}(\text{NO}_3)_3 \cdot 9\text{H}_2\text{O}$ of analytical purity were used. Bismuth nitrate was dissolved in 7 mL of 4 M HNO_3 with stirring for 10 minutes and heating to 70 °C. Then, a portion of iron nitrate was added to the resulting solution with stirring. Weights of salts were calculated to prepare 3 g of bismuth ferrite. After stirring for 10 minutes, 130 mL of distilled water was added and stirred for another 20 minutes. Separately, 1 L of 4 M NaOH solution was prepared. The resulting solutions were used for co-precipitation of bismuth and iron(III) hydroxides in an one-step microreactor with intensively swirling flows (MRISF-1). Co-precipitation was carried out at a temperature of about 22 °C and atmospheric pressure.

A solution of bismuth and iron nitrates was fed into MRISF-1 into one of the tangential inlet pipes, and a solution of NaOH antisolvent into an axial inlet pipe; both solutions were supplied with the same flow rates of 2.1 L/min (Fig. 1).

As a result of solutions intensive mixing in the microreactor, a suspension of co-precipitated bismuth and iron hydroxides was obtained, which was then washed with distilled water using centrifugation and intermediate dispersion using an ultrasonic bath in order to better wash the sediments from alkali residues. The washed samples were dried at 70 °C for 24 hours.

The dried samples were heated in a tubular furnace in a platinum crucible in the “annealing-quenching” mode for 1 minute at temperatures of 500, 515 and 530 °C. The samples were designated “HT 500 °C”, “HT 515 °C” and “HT 530 °C”.

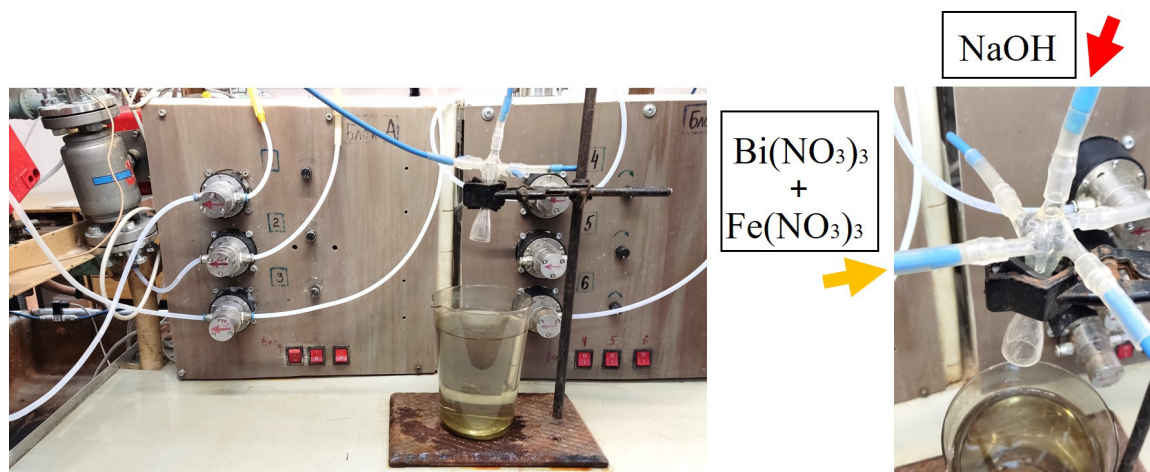


FIG. 1. One-step microreactor with intensively swirling flows: (a) experimental rig; (b) schematic of solutions supply into inlet pipes of the MRISF-1

3. Characterization

Powders were characterized by several methods. X-ray diffraction patterns were taken on a Rigaku SmartLab 3 (Rigaku Corporation, Japan) powder diffractometer ($\text{CuK}\alpha$ radiation) in the angle range $2\theta = 20 - 60^\circ$ with a step of 0.01° and a speed of $0.1^\circ/\text{min}$. The average crystallite size was determined using the SmartLab Studio II software package from Rigaku. The size distribution of crystallites was determined by the method of fundamental parameters in the approximation of a lognormal distribution model using the SmartLab Studio II software package for reflection 024.

The elemental composition of the samples was determined using a Tescan Vega 3 SBH scanning electron microscope (Tescan, Czech Republic) with an energy dispersive X-ray spectroscopy (EDX) Oxford Instruments INCA x-act X-ray microanalysis attachment (Oxford Instruments, Oxford, UK).

Transmission electron microscopy (TEM) studies with the determination of microdiffraction of the samples were performed using a JEOL JEM-2100F microscope (JEOL Ltd., Akishima, Tokyo, Japan) at an accelerating voltage of 200 kV. Samples for research were prepared by preliminary dispersion of the initial powder in ethyl alcohol in an ultrasonic bath for 15 minutes, followed by deposition on a supporting film.

To study the magnetic properties and magnetic structure, Mössbauer spectroscopy was used, which is an informative method for studying the properties of iron-containing materials and differences in the local environments of iron atoms. The measurements were carried out on a Mössbauer spectrometer from WISSEL on the ⁵⁷Fe isotope with registration in the geometry of transmission of γ -radiation through the sample under study from a ⁵⁷Co source in a rhodium (Rh) matrix. The reference signal in the motion system of the Doppler modulator in the spectrometer had the shape of a triangle to set the speed with constant acceleration. The speed scale was calibrated using α -iron foil at room temperature. The Mössbauer spectra of the samples under study were measured at room temperature. Mathematical processing of the spectra was carried out using a program that describes spectral lines by Lorentzian-shaped peaks and minimization using the least squares method. In the procedure for minimizing the functional χ^2 , the program searches for optimal values of the parameters of spectral lines, namely, widths, intensities and positions. The parameters of hyperfine interactions were calculated from the positions of the lines: IS – isomer chemical shift, QS – quadrupole splitting, H_{eff} – effective magnetic field.

The magnetic characteristics of a bismuth ferrite sample were studied using a Lake Shore 7410 vibration magnetometer at room temperature (25 °C) in a field range of up to 30,000 Oe using a standard measuring cell.

The light absorption ability of the samples was investigated by diffuse reflectance spectra (DRS) in the UV-visible region were recorded at room temperature in the range of 400–800 nm using an AvaSphere-30-Refl integrating sphere.

The band gap energy (E_g) was calculated from the plot of the Kubelka–Munk function:

$$F(R) = \frac{(1 - R)^n}{2R} = \frac{K}{S},$$

where K is the molar absorption coefficient, S is the scattering factor, and R is the reflectance of the material. The value of n is determined by the nature of the sample ($n = 2$ for direct allowed transitions and $n = 1/2$ for indirect allowed transitions)

The photocatalytic activity of the samples was studied in the process of photocatalytic and photo-Fenton-like degradation of methyl violet (MV) under visible-light irradiation $\lambda_{max} = 410$ nm (Fig. 2). In a typical manner described previously [48], the 1.5 mg of the catalyst was suspended in 1 mL of distilled water and added to MV solution (3 mmol/L). Before visible light irradiation, the 50 mL reaction solutions were magnetically stirred in the darkness for 30 min to ensure the adsorption-desorption equilibrium. After this stage 10 mL of H₂O₂ solution (20 mmol/L) was added to examine the photo-Fenton-like activity. At appropriate time intervals, 2 mL of the solution was collected to spectrophotometrically determine the concentration of the dye using AvaLight-XE light source and AvaSpec-ULS2048 spectrometer.

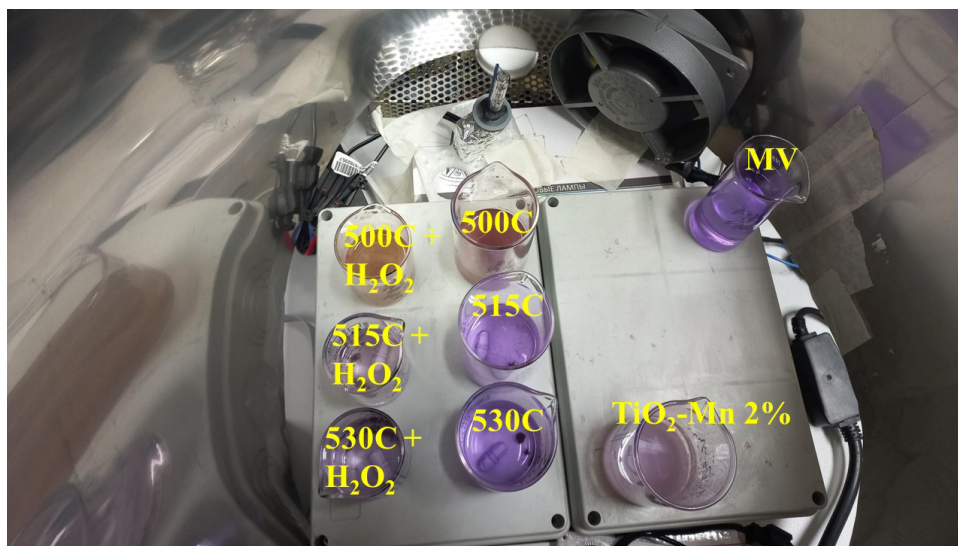


FIG. 2. Solutions of MV dye with a catalyst in the process of studying photocatalytic activity

4. Results and discussion

Energy-dispersive X-ray spectroscopy data of all samples showed that the atomic ratio of bismuth and iron in all samples after heat treatment remains at the same level (Bi : Fe = (52±2) : (48±2)), which, within the error, corresponds to the ratio specified during synthesis, corresponding to the stoichiometry of BiFeO₃.

X-ray diffractometry data of heat-treated samples are shown in Fig. 3. The diffraction pattern of a sample heat-treated at 500 °C has an X-ray amorphous appearance. The diffraction pattern of the sample heat-treated at 515 °C shows the appearance of reflections corresponding to bismuth orthoferrite (ICSD code 163688). The diffraction pattern of the sample heat-treated at 530 °C shows reflections of crystalline bismuth orthoferrite and no X-ray amorphous halo. For this sample, in the inset in Fig. 3, it is shown the crystallite size distribution determined from reflection 024. The weighted average value of the BiFeO_3 crystallite size for the sample heat-treated at 530 °C was 14 ± 7 nm.

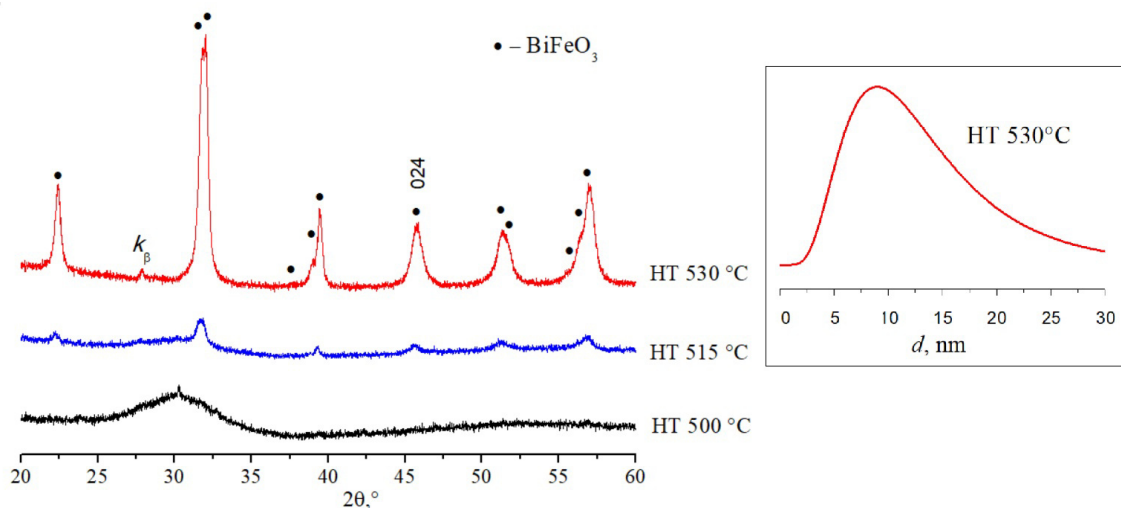


FIG. 3. X-ray diffraction patterns of samples after heat treatment and crystallite size distribution according to reflection 024 for a sample heat treated at 530 °C

TEM micrographs of bismuth orthoferrite samples heat-treated at three different temperatures are presented in Fig. 4.

Images of samples heat-treated at 500, 515 and 530 °C are presented in Figures 4a, 4b, 4c, respectively. All samples are nanoparticles assembled into aggregates. The electron diffraction image in Fig. 4a confirms that the sample is X-ray amorphous, since the electron diffraction (SAED) image in Fig. 4a, wide circles are visible from the carbon substrate and the X-ray amorphous sample. Electron microdiffraction data from samples “HT 515 °C” and “HT 530 °C” confirm the polycrystalline nature of the samples, as well as the presence of a certain amount of X-ray amorphous phase in the sample “HT 515 °C”. For the “HT 530 °C” sample in Fig. 4c on the right it is also shown a dark-field image in which bright spots corresponding to BiFeO_3 nanocrystals of various sizes are visible.

Analysis of the results of studying the crystallization of BiFeO_3 by TEM (Fig. 4) allows us to conclude that the formation of bismuth ferrite nanocrystals occurs according to the following mechanism. After dehydration of a mixture of amorphous bismuth and iron hydroxides and the formation of crystalline BiFeO_3 nuclei (see Fig. 4a), their growth occurs due to the coherent addition of the clusters that make up the amorphous phase to crystalline particles of bismuth ferrite. Such crystal growth is stopped if growing BiFeO_3 crystals collide with each other without oriented intergrowth along the faces (Fig. 5).

Another reason for the suspension of crystal growth is the depletion of the amorphous substance within which it grows. With this mechanism of crystallite growth, their shape and size will be largely determined by both the intensity of the nucleation process and the geometric parameters of the amorphous phase particles. In this case, along with small BiFeO_3 nanocrystals of regular shape, relatively large crystals with complex morphology will be formed (Fig. 4c). It should be noted that a similar nature of the formation of BiFeO_3 crystals is noted in [27].

In the Mössbauer spectrum (Fig. 6) of a sample heat-treated at 500 °C, and which, according to X-ray diffraction data, is X-ray amorphous (Fig. 2), only a paramagnetic component is observed, which can be represented as two doublets – D1, D2 with isomer shifts (IS), characterizing iron in the +3 oxidation state. The results of processing the Mössbauer spectra of the samples are given in Table 1. A comparison of the quadrupole splitting (QS) values of the doublets $\text{QS (D1)} = 0.67$ and $\text{QS (D2)} = 1.13$ shows that the state of Fe^{3+} ions in the “HT 500 °C” sample, corresponding to doublet D2, has a less symmetrical environment than that corresponding to doublet D1. The hyperfine splitting parameters of these doublets are close to the IS and QS values found for BiFeO_3 particles with sizes of 10 – 20 nm [49, 50].

In the Mössbauer spectrum of a sample heat-treated at 515 °C, along with a doublet, the share of which is about 3 %, two superimposed sextets are detected, characteristic of BiFeO_3 with magnetic ordering [51, 52]. It should be noted that the disappearance of the D2 doublet, which corresponds to the most asymmetric environment of iron, indicates that the formation of crystalline bismuth orthoferrite occurs due to the crystallization of an amorphous substance in which iron ions are in the most asymmetric environment. The doublet, apparently, can be correlated with the amorphous state of the substance or with crystalline clusters of bismuth orthoferrite so small that they appear as X-ray amorphous.

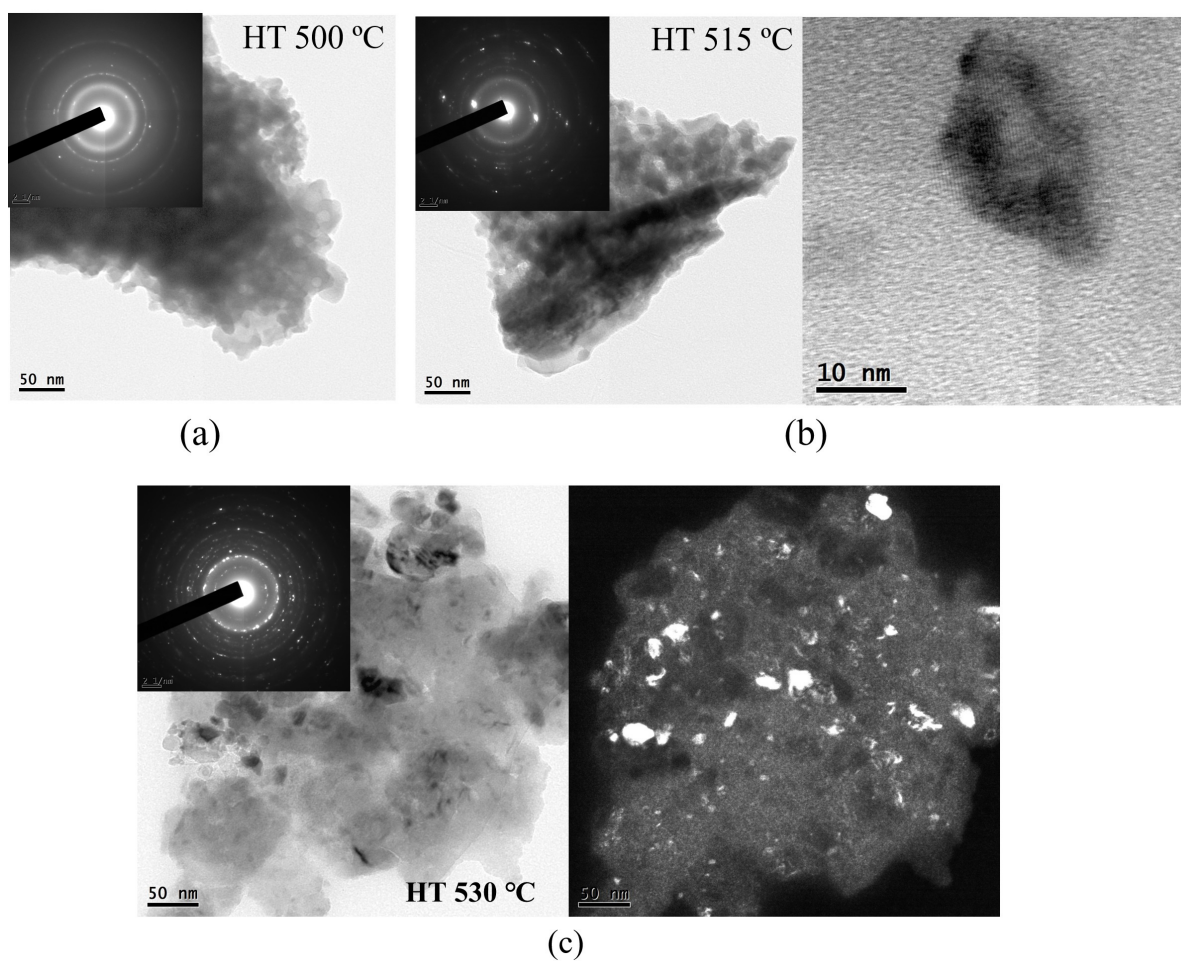


FIG. 4. TEM data of samples heat-treated at 500 (a), 515 (b) and 530 °C (c)

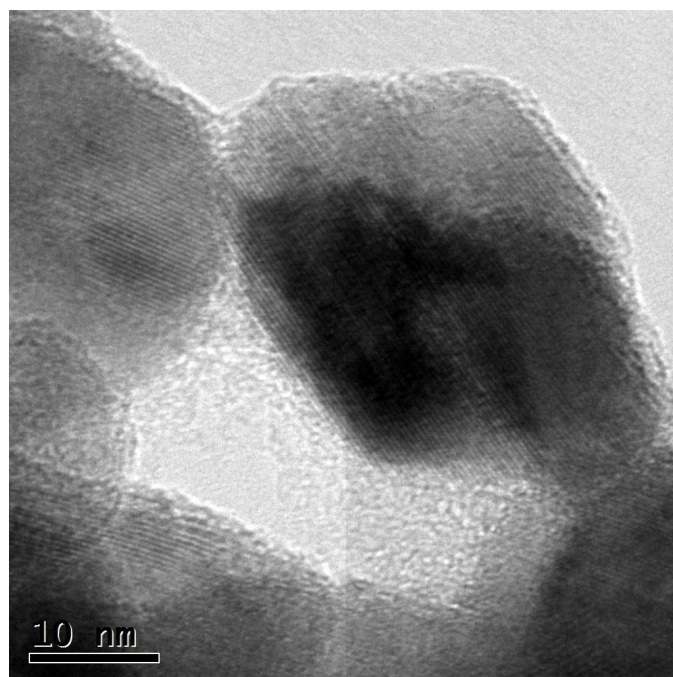


FIG. 5. BiFeO₃ nanocrystals in a sample heat-treated at 530 °C

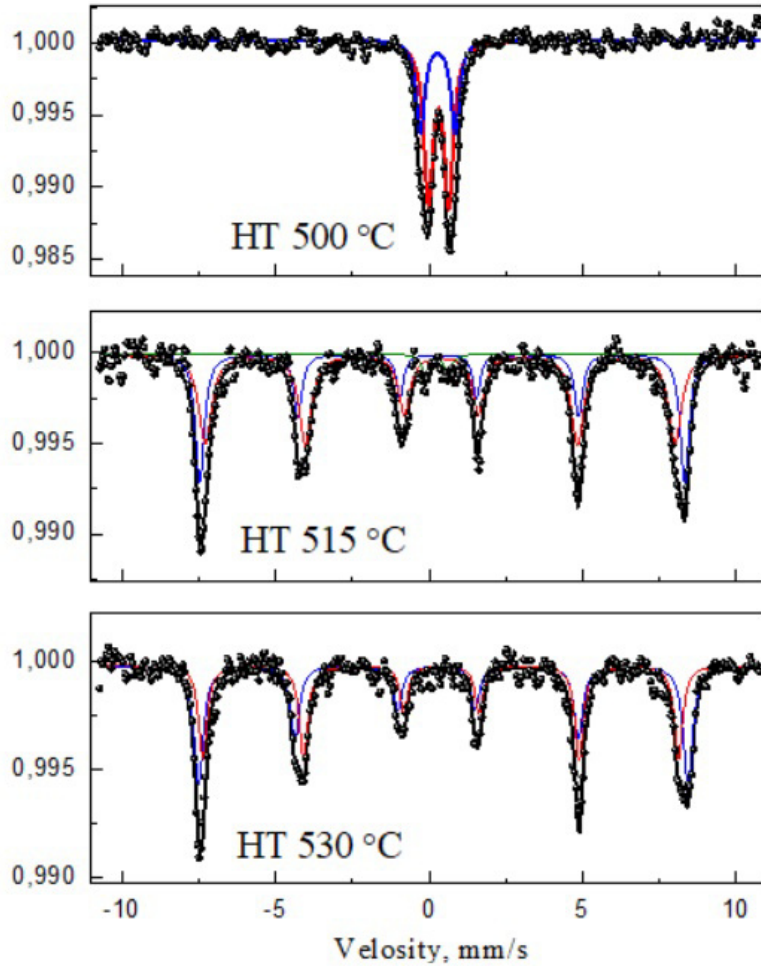


FIG. 6. Mössbauer spectra of samples heat-treated at 500, 515 and 530 °C

In the Mössbauer spectrum of a sample heat-treated at 530 °C, two sextets are observed; there is no doublet component.

TABLE 1. Parameters of Mössbauer spectra of samples at room temperature

Sample	Component	Isomer shift, IS [mm/s]	Quadrupole splitting, QS [mm/s]	Effective magnetic field H_{eff} [T]	Integral intensities ratio [%]
HT 500 °C	Doublet 1	0.31 ± 0.01	0.67 ± 0.02	–	65
	Doublet 2	0.28 ± 0.01	1.13 ± 0.03	–	35
HT 515 °C	Doublet 1	0.24 ± 0.04	0.74 ± 0.08	–	3
	Sextet 1	0.36 ± 0.01	-0.13 ± 0.02	49.1 ± 0.07	39
	Sextet 2	0.38 ± 0.01	0.04 ± 0.02	47.6 ± 0.13	58
HT 530 °C	Sextet 1	0.35 ± 0.01	-0.21 ± 0.01	49.5 ± 0.05	52
	Sextet 2	0.39 ± 0.01	0.02 ± 0.01	48.1 ± 0.05	48

Figure 7 shows the M–H magnetization curve of bismuth ferrite nanopowders heat-treated at 530 °C.

The obtained data shows that the curve does not reach saturation, which indicates the dependence of the magnetic moment of the particles on the applied magnetic field. The values of saturation magnetization and residual magnetization

are 2.31 and 0.48 emu/g, respectively. This magnetic behavior of the sample is explained by the small size of the crystallites (14 ± 7 nm). It was shown in [53] that the magnetization depends on the size of the crystallites and can reach very high values when the crystallite sizes decrease to nanometer values, which was explained by surface effects [53, 54]. The particle size can also affect the anisotropy and coercive force of bismuth ferrite. Small particles usually exhibit a higher coercive force due to an increase in surface anisotropy [55].

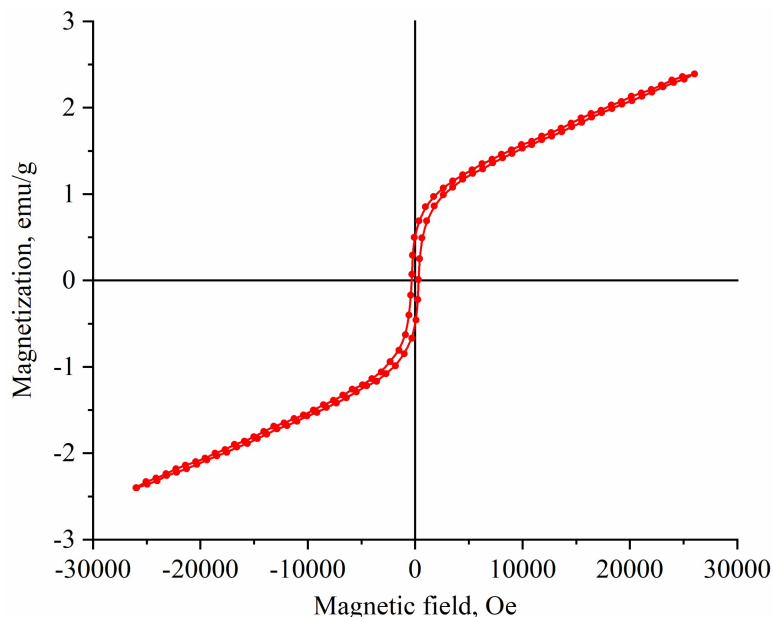


FIG. 7. M-H loop of "HT 530 °C" nanopowder

In the diffuse reflectance spectra (DRS) of the samples (Fig. 8a), absorption bands can be observed in the visible region at 500 nm and 650 nm, which suggests their potential as visible light photocatalysts. The sample calcinated at 530 °C demonstrates the most intensive absorption indicating it as perspective material for visible-light-driven photocatalytic processes.

The absorbance spectra indicated the having direct bang gaps for all samples. The obtained spectra were recalculated to Tauc plot by the Kubelka–Munk function to determine the bang gap values (Fig. 8b). The band gap energy (E_g) for the samples calcinated at 530, 515, and 500 °C were 1.82 eV, 1.86 eV, and 1.91 eV, respectively. The obtained values are close to the previous research data for the sample calcinated at 500 °C ($E_g = 2.16$ eV [48]; $E_g = 2.04$ eV [56]), and lower for other samples.

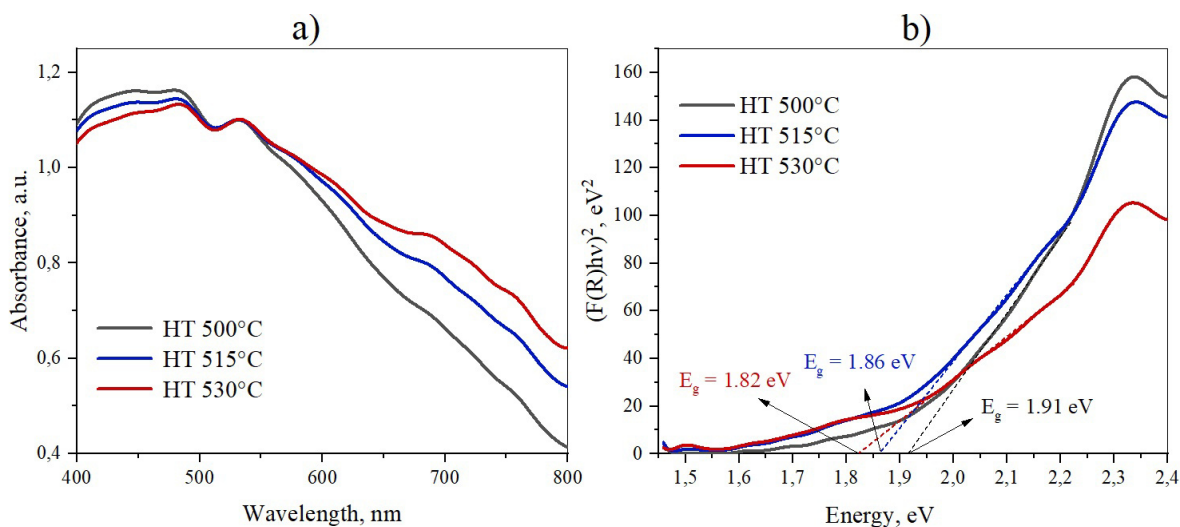


FIG. 8. Diffuse reflectance spectra (a) and Tauc plots (b) of the samples calcinated at different temperatures

A study of the photocatalytic activity of the samples without addition of hydrogen peroxide showed that methyl violet decolorization occurs with an efficiency of 9.8 – 16.1 % (Fig. 9b). The change in color intensity under the action of the

most effective catalyst is shown in Fig. 9a. Linearization of the kinetic curves demonstrated a pseudo-first order reaction for the photocatalytic decolorization of methyl violet (Fig. 9c), and the kinetic constants determined as the slope of the plot were 0.0011, 0.0012, 0.0016 min^{-1} for samples HT 500 °C, HT 515 °C and HT 530 °C, respectively (inset in Fig. 9c). The resulting samples have a relatively low efficiency during the photodegradation of methyl violet, which may be due to the small specific surface area and macroporous structure.

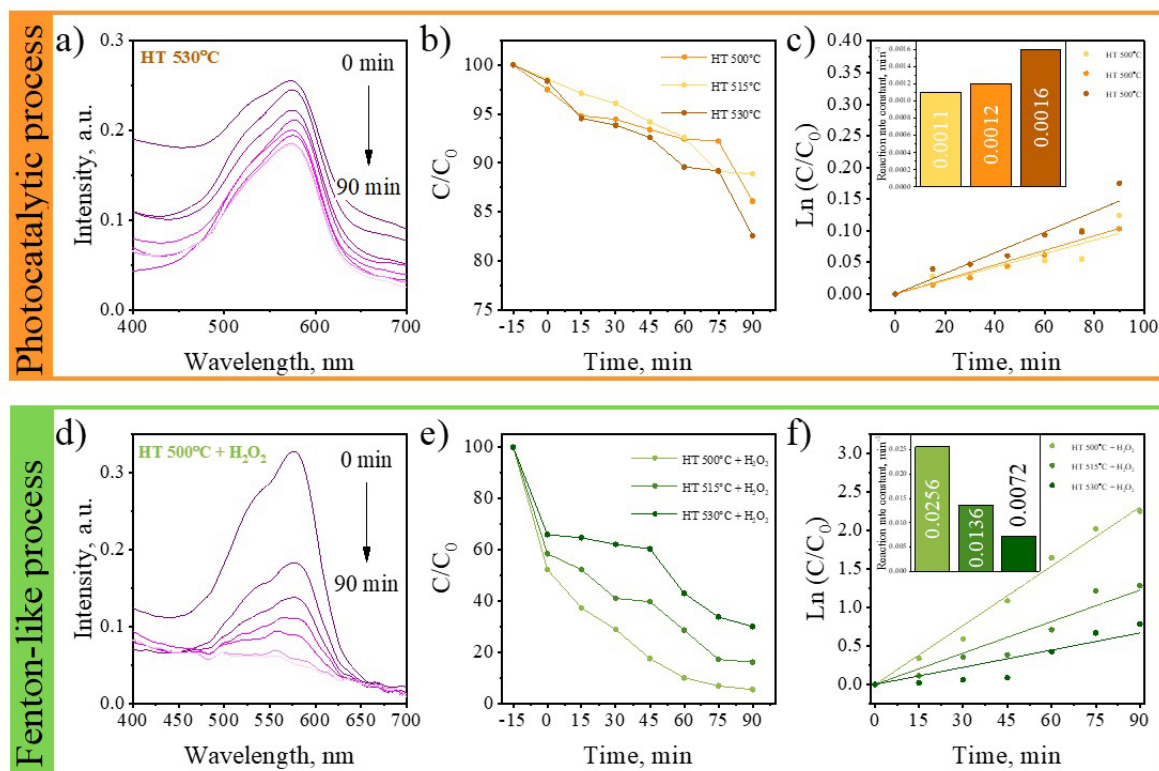


FIG. 9. Photocatalytic activity of samples in classical (a–c) and Fenton-like (d–f) degradation processes of methyl violet: degradation of the dye under the influence of HT 530 °C (a) and HT 500 °C + H₂O₂ (d); kinetic curves (b, e) and linearized kinetic curves (c, f); rate constants for the dye degradation reaction (insets in graphs (c, f))

The photocatalytic activity of the obtained samples was also studied in the process of Fenton-like degradation of methyl violet. With the addition of hydrogen peroxide, the dye decolorization efficiency increased significantly and was 69.9 % for HT 530 °C + H₂O₂, 83.8 % for HT 515 °C + H₂O₂ and 94.5 % for HT 500 °C + H₂O₂ (Fig. 9e). For the latter, spectra are shown presenting the change in the color intensity of the solution depending on the irradiation time (Fig. 9d), indicating almost complete decomposition of the dye. The pseudo-first order kinetic reaction constants determined from the linearized kinetic curves (Fig. 9f) were 0.0265, 0.0136, 0.0072 min^{-1} for the HT 500 °C + H₂O₂, HT 515 °C + H₂O₂ and HT 530 °C + H₂O₂ samples, respectively. (inset in Fig. 9f). The values of pseudo-first order reaction rate constants obtained for the Fenton-like decomposition of methyl violet are 5 – 20 times higher than similar constants for the photocatalytic process (without the addition of hydrogen peroxide). This increase in photocatalytic efficiency is associated with the high activity of ferrites in general and bismuth ferrite in particular in Fenton-like oxidation processes due to the presence of Fe³⁺ and Bi³⁺ ions [57–59].

It was also shown that the HT 500 °C + H₂O₂ sample, containing the largest proportion of the amorphous phase, exhibits greater Fenton photocatalytic activity compared to other samples. The increase in activity in this case, as shown in previous studies [60], is explained by the fact that a certain amount of amorphous component in photocatalysts can significantly increase the efficiency of electron-hole pair separation, visible light absorption and adsorption properties.

5. Conclusion

To obtain bismuth orthoferrite, hydroxide precipitation was used in the one-step microreactor with intensively swirling flows, followed by heat treatment of co-precipitated bismuth and iron hydroxides.

It has been shown that when thermally treating hydroxide precipitates for 1 minute at a temperature of 530 °C, BiFeO₃ nanocrystals with an average crystallite size of 14±7 nm are formed. It has been revealed that the resulting BiFeO₃ nanopowder is represented by agglomerates of individual nanoparticles. The saturation magnetization and remanent magnetization values of these bismuth orthoferrite nanoparticles are 2.31 and 0.48 emu/g, respectively.

The following mechanism of growth of bismuth orthoferrite particles is proposed: after dehydration of a mixture of amorphous bismuth and iron hydroxides and the formation of crystalline BiFeO₃ nuclei, their growth occurs due to the coherent attachment of clusters, which make up the amorphous phase, to crystalline particles of bismuth ferrite. Crystal growth stops if the growing BiFeO₃ crystals collide with each other without oriented accretion along the edges or due to exhaustion of the amorphous substance inside which the BiFeO₃ crystals grow.

According to the DRS results, band gap energy for the samples calculated at 530, 515, and 500 °C were 1.82, 1.86, and 1.91 eV, respectively, which ensures strong absorption of visible light by the samples.

The photocatalytic and Fenton-photocatalytic activity of the obtained nanocrystalline powders was studied during the oxidation of methyl violet. The sample showed higher photocatalytic activity in the X-ray amorphous state compared with nanocrystalline BiFeO₃ in the process of Fenton-like discoloration of methyl violet under the action of visible light with reaction rate constants of the pseudo-first order 0.0256 and 0.0072 min⁻¹, respectively.

References

- [1] Kharbanda S., Dhanda N., Sun A.-C.A., Thakur A., Thakur P. Multiferroic perovskite bismuth ferrite nanostructures: A review on synthesis and applications. *Journal of Magnetism and Magnetic Materials*, 2023, **572**, P. 170569.
- [2] Krishnamoorthy A., Hannah I., Maruthasalamoorthy S., Nirmala R., Punithavelan N., Navamathavan R. Review – State of the Art of the Multifunctional Bismuth Ferrite: Synthesis Method and Applications. *ECS Journal of Solid State Science and Technology*, 2022, **11**, P. 043010.
- [3] Ghuge R.S., Shinde M.D., Rane S.B. Bismuth-Based Gas Sensors: A Comprehensive Review. *Journal of Electronic Materials*, 2021, **50**(11), P. 6060–6072.
- [4] Gervits N.E., Tkachev A.V., Zhurenko S.V., Gunbin A.V., Bogach A.V., Lomanova N.A., Danilovich D.P., Pavlov I.S., Vasiliev A.L., Gippius A.A. The size effect of BiFeO₃ nanocrystals on the spatial spin modulated structure. *Physical Chemistry Chemical Physics*, 2023, **25**(37), P. 25526–25536.
- [5] Kravtsova P.D., Tomkovich M.V., Volkov M.P., Buryanenko I.V., Semenov V.G., Popkov V.I., Lomanova N.A. Magnetic properties of nanocrystalline materials based on the system (1-x)BiFeO₃-(x)YFeO₃. *Physics of the Solid State*, 2023, **65**(12), P. 2120–2123.
- [6] Chinchay-Espino H.A., Montes-Albino G.M., Morales-Cruz C.M., Dobbertin-Sanchez S.E., Rojas-Flores S. Effect of Cobalt Substitution on the Structural and Magnetic Properties of Bismuth Ferrite Powders. *Crystals*, 2022, **12**, P. 1058.
- [7] Zhao X., Menzel S., Polian I., Schmidt H., Du N. Review on Resistive Switching Devices Based on Multiferroic BiFeO₃. *Nanomaterials*, 2023, **13**, P. 1325.
- [8] Dang T.T., Schell J., Boa A.G., Lewin D., Marschick G., Dubey A., Escobar-Castillo M., Noll C., Beck R., Zyabkin D.V., Glukhov K., Yap I.C.J., Mokhles G. A., Lupascu D.C. Temperature dependence of the local electromagnetic field at the Fe site in multiferroic bismuth ferrite. *Physical Review B*, 2022, **106**(5), P. 054416.
- [9] Taha G.M., Rashed M.N., El-Sadek M.S.A., Moghazy M.A.E. Multiferroic BiFeO₃ dithizone functionalized as optical sensor for detection and determination of some heavy metals in environmental samples. *Bulletin of Materials Science*, 2021, **44**(2), P. 122.
- [10] Ahmed I., Naz I., Morley N., Shabbir S., Maraj M., Ismail A.G., Anwar H., Ahmad F. Experimental and DFT investigation of structural and optical properties of lanthanum substituted bismuth ferrites. *Physica B: Condensed Matter*, 2023, **661**, P. 414927.
- [11] Nguyen K., Nguyen C., Pham C., Lim D., Nguyen Q.-B., Le H., Mai N., Dao N. Kinetics and mechanism of photocatalytic degradation of rhodamine B on nanorod bismuth ferrite perovskite prepared by hydrothermal method. *Research on Chemical Intermediates*, 2022, **49**, P. 57–72.
- [12] Cadenbach T., Sanchez V., Chiquito Ríos D., Debut A., Vizuete K., Benitez M.J. Hydrothermal Synthesis of Bismuth Ferrite Hollow Spheres with Enhanced Visible-Light Photocatalytic Activity. *Molecules*, 2023, **28**, P. 5079.
- [13] Zhou T., Zhai T., Shen H., Wang J., Min R., Ma K., Zhang G. Strategies for enhancing performance of perovskite bismuth ferrite photocatalysts (BiFeO₃): A comprehensive review. *Chemosphere*, 2023, **339**, P. 139678.
- [14] Mittal S., Garg S., Bhandari H., Sharma V. A review on recent progressions of Bismuth ferrite modified morphologies as an effective photocatalyst to curb water and air pollution. *Inorganic Chemistry Communications*, 2022, **144**, P. 109834.
- [15] Ceballos-Sanchez O., Sanchez-Martinez A., Flores- Ruiz F.J., Huerta-Flores A.M., Torres-Martínez L.M., Ruelas R, García-Guaderrama M. Study of BiFeO₃ thin film obtained by a simple chemical method for the heterojunction-type solar cell design. *Journal of Alloys and Compounds*, 2020, **832**, P. 154923.
- [16] Eshore A.N., Dey S., Goswami D.K., Guha P.K. Crystallographic Nanojunctions of Bismuth Ferrite for Unconventional Detection of Carbon Monoxide. *ACS Applied Nano Materials*, 2023, **6**(11), P. 9397–9403.
- [17] Dmonte D.J., Bhardwaj A., Wilhelm M., Fischer T., Kuřitka I., Mathur S. Sub PPM Detection of NO₂ Using Strontium Doped Bismuth Ferrite Nanostructures. *Micromachines*, 2023, **14**, P. 644.
- [18] Ji H., Zhang L., Zhang R. Gas sensitive performance and mechanism of multiferroic BiFeO₃ under thermal-magnetic synergetic excitation. *Inorganic Chemistry Communications*, 2023, **150**, P. 110491.
- [19] Zhang Y., Zhang H., Zhang J., Guo J., Zhang D. Fast Response and Low Detection Limit of Ammonia Sensor Based on WO₃ Nanoparticles-Decorated BiFeO₃ Nanoplates. *IEEE Sensors Journal*, 2022, **22**(15), P. 14736–14742.
- [20] Egorysheva A.V., Kraev A.S., Gajtko O.M., Baranchikov A.E., Agafonov A.V., Ivanov V.K. Electrorheological Fluids Based on Bismuth Ferrites BiFeO₃ and Bi₂Fe₄O₉. *Russian Journal of Inorganic Chemistry*, 2020, **65**(8), P. 1253–1263.
- [21] Li Y., Zhang X., Chen L., Sun H., Zhang H., Si W., Wang W., Wang L., Li J. Enhanced magnetic and photocatalytic properties of BiFeO₃ nanotubes with ultrathin wall thickness. *Vacuum*, 2021, **184**, P. 109867.
- [22] Egorysheva A.V., Milenov T.I., Ellert O.G., Avdeev G.V., Rafailov P.M., Efimov N.N., Novotortsev V.M. Magnetic glasseceramics containing multiferroic BiFeO₃ crystals. *Solid State Science*, 2015, **40**, P. 31–35.
- [23] Gao X., Wang Y., Wang Q., Wu X., Zhang W., Zong M., Zhang L. Facile synthesis of a novel flower-like BiFeO₃ microspheres/graphene with superior electromagnetic wave absorption performances. *Ceramics International*, 2019, **45**(3), P. 3325–3332.
- [24] Yastrebov S.G., Lomanova N.A. Specific Features in the Interaction between BiFeO₃ Nanoclusters Synthesized by Solution Combustion. *Technical Physics Letters*, 2021, **47**(1), P. 1–4.
- [25] Alikhanov N.M.-R., Rabadanov M.Kh., Orudzhev F.F., Gadzhimagomedov S.Kh., Emirov R.M., Sadykov S.A., Kallaev S.N., Ramazanov S.M., Abdulvakhidov K.G., Sobola D. Size-dependent structural parameters, optical, and magnetic properties of facile synthesized pure-phase BiFeO₃. *Journal of Materials Science: Materials in Electronics*, 2021, **32**, P. 13323–13335.

- [26] Mhamad S.A., Ali A.A., Mohtar S.S., Aziz F., Aziz M., Jaafar J., Yusof N., Salleh W.N.W., Ismail A.F., Chandren S. Synthesis of bismuth ferrite by sol-gel auto combustion method: Impact of citric acid concentration on its physicochemical properties. *Materials Chemistry and Physics*, 2022, **282**, P. 125983.
- [27] Proskurina O.V., Tomkovich M.V., Bachina A.K., Sokolov V.V., Danilovich D.P., Panchuk V.V., Semenov V.G., Gusarov V.V. Formation of Nanocrystalline BiFeO₃ under Hydrothermal Conditions. *Russian Journal of General Chemistry*, 2017, **87**(11), P. 2507–2515.
- [28] Rouhani Z., Karimi-Sabet J., Mehdipourghazi M., Hadi A., Dastbaz A. Response surface optimization of hydrothermal synthesis of Bismuth ferrite nanoparticles under supercritical water conditions: Application for photocatalytic degradation of Tetracycline. *Environmental Nanotechnology, Monitoring & Management*, 2019, **11**, P. 100198.
- [29] Wang Z.-B., Aldalbahi A., Ahamad T., Alshehri S.M., Feng P.X. Preparation of BiFeO₃ and its photoelectric performance as photoanode of DSSC. *Ceramics International*, 2021, **47**(19), P. 27565–27570.
- [30] Xiaoyan Sun, Zhongwu Liu, Hongya Yu, Zhigang Zheng, Dechang Zeng, Facile synthesis of BiFeO₃ nanoparticles by modified microwave-assisted hydrothermal method as visible light driven photocatalysts. *Materials Letters*, 2018, **219**, P. 225–228.
- [31] Tuluk A., Brouwer H., van der Zwaag S. Controlling the Oxygen Defects Concentration in a Pure BiFeO₃ Bulk Ceramic. *Materials*, 2022, **15**, P. 6509.
- [32] Gil-González E., Perejón A., Sánchez-Jiménez P.E., Sayagués M.J., Raj R., Pérez-Maqueda L.A. Phase-pure BiFeO₃ produced by reaction flash-sintering of Bi₂O₃ and Fe₂O₃. *Journal of Materials Chemistry A*, 2018, **6**(13), P. 5356–5366.
- [33] Carranza-Celis D., Cardona-Rodríguez A., Narváez J., Moscoso-Londono O., Muraca D., Knobel M., Ornelas-Soto N., Reiber A., Ramírez J.G. Control of Multiferroic properties in BiFeO₃ nanoparticles. *Scientific Reports*, 2019, **9**, P. 3182.
- [34] Pedro-García F., Sánchez-De Jesús F., Cortés-Escobedo C.A., Barba-Pingarrón A., Bolarín-Miró A.M. Mechanically assisted synthesis of multi-ferroic BiFeO₃: Effect of synthesis parameters. *Journal of Alloys and Compounds*, 2017, **711**(2004), P. 77–84.
- [35] Selbach S.M., Einarsrud M.-A., Grande T. On the Thermodynamic Stability of BiFeO₃. *Chemistry of Materials*, 2009, **21**(1), P. 169–173.
- [36] Denisov V.M., Belousova N.V., Zhreb V.P., Denisova L.T., Skorikov V.M. Oxide Compounds of Bi₂O₃–Fe₂O₃ System I. The Obtaining and Phase Equilibriums. *Journal of Siberian Federal University. Chemistry*, 2012, **5**(2), P. 146–167.
- [37] Pikula T., Szumiata T., Siedliska K., Mitsiuk V.I., Panek R., Kowalczyk M., Jartych E. The Influence of Annealing Temperature on the Structure and Magnetic Properties of Nanocrystalline BiFeO₃ Prepared by Sol–Gel Method. *Metallurgical and Materials Transactions A*, 2022, **53**, P. 470–483.
- [38] Stankiewicz A.I., Moulijn J.A. Process intensification: Transforming chemical engineering. *Chemical Engineering Progress*, 2000, **96**(1), P. 22–34.
- [39] Abiev R.S. Impinging-Jets Micromixers and Microreactors: State of the Art and Prospects for Use in the Chemical Technology of Nanomaterials (Review). *Theoretical Foundations of Chemical Engineering*, 2020, **54**(6), P. 1131–1147.
- [40] Proskurina O.V., Sivtsov E.V., Enikeeva M.O., Sirotkin A.A., Abiev R.Sh., Gusarov V.V. Formation of rhabdophane-structured lanthanum orthophosphate nanoparticles in an impinging-jets microreactor and rheological properties of sols based on them. *Nanosystems: Physics, Chemistry, Mathematics*, 2019, **10**(2), P. 206–214.
- [41] Baldyga J., Jasińska M., Orciuch W. Barium Sulphate Agglomeration in a Pipe – An Experimental Study and CFD Modeling. *Chemical Engineering & Technology*, 2003, **26**(3), P. 334–340.
- [42] Almjashesha O.V., Popkov V.I., Proskurina O.V., Gusarov V.V. Phase formation under conditions of self-organization of particle growth restrictions in the reaction system. *Nanosystems: Physics, Chemistry, Mathematics*, 2022, **13**(2), P. 164–180.
- [43] Proskurina O.V., Abiev R.S., Danilovich D.P., Panchuk V.V., Semenov V.G., Nevedomskiy V.N., Gusarov V.V. Formation of nanocrystalline BiFeO₃ during heat treatment of hydroxides co-precipitated in an impinging-jets microreactor. *Chemical Engineering and Processing – Process Intensification*, 2019, **143**, P. 107598.
- [44] Lomakin M.S., Proskurina O.V., Abiev R.Sh., Leonov A.A., Nevedomskiy V.N., Voznesenskiy S.S., Gusarov V.V. Pyrochlore phase in the Bi₂O₃–Fe₂O₃–WO₃–(H₂O) system: physicochemical and hydrodynamic aspects of its production using a microreactor with intensively swirled flows. *Advanced Powder Technology*, 2023, **34**, P. 104053.
- [45] Abiev R.Sh., Makusheva I.V. Effect of Macro- and Micromixing on Processes Involved in Solution Synthesis of Oxide Particles in High-Swirl Microreactors. *Theoretical Foundations of Chemical Engineering*, 2022, **56**(2), P. 141–151.
- [46] Proskurina O.V., Sokolova A.N., Sirotkin A.A., Abiev R.Sh., Gusarov V.V. Role of Hydroxide Precipitation Conditions in the Formation of Nanocrystalline BiFeO₃. *Russian Journal of Inorganic Chemistry*, 2021, **66**(2), P. 163–169.
- [47] Proskurina O.V., Abiev R.Sh., Nevedomskiy V.N. Influence of using different types of microreactors on the formation of nanocrystalline BiFeO₃. *Nanosystems: Physics, Chemistry, Mathematics*, 2023, **14**(1), P. 120–126.
- [48] Li X., Tang Z., Ma H., Wu F., Jian R. PVP-assisted hydrothermal synthesis and photocatalytic activity of single-crystalline BiFeO₃ nanorods. *Applied Physics A*, 2019, **125**, P. 598.
- [49] Ortiz-Quiróñez J.L., Díaz D., Zumeta-Dubé I., Arriola-Santamaría H., Betancourt I., Santiago-Jacinto P., Nava-Etzana N. Easy Synthesis of High-Purity BiFeO₃ Nanoparticles: New Insights Derived from the Structural, Optical, and Magnetic Characterization. *Inorganic Chemistry*, 2013, **52**(18), P. 10306–10317.
- [50] Park T.-J., Papaefthymiou G.C., Viescas A.J., Moodenbaugh A.R., Wong S.S. Size-Dependent Magnetic Properties of Single-Crystalline Multiferroic BiFeO₃. *Nanoparticles*, 2007, **7**(3), P. 766–772.
- [51] Lomanova N.A., Tomkovich M.V., Sokolov V.V., Ugolkov V.L., Panchuk V.V., Semenov V.G., Pleshakov I.V., Volkov M.P., Gusarov V.V. Thermal and magnetic behavior of BiFeO₃ nanoparticles prepared by glycine-nitrate combustion. *Journal of Nanoparticle Research*, 2018, **20**, P. 17.
- [52] Freitas V.F., Grande H.L.C., de Medeiros S.N., Santos I.A., Cótica L.F., Coelho A.A. Structural, microstructural and magnetic investigations in high-energy ball milled BiFeO₃ and Bi_{0.95}Eu_{0.05}FeO₃ powders. *Journal of Alloys and Compounds*, 2008, **461**(1-2), P. 48–52.
- [53] Lomanova N.A., Panchuk V.V., Semenov V.G., Pleshakov I.V., Volkov M.P., Gusarov V.V. Bismuth orthoferrite nanocrystals: magnetic characteristics and size effects. *Ferroelectrics*, 2020, **569**(1), P. 240–250.
- [54] Juwita E., Sulistiani F.A., Darmawan M.Y., Istiqomah N.I., Suharyadi E. Microstructural, optical, and magnetic properties and specific absorption rate of bismuth ferrite/SiO₂ nanoparticles. *Materials Research Express*, 2022, **9**, P. 076101.
- [55] Ramazanov S., Sobola D., Orudzhev F., Knapek A., Polcak J., Potocek M., Kaspar M., Dallaev R. Surface Modification and Enhancement of Ferromagnetism in BiFeO₃ Nanofilms Deposited on HOPG. *Nanomaterials*, 2020, **10**(10), P. 1990.
- [56] Thamizharasan G., Eithiraj R.D., Enhtuwshin E., Kim S.J., Sahu N.K., Nayak A.K., Han H.S. Computational and Experimental Study on Electronic Band Structure of Bismuth Ferrite: A Promising Visible Light Photocatalyst. *Ceramist*, 2020, **23**(4), P. 350–357.
- [57] Wang N., Zheng T., Zhang G., Wang P. A review on Fenton-like processes for organic wastewater treatment. *Journal of Environmental Chemical Engineering*, 2016, **4**(1), P. 762–787.
- [58] Mao J., Quan X., Wang J., Gao C., Chen S., Yu H., Zhang Y. Enhanced heterogeneous Fenton-like activity by Cu-doped BiFeO₃ perovskite for degradation of organic pollutants. *Frontiers of Environmental Science & Engineering*, 2018, **12**(6), P. 10.

- [59] Dhanalakshmi R., Muneeswaran M., Vanga P.R.; Ashok M.; Giridharan N.V. Enhanced photocatalytic activity of hydrothermally grown BiFeO₃ nanostructures and role of catalyst recyclability in photocatalysis based on magnetic framework. *Applied Physics A*, 2016, **122**(1), P. 13.
- [60] Liang C., Liu Y., Li K., Wen J., Xing S., Ma Z., Wu Y. Heterogeneous photo-Fenton degradation of organic pollutants with amorphous Fe-Zn-oxide/hydrochar under visible light irradiation. *Separation and Purification Technology*, 2017, **188**, P. 105–111.

Submitted 6 November 2023; revised 20 November 2023; accepted 24 November 2023

Information about the authors:

Olga V. Proskurina – Ioffe Institute, 194021 St. Petersburg, Russia; St. Petersburg State Institute of Technology, 190013 St. Petersburg, Russia; ORCID 0000-0002-2807-375X; proskurinaov@mail.ru

Ksenia I. Babich – Ioffe Institute, 194021 St. Petersburg, Russia; St. Petersburg State Institute of Technology, 190013 St. Petersburg, Russia; ORCID 0009-0000-2239-7721; babich3111@gmail.com

Sofia M. Tikhanova – Ioffe Institute, 194021 St. Petersburg, Russia; St. Petersburg State Institute of Technology, 190013 St. Petersburg, Russia; ORCID 0000-0002-9239-5470; tihanova.sof@gmail.com

Kirill D. Martinson – Ioffe Institute, 194021 St. Petersburg, Russia; St. Petersburg State Institute of Technology, 190013 St. Petersburg, Russia; ORCID 0000-0001-9313-4267; martinsonkirill@mail.ru

Vladimir N. Nevedomskiy – Ioffe Institute, 194021 St. Petersburg, Russia; ORCID 0000-0002-7661-9155; nevedom@mail.ioffe.ru

Valentin G. Semenov – St. Petersburg State University, 26, Universitetsky Ave., Petergof, 198504 St. Petersburg, Russia; ORCID 0000-0002-1530-7289; val_sem@mail.ru

Rufat Sh. Abiev – Ioffe Institute, 194021 St. Petersburg, Russia; St. Petersburg State Institute of Technology, 190013 St. Petersburg, Russia; ORCID 0000-0003-3571-5770; abiev.rufat@gmail.com

Victor V. Gusarov – Ioffe Institute, 194021 St. Petersburg, Russia; ORCID 0000-0003-4375-6388; victor.v.gusarov@gmail.com

Conflict of interest: the authors declare no conflict of interest.

Formation of chrysotile nanotubes with titania in the internal channel

Elmira N. Gatina, Tatiana P. Maslennikova

I. V. Grebenshchikov Institute of Silicate Chemistry, St. Petersburg, Russia

Corresponding author: Elmira N. Gatina, gatina.en@iscras.ru

ABSTRACT The paper studies the influence of titanium-containing compounds on the formation of hydrosilicate nanotubes under hydrothermal conditions. The possibility of titanium ions to enter the crystal structure, and of titania the nanotube channel, has been analyzed. The influence of temperature on the ratio of compounds forming under hydrothermal conditions was determined.

KEYWORDS nanoparticles, nanotubes, chrysotile, lizardite, morphology, hydrothermal synthesis, magnesium titanate, anatase, rutile

ACKNOWLEDGEMENTS TEM was performed by D. A. Kirilenko (the Ioffe Institute) using the equipment of the Joint Research Center 'Materials science and characterization in advanced technology' (Unique project identifier RFMEFI62117X0018). The present work was supported within the framework of the State Assignment No. 1023032900322-9-1.4.3

FOR CITATION Gatina E.N., Maslennikova T.P. Formation of chrysotile nanotubes with titania in the internal channel. *Nanosystems: Phys. Chem. Math.*, 2024, **15** (3), 380–387.

1. Introduction

Both halloysite and chrysotile hydrosilicate nanotubes can be promising for use as fillers of composite materials [1–8], as quasi-one-dimensional and nanotubular particles in modern devices, in technology and medicine [9–22], as well as precursors for the production of new materials [23–32]. Despite the existence of an extensive natural stock of nanotubular halloysite and chrysotile particles [33], their synthetic analogues have a number of advantages. This refers primarily to chrysotile nanotubes, since information on the synthesis of nanotubular halloysite is very limited. Apparently, the synthesis of the halloysite $\text{Al}_2\text{Si}_2\text{O}_5(\text{OH})_4$ compound free from other ions impurities was described for the first time in [34]. The difficulties of synthesizing halloysite and the possibilities of overcoming them were analyzed in [35,36]. The publication of [34] was followed by a number of works [18,37–39], in which halloysite nanotubular particles were also obtained. Theoretical aspects of the formation of crystalline nanotubular structures of any composition and structure were discussed in detail in [40–46]. Still, experimentally, the synthesis of only chrysotile nanotubes of different composition and morphology under different conditions and from different precursors has been studied in more detail [47–58]. Therefore, studies of the behavior and properties of nanotubes depending on their composition, morphological and dimensional parameters, use chrysotile hydrosilicate nanotubes, as a rule [59–61], the synthesis methods and conditions for which are widely presented in the literature [62,63]. One of the advantages of synthetic materials, including nanotubes, compared to the use of natural raw materials, is the possibility of producing them with a strictly specified composition, morphology and particle size [64,65]. Another important advantage of synthetic analogs over natural chrysotile that should also be noted is their significantly lower toxicity, which was shown in [66]. This advantage is especially important because the toxicity of chrysotile often limits its practical use [67–71].

Chrysotile structure is characterized by the possibility of isomorphic substitution of cations in both the octahedral and tetrahedral sublattices. This was noted in many works devoted to both natural minerals [72,73] and synthetically produced nanotubes [48–58,65,74]. At the same time, the high specific surface area, the large thickness of the interlayer gaps, the presence of channels which can also harbor impurity components [75–78], makes the answer to the question about the impurity localization ambiguous, i.e. it can be localized either in the crystal structure (in the octahedral/tetrahedral cation positions), inside the channels, in interlayers, or on the nanotube surface. Depending on their localization, impurity components can affect the structure and properties of nanoparticles in various ways.

Titania may be of significant interest as a modifying additive in the synthesis of chrysotile nanotubes. In [25,79], the titania component was introduced onto the surface of nanotubes by the molecular layering method. In [75,80,81] devoted to the analysis of the natural chrysotile, it was proposed to consider Ti^{4+} ions as isomorphically substituting Mg^{2+} ions localized in the octahedral sublattice. At the same time, a possibility of entrance of a very small amount of titanium ions into the magnesium sublattice was pointed out.

In connection with the above reasons, it is relevant to study the nature of titania impurities localization during the formation of hydrosilicate nanotubes under hydrothermal conditions, including the introduction of titanium-containing additives in the form of various chemical compounds.

2. Experimental

Compounds obtained from the interaction of MgO and TiO₂ taken at 1:1 mole ratio were used as a titania additive for the introduction into the reaction system. The solid-phase synthesis of the additive was carried out by heat treatment of a mixture of MgCO₃ (p.a.) and TiO₂ (as Aldrich anatase). The initial components were mixed in a planetary mill, tablets were pressed and calcinated sequentially at 850, 1100 and 1250 °C.

Magnesium hydrosilicate was synthesized under hydrothermal conditions in aqueous solutions of NaOH with a 0.23 M concentration, isothermal exposure for 24 hours at 300 and 350 °C, and ~ 70 MPa. The components were taken based on the chrysotile Mg₃Si₂O₅(OH)₄ stoichiometry (MgO:SiO₂ = 3:2). MgO (p.a.) and SiO₂ (large fine-porous granular silica gel, GOST 3956-76) were used as the starting components. Additionally, a pre-prepared titanium-containing additive (calculated as about 6 wt. % in terms of titania) was introduced into the reaction medium.

The shape and size of nanoparticles and the nanotube channel filling parameters were determined using the transmission electron microscopy (TEM) on a JEM 2100-F with an accelerating voltage Uac up to 200 kV. Dimensional parameters, morphology and elemental analysis of the samples were also determined by scanning electron microscopy (SEM) and EDX analysis performed on a Tescan Vega 3 SBH (Tescan, Czech Republic) with an EDX analysis attachment (Oxford Instruments, England).

The phase ratio, crystal structure parameters, and crystallite size of the samples were determined using the X-ray powder diffractometry data. These studies were carried out on a DRON-3M X-ray diffractometer (Bourestnik Innovation Center, Russia) in the reflection mode (Bragg–Brentano geometry) using CuKα radiation (λ = 1.54 Å, nickel β-filter). The obtained data were processed and peaks identified using the DFWin software package and the ICDD PDF-2 database, as well as the Rietveld method, and the software described in [82].

The specific surface area was determined from the low-temperature adsorption data (BET method). Measurements were made using a Nova 1200e instrument (Quantochrome).

3. Results and discussion

The X-ray diffraction pattern of a titanium-containing sample after heat treatment at 1250 °C shows that MgTi₂O₅, MgTiO₃, and MgO coexist in it as the main phases (Fig. 1). The ratio of the proportions of all the obtained compounds calculated by the Rietveld method and presented in Table 1, made it possible to determine the Mg:Ti mole ratio as 54:46, which, taking the error of X-ray analysis into account, is close to the (nominal) Mg:Ti ratio of 50:50 specified for the synthesis.

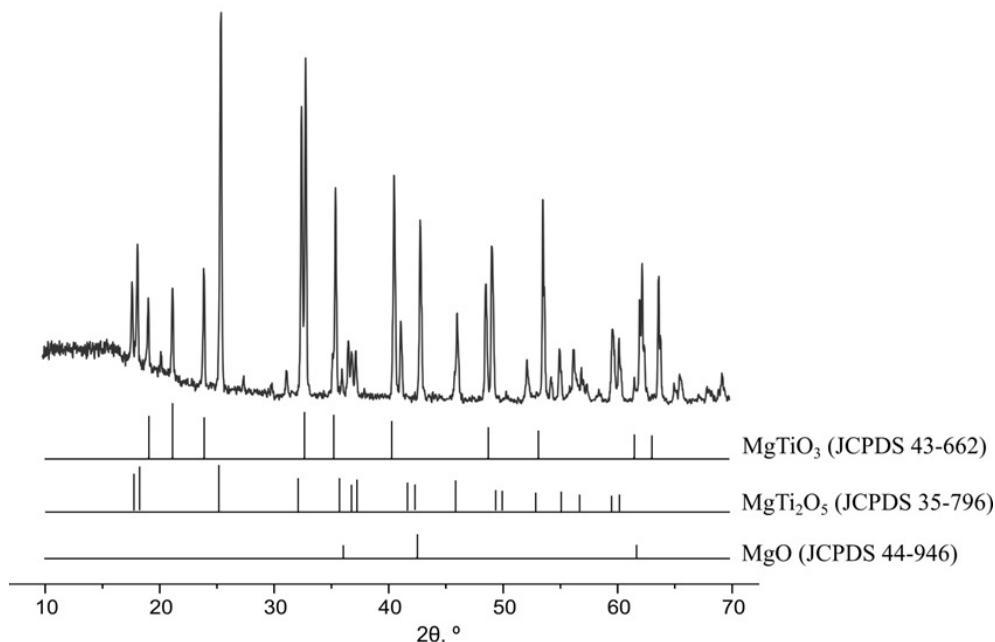


FIG. 1. X-ray diffraction pattern of a sample of the titania additive after heat treatment at 1250 °C. The data on the main compounds detected in the sample are presented as bar diagrams

The X-ray diffractometry data on samples after hydrothermal treatment indicate their multiphase nature; the main peaks are indicated in Fig. 2. The phase ratio calculated from these diffraction patterns shows that the introduction of even a small amount of titanium-containing additive (~ 6 wt.% in terms of titania) into the reaction system significantly affects the phase composition of the reaction products, which varies depending on the hydrothermal treatment temperature (Table 2).

TABLE 1. Phase composition of compounds after heat treatment at 1250 °C according to quantitative X-ray analysis carried out using the software package [82]

Mg:Ti mole ratio (nominal ratio / calculation based on X-ray diffractometry data)	Phase composition according to X-ray diffractometry data, wt. % / mol. %				
	MgTiO ₃	TiO ₂ (rutile)	MgTi ₂ O ₅	Mg ₂ TiO ₄	MgO
50:50 / 54:46	27.0 / 24.9	1.2 / 1.6	51.0 / 28.2	5.7 / 3.9	15.1 / 41.4

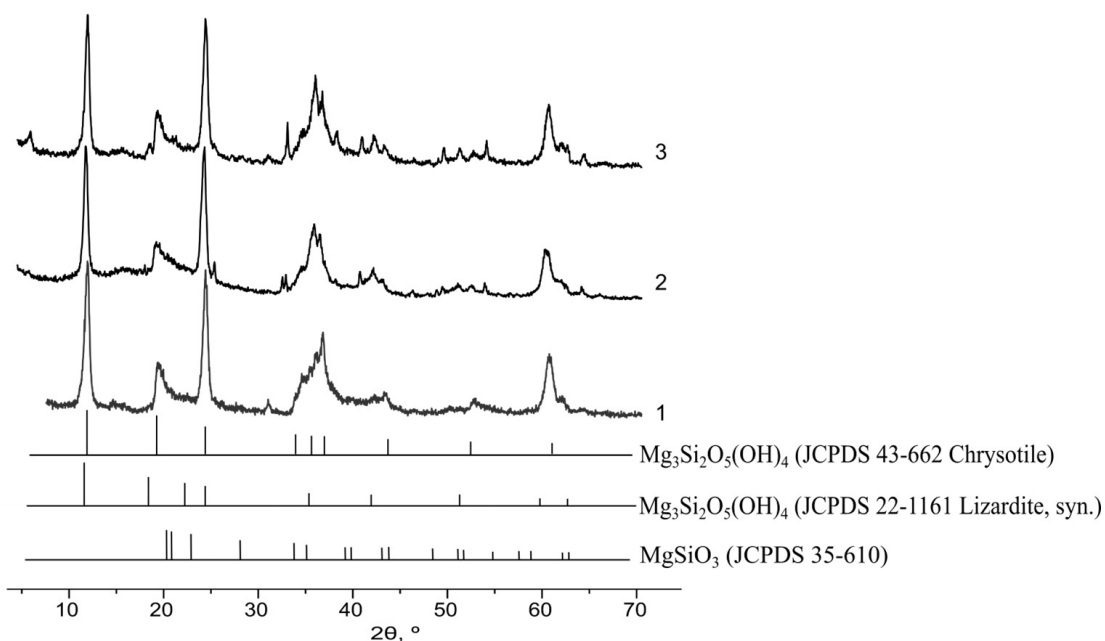


FIG. 2. X-ray diffraction patterns of samples Nos. 1, 2 and 3 (Table 2) after hydrothermal treatment. The data on the main compounds detected in the samples are presented as bar diagrams

TABLE 2. Phase composition of samples Nos. 1, 2 and 3 after hydrothermal treatment under different conditions (T , °C; $P \approx 70$ MPa), according to X-ray diffractometry data

No.	T , °C	Mole ratio of compounds in reaction products, mol. %						
		Mg ₃ Si ₂ O ₅ (OH) ₄ (chrysotile + lizardite)	Mg ₃ Si ₄ O ₁₀ (OH) ₄ (vermiculite)	MgSiO ₃	MgTiO ₃	MgTi ₂ O ₅	TiO ₂ (rutile)	TiO ₂ (anatase)
1	350	100	—	—	—	—	—	—
2	300	93.6	—	1.9	1.6	1.3	1.6	—
3	350	83.8	0.2	12.1	2.7	—	0.2	1.0

Note: sample No. 1 synthesized without addition of titania; samples Nos. 2 and 3 synthesized with the introduction of a titanium-containing oxide additive (~ 6 wt.% in terms of titania)

Comparison of the data given in the Table 3, based on the nominal elemental composition of the samples and determined by different methods, shows their agreement within the error limits of the methods. Therefore, these data allows us to assume that the elemental composition of the samples corresponds to the specified one.

TABLE 3. Mg:Si:Ti mole ratio

Sample No.	Mg:Si:Ti mole ratio		
	Nominal	Calculated from the X-ray diffractometry data	EDX
1	58:42:(-)	58:42:(-)	(63±2):(37±2):(-)
2	57.2:38.9:3.9	59.5:39.3:1.2	—
3	57.2:38.9:3.9	58.7:39.7:1.5	(63.7±1.7):(36.0±1.6):(0.3±0.1)

The size of the rutile-structured titania crystallites calculated from the X-ray diffractometry data for the sample after hydrothermal treatment at 300 °C, was about 8 nm. The sample obtained by hydrothermal treatment at 350 °C had rutile crystallites of ~ 160 nm, and the anatase-structured titania crystallites were about 3 nm.

The differences in the parameter values of unit cells of the chrysotile nanotubes in samples Nos. 1, 2 and 3 do not exceed the error limits of the analytical method. This may be due to the extremely insignificant replacement of magnesium and silicon cations in nanoscrolls with Ti^{4+} ions. This conclusion correlates with the data in [75, 80, 81], in which the entrance of extremely few titanium ions in the magnesium sublattice of natural chrysotile was noted. The slight replacement of magnesium ions with Ti^{4+} ions [75, 80, 81] can be associated with both the difference in their ionic radii ($R_{Mg^{2+(VI)}} = 0.86 \text{ \AA}$, $R_{Ti^{4+(VI)}} = 0.745 \text{ \AA}$ [83]) and with the energy for charge compensation when Mg^{2+} ions are replaced with Ti^{4+} . At the same time, the possibility of some replacement of Si^{4+} with Ti^{4+} ions in the tetrahedral (silicon) sublattice cannot be excluded, although a comparison of the ionic radii $R_{Si^{4+(IV)}} = 0.40 \text{ \AA}$ with $R_{Ti^{4+(IV)}} = 0.56 \text{ \AA}$ [83] shows their significant difference. The ionic radius of Ge^{4+} ions is known to be close to that of Ti^{4+} ions in the tetrahedral position ($R_{Ge^{4+(IV)}} = 0.54 \text{ \AA}$, $R_{Ti^{4+(IV)}} = 0.56 \text{ \AA}$ [83]), and [36] demonstrated the possibility of Si^{4+} cations replacement with Ge^{4+} cations, and stabilization of the nanotubular structure of halloysite, structurally inverse with respect to the chrysotile structure. Both options for the replacement of both magnesium and silicon ions with titanium ions in magnesium hydrosilicate lead to the chrysotile structure destabilization due to a decrease in differences in the size of the octahedral and tetrahedral sublattices and, consequently, to a decrease in the energy effect from the transformation of a flat layer into a cylinder [40, 43]. Apparently, this is related to the fact that even a slight replacement of cations in the structure of magnesium hydrosilicate with Ti^{4+} ions, which is poorly detected by changes in unit cell parameters, leads to a noticeable increase in the lamellar forms of magnesium hydrosilicate according to X-ray diffraction patterns (Fig. 2).

A comparison of the results on the nanoscrolls length distribution, obtained from the scanning electron microscopy data for samples with and without the introduced titanium-containing additive shows that the influence of the additive on the nanoscrolls dimensional parameters is small. A similar statement applies to the effect of the hydrothermal treatment temperature on the outer diameter distribution of nanoscrolls determined from the TEM data.

The TEM data (Fig. 3) show that the channel in a number of nanotubes is partially enriched in a substance containing elements that are heavier than magnesium and silicon. Since only titanium acts as such an element in this case, it is natural to conclude that it is the titanium-containing oxide that is located in the nanotube channel, and since the average crystallite sizes of only titania (rutile-structured after hydrothermal treatment at 300 °C, and anatase-structured after hydrothermal treatment at 350 °C) are comparable with the dimensions of the nanotube channel diameter (Fig. 3), then the nanotubes are filled with titania. During hydrothermal treatment at 300 °C, titania nanoparticles have a structure of rutile with an average crystallite size of about 8 nm. The particles in the channel have an elongated shape that repeats that of the channel with average dimensions of length $L_{TiO_2} \approx 37 \pm 16 \text{ nm}$ and width $d_{TiO_2} \approx 14 \pm 5 \text{ nm}$. For empty nanotubes, the diameter of the internal space (d_0) is $\approx 12 \pm 3 \text{ nm}$. An increase up to 350 °C leads to the localization of the main part of titania in the nanotube channel in the form of anatase with a crystallite size of about 3 nm, and a small part of titania (rutile-structured, with crystallites of about 160 nm) outside the channel. The distribution of nanotubes with the channel unfilled with titania according to their internal diameter is close to bimodal (Fig. 3). The average values of the internal diameter size distribution of these tubes are $d_{0(1)} \approx 17 \pm 3 \text{ nm}$ and $d_{0(2)} \approx 9 \pm 2 \text{ nm}$. The distribution of nanotubes with a TiO_2 -filled channel according to the size of their internal diameter has a clearly defined bimodal character (Fig. 3) with the internal diameter $d_{TiO_2(1)} \approx 17 \pm 4 \text{ nm}$ and $d_{TiO_2(2)} \approx 8 \pm 1 \text{ nm}$. Anatase particles fill the channel in the form of discontinuous inclusions with a length $L_{TiO_2} \approx 42 \pm 3 \text{ nm}$ and a width corresponding to the size of the nanotube inner diameter.

Titania-filled parts of nanotube channels alternate with the unfilled ones (see Fig. 3). Along with that, the characteristic lengths of the titania-filled parts of nanotube channels (L_{TiO_2}) are comparable in length with the unfilled ones. It should

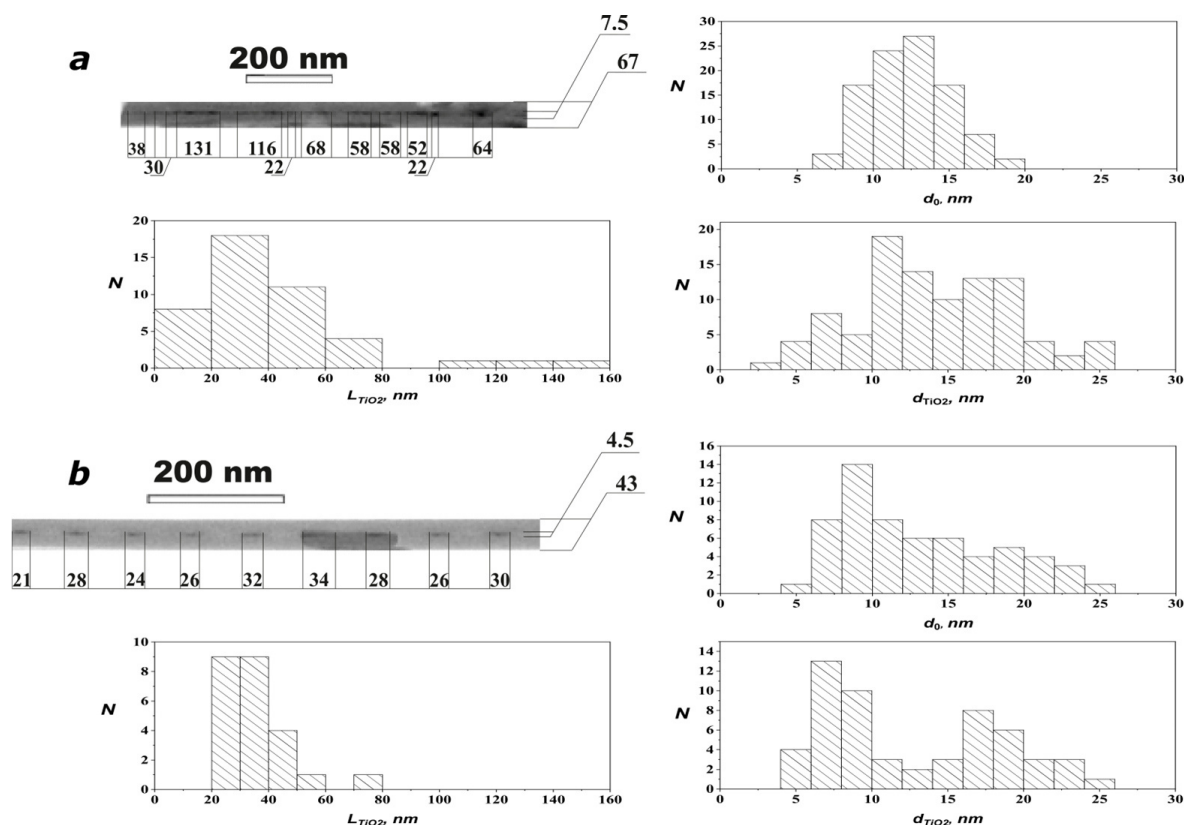


FIG. 3. TEM image of nanotubes with a titania additive obtained under hydrothermal conditions at: a) 300 °C and b) 350 °C, and the corresponding histograms of the length (L_{TiO_2}) distribution of nanotube titania-filled parts, as well as histograms of the internal diameter distribution of the unfilled (d_0), and of the titania-filled (d_{TiO_2}) nanotubes

be noted that the length (L_{TiO_2}) distribution of the titania-filled parts of nanotubes becomes narrower with the increasing temperature of hydrothermal treatment (Fig. 3). Taking into account the differences in the structural state (Table 2) and sizes of titania crystallites in cases of hydrothermal treatment at 300 and 350 °C, it can be concluded that almost all rutile-structured titania is localized inside the nanotube channel at 300 °C, while at 350 °C most of the titania in the form of anatase is located inside the channel, and a smaller part of the rutile-structured crystallites sized at about 160 nm is located outside the nanotube. Differences in the structural state of titania in nanotubes can apparently be associated with an increase in the proportion of nanotubes with a smaller channel diameter with the increase in temperature of hydrothermal treatment, since such changes in the size of spatial restrictions, as was shown in [84], lead to stabilization of the anatase structure of titania.

It is interesting to note that the parameters of intermittent filling (L_{TiO_2} values) of the nanotube channels with titania correlate with the characteristic values of the size of chrysotile nanotube pre-nuclei [32, 85, 86] and with the values of the size of crystallites of which the nanotubes consist, as a rule [87]. This may testify in favor of the aggregation-accommodation mechanism [88] of nanoscrolls formation. It should be noted that the formation and stable existence of the above-described formations can be considered as a synthesis of core-shell type structures, in which the core is titania and the shell is a chrysotile nanotube [89, 90].

Some reduction in the specific surface area of samples obtained with the introduction of titanium-containing additives during the synthesis of hydrosilicate nanotubes under hydrothermal conditions from $S_{N_{o.1}} = 58.9 \text{ m}^2/\text{g}$ for sample No. 1 to $S_{N_{o.2}} = 42.4 \text{ m}^2/\text{g}$ and $S_{N_{o.3}} = 47.3 \text{ m}^2/\text{g}$ for samples Nos. 2 and 3, respectively, can be associated both with the formation of particles of the non-tubular structured compounds (Table 2) with small values of the specific surface area, and with the filling of channels of some part of nanotubes with titania, which prevents the entrance of gas into this channel. However, due to the small values these changes, they cannot be considered critical from the point of view of the use of materials based on such nanotubes in the cases when variations in the specific surface area are not of great importance for the effective functioning of the material.

4. Conclusions

It has been shown that when magnesium titanates are used as an additive in the hydrothermal synthesis of chrysotile, titania forms and localizes in channels of chrysotile nanotubes. At 300 °C of hydrothermal treatment, titania nanoparticles have a rutile structure with an average crystallite size of about 8 nm. The particles in the channel have an elongated shape, repeating that of the channel with average dimensions of length $L_{\text{TiO}_2} \approx 37 \pm 16$ nm and width $d_{\text{TiO}_2} \approx 14 \pm 5$ nm. An increase in the temperature of hydrothermal treatment up to 350 °C leads to the localization of the main part of titania in the nanotube channel in the form of anatase with the crystallite size of about 3 nm, and of a small part of titania outside the channel, with the rutile structure and the crystallite size of about 160 nm. Anatase particles fill the channel as discontinuous formations with sizes $L_{\text{TiO}_2} \approx 42 \pm 3$ nm, $d_{\text{TiO}_2(1)} \approx 17 \pm 4$ nm, and $d_{\text{TiO}_2(2)} \approx 8 \pm 1$ nm.

References

- [1] Gofman I.V., Svetlichnyi V.M., Yudin V.E., Dobrodumov A.V., Didenko A.L., Abalov I.V., Korytkova E.N., Egorov A.I., Gusarov V.V. Modification of films of heat-resistant polyimides by adding hydrosilicate and carbon nanoparticles of various geometries. *Russ. J. Gen. Chem.*, 2007, **77** (7), P. 1158–1163.
- [2] Kononova S.V., Korytkova E.N., Romashkova K.A., Kuznetsov Y.P., Gofman I.V., Svetlichnyi V.M., Gusarov V.V. Nanocomposite based on polyamidoimide with hydrosilicate nanoparticles of varied morphology. *Russ. J. Appl. Chem.*, 2007, **80** (12), P. 2142–2148.
- [3] Yudin V.E., Gladchenko S., Otaigbe J.U., Olson B.G., Nazarenko S., Korytkova E.N., Gusarov V.V. New polyimide nanocomposites based on silicate type nanotubes: Dispersion, processing and properties. *Polymer*, 2007, **48** (5), P. 1306–1315.
- [4] Yudin V.E., Otaigbe J.U., Svetlichnyi V.M., Korytkova E.N., Almjasheva O.V., Gusarov V.V. Effects of nanofiller morphology and aspect ratio on the rheo-mechanical properties of polyimide nanocomposites. *Express Polymer Letters*, 2008, **2** (7), P. 485–493.
- [5] Kononova S.V., Korytkova E.N., Maslennikova T.P., Romashkova K.A., Kruchinina E.V., Potokin I.L., Gusarov V.V. Polymer-inorganic nanocomposites based on aromatic polyamidoimides effective in the processes of liquids separation. *Russ. J. Gen. Chem.*, 2010, **80** (6), P. 1136–1142.
- [6] Yastrebinsky R.N. Nanodisperse hrizotilovy filler for heat-resistant radiation and protective composites. *Int. Research J.*, 2016, **8-3** (50), P. 123–129 (In Russian, abstract in English).
- [7] Kononova S.V., Gubanova G.N., Korytkova E.N., Sapegin D.A. Polymer nanocomposite membranes. *Applied Sciences*, 2018, **8** (7), 1181.
- [8] Kivilcim F.N. Development of halloysite loaded polypropylene sutures with enhanced mechanical and thermal properties. *Cumhuriyet Science J.*, 2023, **44** (1), P. 106–111.
- [9] Yang Y., Liang Q., Li J., Zhuang Y., He Y., Bai B., Wang X. $\text{Ni}_3\text{Si}_2\text{O}_5(\text{OH})_4$ multi-walled nanotubes with tunable magnetic properties and their application as anode materials for lithium batteries. *Nano Res.*, 2011, **4**, P. 882–890.
- [10] Golubeva O.Y., Maslennikova T.P., Ulyanova N.Y., Dyakina M.P. Sorption of lead(II) ions and water vapors by synthetic hydro and aluminosilicates with layered, framework, and nanotube morphology. *Glass Phys. Chem.*, 2014, **40** (2), P. 250–255.
- [11] Cheng L., Zhai L., Liao W., Huang X., Niu B., Yu Sh. An investigation on the behaviors of thorium(IV) adsorption onto chrysotile nanotubes. *J. Environ. Chem. Eng.*, 2014, **2** (3), P. 1236–1242.
- [12] Yuan P., Tan D., Annabi-Bergaya F. Properties and applications of halloysite nanotubes: recent research advances and future prospects. *Appl. Clay Sci.*, 2015, **112–113**, P. 75–93.
- [13] Bian Z., Li Z., Ashok J., Kawi S. A Highly active and stable Ni–Mg phyllosilicate nanotubular catalyst for ultrahigh temperature water-gas shift reaction. *Chem. Commun.*, 2015, **51**, P. 16324–16326.
- [14] Chernyayev A.V., Mikhailin N.Y., Shamsur D.V., Kumzerov Y.A., Fokin A.V., Kalmykov A.E., Parfen'ev R.V., Sorokin L.M., Lashkul A. Electrical and magnetic properties of Pb and In nanofilaments in asbestos near the superconducting transition. *Physics of the Solid State*, 2018, **60** (10), P. 1935–1941.
- [15] López-Salinas E., Toledo-Antonio J.A., Manríquez M.E., Sánchez-Cantú M., Cruz Ramos I., Hernández-Cortez J.G. Synthesis and catalytic activity of chrysotile-type magnesium silicate nanotubes using various silicate sources. *Micropor. Mesopor. Mater.*, 2019, **274**, P. 176–182.
- [16] Krasilin A.A., Straumal E.A., Yurkova L.L., Khrapova E.K., Tomkovich M.V., Shunina I.G., Vasil'eva L.P., Lermontov S.A., Ivanov V.K. Sulfated halloysite nanoscrolls as superacid catalysts for oligomerization of hexene-1. *Russ. J. Appl. Chem.*, 2019, **92** (9), P. 1251–1257.
- [17] Khrapova E.K., Ezhov I.S., Rumyantsev A.M., Zhdanov V.V., Krasilin A.A. Nanotubular nickel hydrosilicate and its thermal annealing products as anode materials for lithium ion batteries. *Inorg. Mater.*, 2020, **56** (12), P. 1248–1257.
- [18] Golubeva O.Yu., Alikina Y.A., Kalashnikova T.A. Influence of hydrothermal synthesis conditions on the morphology and sorption properties of porous aluminosilicates with kaolinite and halloysite structures. *Appl. Clay Sci.*, 2020, **199**, 105879.
- [19] Khrapova E.K., Ugolkov V.L., Straumal E.A., Lermontov S.A., Lebedev V.A., Kozlov D.A., Krasilin A.A. Thermal behavior of Mg-Ni-phyllosilicate nanoscrolls and performance of the resulting composites in hexene-1 and acetone hydrogenation. *Chem. Nano Mat.*, 2020, **7** (3), P. 257–269.
- [20] Liu Z.Y., Zeng H., Wang L., Zhang Q., Wu P., Liu X., Xie H., Xiang W., Liu B., Liu J., Liu X., Xie J., Tang J., Long Z., He L., Xiao M., Xiang L., Cao K. Fe-doped chrysotile nanotubes containing siRNAs to silence SPAG5 to treat bladder cancer. *J. Nanobiotechnol.*, 2021, **19** (1), 189.
- [21] Yada M., Tabata M., Furukawa M. Synthesis and characterization of chrysotile/erythrosine composite to detect asbestos. *J. of the Ceramic Society of Japan*, 2023, **131** (12), P. 906–911.
- [22] Long Q., Yan H., Zhou X., Qiu S., Qiu T. Adsorption and desorption characteristics of rare earth ions on halloysite surfaces. *Physicochem. Probl. Miner. Process*, 2024, **60** (1), 185763.
- [23] Vezenstev A.I., Neiman S.M., Gudkova E.A. Transformations and changes in the properties of chrysotile asbestos under the influence of various factors. *Construction Materials*, 2006, **6**, P. 104–105 (In Russian).
- [24] Malkov A.A., Korytkova E.N., Maslennikova T.P., Shtykova A.M., Gusarov V.V. Effect of heat treatment on structural-chemical transformations in magnesium hydrosilicate $\text{Mg}_3\text{Si}_2\text{O}_5(\text{OH})_4$ nanotubes. *Russ. J. Appl. Chem.*, 2009, **82** (12), P. 2079–2086.
- [25] Kumzerov Yu.A., Naberezhnov A.A. Effect of restricted geometry on superconducting properties of low-melting metals (Review). *Low Temperature Physics*, 2016, **42** (11), P. 1028–1040.
- [26] Gaaz T.S., Sulong A.B., Kadhum A.A.H., Nassir M.H., Al-Amiery A.A. Surface improvement of halloysite nanotubes. *Appl. Sci.*, 2017, **7** (3), 291.
- [27] Krasilin A.A., Bodalyov I.S., Malkov A.A., Khrapova E.K., Maslennikova T.P., Malygin A.A. On an adsorption/photocatalytic performance of nanotubular $\text{Mg}_3\text{Si}_2\text{O}_5(\text{OH})_4/\text{TiO}_2$ composite. *Nanosystems: Phys. Chem. Math.*, 2018, **9** (3), P. 410–416.
- [28] Bloise A., Catalano M., Gualtieri A.F. Effect of grinding on chrysotile, amosite and crocidolite and implications for thermal treatment. *Minerals*, 2018, **8** (4), 135.

- [29] Krasilin A.A., Danilovich D.P., Yudina E.B., Bruyere S., Ghanbaja J., Ivanov V.K. Crystal violet adsorption by oppositely twisted heat-treated halloysite and pecoraite nanoscrolls. *Appl. Clay Sci.*, 2019, **173**, P. 1–11.
- [30] Belotitskii V.I., Fokin A.V., Kumzerov Y.A., Syssoeva A.A. Optical properties of nanowires synthesized in regular nanochannels of porous matrices. *Opt. Quant. Electron.*, 2020, **52** (4), 218.
- [31] Krasilin A., Khalisov M., Khrapova E., Ugolkov V., Enyashin A., Ankudinov A. Thermal treatment impact on the mechanical properties of $Mg_3Si_2O_5(OH)_4$ Nanoscrolls. *Materials*, 2022, **15** (24), 9023.
- [32] Maslennikova T.P., Gatina E.N., Kotova M.E., Ugolkov V.L., Abiev R.Sh., Gusarov V.V. Formation of magnesium hydrosilicate nanoscrolls with the chrysotile structure from nanocrystalline magnesium hydroxide and their thermally stimulated transformation. *Inorg. Mater.*, 2022, **58** (11), P. 1152–1161.
- [33] Krivovichev S.V. Nanotubes in Minerals and Mineral-Related Systems. *Minerals as Advanced Materials I*, ed. Krivovichev S., 2008, P. 179–191.
- [34] Maslennikova T.P., Korytkova E.N., Pivovarova L.N. Hydrothermal synthesis of nanotube composition $Al_2Si_2O_5(OH)_4 \cdot 2H_2O$ with halloysite structure. *Glass Phys. Chem.*, 2012, **S6**, P. 890–893.
- [35] Krasilin A.A., Gusarov V.V. Control over morphology of magnesium-aluminum hydrosilicate nanoscrolls. *Russ. J. Appl. Chem.*, 2015, **88** (12), P. 1928–1935.
- [36] Krasilin A.A. Energy modeling of competition between tubular and platy morphologies of chrysotile and halloysite layers. *Clays and Clay Minerals*, 2020, **68** (5), P. 436–445.
- [37] White R.D., Bavykin D.V., Walsh F.C. Spontaneous scrolling of kaolinite nanosheets into halloysite nanotubes in an aqueous suspension in the presence of GeO_2 . *J. Phys. Chem. C*, 2012, **116**, P. 8824–8833.
- [38] Golubeva O.Y. Effect of synthesis conditions on hydrothermal crystallization, textural characteristics and morphology of aluminium-magnesium montmorillonite. *Micropor. Mesopor. Mater.*, 2016, **224**, P. 271–276.
- [39] Leonov N.A., Kozlov D.A., Kirilenko D.A., Bert N.A., Pelageikina A.O., Nechitailov A.A., Alikin M.B., Krasilin A.A. Formation of a 10 Å phase with halloysite structure under hydrothermal conditions with varying initial chemical composition. *Nanosystems: Phys. Chem. Math.*, 2023, **14** (2), P. 264–271.
- [40] Chivilikhin S.A., Popov I.Y., Gusarov V.V. Dynamics of nanotube twisting in a viscous fluid. *Doklady Physics*, 2007, **52** (1), P. 60–62.
- [41] Chivilikhin S.A., Popov I.Y., Svitenkov A.I., Chivilikhin D.S., Gusarov V.V. Formation and evolution of nanoscroll ensembles based on layered-structure compounds. *Doklady Physics*, 2009, **54** (11), P. 491–493.
- [42] Chivilikhin S.A., Popov I.Y., Bogdanov M.S., Lesnichii V.V., Gusarov V.V. Hydrodynamics of nanorolling. *Russ. Phys. J.*, 2009, **52** (11), P. 1117–1120.
- [43] Krasilin A.A., Gusarov V.V. Energy of formation of chrysotile nanotubes. *Russ. J. Gen. Chem.*, 2014, **84** (12), P. 2359–2363.
- [44] Krasilin A.A., Gusarov V.V. Energy model of bilayer nanoplate scrolling: Formation of chrysotile nanoscroll. *Russ. J. Gen. Chem.*, 2015, **85** (10), P. 2238–2241.
- [45] Krasilin A.A., Gusarov V.V. Energy model of radial growth of a nanotubular crystal. *Technical Physics Letters*, 2016, **42** (1), P. 55–58.
- [46] Krasilin A.A., Nevedomsky V.N., Gusarov V.V. Comparative energy modeling of multi-walled $Mg_3Si_2O_5(OH)_4$ and $Ni_3Si_2O_5(OH)_4$ nanoscrolls growth. *J. Phys. Chem. C*, 2017, **121** (22), P. 12495–12502.
- [47] Korytkova E.N., Pivovarova L.N. Hydrothermal synthesis of nanotubes based on $(Mg,Fe,Co,Ni)_3Si_2O_5(OH)_4$ hydrosilicates. *Glass Phys. Chem.*, 2010, **36** (1), P. 53–60.
- [48] Korytkova E.N., Maslov A.V., Pivovarova L.N., Drozdova I.A., Gusarov V.V. Formation of $Mg_3Si_2O_5(OH)_4$ nanotubes under hydrothermal conditions. *Glass Phys. Chem.*, 2004, **30** (1), P. 51–55.
- [49] Korytkova E.N., Maslov A.V., Pivovarova L.N., Polegotchenkova Y.V., Povinich V.F., Gusarov V.V. Synthesis of nanotubular $Mg_3Si_2O_5(OH)_4$ – $Ni_3Si_2O_5(OH)_4$ silicates at elevated temperatures and pressures. *Inorg. Mater.*, 2005, **41** (7), P. 743–749.
- [50] Korytkova E.N., Pivovarova L.N., Semenova O.E., Drozdova I.A., Povinich V.F., Gusarov V.V. Hydrothermal synthesis of nanotubular Mg-Fe hydrosilicate. *Russ. J. Inorg. Chem.*, 2007, **52** (3), P. 338–344.
- [51] Korytkova E.N., Pivovarova L.N., Drozdova I.A., Gusarov V.V. Hydrothermal synthesis of nanotubular Co-Mg hydrosilicates with the chrysotile structure. *Russ. J. Gen. Chem.*, 2007, **77** (10), P. 1669–1676.
- [52] Korytkova E.N., Semyashkina M.P., Maslennikova T.P., Pivovarova L.N., Al'myashhev V.I., Ugolkov V.L. Synthesis and growth of nanotubes $Mg_3Si_2O_5(OH,F)_4$ composition under hydrothermal conditions. *Glass Phys. Chem.*, 2013, **39** (3), P. 294–300.
- [53] Krasilin A.A., Suprun A.M., Gusarov V.V. Influence of component ratio in the compound $(Mg,Fe)_3Si_2O_5(OH)_4$ on the formation of nanotubular and plate like particles. *Russ. J. Appl. Chem.*, 2013, **86**, P. 1633–1637.
- [54] Krasilin A.A., Suprun A.M., Nevedomsky V.N., Gusarov V.V. Formation of conical $(Mg,Ni)_3Si_2O_5(OH)_4$ nanoscrolls. *Dokl. Phys. Chem.*, 2015, **460** (2), P. 42–44.
- [55] Krasilin A.A., Panchuk V.V., Semenov V.G., Gusarov V.V. Formation of variable-composition iron(III) hydrosilicates with the chrysotile structure. *Russ. J. Gen. Chem.*, 2016, **86** (12), P. 2581–2588.
- [56] Krasilin A.A., Suprun A.M., Ubyivovk E.V., Gusarov V.V. Morphology vs. chemical composition of single Ni-doped hydrosilicate nanoscroll. *Materials Letters*, 2016, **171**, P. 68–71.
- [57] Krasilin A.A., Gusarov V.V. Redistribution of Mg and Ni cations in crystal lattice of conical nanotube with chrysotile structure. *Nanosystems: Phys. Chem. Math.*, 2017, **8** (5), P. 620–627.
- [58] Krasilin A.A., Khrapova E.K., Nomine A., Ghanbaja J., Belmonte T., Gusarov V.V. Cations redistribution along the spiral of Ni-doped phyllosilicate nanoscrolls: energy modelling and STEM/EDS study. *Chem. Phys. Chem.*, 2019, **20** (5), P. 719–726.
- [59] Kumzerov Y.A. Parfenyeva L.S., Smirnov I.A., Krivchikov A.I., Zvyagina G.A., Fil V.D., Misiorek H., Mukha Y., Ezhovsky A. Thermal and acoustic properties of chrysotile asbestos. *Phys. Solid State*, 2005, **47** (2), 370.
- [60] Malkov A.A., Korytkova E.N., Maslennikova T.P., Shtykhova A.M., Gusarov V.V. Effect of heat treatment on structural-chemical transformations in magnesium hydrosilicate $[Mg_3Si_2O_5(OH)_4]$ nanotubes. *Russ. J. Appl. Chem.*, 2009, **82** (12), P. 2079–2086.
- [61] Khrapova E.K., Ugolkov V.L., Straumal E. A., Lermontov S.A., Lebedev V.A., Kozlov D.A., Kunkel T.S., Nomine A., Bruyere S., Ghanbaja J., Belmonte T., Krasilin A.A. Front Cover: Thermal behavior of Mg-Ni-phyllosilicate nanoscrolls and performance of the resulting composites in hexene-1 and acetone hydrogenation. *Chem. Nano Mat.*, 2021, **7** (3), P. 257–269.
- [62] Korytkova E.N., Pivovarova L.N., Gusarov V.V. Influence of iron on the kinetics of formation of chrysotile nanotubes of composition $(Mg,Fe)_3Si_2O_5(OH)_4$ under hydrothermal conditions. *Geochemistry Int.*, 2007, **45** (8), P. 825–831.
- [63] Lafay R., Montes-Hernandez G., Janots E., Chiriac R., Findling N., Toche F. Nucleation and growth of chrysotile nanotubes in $H_2SiO_3/MgCl_2/NaOH$ medium at 90 to 300 °C. *Chem. Eur. J.*, 2013, **19** (17), P. 5417–5424.
- [64] Anuradha G., Esha B.S. A Descriptive review on nanosponges in novel drug delivery, synthetic methods, advantages and applications. *Int. J. of Pharmaceutical Sciences and Nanotechnology*, 2023, **16** (4), P. 6932–6941.

- [65] Krasilin A.A., Khrapova E.K., Maslennikova T.P. Review: Cation doping approach for nanotubular hydrosilicates curvature control and related applications. *Crystals*, 2020, **10** (8), P. 654–695.
- [66] Skuland T., Maslennikova T., Låg M., Gatina E., Serebryakova M.K., Trulioff A.S., Kudryavtsev I.V., Klebnikova N., Kruchinina I., Schwarze P.E., Refsnes M. Synthetic hydrosilicate nanotubes induce low pro-inflammatory and cytotoxic responses compared to natural chrysotile in lung cell cultures. *Basic Clin Pharmacol Toxicol.*, 2020, **126** (4), P. 374–388.
- [67] Vezentsev A.I., Smolikov A.A., Pylev L.N., Vasilyeva L.A. Preparation of chrysotile asbestos and its isomorphous analogues and assessment of their carcinogenic activity. *J. of Environmental Chemistry*, 1993, **2**, P. 127–113 (In Russian).
- [68] Bernstein D.M., Hoskins J.A. The health effects of chrysotile: current perspective based upon recent data. *Regul. Toxicol. Pharm.*, 2006, **45** (3), P. 252–264.
- [69] Pylev L.N., Smirnova O.V., Vasil'eva L.A., Vezentsev A.I., Gudkova E.A., Naumova L.N., Neiman S.M. Impact of modification of the fiber surface of chrysotile on its biological activity. *Gig Sanit*, 2007, **2**, P. 77–80 (In Russian).
- [70] Gazzano E., Turci F., Foresti E., Putzu M. G., Aldieri E., Silvagno F., Lesci I.G., Tomatis M., Riganti C., Romano C., Fubini B., Roveri N., Ghigo D. Iron-loaded synthetic chrysotile: a new model solid for studying the role of iron in asbestos toxicity. *Chem. Res. Toxicol.*, 2007, **20** (3), P. 380–387.
- [71] Vezentsev A.I., Pylev L.N., Poutlyayev V.I., Knot'ko A.V., Naumova L.N., Goudkova E.A., Smirnova O.V. Increase the ecological safety of chrysotile-asbestos due to action of Portland cement hydration. *Ecology and Industry of Russia*, 2009, **7**, P. 34–37 (In Russian).
- [72] Liu X., Ma Y., Yan W., He M., Li L., Sui X., Peng B. Identify key serpentines antigorite, lizardite and chrysotile with various compositions and crystallographic orientations using micro-Raman spectroscopy. *Solid Earth Sciences*, 2023, **8** (4).
- [73] Ono Y., Kikuchi N., Watanabe H. Preparation of nickel catalyst from nickel containing chrysotile. *Studies in Surface Science and Catalysis*, 1987, **31**, P. 519–529.
- [74] Bloise A. Growth and Hydrothermal alteration of silicates doped with Ti^{4+} , Ni^{2+} : synthesis of Ni-, Ti-, Fe-serpentine phases. *Plinies*, 2006, **32**, P. 70–75.
- [75] Maslennikova T.P., Korytkova E.N., Gusarov V.V. Interaction of $Mg_3Si_2O_5(OH)_4$ nanotubes with potassium hydroxide. *Russ. J. Appl. Chem.*, 2008, **81** (3), P. 375–379.
- [76] Bloise A., Barrese E., Apollaro C. Hydrothermal alteration of Ti-doped forsterite to chrysotile and characterization of the resulting chrysotile fibers. *Neues Jahrbuch für Mineralogie – Abhandlungen*, 2009, **185** (3), P. 972–304.
- [77] Maslennikova T.P., Korytkova E.N. Aqueous solutions of cesium salts and cesium hydroxide in hydrosilicate nanotubes of the $Mg_3Si_2O_5(OH)_4$ composition. *Glass Phys. Chem.*, 2010, **36** (3), P. 345–350.
- [78] Maslennikova T.P., Gatina E.N. Modification of $Mg_3Si_2O_5(OH)_4$ nanotubes by magnetite nanoparticles. *Glass Phys. Chem.*, 2016, **43** (3), P. 257–262.
- [79] Bodalyov I.S., Malkov A.A., Korytkova E.N., Maslennikova T.P., Malygin A.A. Temperature factor in interaction of nanotubular magnesium hydrosilicate, $Mg_3Si_2O_5(OH)_4$, with titanium tetrachloride and water vapors. *Russ. J. Appl. Chem.*, 2014, **87** (2), P. 151–159.
- [80] Maslennikova T.P., Korytkova E.N., Gatina E.N., Pivovarova L.N. Effect of temperature on the synthesis of nanoparticles with different morphology in the system $MgO-SiO_2-TiO_2-H_2O$ under hydrothermal conditions. *Glass Phys. Chem.*, 2016, **42** (6), P. 627–630.
- [81] Maslennikova T.P., Gatina E.N. Hydrothermal synthesis of Ti-doped nickel hydrosilicates of various morphologies. *Russ. J. Appl. Chem.*, 2018, **91** (2), P. 286–291.
- [82] Bubnova R.S., Firsova V.A., Volkov S.N., Filatov S.K. RietveldToTensor: program for processing powder X-Ray diffraction data under variable conditions. *Glass Phys. Chem.*, 2018, **44** (1), P. 33–40.
- [83] Shannon R.D. Revised effective ionic radii and systematic studies of interatomic distances in halides and chalcogenides. *Acta Crystallographica Section A*, 1976, **32**, P. 751–767.
- [84] Almjasheva O.V. Formation and structural transformations of nanoparticles in the TiO_2-H_2O system. *Nanosystems: Phys. Chem. Math.*, 2016, **7** (6), P. 1031–1049.
- [85] Sharikov F. Y., Korytkova E. N., Gusarov V.V. Effect of the thermal prehistory of components on the hydration and crystallization of $Mg_3Si_2O_5(OH)_4$ nanotubes under hydrothermal conditions. *Glass Phys. Chem.*, 2007, **33** (5), P. 515–520.
- [86] Krasilin A.A., Almjasheva O.V., Gusarov V.V. Effect of the structure of precursors on the formation of nanotubular magnesium hydrosilicate. *Inorg. Mater.*, 2011, **47** (10), P. 1111–1115.
- [87] Levin A., Khrapova E., Kozlov D., Krasilin A., Gusarov V. Structure refinement, microstrains and crystallite sizes of Mg-Ni-phyllsilicate nanoscroll powders. *J. Appl. Cryst.*, 2022, **55** (3), P. 484–502.
- [88] Almjasheva O.V., Gusarov V.V. Metastable clusters and aggregative nucleation mechanism. *Nanosystems: Phys. Chem. Math.*, 2014, **5**(3), P. 405–416.
- [89] Almjasheva O.V., Krasilin A.A., Gusarov V.V. Formation mechanism of core-shell nanocrystals obtained via dehydration of coprecipitated hydroxides at hydrothermal conditions. *Nanosystems: Phys. Chem. Math.*, 2018, **9** (4), P. 568–572.
- [90] Almjasheva O.V., Popkov V.I., Proskurina O.V., Gusarov V.V. Phase formation under conditions of self-organization of particle growth restrictions in the reaction system. *Nanosystems: Phys., Chem. Math.*, 2022, **13** (2), P. 164–180.

Submitted 22 November 2023; revised 25 December 2023; accepted 26 December 2023

Information about the authors:

Elmira N. Gatina – I. V. Grebenshchikov Institute of Silicate Chemistry of the Russian Academy of Sciences, 2 Makarova Emb., 199034, St. Petersburg, Russia; ORCID 0000-0001-9294-4428; gatina.en@iscras.ru

Tatiana P. Maslennikova – I. V. Grebenshchikov Institute of Silicate Chemistry of the Russian Academy of Sciences, 2 Makarova Emb., 199034, St. Petersburg, Russia; ORCID 0000-0002-0872-7592; maslennikova.tp@iscras.ru

Conflict of interest: the authors declare no conflict of interest.

Copper-modified g-C₃N₄/TiO₂ nanostructured photocatalysts for H₂ evolution from glucose aqueous solution

Sofiya N. Kharina^a, Anna Yu. Kurenkova^b, Andrey A. Saraev^c, Evgeny Yu. Gerasimov^d, Ekaterina A. Kozlova^e

Boreskov Institute of Catalysis SB RAS, Novosibirsk, Russia

^askharina@catalysis.ru, ^bkurenkova@catalysis.ru, ^casaraev@catalysis.ru, ^dgerasimov@catalysis.ru, ^ekozlova@catalysis.ru

Corresponding author: Sofiya N. Kharina, skharina@catalysis.ru

ABSTRACT Two strategies for synthesis of copper-modified composite photocatalysts based on graphitic carbon nitride and titanium dioxide for hydrogen evolution reaction are presented. The first one is based on the mechanical dispersion of separately prepared g-C₃N₄ and commercial TiO₂ (Evonik P25), modified with copper. Another approach is co-calcination of melamine and commercial TiO₂ with subsequent modification by copper. The samples were characterized using X-ray diffraction (XRD), UV-vis diffuse reflectance spectroscopy (UV-vis DRS), X-ray photoelectron spectroscopy (XPS), and high-resolution transmission electron microscopy (HRTEM). The synthesized photocatalysts were tested in hydrogen evolution from glucose aqueous solution under visible light irradiation (440 nm). The largest photocatalytic activities met 235 and 259 μmol·g⁻¹·h⁻¹, corresponding to the first and the second photocatalyst series, respectively. The most active photocatalyst from the first series 1 wt.% g-C₃N₄/1 wt.% CuO_n/TiO₂ maintained its hydrogen production rate during a 6-hour cyclic stability test.

KEYWORDS photocatalysis, photocatalytic H₂ production, biomass photoreforming, glucose photoconversion, composite photocatalysts, titanium dioxide, graphitic carbon nitride, visible light irradiation

ACKNOWLEDGEMENTS This study was supported by Russian Science Foundation, project No. 23-73-01161. Authors thank to A. V. Zhurenok for UV-Vis spectra measurements and D. D. Mishchenko for XRD analysis.

FOR CITATION Kharina S.N., Kurenkova A.Yu., Saraev A.A., Gerasimov E.Yu., Kozlova E.A. Copper-modified g-C₃N₄/TiO₂ nanostructured photocatalysts for H₂ evolution from glucose aqueous solution. *Nanosystems: Phys. Chem. Math.*, 2024, **15** (3), 388–397.

1. Introduction

To overcome the energy shortage and ensure the sustainable development of mankind, the use of hydrogen as an energy carrier rather than traditional fuels is considered to be the most reasonable trend. Despite the fact that hydrogen is mainly produced from non-renewable sources such as coal and natural gas, more attention must be paid to the use of renewable energy sources. The promising approach is the photoreforming of biomass. Its key advantages are simplicity, low operating cost, non-requirement of high pressure and temperature during the treatment and wide variety of catalysts [1, 2]. Moreover, this technique is not only based on solar energy inputs and inexhaustible biomass substrates, but could use the byproducts from industrial biomass conversion, e.g. alcohols (methanol, ethanol, glycerol, isopropanol), carboxylic acids (lactic, formic, acetic) mono-, di- and polysaccharides [3–11]. Although biomass-derived products have long been utilized as an energy source, they are often used for hydrogen production through high-energy consuming thermochemical or low-efficiency biorefinery processes. Therefore, developing an effective photoreforming process does remain of the great demand.

Titanium dioxide being one of the best n-type semiconducting and widely studied photocatalysts has been employed for various applications [12–14]. Providing its strong oxidizing and moderate reducing abilities, the band structure of TiO₂ limits its activity within the UV range. To shift its light absorption edge to a greater wavelength region, the use is made of visible light sensitive semiconductors. This helpful strategy is to obtain the heterostructure, which contains TiO₂ and some narrow-band gap semiconducting material intimately connected. The formation of heterojunction between two semiconductors leads to increased charge separation and, therefore, to higher light absorption efficiency [15–17].

Among the vary of prospective narrow band semiconductors [18, 19], graphitic carbon nitride g-C₃N₄ is believed to be a promising candidate. Its narrow band gap (2.7 eV) and the strongly negative conduction band position (–1.3 eV vs. NHE) make g-C₃N₄ an effective material for proton reduction with hydrogen formation under visible light [20–22]. In comparison with traditional photocatalysts being active under visible radiation – metal chalcogenides, the important advantages of g-C₃N₄ are non-toxicity and outstanding chemical and thermal stability (up to 600 °C) [23]. As many other

pristine semiconductors $g\text{-C}_3\text{N}_4$ suffers from the fast charge-carrier recombination, which restrains its application. To increase the life time of photogenerated charge carriers, a lot of efforts has been made to synthesize the composites based on $g\text{-C}_3\text{N}_4$ and wide bandgap semiconductors such as TiO_2 . Such strategy allows one to promote the charge separation and increase their lifetime.

There are multiple photocatalytic applications where $g\text{-C}_3\text{N}_4/\text{TiO}_2$ is utilized [24], with H_2 production being among them. For instance, Hongjian [16] fabricated $g\text{-C}_3\text{N}_4/\text{TiO}_2$ by ball-milling, after than 0.5 wt.% Pt cocatalyst was photodeposited on the composite. The photocatalyst 50 % $g\text{-C}_3\text{N}_4/\text{TiO}_2$ has demonstrated the greatest H_2 production rate ($22.4 \text{ mol}\cdot\text{h}^{-1}$), which is twice as higher as unmodified $g\text{-C}_3\text{N}_4$. Another effective technique to modify semiconductor photocatalyst and increase the life time of photogenerated electrons and holes is the deposition of metal particles, such as Pt, Ni, Cu, etc., which act as electron mediators between two semiconductors. Bo Chai and colleagues [15] have developed $g\text{-C}_3\text{N}_4/\text{Pt}/\text{TiO}_2$ nanocomposite via a facile chemical adsorption followed by a calcination process. As a sacrificial agent the use was made of triethanolamine (TEOA) – one of the most effective electron donors for $g\text{-C}_3\text{N}_4$ -based photocatalysts. The results have revealed the H_2 production rate rising with the increasing of $g\text{-C}_3\text{N}_4$ content and the activity reaching the maximum – $178 \mu\text{mol}\cdot\text{h}^{-1}$ for the photocatalyst, which contains 30 % $g\text{-C}_3\text{N}_4$ loaded on Pt/TiO_2 . A comprehensive study [17] has been carried out on ternary $\text{CdS}/\text{TiO}_2/g\text{-C}_3\text{N}_4$ composites applied both in H_2 evolution and dye degradation processes. The authors have reported that the system accomplishes an S-scheme heterojunction, which leads to enhanced photocatalyst activity compared to the individual components.

Despite the examples mentioned above, there is still insufficient information on studies that aim to expand the application area of $g\text{-C}_3\text{N}_4$ and its activation for photocatalytic H_2 production from biomass components. The article presented compares two different synthetic approaches for composite photocatalysts based on $g\text{-C}_3\text{N}_4$ and TiO_2 for H_2 generation from glucose aqueous solutions under visible light irradiation (440 nm). The main purpose of this work is to determine the effect of $g\text{-C}_3\text{N}_4$ loading on the photocatalytic activity of TiO_2 under visible light. Additionally, two synthetic strategies are proposed and their comparison is discussed herein. In our previous study [25] the influence of copper cocatalyst particles dispersed on TiO_2 was comprehensively discussed and it was found that CuO_n ($n = 0.5 - 1$) enhanced the photocatalytic H_2 evolution rate over TiO_2 -based photocatalysts. In the present work, the CuO_n cocatalyst was used as well. Two series of nanostructured composites have been synthesized. The first one has been made through the mechanical dispersion of $g\text{-C}_3\text{N}_4$ and copper-modified TiO_2 . To compare, the second series has been obtained by calcining melamine and TiO_2 mechanical mixture followed by copper deposition.

2. Experimental section

2.1. Photocatalyst characterization

The photocatalysts were analyzed by X-ray diffraction (XRD), UV-vis spectroscopy, X-ray photoelectron spectroscopy (XPS), and high-resolution transmission electron microscopy (HRTEM).

XRD pattern of the $g\text{-C}_3\text{N}_4$ was obtained using a D8 ADVANCE diffractometer equipped with a LYNXEYE linear detector (Bruker AXS GmbH, Karlsruhe, Germany) at room temperature in the 2θ of $10 - 60^\circ$ with a step of 0.05° with Ni-filtered $\text{CuK}\alpha$ radiation ($\lambda = 1.5418 \text{ \AA}$). Diffuse reflectance UV-vis spectra were recorded using a UV-2501 PC spectrophotometer with an ISR-240A diffuse reflectance unit (Shimadzu, Kyoto, Japan). The morphology of the photocatalysts was studied by HRTEM using a ThemisZ electron microscope (Thermo Fisher Scientific, Waltham, MA, USA) at an accelerating voltage of 200 kV. The study of the chemical composition of the photocatalysts was carried out by XPS on an electronic spectrometer SPECS SurfaceNanoAnalysis GmbH (Germany). The spectrometer was equipped with a PHOIBOS-150-MCD-9 hemispherical analyzer, an XR-50 characteristic X-ray source with a double Al/Mg anode. Non-monochromatic $\text{MgK}\alpha$ radiation ($h\nu = 1253.6 \text{ eV}$) was used to record the spectra. To take into account the effect of charging the samples, we used the position of the peak corresponding to titanium dioxide ($E(\text{Ti}2p_{3/2}) = 458.7 \text{ eV}$).

2.2. Synthesis of the photocatalysts

In order to synthesize the photocatalysts, all chemicals were taken in analytical grade without any additional purification.

2.2.1. TiO_2 pretreatment. TiO_2 samples were obtained using commercially available Evonik P25. Evonik P25 (0.500 g) was placed in a crucible and calcined at $600 - 750^\circ\text{C}$ for 3 h at a heating rate of $3^\circ\text{C}\cdot\text{min}^{-1}$. The resulting powder was then collected and ground thoroughly in a ceramic mortar.

2.2.2. $g\text{-C}_3\text{N}_4$ synthesis. Melamine was used as a precursor for graphitic carbon nitride formation via thermal condensation process. 20 g of melamine to be loaded in a covered crucible was heated to 600°C at a rate of $10^\circ\text{C}\cdot\text{min}^{-1}$ and held for 2 h. The yellow powder was ground in mortar for the further usage.

2.2.3. *1st series of composite photocatalysts.* The first series of photocatalysts were obtained by copper deposition on the TiO_2 surface and subsequent dispersing it with $\text{g-C}_3\text{N}_4$. Copper loading (1 and 5 wt.%) was carried out via chemical precipitation route. A 0.1 M $\text{Cu}(\text{NO}_3)_2$ aqueous solution was added to proper amounts (495 and 475 g) of calcined or pristine TiO_2 and stirred for 1 hour. An excess of NaBH_4 aqueous solution was appended and the mixture was stirred for 1.5 hours followed by washing with deionized water and centrifugation. The damp precipitate was then dried at 60°C in air during 12 hours. The samples containing 1 wt.% of CuO_n ($n = 0.5 - 1$) and TiO_2 calcined at different temperatures were separated off to investigate their photocatalytic properties. Further, 1 and 5 wt.% of $\text{g-C}_3\text{N}_4$ was mixed with 1 or 5 wt. % $\text{CuO}_n/\text{TiO}_2$ -750 in acetone and kept under constant stirring at 50°C for 60 minutes to obtain particles distributed homogeneously. Then the suspension was heated on a water bath until acetone evaporated and dried at 60°C in air for 12 hours. The first series of composites was referred to as X-CN/Y-Cu/ TiO_2 -750 (where X and Y represent weight content of $\text{g-C}_3\text{N}_4$ and CuO_n respectively).

2.2.4. *2st series of composite photocatalysts.* To obtain the second photocatalyst series, melamine and TiO_2 -750 were mixed and ground in a mortar with mass ratios (wt. %) melamine : TiO_2 ranging from 10 : 90 to 50 : 50. The mixture was calcined under the same thermal treatment conditions as described above. Following the calcination, 1 wt. % of copper was deposited on the composite surface using the method mentioned in the previous paragraph. The composites were labelled as 1-Cu/X-M/ TiO_2 -750, where X represents the weight percentage of melamine.

2.3. Photocatalytic experiments

The photocatalytic activity tests were carried out in a glass reactor containing the quartz window and the sampler to analyze the gas phase (Fig. 1). The reaction mixture was obtained by suspending 50 mg of the photocatalyst in 100 ml 0.1 M glucose aqueous solution. Prior to each experiment, the reactor was purged with argon for 20 minutes to remove oxygen in the gas phase. The use was made of the commercially available visible light LED (440 nm , $580\text{ mW}\cdot\text{cm}^{-2}$) placed on a distance of 1 cm away from the quartz window. Also, the rate of H_2 evolution on the most active photocatalyst was studied under AM1.5G illumination using a sunlight simulator "Pico" (G2V Optics, Canada). Gas phase analysis was carried out using a gas chromatograph CHROMOS GC-1000 equipped with a thermal conductivity detector and a NaX zeolite column to determine the amount of H_2 evolved quantitatively.

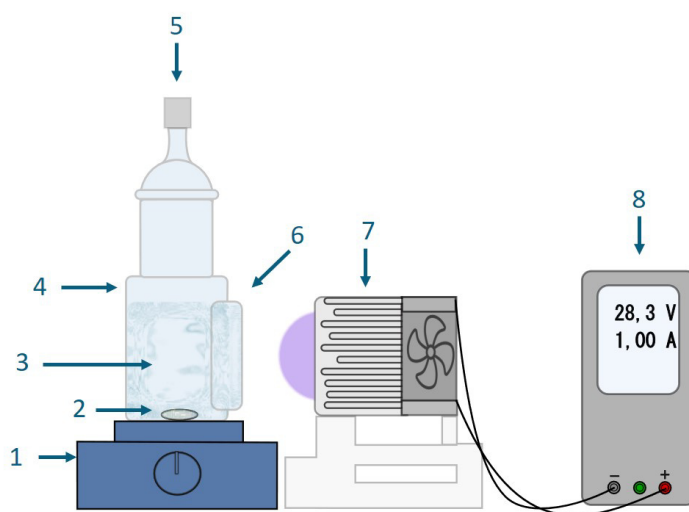


FIG. 1. Scheme of set-up for photocatalytic activity test. 1 – magnetic stirrer, 2 – stir bar, 3 – reaction suspension, 4 – glass reactor, 5 – sampler, 6 – quartz window, 7 – LED, 8 – power supply.

3. Results and discussions

3.1. Catalysts characterization

The photocatalyst synthesized were characterized by X-ray diffraction (XRD), diffuse reflectance spectroscopy (DRS), X-ray photoelectron spectroscopy (XPS), high-resolution transmission electron microscopy (HR TEM) and high-angle annular dark-field scanning transmission electron microscopy (HAADF-STEM).

The X-ray diffraction pattern of the synthesized $\text{g-C}_3\text{N}_4$ shown in Fig. 2a demonstrates two characteristic peaks at $2\theta = 12.8^\circ$ and 27.8° , which corresponds to the (210) and (002) crystal planes, respectively. The signal attributed to periodic stacking of triazine units is indicated as (210), thus suggesting that $\text{g-C}_3\text{N}_4$ forms a rhombic structure rather than a hexagonal structure.

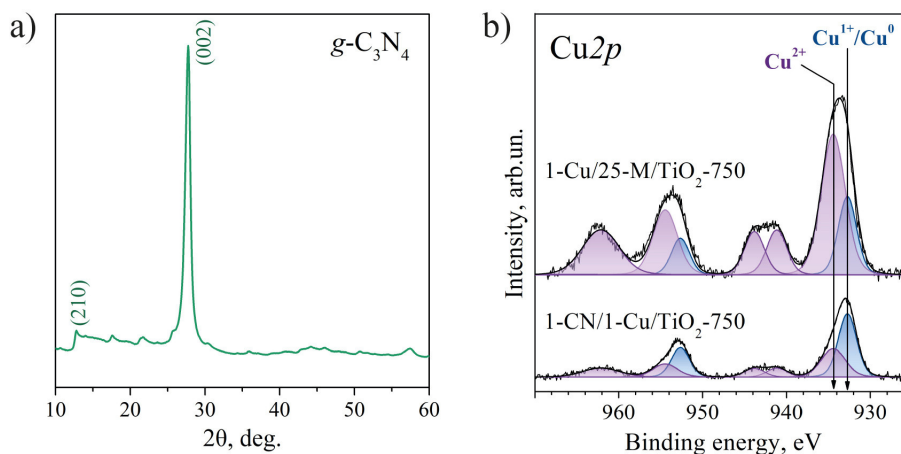


FIG. 2. a) XRD patterns of g-C₃N₄; b) Cu2p core-level spectra of photocatalysts. The spectra are normalized to the integral intensity of the corresponding Ti2p spectra.

The state and relative concentrations of elements in the surface layer of photocatalysts were analyzed by XPS (Table 1). At the survey spectra of the catalysts, peaks corresponding to Cu, Ti, N, C and O were found. The peaks related to g-C₃N₄ cannot be identified in the spectrum of C1s carbon due to the low concentration of g-C₃N₄ in the photocatalysts studied and the presence of carbon impurities from the atmosphere. The g-C₃N₄ content was estimated based on analysis of the N1s spectrum. It is worth noting that the near-surface layer of the photocatalyst 1-CN/1-Cu/TiO₂-750 contains a larger amount of nitrogen compared to the sample 1-Cu/25-M/TiO₂-750. At the same time, the concentration of copper on the surface, on the contrary, is higher in the case of 1-Cu/25-M/TiO₂-750. The g-C₃N₄ concentration in these photocatalysts may indeed differ due to different syntheses, however, since copper is deposited using the same method, its content in the volume of photocatalysts should be the same. It can be concluded that, in the case of the 1-CN/1-Cu/TiO₂-750 sample, the copper particles are partially shielded by g-C₃N₄; while in the 1-Cu/25-M/TiO₂-750 photocatalyst, copper is predominantly located on the surface of the photocatalyst.

TABLE 1. Relative atomic concentrations of elements in the surface area of the photocatalysts and N1s, Cu2p_{3/2}, and Ti2p_{3/2} binding energies

Photocatalysts	[N]/[Ti]	[Cu]/[Ti]	Cu ^{0/1+} , %	N1s			Cu2p _{3/2}		Ti2p _{3/2}
				C-N=C	(C) ₃ -N	N-H	Cu ^{0/1+}	Cu ²⁺	TiO ₂
1-CN/1-Cu/TiO₂-750	0.11	0.07	50	398.7	400.0	401.1	932.7	934.5	458.7
1-Cu/25-M/TiO₂-750	0.04	0.22	20	398.7	400.0	401.1	932.7	934.5	458.7

The Cu2p spectra demonstrates the presence of copper in the Cu²⁺, Cu⁺, and/or Cu⁰ states (Fig. 2b). The Cu2p core-level spectrum of both shows two intense Cu2p_{3/2} and Cu2p_{1/2} peaks at 932.7 and 952.7 eV and corresponding core-level satellite peaks at 941.1 – 943.8 eV and 962.1 eV, respectively. The presence of satellite peaks is observed for Cu²⁺ state, while Cu2p spectrum of Cu^{0/1+} does not have the satellite peaks [26, 27]. The Cu2p_{3/2} peak at 932.7 eV corresponds to copper in the metallic and/or Cu¹⁺ state. Due to the close binding energies of the corresponding Cu2p_{3/2} peaks, it is quite difficult to distinguish the Cu⁰ and Cu¹⁺ state by XPS technique [26, 28].

The UV-vis diffuse reflection spectra and Tauc plots of the photocatalysts are shown in Fig. 3. To plot the absorption spectra in Tauc coordinates the adsorption coefficient F(R) was found from the DRS data using the Kubelka–Munk equation [25] (1):

$$F(R) = \frac{(1 - R)^2}{2R}, \quad (1)$$

where R is the reflection coefficient of the sample. When comparing the spectra of 1 % CuO_n/TiO₂ and pure TiO₂ (Fig. 3a), it is evident that the absorption edge of 1 % CuO_n/TiO₂ has shifted to the long-wavelength region and the reflection decreases within the 500 – 800 nm. Such effect suggests that the separation of photogenerated electron-hole pairs in the CuO_n/TiO₂ heterojunction has been effectively improved [29–31]. Notably, there is almost no difference observed between 1-CN/1-Cu/TiO₂ and 1-Cu/25-M/TiO₂. The composites reflectance spectra are characterized by a

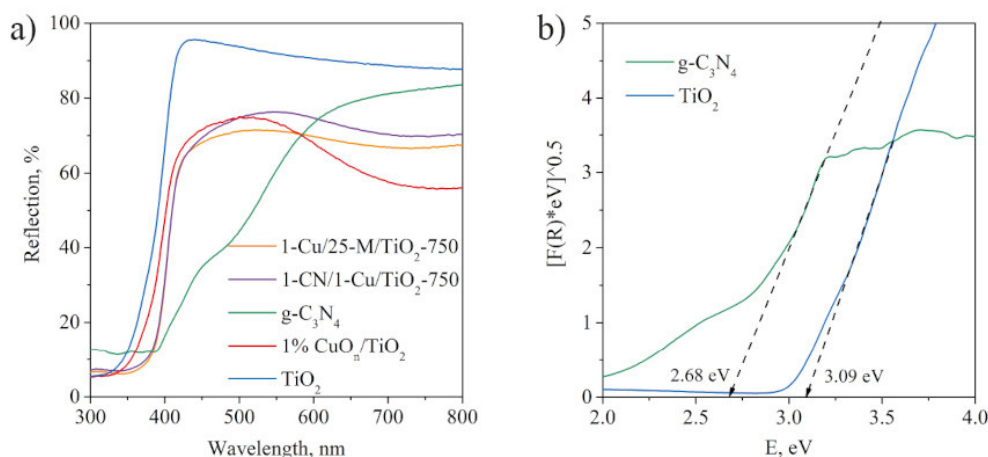


FIG. 3. (a) UV-VIS spectra for the TiO₂, g-C₃N₄, 1 % CuO_n/TiO₂, 1-CN/1-Cu/TiO₂-750 and 1-Cu/25-M/TiO₂-750 and (b) Tauc plots for the TiO₂ and g-C₃N₄

greater redshift compared with 1 % CuO_n/TiO₂. The results obtained consider, that modifying TiO₂ with a small amount (1 – 2 wt.%) of narrow band semiconductors enhances light harvesting and promotes photocatalytic activity under visible light irradiation.

The study of morphology of the 1-CN/1-Cu/TiO₂-750 photocatalyst showed that the composite consists of well-crystallized TiO₂ polyhedrons covered with copper nanoparticles and 2D nanosheets of g-C₃N₄ (Fig. 4a,b). Due to the fact that copper deposition has been followed by composite synthesis, g-C₃N₄ surface is copper-free. The size of TiO₂ particles is in the range of 20 – 200 nm, while copper particles have a narrow particle size distribution not exceeding the value of 5 nm (Fig. 4c). The photocatalyst microstructure was investigated in details using EDS elemental mapping. Despite the tendency of g-C₃N₄ layers to stick together, the EDS analysis (Fig. 4d,e,f) shows that the elements are uniformly distributed across the entire catalyst surface.

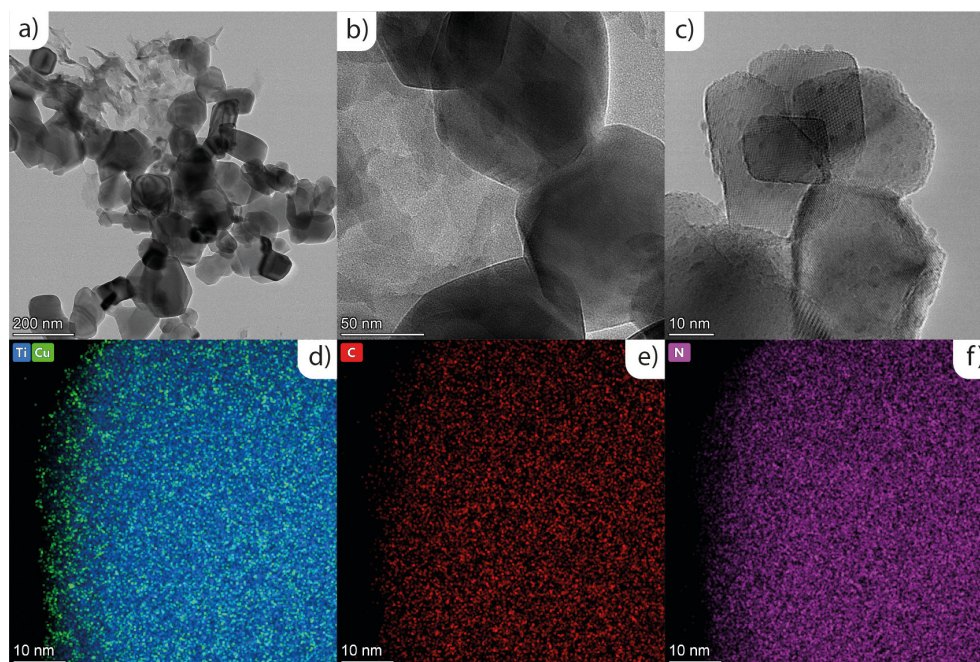


FIG. 4. TEM images and HAADF analysis with EDS of 1-CN/1-Cu/TiO₂-750

Although, different synthetic processes have been applied, the morphology of 1-Cu/10-M/TiO₂-750 (as shown in Fig. 5) resembles one for 1-CN/1-Cu/TiO₂-750. As the sample discussed previously, 1-Cu/25-M/TiO₂-750 has well-distinguished particles with an average diameter from 20 to 200 nm. The TEM image (Fig. 5c) displays some CuO_n nanoparticles (with average diameter of less than 5 nm) adsorbed onto the photocatalyst surface. Due to visually unresolved crystal structure in the Fig. 5c, the photocatalyst surface is believed to consist of TiO₂ in intimate contact with g-C₃N₄ and CuO_n hemispheres on top. Moreover, g-C₃N₄ is clearly seen to have extended nanosheet morphology as

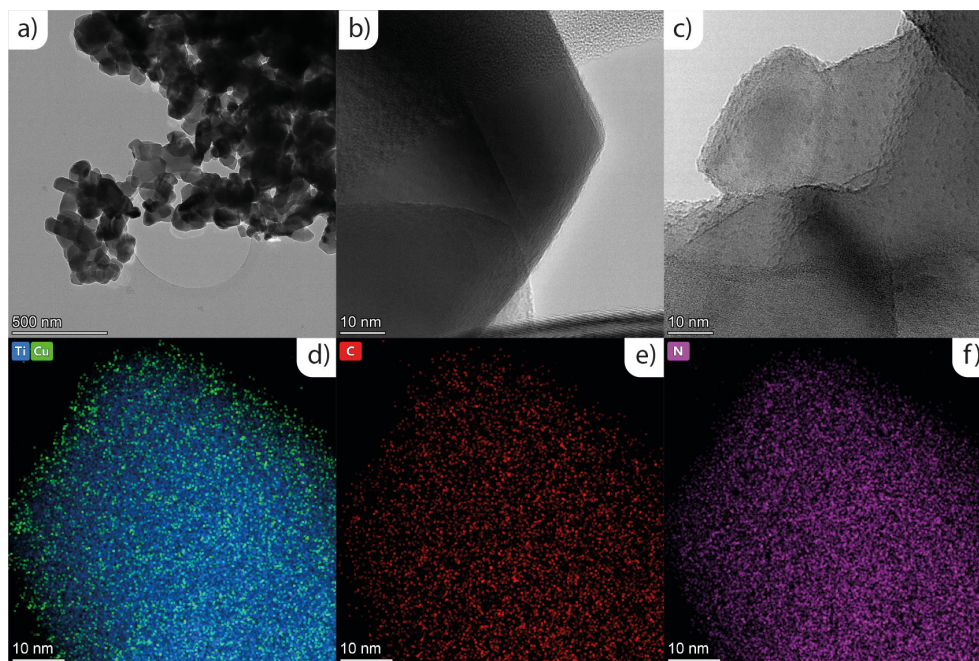


FIG. 5. TEM images and HAADF analysis with EDS of 1-Cu/25-M/TiO₂-750

presented in Fig. 5b. Finally, HAADF analysis with elemental mapping demonstrates uniform distribution of CuO_n and g-C₃N₄ particles on the TiO₂ surface.

3.2. Photocatalytic activity

At the beginning, synergistic effect of TiO₂ modification with g-C₃N₄ and copper cocatalyst was investigated. The activities of unmodified TiO₂, 1 wt.% Cu/TiO₂, 1 wt.% g-C₃N₄/TiO₂, and 1 wt.% g-C₃N₄/1 wt.% Cu/TiO₂ photocatalysts were tested in the H₂ evolution reaction from glucose solution under visible light irradiation (440 nm). The deposition of g-C₃N₄ and copper leads to a decrease in the rate of H₂ evolution compared to unmodified TiO₂, probably due to a decrease in the adsorption of glucose on the surface of the photocatalyst (Fig. 6a). However, the co-deposition of both g-C₃N₄ and CuO_n on the TiO₂ surface promotes the rate of H₂ evolution. This synergistic effect is caused by an increase in light absorption by the composite photocatalyst and an increase in the lifetime of photogenerated charge carriers.

In the previous works, we studied the effect of calcination of TiO₂ on photocatalytic activity and showed that heat treatment in some cases leads to an increase in the activity of the photocatalyst [32]. Therefore, further for the synthesis of composite photocatalysts, TiO₂ was calcined at 750 °C.

The first series of photocatalysts was tested in the photocatalytic H₂ production from glucose aqueous solution. The results obtained are summarized in the Fig. 6b and Table 2. The maximum activity of 235 μmol·h⁻¹·g⁻¹ is achieved for 1-CN/1-Cu/TiO₂-750, considering the variation of g-C₃N₄ content. Further increasing the g-C₃N₄ loading up to 5 wt.% causes a decline in activity to 174 μmol·h⁻¹·g⁻¹. Additionally, an increase in copper loading results in a decrease in the H₂ production rate, consistent with the earlier study [25]. However, the activity of all composite photocatalysts significantly exceeds the activity of commercial TiO₂.

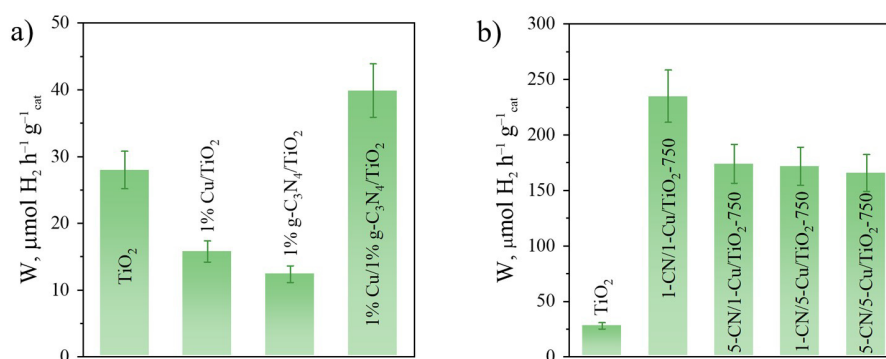


FIG. 6. Photocatalytic activity of the first photocatalyst series depending on copper and g-C₃N₄ amount

To investigate the impact of the synthetic method on photocatalyst activity, we examined the second series of composites under the same conditions (Fig. 7). Starting with the equal melamine: TiO_2 ratio, the H_2 production rate increases from 172 up to 259 $\mu\text{mol}\cdot\text{h}^{-1}\cdot\text{g}^{-1}$ (Table 2) for 1-Cu/50-M/ TiO_2 and 1-Cu/25-M/ TiO_2 , respectively. However, decreasing the melamine content may slightly depress the photocatalytic activity. The trend involved is observed for the previous photocatalyst as well. When g- C_3N_4 content raised, it covers the large portion of TiO_2 surface and impedes the glucose adsorption due to low affinity. The samples, corresponding to 10 and 25 wt.% melamine content before calcination, exhibit 243 and 259 $\mu\text{mol}\cdot\text{h}^{-1}\cdot\text{g}^{-1}$, respectively. These values are comparable to each other and indicate that the samples are among the most prominent photocatalysts in the series concerned.

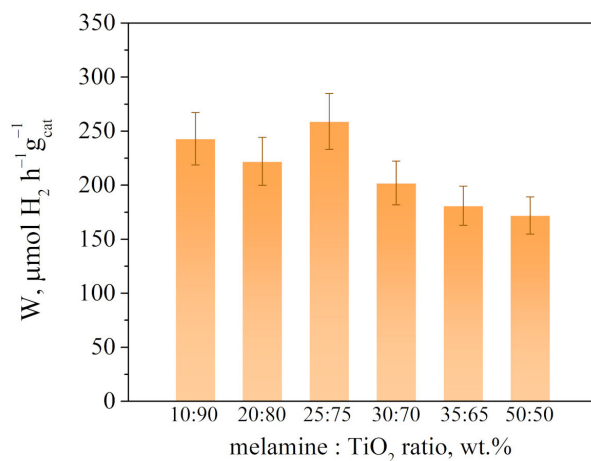


FIG. 7. Photocatalytic activity of the second photocatalyst series depending on melamine: TiO_2 mass ratio. Photocatalysts: 1-Cu/X-M/ TiO_2 -750.

The rate of H_2 evolution under the solar light was determined using the most active photocatalyst 1-Cu/25-M/ TiO_2 -750 (Table 3). Its activity is on par with other data in the literature and is inferior only to data obtained using a more powerful light source. In addition, it is worth noting that this photocatalyst does not contain expensive platinum group metals and can be synthesized from available precursors. The synthetic approach proposed in the work can significantly reduce the cost of the generated H_2 solar fuel.

3.3. Photocatalytic stability test

In our previous work, it has been established for $\text{CuO}_n/\text{TiO}_2$ photoactivity that it is fluctuant and dramatically decreases under long-term light irradiation [38]. To test the impact of g- C_3N_4 loading on the catalyst stability, we are to screen the 1-CN/1-Cu/ TiO_2 -750 in cyclic experiments. As shown in Fig. 8, the H_2 amount on 1-CN/1-Cu/ TiO_2 -750 does not lower significantly after each cycle and the rate of H_2 evolution is the same within the experimental error. It is worth mentioning that the addition of g- C_3N_4 allows increasing the stability of copper-modified TiO_2 , if compare to the previous study. Thus, this fact suggests composite heterostructure with g- C_3N_4 being responsible for enhanced reusability of the catalyst.

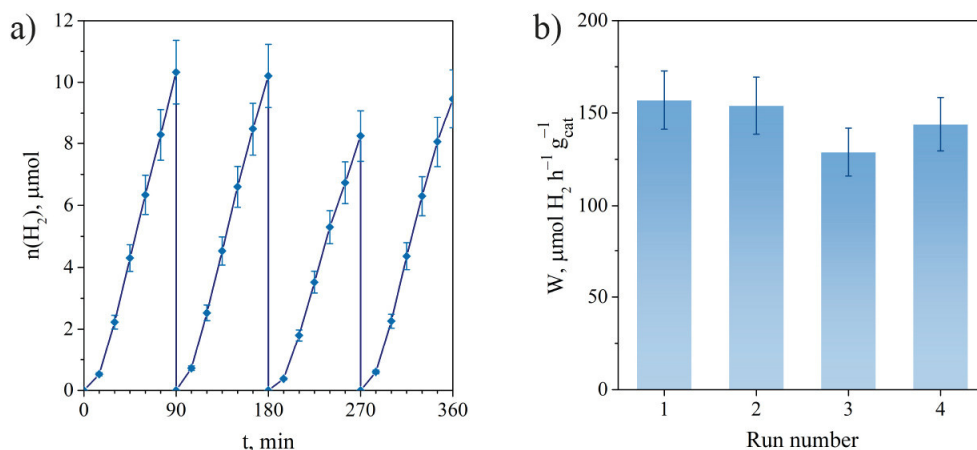


FIG. 8. Photocatalytic stability test: the kinetic curves of H_2 production (a), the dependence of H_2 generation rate on cycle number (b)

TABLE 2. Activities of the photocatalysts synthesized

Photocatalyst	Designation	W(H ₂), $\mu\text{mol}\cdot\text{g}^{-1}\cdot\text{h}^{-1}$
TiO ₂ unmodified		28
1st series of photocatalysts		
1 % g-C ₃ N ₄ 1 % CuO _n TiO ₂ -750	1-CN/1-Cu/TiO ₂ -750	235
5 % g-C ₃ N ₄ 1 % CuO _n TiO ₂ -750	5-CN/1-Cu/TiO ₂ -750	174
1 % g-C ₃ N ₄ 5 % CuO _n TiO ₂ -750	1-CN/5-Cu/TiO ₂ -750	172
5 % g-C ₃ N ₄ 5 % CuO _n TiO ₂ -750	5-CN/5-Cu/TiO ₂ -750	166
2st series of photocatalysts		
1 % CuO _n g-C ₃ N ₄ TiO ₂ -750 (melamine : TiO ₂ = 10 : 90)	1-Cu/10-M/TiO ₂ -750	243
1 % CuO _n g-C ₃ N ₄ TiO ₂ -750 (melamine : TiO ₂ = 20 : 80)	1-Cu/20-M/TiO ₂ -750	222
1 % CuO _n g-C ₃ N ₄ TiO ₂ -750 (melamine : TiO ₂ = 25 : 75)	1-Cu/25-M/TiO ₂ -750	259
1 % CuO _n g-C ₃ N ₄ TiO ₂ -750 (melamine : TiO ₂ = 30 : 70)	1-Cu/30-M/TiO ₂ -750	202
1 % CuO _n g-C ₃ N ₄ TiO ₂ -750 (melamine : TiO ₂ = 35 : 50)	1-Cu/35-M/TiO ₂ -750	181
1 % CuO _n g-C ₃ N ₄ TiO ₂ -750 (melamine : TiO ₂ = 50 : 50)	1-Cu/50-M/TiO ₂ -750	172

TABLE 3. The comparison of activity values of the photocatalysts based on g-C₃N₄ and TiO₂ with previously published data on H₂ photogeneration from a glucose solution

No.	Photocatalyst	Conditions			W(H ₂), $\mu\text{mol}\cdot\text{g}^{-1}\cdot\text{h}^{-1}$	Article
		C ₀ (glucose)	C(catalyst), $\text{g}\cdot\text{L}^{-1}$	Light source		
1	1-Cu/25-M/TiO ₂ -750	0.1 M	0.5	Simulated solar light (AM1.5G, 100 mW/cm ²)	295	Present work
2	3 wt. % Pt/O-g-C ₃ N ₄	0.1 M	0.25	Simulated solar light (500 W/m ²)	870	[33]
3	0.5 wt. % Pd/TiO ₂	0.5 g·L ⁻¹	0.5	LED, 375 – 380 nm, 1.5 W/m ²	590	[34]
4	2 wt. % PtAu/g- C ₃ N ₄	0.16 M (pH = 13)	0.3	Xenon lamp (350 – 800 nm, 170 mW/cm ²)	2370	[35]
5	W- and N-doped Pt-TiO ₂	1 mM	1.0	Natural solar irradiation	1000	[36]
6	Cd _{0.8} Zn _{0.2} S/Au/g-C ₃ N ₄	0.1 M	0.5	Xenon lamp ($\lambda > 420$ nm)	123	[37]

4. Conclusion

This work proposed and investigated new photocatalysts based on TiO₂ and g-C₃N₄ for H₂ production from glucose aqueous solution under visible radiation (440 nm) and solar light (AM1.5G). Two series of photocatalysts were synthesized: one by mechanically dispersing g-C₃N₄ with TiO₂ and the other by co-calcinating melamine and TiO₂. The structure and properties of photocatalysts were established using the complex of physicochemical methods. The deposition of CuO_n and g-C₃N₄ particles on the TiO₂ surface was shown to alter its optical properties, resulting in a redshift of the absorption edge. Photocatalytic experiments were conducted to test the H₂ evolution rate over the samples obtained. The first series had a maximum rate of 235 μmol·h⁻¹·g⁻¹, while the second series – 259 μmol·h⁻¹·g⁻¹ (440 nm), corresponding to 1-CN/1-Cu/TiO₂-750 and 1-Cu/25-M/TiO₂-750, respectively. The cyclic stability tests of the 1-CN/1-Cu/TiO₂-750 showed the rate of photocatalytic H₂ evolution kept the same during 4 cycle of experiments. Thus, in this work, active and stable photocatalysts were proposed for the production of H₂ under the solar light. It is worth noting that these photocatalysts could be obtained from inexpensive and available precursors such melamine, copper nitrate, and commercial TiO₂.

References

- [1] Kou J., Lu, C., Wang J., Chen Y., Xu Z., Varma R.S. Selectivity Enhancement in Heterogeneous Photocatalytic Transformations. *Chem. Rev.*, 2017, **117** (3), P. 1445–1514.
- [2] de Assis G.C., Silva I.M.A., dos Santos T.G., dos Santos T. V. Meneghetti M.R., Meneghetti S.M.P. Photocatalytic Processes for Biomass Conversion. *Catal. Sci. Technol.*, 2021, **11** (7), P. 2354–2360.
- [3] Valeeva A.A., Dorosheva I.B., Kozlova E.A., Sushnikova A.A., Yu A., Saraev A.A., Schroettner H., Rempel A.A. Solar Photocatalysts Based on Titanium Dioxide Nanotubes for Hydrogen Evolution from Aqueous Solutions of Ethanol. *Int. J. Hydrogen Energy*, 2021, **46** (32), P. 16917–16924.
- [4] Kurnosenko S.A., Zvereva I.A., Voytovich V. V., Silyukov O.I., Rodionov I.A. Photocatalytic Activity and Stability of Organically Modified Layered Perovskite-like Titanates HLnTiO₄ (Ln = La, Nd) in the Reaction of Hydrogen Evolution from Aqueous Methanol. *Catalysts*, 2023, **13** (4), 749.
- [5] Kurnosenko S.A., Voytovich V.V., Silyukov O.I., Rodionov I.A., Zvereva I.A. Photocatalytic Hydrogen Production from Aqueous Solutions of Glucose and Xylose over Layered Perovskite-like Oxides HCa₂Nb₃O₁₀, H₂La₂Ti₃O₁₀ and Their Inorganic-Organic Derivatives. *Nanomaterials*, 2022, **12** (15), 2717.
- [6] Samage A., Gupta P., Halakarni M.A., Nataraj S.K., Sinhamahapatra A. Progress in the Photoreforming of Carboxylic Acids for Hydrogen Production. *Photochem.*, 2022, **2** (3), P. 580–608.
- [7] Imizcoz M., Puga A.V. Acid Photoreforming on Cu/TiO₂. *Catalysis Science & Technology*, 2019, **9** (5), P. 1098–1102.
- [8] Davis K.A., Yoo S., Shuler E.W., Sherman B.D., Lee S., Leem G. Photocatalytic Hydrogen Evolution from Biomass Conversion. *Nano Convergence*, 2021, **8** (6), P. 1–19.
- [9] Huang Z., Luo N., Zhang C., Wang F. Radical Generation and Fate Control for Photocatalytic Biomass Conversion. *Nature Reviews Chemistry*, 2022, **6**, P. 197–214.
- [10] Butburee T., Chakthranont P., Phawa C., Faungnawakij K. Beyond Artificial Photosynthesis: Prospects on Photobiorefinery. *Chem. Cat. Chem.*, 2020, **12** (7), P. 1873–1890.
- [11] Liu X., Duan X., Wei W., Wang S., Ni B.J. Photocatalytic Conversion of Lignocellulosic Biomass to Valuable Products. *Green Chemistry*, 2019, **21**, P. 4266–4289.
- [12] Chu Y.M., Bach Q.V. Application of TiO₂ Nanoparticle for Solar Photocatalytic Oxidation System. *Appl. Nanosci.*, 2023, **13** (3), P. 1729–1736.
- [13] Qian R., Zong H., Schneider J., Zhou G., Zhao T., Li Y., Yang J., Bahnemann D.W., Pan J.H. Charge Carrier Trapping, Recombination and Transfer during TiO₂ Photocatalysis: An Overview. *Catal. Today*, 2019, **335**, P. 78–90.
- [14] Shiraishi Y., Hirai T. Selective Organic Transformations on Titanium Oxide-Based Photocatalysts. *J. of Photochemistry and Photobiology C: Photochemistry Reviews*, 2008, **9** (4), P. 157–170.
- [15] Chai B., Peng T., Mao J., Li K., Zan L. Graphitic Carbon Nitride (g-C₃N₄)-Pt-TiO₂ Nanocomposite as an Efficient Photocatalyst for Hydrogen Production under Visible Light Irradiation. *Phys. Chem. Chem. Phys.*, 2012, **14** (48), P. 16745–16752.
- [16] Yan H., Yang H. TiO₂-g-C₃N₄ Composite Materials for Photocatalytic H₂ Evolution under Visible Light Irradiation. *J. of Alloys and Compounds*, 2011, **509** (4), L26–L29.
- [17] Shoaib M., Naz M.Y., Shukrullah S., Munir M.A., Irfan M., Rahman S., Ghanim A.A.J. Dual S-Scheme Heterojunction CdS/TiO₂/g-C₃N₄ Photocatalyst for Hydrogen Production and Dye Degradation Applications. *ACS Omega*, 2023, **8** (45), P. 43139–43150.
- [18] Wei D.W., DuChene J.S., Sweeny B.C., Wang J., Niu W. Current Development of Photocatalysts for Solar Energy Conversion. *New and Future Developments in Catalysis: Solar Photocatalysis*, Elsevier, USA, 2013, P. 279–304.
- [19] Li J., Chu D. Energy Band Engineering of Metal Oxide for Enhanced Visible Light Absorption. *Multifunctional Photocatalytic Materials for Energy*, 2018, P. 49–78.
- [20] Ye S., Wang R., Wu M.Z., Yuan Y.P. A Review on g-C₃N₄ for Photocatalytic Water Splitting and CO₂ Reduction. *Applied Surface Science*, 2015, **358**, P. 15–27.
- [21] Mamba G., Mishra A.K. Graphitic Carbon Nitride (g-C₃N₄) Nanocomposites: A New and Exciting Generation of Visible Light Driven Photocatalysts for Environmental Pollution Remediation. *Appl. Catal. B Environ.*, 2016, **198**, P. 347–377.
- [22] Zheng Y., Lin L., Wang B., Wang, X. Graphitic Carbon Nitride Polymers toward Sustainable Photoredox Catalysis. *Angew. Chemie – Int. Ed.*, 2015, **54** (44), P. 12868–12884.
- [23] Dong J., Zhang Y., Hussain M.I., Zhou W., Chen Y., Wang L.N. g-C₃N₄: Properties, Pore Modifications, and Photocatalytic Applications. *Nanomaterials*, 2021, **12** (1), 121.
- [24] Lingzhiiwang J.B., Juyingglei M. *Photocatalysis Fundamentals, Materials and Applications*, Springer, Singapore, 2018, 414 p.
- [25] Kurenkova A.Y., Yakovleva A.Y., Saraev A.A., Gerasimov E.Y., Kozlova E.A., Kaichev V.V. Copper-Modified Titania-Based Photocatalysts for the Efficient Hydrogen Production under UV and Visible Light from Aqueous Solutions of Glycerol. *Nanomaterials*, 2022, **12** (18), 3106.
- [26] Wöllner A., Lange F., Schmelz H., Knözinger H. Characterization of Mixed Copper-Manganese Oxides Supported on Titania Catalysts for Selective Oxidation of Ammonia. *Appl. Catal. A, Gen.*, 1993, **94** (2), P. 181–203.

- [27] Fedorov A., Saraev A., Kremneva A., Selivanova A., Vorokhta M., Šmíd, B., Bulavchenko, O., Yakovlev, V., Kaichev, V. Kinetic and Mechanistic Study of CO Oxidation over Nanocomposite Cu–Fe–Al Oxide Catalysts. *Chem. Cat. Chem.*, 2020, **12** (19), P. 4911–4921.
- [28] Bukhtiyarov V.I., Kaichev V.V., Prosvirin I.P. X-Ray Photoelectron Spectroscopy as a Tool for in-Situ Study of the Mechanisms of Heterogeneous Catalytic Reactions. *Top. Catal.*, 2005, **32** (1–2), P. 3–15.
- [29] Muscetta M., Andreozzi R., Clarizia L., Di Somma L., Marotta R. Hydrogen Production through Photoreforming Processes over Cu₂O/TiO₂ Composite Materials: A Mini-Review. *Int. J. Hydrogen Energy*, 2020, **45** (53), P. 28531–28552.
- [30] Nishikiori H., Harata N., Yamaguchi S., Ishikawa T., Kondo H., Kikuchi A., Yamakami T., Teshima K. Formation of CuO on TiO₂ Surface Using Its Photocatalytic Activity. *Catalysts*, 2019, **9** (4), 383.
- [31] Segovia-Guzmán M.O., Román-Aguirre M., Verde-Gomez J.Y., Collins-Martínez V.H., Zaragoza-Galán G., Ramos-Sánchez V.H. Green Cu₂O/TiO₂ Heterojunction for Glycerol Photoreforming. *Catal. Today*, 2020, **349**, P. 88–97.
- [32] Kurenkova A.Y., Kremneva A.M., Saraev A.A., Murzin V., Kozlova E.A., Kaichev V.V. Influence of Thermal Activation of Titania on Photoreactivity of Pt/TiO₂ in Hydrogen Production. *Catal. Letters*, 2021, **151**, P. 748–754.
- [33] Speltini A., Scalabrini A., Maraschi F., Sturini M., Pisanu A., Malavasi L., Profumo A. Improved Photocatalytic H₂ Production Assisted by Aqueous Glucose Biomass by Oxidized g-C₃N₄. *Int. J. Hydrogen Energy*, 2018, **43** (32), P. 14925–14933.
- [34] Vaiano V., Iervolino G., Sarno G., Sannino D., Rizzo L., Murcia Mesa J. J., Hidalgo M.C., Navío J.A. Production Simultanée de CH₄ et H₂ Par Réformage Photocatalytique d'une Solution Aqueuse de Glucose Sur Un Catalyseur Pd-TiO₂ Sulfaté. *Oil Gas Sci. Technol.*, 2015, **70** (5), P. 891–902.
- [35] Ding F., Yu H., Liu W., Zeng X., Li S., Chen L., Li B., Guo J., Wu C. Au-Pt Heterostructure Cocatalysts on g-C₃N₄ for Enhanced H₂ Evolution from Photocatalytic Glucose Reforming. *Mater. Des.*, 2024, **238**, 112678.
- [36] Bellardita M., García-López E. I., Marci G., Nasillo G., Palmisano, L. Photocatalytic Solar Light H₂ Production by Aqueous Glucose Reforming. *Eur. J. Inorg. Chem.*, 2018, **41**, P. 4522–4532.
- [37] Zhao H., Ding X., Zhang B., Li Y., Wang C. Enhanced Photocatalytic Hydrogen Evolution along with Byproducts Suppressing over Z-Scheme Cd_xZn_{1-x}S/Au/g-C₃N₄ Photocatalysts under Visible Light. *Sci. Bull.*, 2017, **62** (9), P. 602–609.
- [38] Kozlova E.A., Kurenkova A.Y., Gerasimov E.Y., Gromov N.V., Medvedeva T.B., Saraev A.A., Kaichev V.V. Comparative Study of Photoreforming of Glycerol on Pt/TiO₂ and CuO_x/TiO₂ Photocatalysts under UV Light. *Mater. Lett.*, 2021, **283**, 128901.

Submitted 18 April 2024; revised 9 May 2024; accepted 10 May 2024

Information about the authors:

Sofiya N. Kharina – Boreskov Institute of Catalysis SB RAS, Lavrentieva Ave, 5, Novosibirsk, 630090, Russia;
ORCID 0009-0000-9399-0231; skharina@catalysis.ru

Anna Yu. Kurenkova – Boreskov Institute of Catalysis SB RAS, Lavrentieva Ave, 5, Novosibirsk, 630090, Russia;
ORCID 0000-0002-4150-7049; kurenkova@catalysis.ru

Andrey A. Saraev – Boreskov Institute of Catalysis SB RAS, Lavrentieva Ave, 5, Novosibirsk, 630090, Russia;
ORCID 0000-0001-9610-9921; asaraev@catalysis.ru

Evgeny Yu. Gerasimov – Boreskov Institute of Catalysis SB RAS, Lavrentieva Ave, 5, Novosibirsk, 630090, Russia;
ORCID 0000-0002-3230-3335; gerasimov@catalysis.ru

Ekaterina A. Kozlova – Boreskov Institute of Catalysis SB RAS, Lavrentieva Ave, 5, Novosibirsk, 630090, Russia;
ORCID 0000-0001-8944-7666; kozlova@catalysis.ru

Conflict of interest: the authors declare no conflict of interest.

Synthesis and study of nickel sulfide nanoparticles and nanostructures for energy storage device applications

Mahesh M. Kamble¹, Bharat R. Bade², Avinash V. Rokade², Vaishali S. Waman³, Sachin V. Bangale⁴, Sandesh R. Jadkar²

¹PDEA'S Anantrao Pawar College, Pirangut, Mulshi, Pune 412115 India

²Department of Physics, Savitribai Phule Pune University, Pune 411007 India

³P. E. S. Modern College of Arts, Science and Commerce, Shivajinagar, Pune 411005 India

⁴Chemical Research Lab, UG and PG Department of Chemistry, G. M. Vedak College of Science, Tala-Raigad, 402111 India

Corresponding author: Mahesh M. Kamble, mmkamble14@gmail.com

ABSTRACT Nickel sulfide (NiS) nanostructures were synthesized by simple and low-cost hot injection method (HIM). The effects of sulfur concentration on the compositional, morphological, optical and structural properties of NiS nanoparticles were investigated in detail. The X-ray diffraction pattern confirms the formation of NiS nanoparticles without any impurities. The Raman spectra show the presence of NiS active modes in the synthesized material prepared at different sulphur concentration. The electrochemical performance of the synthesized NiS powder was estimated through cyclic voltammetry, galvanostatic charge-discharge, and electrochemical impedance spectroscopy in KOH electrolyte. The specific capacitance (CS) of the NiS powder electrode was measured with the three-electrode method, and it confirms the maximum CS of 315.8 F/g at a scan rate of 5 mVs⁻¹. The calculated value of energy density and power density of the NiS powder electrode is 3.324 WhKg⁻¹ and 199 WKg⁻¹ respectively at a lower current density. Present study provides a simple and low-cost HIM is capable of controlling the structural, optical, and morphological properties of nickel sulfide series, which would be of great potential for the synthesis of other metal sulfides.

KEYWORDS nickel sulfide, nanoparticles, nanostructures, electrochemical measurements, supercapacitor, hot injection method

ACKNOWLEDGEMENTS The author MMK is thankful to the Department of Physics, Savitribai Phule Pune University, Pune, Maharashtra, India for using their facility.

FOR CITATION Kamble M.M., Bade B.R., Rokade A.V., Waman V.S., Bangale S.V., Jadkar S.R. Synthesis and study of nickel sulfide nanoparticles and nanostructures for energy storage device applications. *Nanosystems: Phys. Chem. Math.*, 2024, **15** (3), 398–409.

1. Introduction

The development of efficient, clean and high-performance energy storage systems is a basic need of the community. There are different energy storage systems like batteries, fuel cells, supercapacitors etc. among them supercapacitors have attracted much attention due to their excellent electrochemical performance. The supercapacitors are significant part of energy storage systems due to its outstanding properties like high power densities, fast charge-discharge rates, relatively low costs, long operational life, and environmental friendliness. Moreover, the supercapacitor possesses more energy and power density as compared with rechargeable lithium batteries. Supercapacitors have been extensively used in many fields including electronics, defense, transportation, communications etc. To develop high-performance supercapacitors, good choice of electrode materials is important. It is the key parameter for the capacitance performance in the energy storage device applications [1]. So, the synthesis of novel materials using low-cost techniques along with higher specific capacitance and power densities is a challenge for many researchers. Hence, there is a strong inspiration to search inexpensive and promising alternative electrode materials for supercapacitor applications. The metal oxides/metal hydroxides, conductive polymers, carbonaceous materials etc. have been used to construct supercapacitor electrodes [2–4]. The high resistivity of metal oxides affects the storing capacities and cyclic performance. Various conducting polymers have been utilized for the fabrication of supercapacitor electrodes but they have poor cyclic stability. Nowadays, transition metal sulfides like NiS, CoS, CuS, ZnS etc. have attracted more attention in energy applications because of their excellent properties such as high electrical conductivity, better electrochemical stability, eco-friendly nature, and low-cost [5].

Among all the existing electrode materials, transition metal sulfides have been studied more due to their excellent electrical properties and capacity to exhibit various redox states [6–9]. Among the transition metal sulfides, NiS has made more interest due to its superior properties such as high electron conduction, low cost, rich chemical composition, natural

abundance, environmental benignity, ease of fabrication and low toxicity [10–13]. Thus, due to its outstanding properties, nickel sulfide has been widely used in rechargeable lithium batteries, infrared detectors, hydro sulfurization catalysis, photoconductive material, dye-synthesized solar cells, solar energy storages etc. [14]. There are several methods used for the synthesis of nickel sulfide which includes high temperature solid state and vapour phase reaction [15], hydrothermal [16], solvothermal [17], microwave radiation [18], sonochemical method [19] etc. In solvothermal and vapor phase, process requires high temperature; in this method, it is difficult to get a controlled NiS phases. In the hydrothermal method, other phases are created in the synthesized material. In this work, we have synthesized device quality NiS nanoparticles at different sulphur concentrations by using a locally fabricated hot injection system, particulars of which have been explained elsewhere [20].

2. Experimental

2.1. Materials

Oleylamine (OAm, 70 %), nickel nitrate hexahydrate ($\text{Ni}(\text{NO}_3)_2 \cdot 6\text{H}_2\text{O}$, 99.999 %), sulphur powder (S, 99.98 %), acetone (99.9 %), toluene (99 %) and isopropanol (IPA, 99.5 %) were used for NiS synthesis with the purity level mentioned in parenthesis. The chemicals mentioned above used for the synthesis of nickel sulfide were procured from Sigma-Aldrich and used without further filtering and processing.

2.2. Synthesis of high-quality NiS nanoparticles

The colloidal NiS nanoparticles were synthesized by the hot injection method. The oleylamine is used as a solvent, surfactant and capping ligand. In a 100 mL three necked glass flask, 0.2 molar nickel nitrate hexahydrate [$\text{Ni}(\text{NO}_3)_2 \cdot 6\text{H}_2\text{O}$] and 15 mL of oleylamine were added. The one end of three necked flasks is connected to alternately vacuum and argon gas balloon, the other end is used for injecting sulfur and the third end is used for thermocouple to measure reaction temperature. The resultant solution was constantly stirred using a magnetic stirrer and heated to a steady temperature of 140 °C in an alternate vacuum and argon gas environment to remove moisture and air from the reaction zone. Once the Ni-Oleyamine complex turned into the light brown-black solution, the reaction temperature was raised to 210 °C and kept constant for an hour, as the required crystal size and morphology depend on the temperature of the reaction.

Meanwhile, another solution was prepared, for which one molar sulphur powder was mixed with 5 mL oleylamine, which is named as S-Oleyamine solution. The S-Oleyamine solution was stirred and heated at 80 °C for 45 minutes. The resulting heated S-Oleyamine solution was rapidly injected into the preheated Ni-Oleyamine complex solution. The resulting mixture was heated to 210 °C for 30 minutes, getting a homogeneous blackish solution. All reactions were carried out in alternate vacuum and argon gas atmospheres. After that the three-necked glass flask was kept in a cold water bath to cool the reaction mixture. The same experiments were repeated in this set for 2 and 3 molar sulphur concentrations. The 1, 2 and 3 molar sulphur concentration means 1, 2 and 3 molar sulphur powder was mixed with 5 mL oleylamine.

The NiS nanoparticles are dispersible in organic solvents such as toluene and isopropanol, so 5 mL of toluene and 40 mL of isopropanol were added in resulting mixture to precipitate the NiS nanoparticles. The precipitate was recovered by centrifugation at 3000 rpm to yield colloidal black NiS nanoparticles. The isopropanol and toluene were used to remove polar and non-polar impurities respectively. The colloidal NiS nanoparticles were annealed at a temperature of 350 °C for one hour. Finally, NiS powders were taken out for characterization and confirmation. Fig. 1 shows the schematic for the synthesis of NiS powder.

2.3. Characterization

The structural properties of NiS nanoparticles were confirmed from the XRD pattern recorded on a Bruker D8 advanced diffraction meter with $\text{CuK}\alpha$ radiation at a wavelength of $\lambda = 1.54 \text{ \AA}$. The optical properties of synthesized materials were confirmed from a UV-Vis spectrophotometer (Jasco, model V-670) in the wavelength range of 200 – 1400 nm. Scanning Electron Microscopy (SEM) (JEOL-6360-LA instrument) is used for the study of surface morphology. The elemental compositions were confirmed from Energy Dispersive X-ray Analysis (EDAX). The Raman Spectroscopy is used to identify active modes of NiS nanoparticles and it is recorded with a Renishaw Raman Microscope with argon laser at 532 nm in the 200 – 900 cm^{-1} range. The bonding configurations in the materials were confirmed from Fourier Transform Infrared Spectroscopy (FTIR) (Jasco, 6100-type A) in the range 400 – 4000 cm^{-1} . The electrochemical performance of synthesized NiS powder electrode was estimated by cyclic voltammetry, galvanostatic charge-discharge and electrochemical impedance spectroscopy.

3. Results and discussion

3.1. XRD Analysis

The X-ray diffraction patterns of the nickel sulfide nanoparticles synthesized using the hot injection method at various sulphur concentrations are shown in Fig. 2. The crystallographic information of NiS nanoparticles was confirmed by the XRD analysis. The XRD pattern of the synthesized material was recorded in the range of diffraction angle from 15 to 80°.

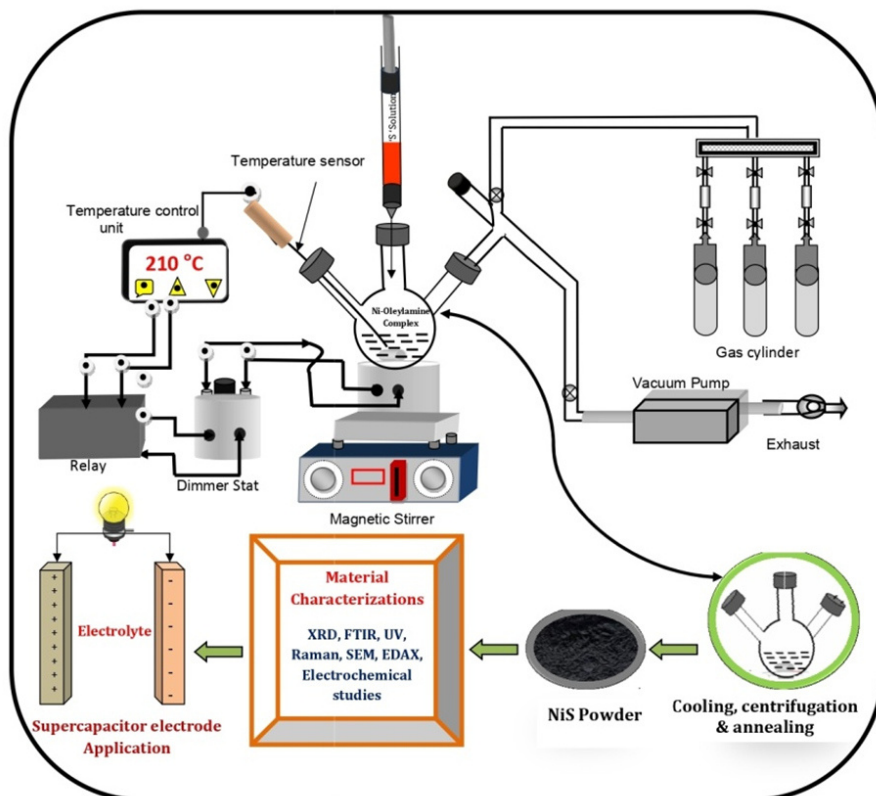


FIG. 1. Schematic for the synthesis of NiS powder

The XRD pattern of NiS synthesized at 2 molar sulphur concentration shows major diffraction peaks at two theta equal to 30.24, 34.54, 45.74, 53.57, 60.80, 62.68, 65.31, 70.64, and 73.10° which is perfectly indexed to the NiS reflections of (100), (101), (102), (110), (103), (200), (201), (004), and (202) crystal planes respectively. The observed well-defined diffraction peaks of NiS nanoparticles are well indexed to the hexagonal phase of NiS with space group $P6_3/mmc$ (JCPDS No.: 10-075-0613) [21]. No other peaks were observed in the XRD pattern, indicating that pure NiS nanoparticles were successfully synthesized. The NiS nanoparticles synthesized at 1 molar sulphur concentration confirm a major diffraction peak of 100 plane whereas NiS nanoparticles synthesized at 3 molar sulphur concentrations shows 100, 101, 102 and 110 diffraction peaks. The NiS nanoparticles synthesized at 2 molar sulphur concentration show well crystalline nature as compared with the other two samples. Thus, the sulphur concentrations play an important role in the synthesis of well crystalline NiS nanoparticles. The intense and sharp diffraction peaks suggest that the synthesized NiS is well crystalline. The average crystalline size of synthesized NiS materials has been calculated from the Debye–Scherrer formula

$$d_{x\text{-ray}} = \frac{0.9\lambda}{\beta \cos \theta}, \quad (1)$$

where $d_{x\text{-ray}}$ is the crystalline size, λ is the wavelength of X-ray, β is full width half maxima (FWHM) and θ is the diffraction angle. The average crystalline size of synthesized NiS nanoparticles synthesized at 2 molar sulphur concentrations is found to be 58 nm. The lattice constants and average crystalline size of NiS nanoparticles synthesized at different sulphur concentrations are listed in Table 1. The observed and calculated XRD parameters of the NiS sample are listed in Table 2.

TABLE 1. Lattice constants and average crystalline size of NiS nanoparticles synthesized at different sulphur concentration

Sulphur concentration (Mole)	Lattice constant (Å)		Average crystalline size (nm)
	a	c	
1	3.4152	5.2264	42
2	3.4197	5.3174	58
3	3.4086	5.3268	46

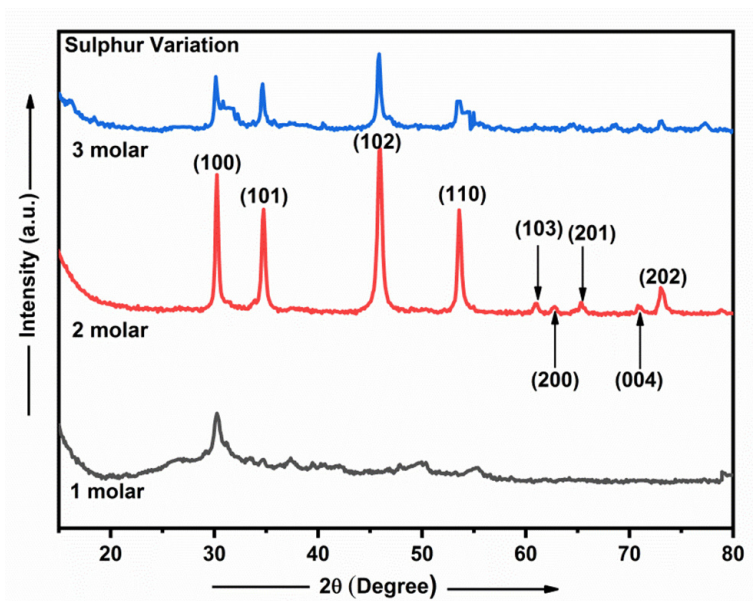


FIG. 2. XRD pattern of NiS nanoparticles synthesized at different sulphur concentration

TABLE 2. Indexed X-ray diffraction pattern of NiS nanoparticles

Sr. No.	2θ	Interplaner spacing (observed) Å	Interplaner Spacing (calculated) Å	[hkl]
1	30.14	2.9618	2.9615	100
2	34.54	2.5854	2.5936	101
3	45.74	1.9749	1.9812	102
4	53.57	1.7100	1.7086	110
5	60.80	1.5172	1.5216	103
6	62.68	1.4809	1.4804	200
7	65.31	1.4262	1.4270	201
8	70.64	1.3250	1.3318	004
9	73.10	1.2927	1.2929	202

3.2. Raman analysis

The Raman spectrum of NiS nanoparticles synthesized at different sulphur concentrations is shown in Fig. 3. Raman bands observed at 181, 345 and 533 cm^{-1} indicates the formation of NiS [22]. However, not all vibrational modes of NiS have been observed, which could affect the effect of quantum confinement on the vibrational modes of NiS nanoparticles [23]. The decrease in the sharpness of the peak is related to a reduction of the volume fraction of crystallites in the material [24]. Fig. 3 shows that material synthesized at 2 molar sulphur concentration is more crystalline as compared with the other two samples.

3.3. Optical properties

The optical properties of NiS nanoparticles synthesized using the hot injection method at different sulphur concentrations are shown in Fig. 4. For NiS nanoparticles, the UV-Vis absorption spectra show peaks at 285, 287 and 290 nm for the sample synthesized at 1, 2 and 3 molar sulphur concentrations, respectively. These peaks can be attributed to the band edge absorption of NiS nanoparticles. The absorption spectrum shows a blue shift compared to the NiS bulk (295 nm) [25], due to the small size of the particles [26].

The optical band gap of NiS nanoparticles is calculated using Tauc's relation [27]

$$\alpha h\nu = k(h\nu - E_g)^n, \quad (2)$$

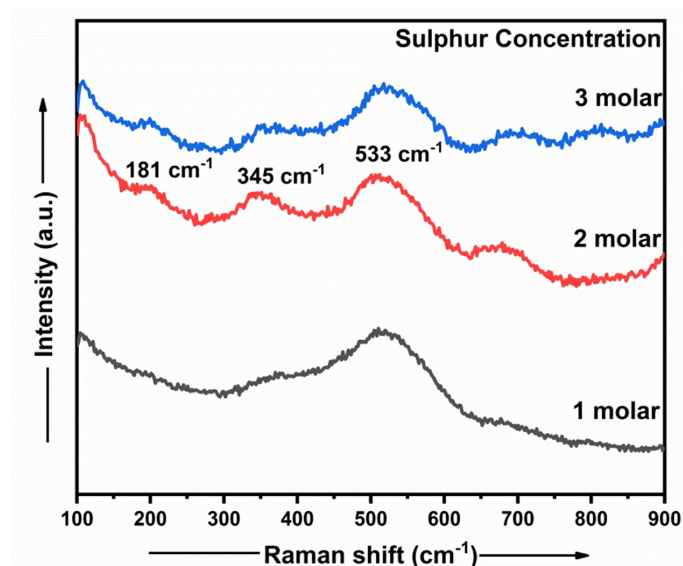


FIG. 3. Raman spectra of NiS nanoparticles synthesized at different sulphur concentration

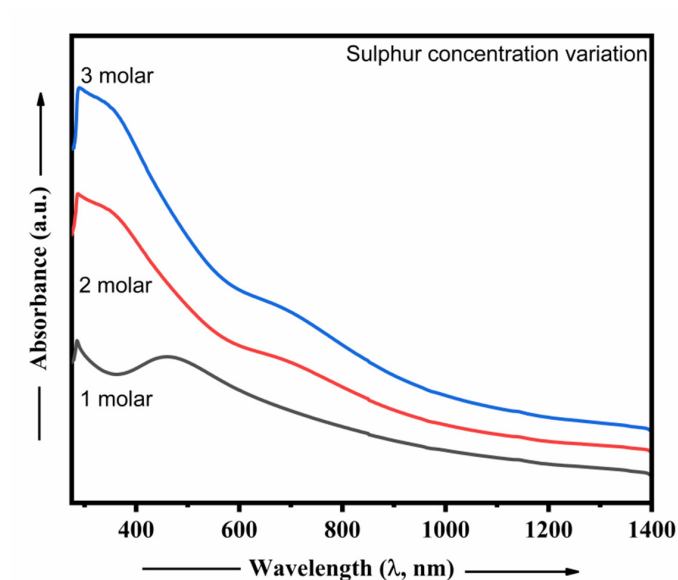


FIG. 4. Absorbance spectra of NiS nanoparticles

where, α is the absorption coefficient, ν is the frequency, h is Planck's constant, k and n are constants. The plots of $(\alpha h\nu)^2$ Vs. $h\nu$ for NiS nanoparticles are shown in Fig. 5. The optical band gap energy is calculated by extrapolating the linear portion of the curve to the energy axis. The band gap energy of NiS nanoparticles synthesized at 1, 2 and 3 molar sulphur concentration was found to be 1.9, 1.98 and 1.81 eV, respectively. We have observed that the band gap energy of the synthesized material is higher than its bulk [28].

3.4. Morphological properties of NiS nanoparticles

The surface morphological features of NiS nanostructures were studied by using SEM. The SEM images of NiS nanostructures synthesized at different sulphur concentrations by the hot injection method are shown in Fig. 6. From the SEM images agglomeration of nanoparticles with irregular shapes were observed. The SEM images of NiS nanostructures synthesized at different sulphur concentrations show porous in nature.

The EDAX spectra were used for knowing the atomic % of the elements in the synthesized samples. The EDAX spectrum shows the presence of nickel and sulphur in the synthesized material. Table 3 shows the elements in atomic % of the samples synthesized at different sulphur concentrations. From Table 3, it is clear that as sulphur concentration increases atomic % of sulphur enhances whereas the atomic % of nickel reduces in the synthesized material and it is equivalent to the initial mixture used for the synthesis. Fig. 7 shows the EDAX spectra of the NiS nanostructures synthesized at different sulphur concentrations.

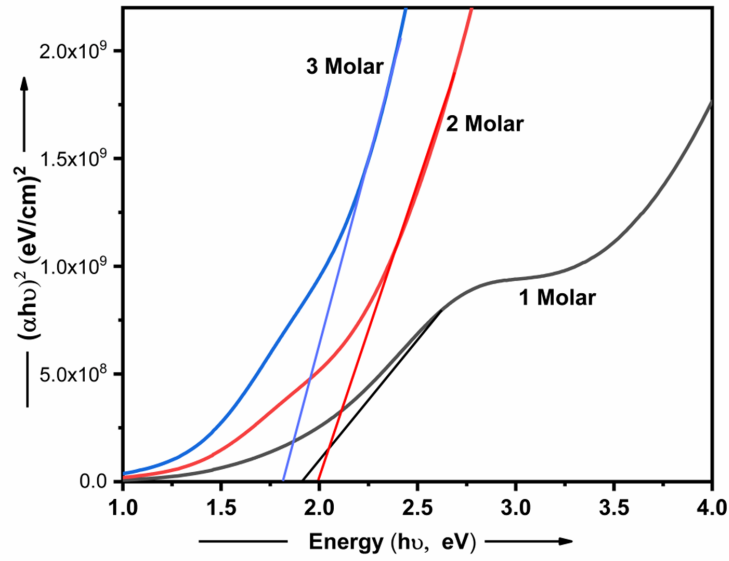


FIG. 5. Tauc's plot of NiS nanoparticles

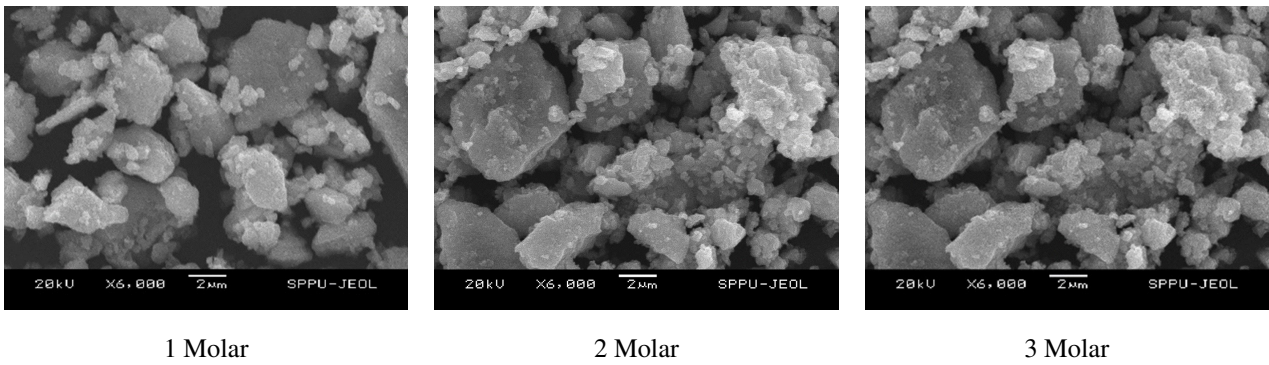


FIG. 6. SEM images of NiS nanostructures synthesized at different sulphur concentration

TABLE 3. The elemental compositions of NiS nanostructures synthesized at different sulphur concentrations in terms of atomic %

Sulphur concentrations	Elements	Atomic %
1 molar	Sulphur	54.41
	Nickel	45.59
2 molar	Sulphur	56.10
	Nickel	43.90
3 molar	Sulphur	60.72
	Nickel	39.28

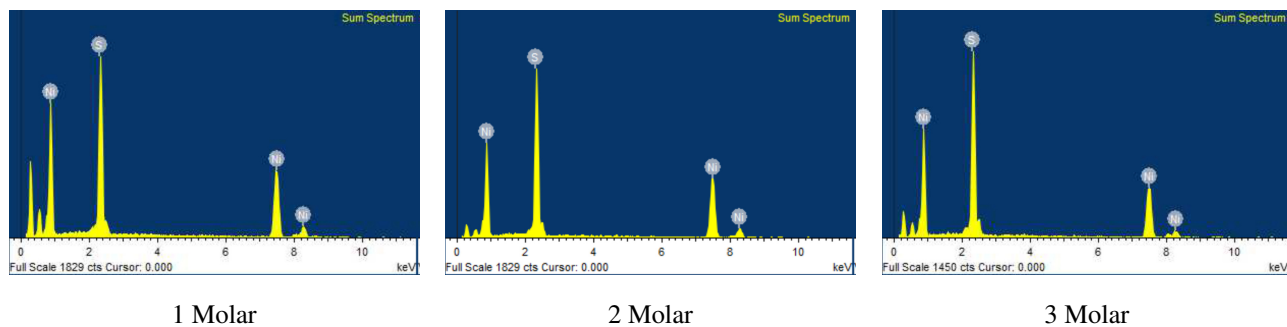


FIG. 7. EDAX spectra of NiS nanostructures synthesized at different sulphur concentration

3.5. FTIR analysis

The synthesized NiS nanoparticles were further examined by FTIR spectroscopy. Fig. 8 shows the FTIR spectra of nickel sulphide nanoparticles synthesized at different sulphur concentrations by the hot injection system. The absorption bands observed nearly at 640 and 960 cm^{-1} are associated to the symmetrical and asymmetrical stretching of the nickel-sulphur (Ni-S) band in NiS particles. The bending vibrations of the sulfonated group were confirmed from the peak observed at 1140 cm^{-1} [29]. The peak observed nearly at 652 cm^{-1} is related to Ni-S-Ni bending vibration mode and the absorption band nearly at 503 cm^{-1} is due to Ni-S bending vibration [30]. The very small bands appeared in the FTIR spectra nearly at 2920 cm^{-1} is due to the bending vibration of H_2O molecules. The IR bands appeared nearly at 1464 and 3005 cm^{-1} , indicating amine ligand is bound to the nanoparticles [31]. Thus, from FTIR spectra, it is clear that no additional IR vibrational peaks were observed indicates the high purity of synthesized powder.

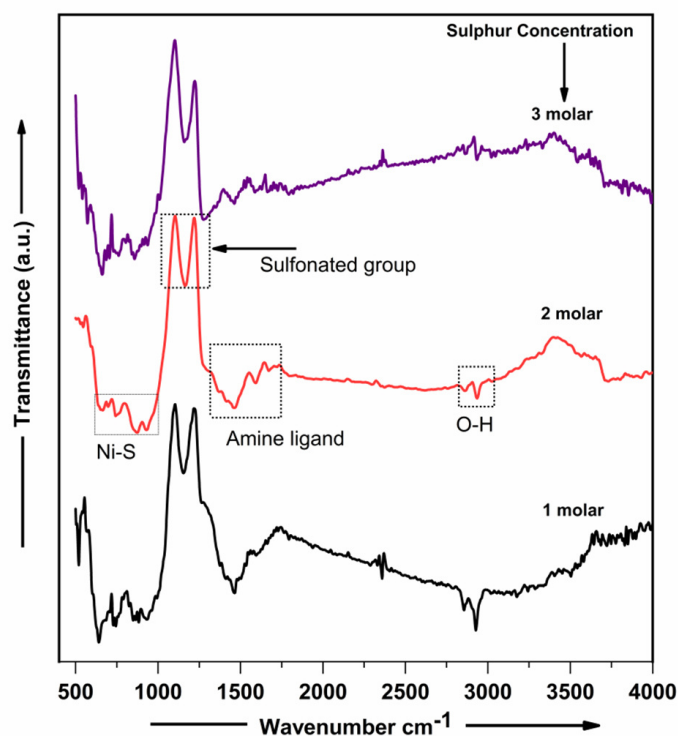


FIG. 8. FTIR spectra of NiS nanoparticles synthesized at different sulphur concentration

3.6. Electrochemical studies

3.6.1. Electrode preparation. The electrode was prepared by mixing 80 wt% nanocrystalline NiS powder as an active material, 10 wt% activated carbon as a conducting additive and 10 wt% Polyvinyl difluoride (PVDF) as a binder in N-Methyl Pyrrolidone (NMP) solvent. The slurry was grinded adequately in the mortar pestle to get a homogeneous mixture, after that it was coated on a carbon paper substrate ($1\text{ cm} \times 1\text{ cm}$ area) using the doctor blade technique. This technique was firstly developed by Glen Howatt for the fabrication of thin sheets of ceramic capacitors [32]. In this technique,

material to be deposited (slurry) is fixed between the blade and substrate. During the fabrication of the film, there is a constant relative movement between the blade and substrate in which slurry uniformly spreads on the substrate. The doctor blade technique is used for large area film fabrication. It is technologically simple and low-cost. Despite these nearly 100 % materials are utilized for film fabrication and hence the small quantity of material is sufficient to form the well defined thickness of film [33]. The mass of the material loaded on the substrate was calculated via the weight difference method. The fabricated electrodes were dried at 150 °C for overnight inside a hot air oven to remove solvent and were used as a working electrode for further electrochemical analysis.

3.6.2. Electrochemical studies. Herein, the cyclic voltammetry (CV), galvanostatic charge-discharge (GCD), and electrochemical impedance spectroscopy (EIS) measurements of NiS powder electrode synthesized at 2 molar sulphur concentration was carried out to examine and evaluate supercapacitive performance using a potentiostat (Metrohm Autolab: PGSTAT302N model). The measurement system consists of a cell in three-electrode configurations adopting the carbon paper coated with active material as a working electrode, Platinum foil as a counter and Hg/HgO as a reference electrode. All measurements were evaluated in aqueous solution of 2 M KOH. The EIS measurements were investigated using the same potentiostat with three-electrode cell configurations under open circuit voltage with amplitude of 10 mV between applied frequency sweeps from 1 MHz to 0.1 Hz.

3.6.3. Cyclic voltammetry (CV). The specific capacitance (CS in F/g) and energy density (E) of the NiS powder electrode was calculated from cyclic voltammetry (CV) measurements using equations (3) and (4):

$$C_p = \frac{1}{ms\Delta V} \int I(V)dV, \quad (3)$$

$$E_{cv} = \frac{1}{2} C_p \cdot \Delta V^2, \quad (4)$$

where m is the mass of active materials loaded on working electrode (in gm), I is the response current (in A), $\int I(V)dV$ is area under the current-voltage (CV) curve, s is the scan rate (in mVs^{-1}) and ΔV is operating potential windows (in volt).

CV measurements of the synthesized NiS powder electrode were carried out with potential range from 0.0 to 0.5 V at different scan rates of 5, 10, 20, 50 and 100 mV/s is presented in Fig. 9. The material synthesized at 2 molar sulphur concentration shows better electrochemical performance compared with the others. As the scan rate increases the shapes of CV graphs remain almost the same showing the excellent electrode capabilities and ideal supercapacitor nature [34]. The CV measurements show that as the scan rate increases, the area of the CV curve enhances denoting the behavior of an ideal capacitor. The highest specific capacitance value is 315.8 F/gm for 2 molar sulphur concentrations due to the great synergistic interaction between nickel and sulphur. The maximum value of specific capacitance may be due to the porous nature of the material as examined from SEM in which superior exposure of active sites and easier electrolyte access [35]. As the scan rate decreases the specific capacitance enhances, and the maximum capacitance was observed at lowest scan rate 5 mVs^{-1} . The calculated energy density values from CV graph is 6.99 WhKg^{-1} . Moreover, to illustrate the importance of this work, we have compared the present study with the earlier work reported in literature by considering different materials for supercapacitor electrode applications.

TABLE 4. Comparisons of the earlier studies reported for supercapacitor electrode applications

Sr. no.	Material	Method of synthesis	Electrolyte	Potential Window V	Specific capacitance (Fg^{-1})	Reference
1	CoS	Chemical bath deposition	Ethanol	-0.4 to 0.6	41.36	[36]
2	Nickel sulfide/ reduced graphene oxide	Solution combustion Method	KOH	0.0 to 0.4	305	[37]
3	NiFe_2O_4	Chemical oxidation	KOH	0.0 to 0.45	266	[38]
4	$\text{Mg}_{0.1}\text{Mn}_{0.9}\text{Fe}_2\text{O}_4$	Solvothermal reflux	KOH	0.0 to 0.6	226.4	[39]
5	NiS	Hot injection method	KOH	0.0 to 0.5	315.8	Present work

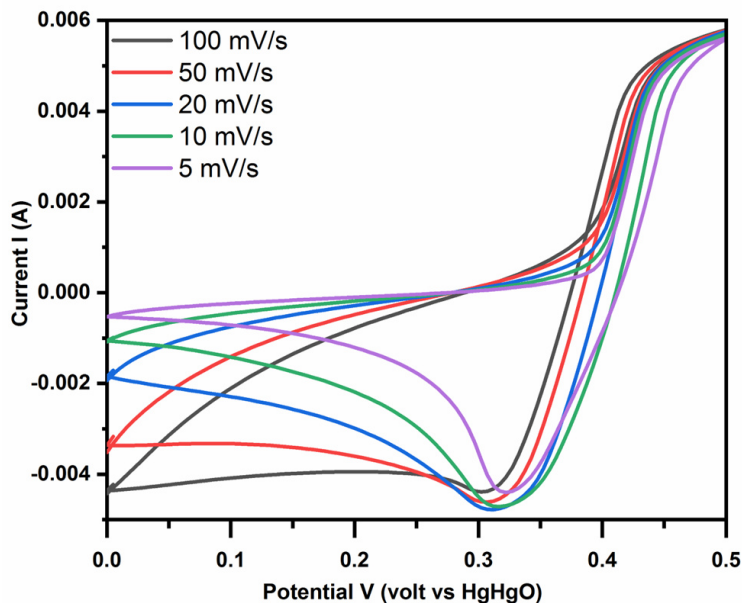


FIG. 9. CV measurements of the synthesized NiS powder electrode recorded in the voltage range of 0 to 0.5 V at different scan rates

3.6.4. *Galvanostatic charge-discharge (GCD)*. The GCD study of the NiS powder electrode was carried out at different current densities 1.0, 1.5 and 2.0 A/g within the potential window 0 to 0.4 V in 2 M KOH electrolyte. Fig. 10 shows the GCD curves of NiS powder electrode at different current densities. The specific capacitance C_s (Fg^{-1}), energy density E (WhKg^{-1}) and power density P (WKg^{-1}) can also be calculated from the galvanostatic charge-discharge plot using the following equation.

$$C_s = \frac{I \cdot t_d}{m \cdot \Delta V}, \quad (5)$$

$$E = \frac{1}{2} C_s \cdot \Delta V^2, \quad (6)$$

$$P = \frac{E}{t_d}, \quad (7)$$

where I is the response current (A), m is the mass of active material (kg), ΔV is the potential window (V), and t_d is the discharge time (h). The calculated value of energy density is 3.324 WhKg^{-1} and power density 199 WKg^{-1} for lower current density.

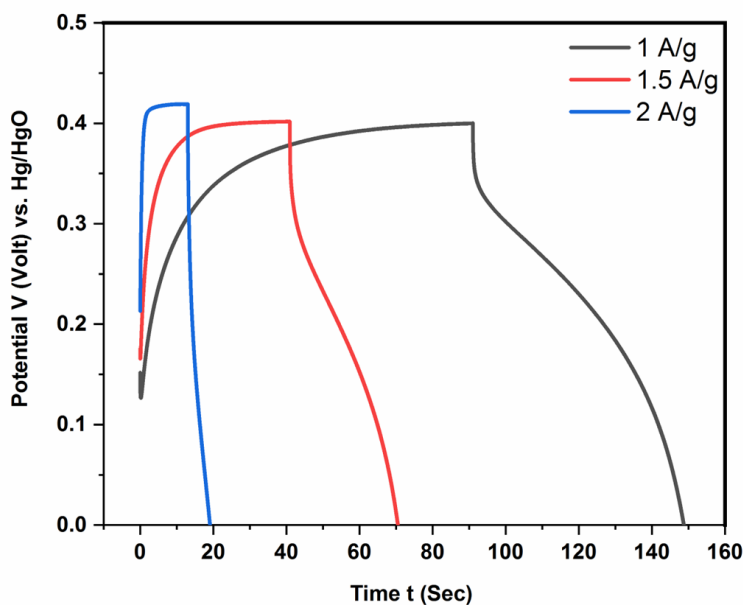


FIG. 10. Charging-discharging performance of NiS electrode at different current densities

The Nyquist plot of the NiS powder electrode synthesized at 2 molar sulphur concentrations was measured in the frequency range from 1 Mhz to 0.1 Hz as presented in Fig. 11. The nearly vertical line in the Nyquist plot shows the ideal supercapacitor nature and the diameter of the small semicircle in high-frequency range represents the interfacial charge transfer resistance (R_{ct}) between the electrolyte and electrode. The intersecting point with the real axis in the high-frequency region represents the internal resistance (R_s) of the electrode material (including ionic resistance, inherent resistance of material and contact resistance of electrode material and electrolyte). The Nyquist plot is fitted to an equivalent electronic circuit, as shown in the inset of the Fig. 11. The values of R_s and R_{ct} are 9 and 7.3 ohm. The Warburg resistance was due to the diffusion of the electrolyte in the bulk of the electrode. The small semicircle arc in high-frequency region indicates good electrical conductivity and low charge transfer resistance of the electrode materials. Thus, the Nyquist plot shows NiS powder synthesized at 2 molar sulphur concentration shows good electrical conductance with high specific capacitance.

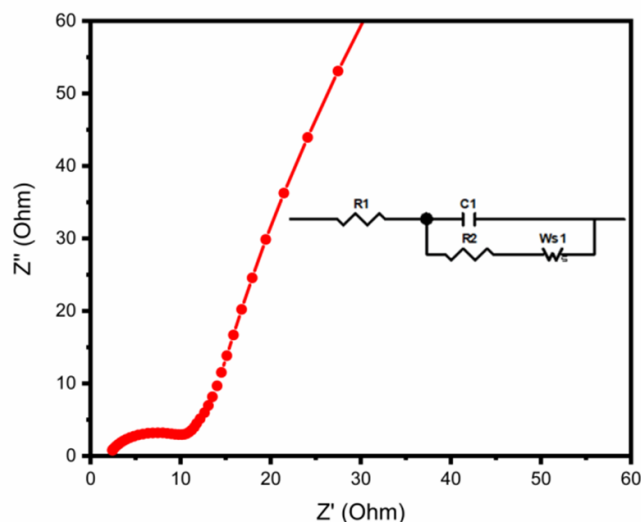


FIG. 11. The Nyquist plot of NiS powder electrode synthesized at 2 molar sulphur concentrations. Inset shows the electrical equivalent circuit used for the fitting impedance spectra.

4. Conclusion

We have successfully synthesized nickel sulfide nanoparticles using the simple and low-cost hot injection method in oleylamine solvent. The absorption spectrum of NiS nanoparticles is blue-shifted compared to bulk material, indicating the presence of small size of crystallites in the synthesized material. The optical band gap energy of NiS nanoparticles was found in the range of 1.81 to 1.98 eV. It shows that the synthesized NiS nanoparticles are suitable for energy conversion device applications. The X-ray diffraction pattern and the Raman spectra confirm the formation of high purity NiS nanoparticles. The samples synthesized at 2 molar sulphur concentrations have a good crystalline nature as compared with the other two samples. Thus, the crystallinity of the synthesized materials highly depends on sulphur concentrations. The agglomeration of nanoparticles was observed from SEM images. The electrochemical studies show that synthesized NiS nanoparticles is a promising material for supercapacitor electrode applications. The estimated values of specific capacitance, energy density and power density are 315.8 F/g, 6.99 WhKg⁻¹ and 199 Wkg⁻¹, respectively. In this work, 2 molar sulphur concentrations are optimized for the synthesis of superiority nanoparticles. The crystallinity, particle size, morphology and electrochemical performance of NiS nanoparticles strongly depend on sulphur concentration. Thus, the present study shows that sulphur concentration plays an important role in the synthesis of high-quality NiS nanoparticles. This work provides that the hot injection method is a novel method for the synthesis of device quality nickel sulfide and other metal sulfides for energy conversion and energy storage applications.

References

- [1] Wang G., Zhang L., Zhang J. A review of electrode materials for electrochemical supercapacitors. *Chem. Soc. Rev.*, 2012, **41**, P. 797–828.
- [2] Gao Y.P., Wu X., Huang K.J., Xing L.L., Zhang Y.Y., Liu L. Two-dimensional transition metal diseleniums for energy storage application: a review of recent developments. *Cryst. Eng. Comm.*, 2017, **19**, P. 404–418.
- [3] Parveen N., Ansari M.O., Ansari S.A., Cho M.H. Simultaneous sulfur doping and exfoliation of graphene from graphite using an electrochemical method for supercapacitor electrode materials. *J. Mater. Chem. A*, 2016, **4**, P. 233–240.
- [4] Zhang L.L., Zhao X.S. Carbon-based materials as supercapacitor electrodes. *Chem. Soc. Rev.*, 2009, **38**, P. 2520–2535.
- [5] De B., Balamurugan J., Kimand N.H., Lee J.H. Enhanced electrochemical and photocatalytic performance of core-shell CuS@ carbon quantum dots@ carbon hollow nanospheres. *ACS applied materials & interface*, 2017, **9** (3), P. 2459–2468.

- [6] Guan B.Y., Yu L., Wang X., Song S., Lou X.W. Formation of Onion-Like NiCo₂S₄ Particles via Sequential Ion-Exchange for Hybrid Supercapacitors. *Adv. Mater.*, 2017, **29**, 1605051.
- [7] Chen H., Jiang J., Zhang L., Xia D., Zhao Y., Guo D., Qi T., Wan H. In situ growth of NiCo₂S₄ nanotube arrays on Ni foam for supercapacitors: Maximizing utilization efficiency at high mass loading to achieve ultrahigh areal pseudocapacitance. *J. Power Sources*, 2014, **254**, P. 249–257.
- [8] Zhang Z., Wang Q., Zhao C., Min S., Qian X. One-step hydrothermal synthesis of 3D petal-like Co₉S₈/RGO/Ni₃S₂ composite on nickel foam for high-performance supercapacitors. *ACS Appl. Mater. Inter.*, 2015, **7**, P. 4861–4868.
- [9] Gou J., Xie S., Yang Z., Liu Y., Chen Y., Liu Y., Liu C. A high-performance supercapacitor electrode material based on NiS/Ni₃S₄ composite. *Electrochim. Acta*, 2017, **229**, P. 299–305.
- [10] Yang J., Duan X., Guo W., Li D., Zhang H., Zheng W. Electrochemical performances investigation of NiS/rGO composite as electrode material for supercapacitors. *Nano Energy*, 2014, **5**, P. 74–81.
- [11] Wang P.T., Zhang X., Zhang J., Wan S., Guo S.J., Lu G., Yao J.L., Huang X.Q. Precise tuning in platinum-nickel/nickel sulfide interface nanowires for synergistic hydrogen evolution catalysis. *Nat. Commun.*, 2017, **8**, 14580.
- [12] Ye C., Zhang L., Guo C.X., Li D.D., Vasileff A., Wang H.H., Qiao S.Z. A 3D Hybrid of chemically coupled nickel sulfide and hollow carbon spheres for high performance lithium-sulfur batteries. *Adv. Funct. Mater.*, 2017, **27** (33), 1702524.
- [13] Sun H.C., Qin D., Huang S.Q., Guo X.Z., Li D.M., Luo Y.H., Meng Q.B. Dye-sensitized solar cells with NiS counter electrodes electrodeposited by a potential reversal technique. *Energy Environ. Sci.*, 2011, **4** (8), P. 2630–2637.
- [14] Ajibade P.A., Nqombolo A. Synthesis and Structural Studies Of Nickel Sulphide And Palladium Sulphide Nanocrystals. *Chalcogenide Letters*, 2016, **13** (9), P. 427–434.
- [15] Salavati-Niasari M., Banaiean-Monfared G., Emadi H., Enhessari M. Synthesis and characterization of nickel sulfide nanoparticles via cyclic microwave radiation. *Comptes Rendus Chimie*, 2013, **16** (10), P. 929–936.
- [16] Karthikeyan R., Navaneethan M., Archana J., Thangaraju D., Arivanandhan M., Hayakawa Y. Shape controlled synthesis of hierarchical nickel sulfide by the hydrothermal method. *Dalton Trans.*, 2014, **43** (46), P. 17445–17452.
- [17] Yang P., Song B., Zheng Y., Sun Y., Jian J.K. Solvothermal growth of NiS single-crystalline nanorods. *J. Alloy Compd.*, 2009, **481**, P. 450–454.
- [18] Peng L., Ji X., Wan H., Ruan Y., Xu K., Chen C., Miao L., Jiang J. Nickel Sulfide Nanoparticles Synthesized by Microwave-assisted Method as Promising Supercapacitor Electrodes: An Experimental and Computational Study. *Electrochimica Acta*, 2015, **182**, P. 361–367.
- [19] Kristl M., Dojer B., Gyergyek S., Kristl J. Synthesis of nickel and cobalt sulfide nanoparticles using a low cost sonochemical method. *Heliyon*, 2017, **3** (3), e-00273-00292.
- [20] Kamble M.M., Nasane M.P., Rondiya S.R., Dzade N.Y., Bade B.R., Funde A.M., Kore K.B., Jadkar S.R. Optical, structural and morphological study of CdS nanoparticles: role of sulfur source. *Nanomaterials and Energy*, 2020, **9** (1), P. 72–81.
- [21] Karthikeyan R., Thangaraju D., Prakashand N., Hayakawa Y. Single-step synthesis and catalytic activity of structure-controlled nickel sulfide nanoparticles. *Cryst. Eng. Comm.*, 2015, **17**, P. 5431–5439.
- [22] Bishop D.W., Thoms P.S., Ray A.S. Raman Spectra of Nickel(II) Sulfide. *Mater. Res. Bull.*, 1998, **33** (9), P. 1303–1306.
- [23] Yoshikawa M., Murakami M., Matsuda K., Matsunobe T., Sugie S., Okada K., Ishida H. Characterization of Si nano-polycrystalline films at the nanometer level using resonant Raman scattering. *J. Appl. Phys.*, 2005, **98**, P. 63531–63533.
- [24] Kamble M.M., Waman V.S., Maybadi A., Funde A.M., Sathe V.G., Shripati T., Pathan H.M., Jadkar S.R. Synthesis of cubic nanocrystalline silicon carbide (3C-SiC) films by HW-CVD method. *Silicon*, 2017, **9** (3), P. 421–429.
- [25] Chen X.Y., Wang Z.H., Wang X., Wan J.X., Liu J.W., Qian Y.T. A single-source approach to metastable Ni₃S₄ crystallites and their optical properties. *Chem. Lett.*, 2004, **33** (10), P. 1294–1295.
- [26] Hu Y., Chen J.F., Chen W.M., Lin X.H., Li X.L. Synthesis of Novel Nickel Sulfide Submicrometer Hollow Spheres. *Adv. Mater.*, 2003, **15**, P. 726–729.
- [27] Tauc J. (Ed.) *Amorphous and Liquid Semiconductor*, Plenum Press, New York, 1974, **159**.
- [28] Yong Xu, Martin A.A. Schoonen. The absolute energy positions of conduction and valence bands of selected semiconducting minerals. *American Mineralogist*, 2000, **85**, P. 543–556.
- [29] Darezereshki E., Vakylabad A.B., Hassanzadeh A., Niedoba T., Surowiak A., Koohestani B. Hydrometallurgical Synthesis of Nickel Nano-Sulfides from Spent Lithium-Ion Batteries. *Minerals*, 2021, **11**, P. 419–431.
- [30] Bobinihi F.F., Fayemi O.E., Onwudiwe D.C. Synthesis, characterization, and cyclic voltammetry of nickel sulphide and nickel oxide nanoparticles obtained from Ni(II) dithiocarbamate. *Materials Science in Semiconductor Processing*, 2021, **121**, P. 105315–105327.
- [31] Buchmaier C., Glanzer M., Torvisco A., Poelt P., Wewerka K., Kunert B., Gatterer K., Trimmel G., Rath T. Nickel sulfide thin films and nanocrystals synthesized from nickel xanthate precursors. *J. Mater. Sci. Electronic materials*, 2017, **52** (18), P. 1–17.
- [32] Howatt G., Breckenridg R. Fabrication of Thin ceramic Sheets for Capacitors. *J. Brownlow, J. Am. Ceram. Soc.*, 1947, **30**, P. 237–242.
- [33] Krebs F.C. Fabrication and processing of polymer solar cells: a review of printing and coating techniques. *Solar Energy Materials and Solar Cells*, 2009, **93**, P. 394–412.
- [34] Emmenegger C., Mauron P., Sudan P., Wenger P., Hermann V., Gallay R., Zuttel A. Investigation of electrochemical double-layer (ECDL) capacitors electrodes based on carbon nanotubes and activated carbon materials. *J. Power Sources*, 2003, **124**, P. 321–329.
- [35] Sylla N.F., Ndiaye N.M., Ngom B.D., Momodu D., Madito M.J., Mutuma B.K., Manyala N. Effect of porosity enhancing agents on the electrochemical performance of high-energy ultracapacitor electrodes derived from peanut shell waste. *Sci. Rep.*, 2019, **9** (2019), P. 13673–13688.
- [36] Kumar Y.A., Rao S.S., Punnoose D., Tulasivarma C.V., Chandu V.V.M. Gopi, Prabakar K., Kim H.J. Influence of solvents in the preparation of cobalt sulfide for supercapacitors. *R. Soc. Open Sci.*, 2017, **4**, P. 170427–170438.
- [37] Marand N.A., Masoudpanah S.M., Alamolhoda S., Bafghi M.Sh. Solution combustion synthesis of nickel sulfide/reduced graphene oxide composite powders as electrode materials for high-performance supercapacitors. *J. of Energy Storage*, 2021, **39**, P. 102637–102644.
- [38] Meena S., Anantharaju K., Malini S., Dey A., Renuka L., Prashantha S., Vidya Y. Impact of temperature-induced oxygen vacancies in polyhedron MnFe₂O₄ nanoparticles: As excellent electrochemical sensor, supercapacitor and active photocatalyst. *Ceram. Int.*, 2021, **10**, P. 14723–14740.
- [39] Manohar A., Vijayakanth V., Vattikuti S., Kim K.H. Structural and electrochemical properties of mixed calcium-zinc spinel ferrites nanoparticles. *Ceram. Int.*, 2022, **48** (20), P. 30695–33070.

Information about the authors:

Mahesh Mahadev Kamble – PDEA'S Anantrao Pawar College, Pirangut, Mulshi, Pune 412115 India;
ORCID 0000-0001-6835-5674; mmkamble14@gmail.com

Bharat Rambhau Bade – Department of Physics, Savitribai Phule Pune University, Pune 411007 India;
ORCID 0000-0001-8450-6807; badebharat94@gmail.com

Avinash Vinayak Rokade – Department of Physics, Savitribai Phule Pune University, Pune 411007 India;
ORCID 0009-0002-3892-2580; avinashrokade12@gmail.com

Vaishali Sambhaji Waman – P. E. S. Modern College of Arts, Science and Commerce, Shivajinagar, Pune 411005 India;
ORCID 0009-0003-1925-9637; vaishaliwaman@gmail.com

Sachin Vasant Bangale – Chemical Research Lab, UG and PG Department of Chemistry, G. M. Vedak College of Science, Tala-Raigad, 402111 India; ORCID 0000-0003-3495-7313; sachinbangale98@gmail.com

Sandesh Rohidas Jadkar – Department of Physics, Savitribai Phule Pune University, Pune 411007 India;
ORCID 0000-0002-0610-7242; sandesh@physics.unipune.ac.in

Author's Contributions: MMK, BRB and SRJ carried out the experimental study, participated in the sequence of alignment and drafted the manuscript. AVR, SVB and VSW helped in data analysis and interpretation.

Data Availability Statement: Data available on request from the authors.

Conflict of interest: the authors declare no conflict of interest.

The effect of layered silicates on the morphological, rheological and mechanical properties of PA and PP blends

Qodirbek Nuridin ugli Berdinazarov^{1,a}, Elshod Olmosovich Khakberdiev^{1,b},
Nigmat Rustamovich Ashurov^{1,c}

¹Institute of Polymer Chemistry and Physics, Uzbekistan Academy of Sciences, Tashkent, Uzbekistan

^aqodirberdinazarov@mail.ru, ^bprofhaqberdiyev@gmail.com, ^cnigmat.ashurov@gmail.com

Corresponding author: Q. Berdinazarov, qodirberdinazarov@mail.ru

PACS 83.80.Tc, 82.35.Np, 82.35.Lr

ABSTRACT We study rheological, morphological and mechanical properties of polyamide-6 (PA) and polypropylene (PP) blends in the presence of layered silicates (two types of organically modified montmorillonite - Cloisite30B for PA and Cloisite20A for PP). For comparison, we used maleic anhydride grafted polypropylene (PP-g-MA) as a compatibilizer and in all compositions weight ratio of PA and PP was constant 80/20, respectively. Introduction of layered silicates always led to more viscous melt and increased storage modulus. It is also identified that layered silicates cause more finer-dispersed morphology than PP-g-MA. Elastic modulus and yield strength were increased when the layered silicates were introduced in either composites or blends.

KEYWORDS Polyamide-6, polypropylene, montmorillonite, polymer composite, polymer blend, compatibilizer

ACKNOWLEDGEMENTS The authors acknowledge prof. Paula Moldenaers and her SMaRT team for their assistance in conducting practical experiments. The study was financed by the project of "Nanocomposite polymer-polymer blend materials on the basis of polyolefins produced in Uzbekistan".

FOR CITATION Berdinazarov Q., Khakberdiev E., Ashurov N. The effect of layered silicates on the morphological, rheological and mechanical properties of PA and PP blends. *Nanosystems: Phys. Chem. Math.*, 2024, **15** (3), 410–417.

1. Introduction

Blends of polyamide (PA) and polypropylene (PP) have gained significant prominence in various industrial applications due to their multifaceted advantages. Combining the inherent chemical resistance of PA with the lightweight characteristics of PP results in a material that not only exhibits robust resistance to a variety of chemicals but also facilitates weight reduction in applications where mass is a crucial factor. Furthermore, the synergistic combination of these polymers contributes to enhanced thermal stability, making the blend suitable for applications demanding resilience to elevated temperatures. The incorporation of cost-effective PP into the blend not only reduces overall material costs but also imparts improved mechanical properties by balancing the high tensile strength and impact resistance of PA with the stiffness of PP. This combination of chemical resistance, weight reduction, enhanced thermal stability, cost reduction, and improved mechanical properties positions PA-PP blends as versatile and economically viable solutions across diverse industrial sectors. Aside from their common applications in automobile interior and exterior components such as dashboard panels, door trims, bumpers, and wheel arch liners, PP/PA blends prove invaluable under the hood as well. With their notable heat resistance and durability, these blends find ideal use in critical under-the-hood components like air intake manifolds [1, 2]. Furthermore, their exceptional thermal stability and resistance to automotive fluids render them suitable candidates for engine covers, contributing to the reliable performance and longevity of automotive engines [3, 4].

At the same time, the incompatibility of these polymer pairs limits the achievement of the set goals. The incompatibility of polymers is rooted in low interfacial adhesion; conversely, high interfacial tension exacerbates this issue [5–8]. The solution to this problem has been demonstrated in numerous compatibilization experiments, wherein a third functionalized polymer is introduced to enhance compatibility with one of the components of the blend and react effectively with the other component. This approach is called reactive compatibilization, forming a copolymer (graft or block copolymer), as a rule, reaches the phase boundary and prevents the process of coalescence of particles of the dispersed phase and stabilizes the desired blend morphology [9, 10]. The implementation of such an approach to the PA and PP pairs by using compatibilizers such as maleic anhydride grafted PP (PP-g-MA) or ethylene-polypropylene copolymer can significantly reduce the water absorption of PA and significantly increase the dimensional stability and impact resistance of the polymer blend [11–13].

Another important approach is the introduction of nanosized non-organic fillers into polymer blends, among which layered silicates occupy a special place. Dispersion of particles of layered silicate to nanosizes (particles in the form of

discs with a thickness of less than one nanometer and a perimeter is approximately 100 nm) or intercalation of macromolecules into the interlayer space of layered silicate allows a very significant increase in the elastic modulus, yield strength, and reduces permeability [14, 15].

Composites in which the necessary levels of specific interaction with the surface of the particles of layered silicate and modifier are provided lead to the formation of exfoliated and intercalated nanocomposites, respectively. Specific interaction is easily achieved for polar PA, while polyolefins require the introduction of a certain proportion of a functionalized polymer, that is, a compatibilizer, for which the earlier maleic anhydride grafted polyolefins have proven to be effective [16].

The combination of these two approaches for a PA/PP blend has been the subject of a number of studies [17–20]. At the same time, in many works, the components of the blend, two polymers and particles of layered silicate, and in some cases with the addition of functionalized PP for compounding, were loaded into the extruder at the same time. This method was initiated in work [21], in which it was shown that the introduction of nanosized inorganic third particles in a blend of polymers leads to their indication at the phase boundary, that is, a compatibilizing effect was discovered. Depending on the degree of polarity, the mixing of blend components and the type of modifier of the organically modified layered silicate, the particles can be located in one of the phases, in two phases simultaneously or at the phase boundary [22].

The compatibilizing effect, which is manifested in the case of particles of layered silicate in one of the polymer phases, especially dispersed, the other two cases determine the possibility of transition from dispersed morphology to coexisting two continuous phases and changing the pattern over the phases. A slightly different, combined method for the formation of PA/PP polymer blends in the presence of modified montmorillonite (MMT) has been proposed [21]. The difference is that the first family of compositions was obtained in one stage (introduction of the blend components, simultaneous), in second the approach - the compositions were obtained in two stages, that is the second polymer (PA or PP) was extruded with finished compositions in the second stage. That is, the authors, as it were, considered 2 variants of components based on PA/PP with the introduction of a modified MMT in the presence and absence of a compatibilizer (PP-g-MA). In all cases, with the exception of the two-stage variant of obtaining the composition of PA and organically modified (OMMMT) at the first stage and with the subsequent addition of PP, the authors observed the formation of various levels of intercalated structures. Moreover, the same composition, with the addition of a compatibilizer, formed only an intercalated structure. The mechanism of such a phenomenon was not disclosed in the work. Unfortunately, the authors of the work did not present the characteristics of the layered silicate sample, one thing is clear that these particles are concentrated in the PA phase. The authors formulate the final conclusions as follows: finer dispersion of layered silicate particles leads to a noticeable increase in the elastic modulus up to 42%, while compatibilization of a blend of two polymers contributes to an increase in the yield strength of nanocomposite polymer blends. In addition to this, the authors did not take into account the formation of a third polymer phase in the form of a well-known copolymer of PA with PP-g-MA. As noted by the authors of the work [23, 24], this copolymer not only contributes to the increase in interfacial adhesion between PA and PP, but also to a certain extent they are preferential territories for the introduction of layered silicate particles.

In this work, the PA:PP blend in 80:20 ratio was selected as the most favorable after evaluating the physicochemical characteristics across a range of sample compositions we also chose a two-stage variant preparation of the PA/PP polymer blends. At the first stage, a sample was obtained from pure components, separately compositions of PA/PP with OMMMT (Cloisite20A and Cloisite30B, respectively, in the presence and absence of a compatibilizer in the form of PP-g-MA), at the second stage, various compatibilization of PA and PP were mixed in the ratio of 80/20 wt.%. Knowledge of the initial structures and their transformation into mixing processes made it possible to establish the correlation dependences between the rheological characteristics, the features of the structure and morphology of the blends, and the final elastic-strength properties of multi-component nanostructured systems based on PA and PP.

2. Experimental

PA6, Toplon grade 1027 BRT, with $M_w = 80$ kDa, relative viscosity 2.7 was purchased. Isotactic PP (J-170T) with $M_w = 200$ kDa, MFI = (2.16 kg, 230°C) 21 g/10 min was kindly provided by JV Uz-Kor Gas Chemical LLC. PP-g-MA with 2.5 wt.% maleic anhydride content and MFI = (2.16 kg, 230°C) >200 g/min was provided by JV UzAuto CE-PLA LLC, as a gift. Cloisite30B, (spacing $d_{001} = 1.83$ nm, methylbis(2-hydroxyethyl)-tallow ammonium chloride conc. 0.9 mEq/g) and Cloisite20A, (spacing $d_{001} = 247$ nm., dimethyl dehydrogenated tallow ammonium conc. 0.95 mEq/g) Southern Clay Products, Inc., Gonzales, TX were used. The particle size in both clay types is less than 13 μm . Cloisite 20A and Cloisite 30B are modified montmorillonite clays through the incorporation of quaternary ammonium salts. Cloisite 20A is enriched with dimethyl dihydrogenated tallow ammonium chloride, while Cloisite 30B contains methyl tallow bis-2-hydroxyethyl ammonium chloride. Tallow, sourced from beef, primarily consists of carbon chains with 18 carbons (about 65% C18, approximately 30% C16, and roughly 5% C14). Hydrogenated tallow is obtained from tallow through the hydrogenation process, eliminating double bonds. With two tallow groups, Cloisite 20A exhibits greater hydrophobicity compared to Cloisite 30B.

Prior to obtaining the composites and blends by melt-blending, PA was dried under vacuum overnight at 80°C. The melt-blending process was performed using a conical co-rotating fully intermeshing twin-screw midi-extruder (DSM

Research, The Netherlands). On the first stage, PA and PP nanocomposites and their blends in the absence and presence of PP-g-MA were obtained, listed in Table 1. On the second stage, PAClay and PPCLay, were mixed separately with pure PA and PP, as well as together without pure components (Table 2). The compositions of PAClay and PPCLay composites shown in Table 2 were subjected to the same processing as the second cycle. The melt-blending process was carried out for 5 minutes at 50 rpm and at temperature profiles of 230, 235, and 240 °C. The dog bone shaped specimens for mechanical experiments are obtained on Laboratory injection molding machine of ZAMAK Mercator 1947 (Poland) and the and dimensions of the specimen were illustrated in details elsewhere [25].

TABLE 1. Composition of polymer composites and blends

	PA	PP	PP-g-MA	Cloisite20A	Cloisite30B
PPCLay	–	91	6	3	–
PAClay	97	–	–	–	3
PA/PP 80/20	80	20	–	–	–
PA/PP/PP-g-MA 72/18/10	72	18	10	–	–

TABLE 2. Composition of polymer blends (subjected the second cycle)

	PAClay	PPCLay	PA	PP
PA/PPCLay 80/20	–	20	80	–
PAClay/PP 80/20	80	–	–	20
PAClay/PPCLay 80/20	80	20	80	–

XRD measurements were conducted with Rigaku Miniflex 600, the condition of 40 kV voltage, 15 mA current and 0.02° step. The measurements were carried out from 2° to 30°, and interplanar distances were calculated according to Bragg's law using SmartLab Studio II.

$$n\lambda = 2d \sin \theta$$

where, n is the diffraction order, λ is the wavelength of X-ray (1.5406 Å), θ is the incident angle, and d is the interplanar distance.

Rheological tests were carried out on TA instruments ARES-2K strain controlled remoter in nitrogen atmosphere, at 240 °C. Frequency sweep and time sweep were done in linear regime. Tensile tests were conducted according to ASTM D 638 in Shimadzu AG-X PLUS (Japan). For measuring tensile module (E), 1 mm/min crosshead speed was chosen until 0.3 % deformation, after that crosshead speed increased immediately to 20 mm/min for further exploration yield stress (σ) and deformation (ε). The morphological properties of obtained samples were investigated on JEOL JSM-6010LM SEM, at 20 kV accelerating voltage. Before visualization, all samples were coated with a thin Au/Pd layer by JEOL JFC-1300 autofine coater (JEOL, Lireweg, The Netherlands) on order to avoid charging during imaging.

3. Results and discussions

3.1. X-ray diffraction (XRD) measurements

XRD patterns of PA, Cloisite30B and their composites are illustrated in Fig. 1. Interlayer distance accounts for 18.29 Å in Cloisite30B which corresponds to intensive peak in 4.83°. In the XRD pattern of PAClay composite, this peak becomes a flat, indicating exfoliated structure.

With regard to PP and its composite with Cloisite20A, XRD results show intercalation of clay particles within PP matrix (Fig. 2). Interlayer distance d increases from 24.66 to 34.75 Å as a result of insertion of PP macromolecules into between clay platelets. Even though in our previous work, we obtained exfoliated structure for the same composition due to the difference between processing conditions, intercalated nanostructures were identified by XRD measurements. Moreover, distribution of clay particles in polymer matrix affected crystallization behavior of the polymer. In both cases, nucleating effect led to increase intensity of the crystallization peak. In PA, alone peak in 21,5° and in PP, peak i 16.9° increased remarkably, contributing more perfect crystallization.

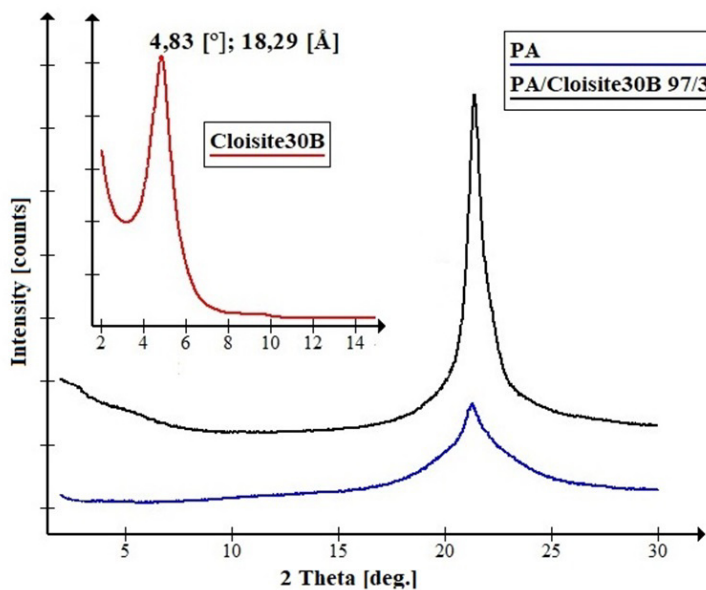


FIG. 1. XRD patterns of PA, Cloisite30B and their composites

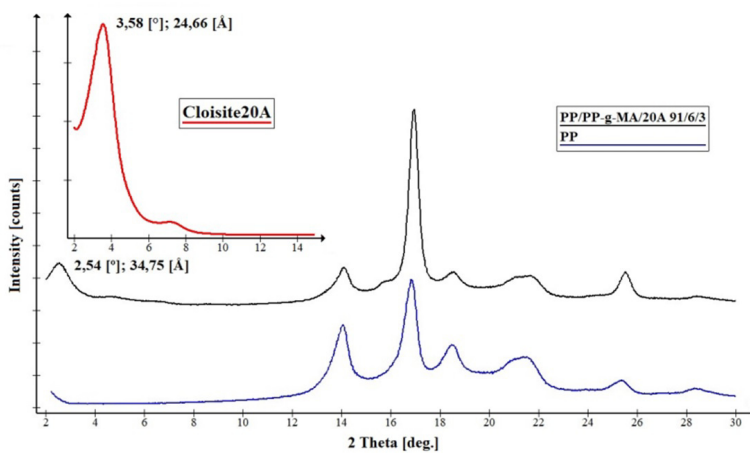


FIG. 2. XRD patterns of PP, Cloisite20A and their composites

3.2. Rheological measurements

In Fig. 3, the dependencies of complex viscosity and dynamic modulus of the initial components in blends and nanocomposites based on PA and PP with modified MMT are presented as an example against shear rate (frequency sweep). Similar curves were obtained for all investigated compositions, and viscosity values for three velocity gradients.

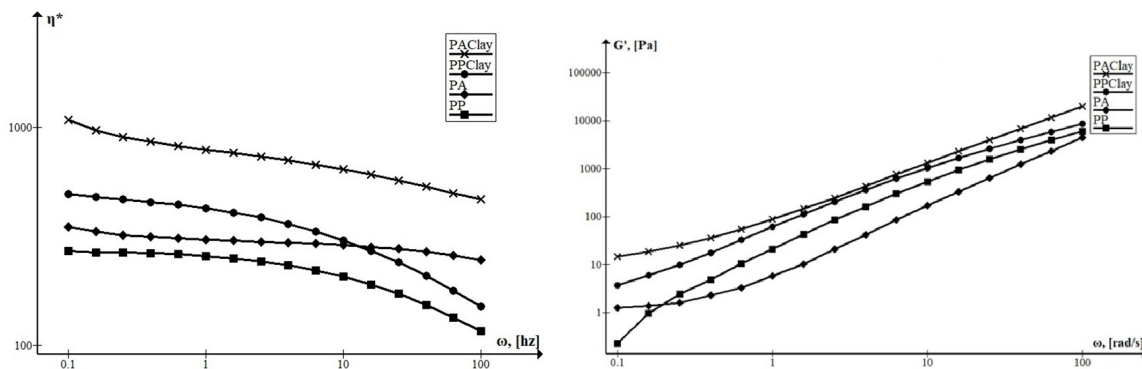


FIG. 3. Complex viscosity and storage modulus of PA, PP and their nanocomposites with 3 wt. % of clay

It is also known [19, 26] that the viscosity of melt nanocomposites is highly sensitive to the degree of dispersion of layered silicate particles, i.e., the aspect ratio, which in turn directly depends on the level of macromolecule intercalation into the interlayer space of the MMT, up to the exfoliation of the latter into individual nanoscale plates, the anisotropy coefficient of which is maximal. The viscosity values of exfoliated PA nanocomposites are significantly higher throughout the range of shear rate gradients compared to intercalated PP nanocomposites.

In Fig. 4., complex viscosity and storage modulus of 5 blends are shown. As expected, for all blend compositions, the complex viscosity decreases with an increase in shear rate [27, 28]. Upon the introduction of a compatibilizer and nanocomposites based on the virgin components, the complex viscosity notably increases. The highest viscosities to blends in which the original components are replaced with corresponding nanocomposites and, in place of the PP phase, an intercalated PP nanocomposite, respectively. As is hypothesized, such rheological behavior is associated with the structuring of the composition during the mixing process, that is, with the emergence of varying levels of specific interactions between components. In PA/PPClay blend, an intercalated PP nanocomposite is present, which was obtained by introducing 6 wt.% PP-g-MA. It is known that PP-g-MA reacts with PA macromolecules, forming a grafted copolymer of PA with PP [29]. Apparently, the structuring and degradation of PP under the selected temperature conditions of mixing also contribute to this process [30].

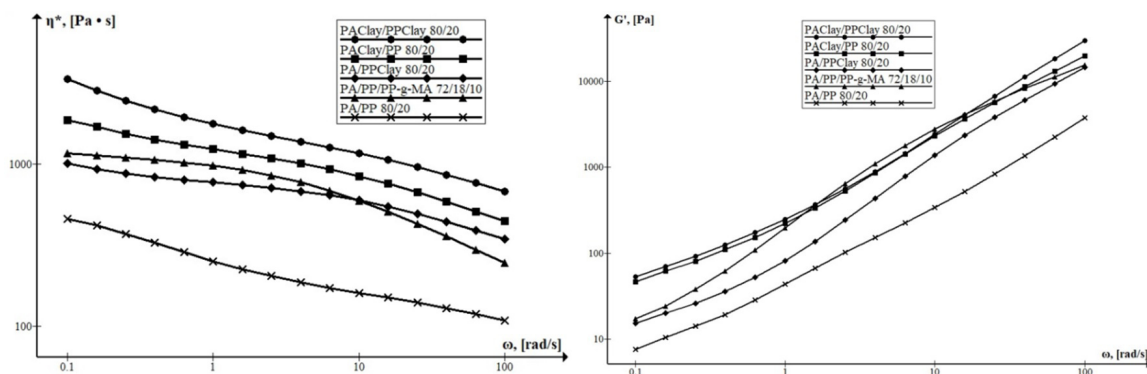


FIG. 4. Complex viscosity and storage modulus of PA/PP blends

3.3. Morphological investigations

Analysis of the cryo-fractured surface of the samples under SEM revealed that the particle size of the dispersed phase compared to samples of PA/PP blends indicates that the compatibilized blend is 7–8 times smaller than that of a conventional one (Fig. 5). Thanks to good interfacial adhesion resulting from the presence of a reaction between the amino group of PA and PP-g-MA, leading to the formation of a grafted copolymer, the particles of the PP dispersed phase remain bound to the PA matrix during the low-temperature fracture process. For blends of samples without a compatibilizer, particles of the dispersed phase torn from the surface are clearly seen. For a PA/PPClay, the size of the particles of the dispersed phase uniformly distributed in the PA phase is 500 ± 150 nm on average (Fig. 3c,d).

The intercalated PP nanocomposite acts as a more effective compatibilizer in comparison with the classical PP-g-MA for this blend of polymers.

The replacement of the PA phase with exfoliated PA nanocomposite also brings an insignificant compatibilizing effect (Fig. 5e,f). The sizes of the dispersed PP phase exhibit a broad particle size distribution ranging from 1 – 8 μm , contrasting with conventional blends where these sizes vary within the range of 3 – 14 μm . The absence of a pronounced effect of compatibilization is apparently due to the fact that exfoliated MMT particles are distributed in the bulk of the PA phase and practically does not participate in the processes of coalescence of the dispersed phase particles.

3.4. Mechanical analysis

It is well known that blending two incompatible polymers can result in different expressions of final mechanical properties, depending on the blend composition, individual polymer characteristics, and blend morphology [31]. In the case of nanocomposites based on layered silicates, besides interfacial adhesion, the elastic-strength characteristics, particularly the modulus of elasticity, are influenced by the dispersion of modified MMT, meaning the anisotropy coefficient (aspect ratio – the ratio of particle length to thickness).

The mechanical properties such as the elastic modulus (E), the yield strength (σ), and the relative elongation at break (ϵ) of PA and PP, along with the nanocomposites containing Cloisite30B and Cloisite20A, as well as their blends are outlined in Table 3. We will analyze how these parameters change as we transit from individual components to multi-component compositions.

The initial modulus of elasticity slightly differs (higher for PA), with an increase of 10 % for the intercalated PP nanocomposite and over 50% enhancement in the modulus of elasticity for the exfoliated PA nanocomposite, consistent

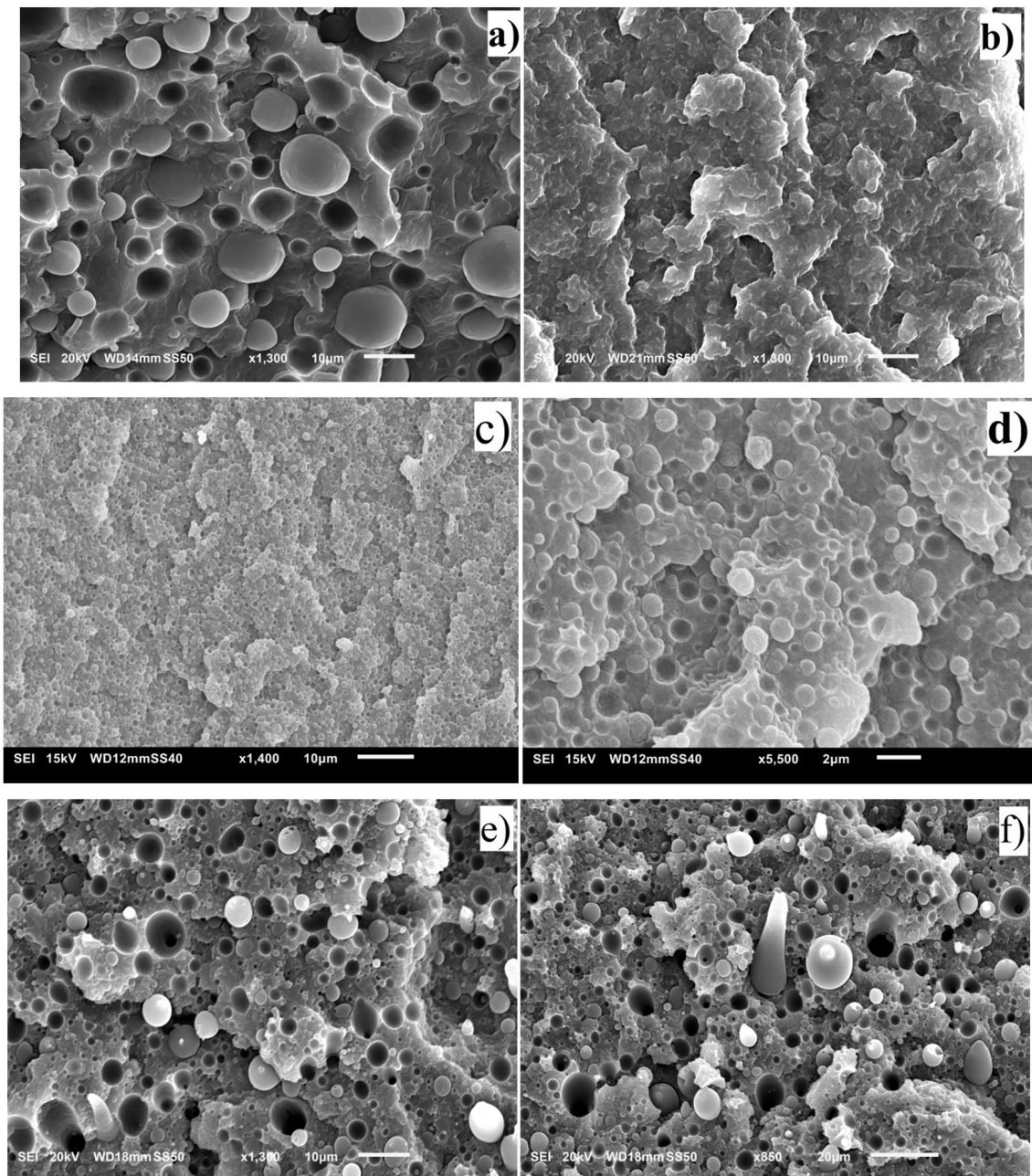


FIG. 5. SEM images of PA/PP blends 80/20 ratio series. a) PA/PP, b) PA/PP/PP-g-MA, c) and d) PA/PP/clay, e) and f) PA/clay/PP

with similar findings reported in previous studies [32]. A minor enhancement effect in terms of yield strength is observed in the corresponding nanocomposites based on PP and PA. The deformability of the intercalated nanocomposite decreases by more than 4 times, whereas for the exfoliated nanocomposite, deformability is somewhat preserved, resulting in a twofold reduction in ε .

For polymer blends, considering the incorporation of the respective nanocomposites, the followings can be stated. The modulus of elasticity for these blends takes an intermediate position according to the rule of additives. Enhancement of interfacial adhesion through the introduction of a compatibilizer in the form of PP-g-MA (formation of grafted copolymer of PA with PP at the phase interface) leads to a 20% increase in Young's modulus. Replacing PP with intercalated nanocomposite, PA with exfoliated nanocomposite, and their simultaneous replacement without a compatibilizer revealed increases in the modulus of elasticity by 28, 40, and 44 %, respectively. Of particular significance is the composition involving PA/PP/clay, which exhibits a remarkable combination of high elastic modulus and noticeable plasticity.

TABLE 3. Mechanical properties of the blends and components

	E , [MPa]	σ , [MPa]	ε , [%]
PP	854 ± 49	32.5 ± 0.9	371 ± 53
PPClay	929 ± 65	33.6 ± 2.6	84 ± 31
PA	973 ± 31	58.2 ± 2.1	222 ± 39
PAClay	1477 ± 68	66.9 ± 2.3	112 ± 33
PA/PP	896 ± 69	38.5 ± 2.3	18 ± 6
PA/PP/PP-g-MA	1075 ± 20	43.3 ± 5.5	50 ± 7
PA/PPClay	1148 ± 96	53.1 ± 2.6	356 ± 39
PAClay/PP	1254 ± 75	43.6 ± 9.7	9 ± 4
PAClay/PPClay	1290 ± 58	47.3 ± 1.4	23 ± 7

4. Conclusion

In this paper, we studied the rheological, morphological and mechanical properties of PA and PP blends in the presence of layered silicates. The melt viscosity of nanocomposites is highly influenced by the dispersion of layered silicate particles, exfoliated PA nanocomposites exhibited notably higher viscosity compared to intercalated PP nanocomposites. In the blends, the introduction of a compatibilizer or nanocomposites derived from original components always increases complex viscosity. In terms of morphology, the PA/PPClay blend indicates the most finely dispersed morphology rather than PAClay/PP or the blend with traditional PP-g-MA. The increased viscosity of the PPClay leads to an equal amount of viscosity of the blend components, in turn; this will create the necessary condition for dispersion of minor phase particles. Moreover, intercalated clay particles and PP-g-MA, in the PPClay content, avoid agglomeration because they tend to interact with PA molecules. As to PAClay/PP blend, as long as particles with $10 \mu\text{m}$ there are also nanosized particles and better dispersion of PP dispersed phase too. Even though the occurrence of interaction between PP and clay particles, in the PAClay content, is not possible, better dispersion than pure blend was caused due to the higher viscosity of PAClay. The increase of matrix viscosity resists coalescence and particularly thanks to this reason PAClay/PP indicates more finer dispersed morphology than PA/PP blend. With regard to mechanical properties, compatibilization enhances all mechanical characteristics relative to the blend with pure components while all blends with clay are superior to compatibilized one. Due to the advantage of PA/PPClay in terms of dispersion, it has the highest values of σ and ε amongst all blends obtained while blends with PAClay are dominant by elastic modulus.

References

- [1] Begum S.A., Rane A.V., & Kanny K. Applications of compatibilized polymer blends in automobile industry. *Compatibilization of polymer blends*, 2020, P. 563–593.
- [2] Annandarajah C., Langhorst A., Kiziltas A., Grewell D., Mielewski D., & Montazami R. Hybrid cellulose-glass fiber composites for automotive applications. *Materials*, 2019, **12**(19), P. 3189.
- [3] Tokumitsu K., Nakajima Y., & Aoki K. Mechanical properties of PP/PA blends in addition with PP-g-MAH with different PP molecular weight and MAH content. *AIP Conference Proceedings*, 2016, **1713**(1).
- [4] Sehanobish K. *Engineering plastics and plastic composites in automotive applications*, 2009, Vol. 122.
- [5] Occhiello E., Giannotta G., Penco M., Garbassi F. Interfacial adhesion in incompatible polymer blends. *First International Congress on Adhesion Science and Technology*, 2000, **1**(3), P. 693–702.
- [6] Mostafapoor F., Khosravi A., Fereidoon A., Khalili R., Jafari S.H., Vahabi H., & Saeb M.R. Interface analysis of compatibilized polymer blends. *Compatibilization of Polymer Blends*, 2020, P. 349–371.
- [7] Jordan A.M., Kim K., Bates F.S., Macosko C.W., Jaffer S., & Lhost O. Rheological characterization and thermal modeling of polyolefins for process design and tailored interfaces. *AIP Conference Proceedings*, 2017, **1843**(1). AIP Publishing.
- [8] Ubonnut L., Thongyai S., & Praserttham P. Interfacial adhesion enhancement of polyethylene–polypropylene mixtures by adding synthesized diisocyanate compatibilizers. *Journal of applied polymer science*, 2007, **104**(6), P. 3766–3773.
- [9] Ajitha A.R., & Thomas S. Compatibilization of polymer blends. *Compatibilization of Polymer Blends*, 2019, **640**.
- [10] Zhang W., Gui Z., Lu C., Cheng S., Cai D., & Gao Y. Improving transparency of incompatible polymer blends by reactive compatibilization. *Materials Letters*, 2013, **92**, P. 68–70.
- [11] Nguyen-Tran H.D., Hoang V.T., Do V.T., Chun D.M., & Yum Y.J. Effect of multiwalled carbon nanotubes on the mechanical properties of carbon fiber-reinforced polyamide-6/polypropylene composites for lightweight automotive parts. *Materials*, 2018, **11**(3), P. 429.
- [12] Xu M., Lu J., Qiao Y., Wei L., Liu T., Lee P.C., ... & Park C.B. Toughening mechanism of long chain branched polyamide 6. *Materials & Design*, 2020, **196**, P. 109173.
- [13] Jang H.G., Yang B., Khil M.S., Kim S.Y., & Kim J. Comprehensive study of effects of filler length on mechanical, electrical, and thermal properties of multi-walled carbon nanotube/polyamide 6 composites. *Composites Part A: Applied Science and Manufacturing*, 2019, **125**, P. 105542.

- [14] Ghanta T.S., Aparna S., Verma N., & Purnima D. Review on nano- and microfiller-based polyamide 6 hybrid composite: Effect on mechanical properties and morphology. *Polymer Engineering & Science*, 2020, **60**(8), P. 1717–1759.
- [15] Raji M., Mekhzoum M.E.M., Rodrigue D., & Bouhfid R. Effect of silane functionalization on properties of polypropylene/clay nanocomposites. *Composites Part B: Engineering*, 2018, **146**, P. 106–115.
- [16] Berdinazarov Q.N., Khakberdiev E.O., Normurodov N.F., & Ashurov N.R. Mechanical and Thermal Degradation Properties of Isotactic Polypropylene Composites with Cloisite15A and Cloisite20A. *Bulletin of the University of Karaganda – Chemistry*, 2022, **3**.
- [17] Banerjee S.S., Janke A., Gohs U., & Heinrich G. Electron-induced reactive processing of polyamide 6/polypropylene blends: Morphology and properties. *European Polymer Journal*, 2018, **98**, P. 295–301.
- [18] Hasanpour M., Razavi Aghjeh M.K., Mehrabi Mazidi M., & Afsari B. Effect of morphology alteration on mechanical properties and fracture toughness of polypropylene/polyamide 6/ethylene polypropylene diene monomer graft maleic anhydride (PP/PA6/EPDM-g-MA) reactive ternary blends. *Polymer Bulletin*, 2020, **77**, P. 3767–3794.
- [19] Afshari M., Kotek R., Haghighat Kish M., Nazock Dast H., & Gupta B.S. Effect of blend ratio on bulk properties and matrix–fibril morphology of polypropylene/nylon 6 polyblend fibers. *Polymer*, 2002, **43**(4), P. 1331–1341.
- [20] Rocha J.A., Steffen T.T., Fontana L.C., & Becker D. Effect of maleic anhydride and oxygen functionalized carbon nanotube on polyamide 6 and polypropylene blend properties. *Polymer Bulletin*, 2021, **78**, P. 5623–5639.
- [21] Motamedi P., & Bagheri R. Modification of nanostructure and improvement of mechanical properties of polypropylene/polyamide 6/layered silicate ternary nanocomposites through variation of processing route. *Composites Part B: Engineering*, 2016, **85**, P. 207–215.
- [22] Motamedi P., & Bagheri R. Investigation of the nanostructure and mechanical properties of polypropylene/polyamide 6/layered silicate ternary nanocomposites. *Materials & design*, 2010, **31**(4), P. 1776–1784.
- [23] Ou B., Li D., & Liu Y. Compatibilizing effect of maleated polypropylene on the mechanical properties of injection molded polypropylene/polyamide 6/functionalized-TiO₂ nanocomposites. *Composites science and technology*, 2009, **69**(3-4), P. 421–426.
- [24] Chow W.S., Mohd Ishak Z.A., & Karger, J. Morphological and rheological properties of polyamide 6/poly (propylene)/organoclay nanocomposites. *Macromolecular Materials and Engineering*, 2005, **290**(2), P. 122–127.
- [25] Khakberdiev E.O., Berdinazarov Q.N.U., Toshmamatov D.A.U., & Ashurov N.R. Mechanical and morphological properties of poly (vinyl chloride) and linear low-density polyethylene polymer blends. *Journal of Vinyl and Additive Technology*, 2022, **28**(3), P. 659–666.
- [26] De Almeida F., Correia A., e Silva E.C., Lopes I.C., & Silva F.J.G. Compatibilization effect of organophilic clays in PA6/PP polymer blend. *Procedia Manufacturing*, 2018, **17**, P. 1154–1161.
- [27] Harrats C., Omonov T., Groeninckx G., & Moldenaers P. Phase morphology development and stabilization in polycyclohexylmethacrylate/polypropylene blends: uncompatibilized and reactively compatibilized blends using two reactive precursors. *Polymer*, 2004, **45**(24), P. 8115–8126.
- [28] Hsissou R., Bekhta A., Dagdag O., El Bachiri A., Rafik M., & Elharfi A. Rheological properties of composite polymers and hybrid nanocomposites. *Heliyon*, 2020, **6**(6).
- [29] Zeng N., Bai S.L., G'sell C., Hiver J.M., & Mai Y.W. Study on the microstructures and mechanical behaviour of compatibilized polypropylene/polyamide-6 blends. *Polymer International*, 2002, **51**(12), P. 1439–1447.
- [30] Saikrishnan S., Jubinville D., Tzoganakis C., & Mekonnen T.H. Thermo-mechanical degradation of polypropylene (PP) and low-density polyethylene (LDPE) blends exposed to simulated recycling. *Polymer Degradation and Stability*, 2020, **182**, P. 109390.
- [31] Aparna S., Purnima D., & Adusumalli R.B. Review on various compatibilizers and its effect on mechanical properties of compatibilized nylon blends. *Polymer-Plastics Technology and Engineering*, 2017, **56**(6), P. 617–634.
- [32] Liu L., Qi Z., & Zhu X. Studies on nylon 6/clay nanocomposites by melt-intercalation process. *Journal of Applied Polymer Science*, 1999, **71**(7), P. 1133–1138.

Submitted 27 October 2023; revised 31 January 2024; second revision 3 April 2024; third revision 11 June 2024;
accepted 12 June 2024

Information about the authors:

Qodirbek Nuridin ugli Berdinazarov – Institute of Polymer Chemistry and Physics, Uzbekistan Academy of Sciences, A. Kadyri str. 7b, 100128, Tashkent, Uzbekistan; ORCID 0000-0002-4422-2305; qodirberdinazarov@mail.ru

Elshod Olmosovich Khakberdiev – Institute of Polymer Chemistry and Physics, Uzbekistan Academy of Sciences, A. Kadyri str. 7b, 100128, Tashkent, Uzbekistan; ORCID 0000-0002-7707-2219; profhaqberdiyev@gmail.com

Nigmat Rustamovich Ashurov – Institute of Polymer Chemistry and Physics, Uzbekistan Academy of Sciences, A. Kadyri str. 7b, 100128, Tashkent, Uzbekistan; ORCID 0000-0003-0765-5942; nigmat.ashurov@gmail.com

Conflict of interest: the authors declare no conflict of interest.

Investigation of sensing performance of silicene nanoribbon towards methanol and ethanol molecules: A computational study

Shazia Showket¹, Khurshed A. Shah², Ghulam N. Dar¹, Muzaffar Ali Andrabi³

¹Department of Physics, University of Kashmir, Srinagar, J&K–190006, India

²Postgraduate Department of Physics, Sri Pratap College, Cluster University Srinagar, J&K–190001, India

³Department of Applied Sciences, Institute of Technology, University of Kashmir, Srinagar, J&K–190006, India

Corresponding author: Dr. Khurshed A. Shah, drkhursheda@gmail.com

ABSTRACT In this work, we perform an intricate computational analysis to investigate the adsorption mechanism of human breath exhaled VOCs, namely, methanol and ethanol, along with interfering water vapour on the surface of armchair silicene nanoribbon (ASiNR) by employing density functional theory to analyse the structural, electronic, and transport properties. The findings indicate that the most favorable adsorption configuration for methanol and ethanol involves the hydroxyl group (-OH) oriented towards the silicene surface, after optimisation. Moreover, we have calculated the adsorption energies which shows that ethanol is strongly physisorbed than methanol and water molecules on the ASiNR surface. Apart from that, the results of IV characteristics, transmission spectra and density of states corroborate these observations. In addition, we have computed the sensitivity (%), the results of which revealed that methanol demonstrates a high sensitivity of 42 % compared to other molecules towards the surface of ASiNR. Furthermore, the recovery time of the sensor was found to be extremely long, which indicates that ASiNR based device has great potential for use as disposable sensors and scavengers for toxic gas molecules.

KEYWORDS armchair silicene nanoribbon, DFT, volatile organic compounds, sensitivity

ACKNOWLEDGEMENTS This work has been supported by JKST&IC funded project (Grant No. JKST&IC/SRE/1172-74) and SERB (Grant No. CRG2022/006428-G).

FOR CITATION Showket S., Shah K.A., Dar G.N., Ali Andrabi M. Investigation of sensing performance of silicene nanoribbon towards methanol and ethanol molecules: A computational study. *Nanosystems: Phys. Chem. Math.*, 2024, **15** (3), 418–428.

1. Introduction

The swift advancement of industrial technology and contemporary living have made gas detectors indispensable for safeguarding both the environment and human health [1, 2]. The diagnosis of diseases and the biological field are two important uses for gas sensors. Among many diseases, malignancies have been identified as one of the largest and most significant categories. Prostate and lung cancers are among the most common types of tumours that cause death in this group. Gas sensors, being a noninvasive technology, have the potential to aid in the early diagnosis of cancer by identifying cancer biomarkers in patients' exhaled breath [1, 3, 4]. A great deal of work has gone into finding cancer biomarkers, and it has been found that distinct volatile organic compound (VOC) patterns are associated with various diseases and cancers [5–7]. Breath, as everyone knows, contains about a thousand different types of volatile organic compounds (VOCs) at quantities ranging from parts per million to parts per trillion (ppmv to pptv) [8, 9]. Common volatile organic compounds (VOCs) found in human breath include alcohols, ketones, and toluene. These can be measured and identified using a variety of methods, but one interesting method is the use of gas sensors based on nanomaterials [10]. It is important to note, though, that fuel combustion, industry, and transportation all produce exhaust fumes, which are another source of VOCs [11]. Thus, the detection of these gas molecules appears to be essential for environmental safety and monitoring.

Since the revelation of graphene, 2D materials, characterized by their substantial surface area-to-volume ratio, have garnered significant attention from scientists as potential options. Notable examples include silicene, germanene, stanene, and transition-metal dichalcogenides, owing to their remarkable electrical, magnetic, optical, and gas sensing capabilities [12–15]. Silicene, an allotrope of silicon with a two-dimensional hexagonal lattice structure akin to graphene, is a focal point of research due to its exceptional properties and potential applications in the field of nanoelectronics [16–19]. Silicene lacks a band gap, however, due to its unique buckled structure, its band gap can be easily adjusted using various techniques [20–26]. Despite the fact that free standing silicene is not stable, it was experimentally fabricated on Ag [27], Ir [28], ZrB₂ [29] and ZrC [30]. The extraordinary properties of silicene including ferromagnetism [31], half metallicity [32], quantum Hall effect [33], giant magnetoresistance [34], and superconductivity [35] along with its compatibility with silicon based nanoelectronics may give edge to silicene rather than graphene. Though silicene is a zero-band gap

material, the band gap issue can be resolved by slicing it into strips called silicene nanoribbons (SiNRs). Substrates like; Ag (100), Ag (110), Au (110) [36–39] have been used to generate SiNRs. An array of highly uniform parallel SiNRs having width of ~ 1.7 nm have been synthesised by Afuray et al. on Ag (110) substrate [36]. When it comes to gas nanosensor applications, nanoribbons are more appealing than sheets because of their intrinsic band gap, small dimensions, and free reactive edges. Armchair silicene nanoribbons (ASiNRs) and zigzag silicene nanoribbons (ZSiNRs) are the two types of SiNRs [40]. ASiNRs have been chosen because adsorption of gases has comparatively smaller effect on electronic properties of ZSiNRs [41].

Numerous researches [42–44] suggest that silicene holds a great promise for gas sensing applications. However, the majority of these studies primarily focused on basic gases such as; CO, NO, NO₂, NH₃ and CH₄, CO₂. Moreover, silicene [45–47] and other 2D materials [9,48] have also been explored for the sensing applications of VOCs. These findings highlight silicene's potential as a highly effective sensor, inspiring us to further develop it for the detection of harmful VOCs, including methanol and ethanol. To investigate the viability of employing silicene for the development of volatile organic compound (VOC) sensors, we performed rigorous calculations utilizing density functional theory. This analysis encompasses a comprehensive examination of various facets, including electronic properties (such as adsorption energy, interaction distance, and density of states), structural attributes (bond length and buckling distance), transport characteristics (transmission spectra and conductance), as well as sensitivity (%) and recovery time (τ). The aim is to elucidate and quantify the intricate interplay between the surface of ASiNR and VOCs, providing valuable insights into the material's potential as a highly efficient sensor for volatile organic compounds. Numerous investigations have been conducted by the researchers to examine the adsorption characteristics of Volatile Organic Compounds (VOCs), encompassing methanol and ethanol, on diverse substrates. These substrates include Pd-decorated Phosphorene [49], Al-doped GeS [50] and green phosphorene nanosheets [51]. Moreover, the study has highlighted the efficacy of graphyne nanosheets as a sensing material for methanol and ethanol, indicating a preferential adsorption of ethanol over methanol [52]. Additionally, MoSe₂ monolayers have been identified as effective chemi-resistors for the detection of methanol and ethanol vapors in the ambient environment, as elucidated in the research paper authored by V. Nagarajan et al. [53].

In the current study, our central objective is dedicated to scrutinizing the structural, electronic, and transport characteristics of armchair silicene nanoribbon (ASiNR) for the purpose of sensing VOCs (methanol and ethanol) and water molecule. Our empirical observations indicate that the simulated armchair silicene nanoribbon-based two-probe device holds considerable promise as disposable sensor and scavenger for toxic gas molecules within the ambient environment.

2. Models and methods

In the ongoing study, we have modelled a 7 atom-wide armchair silicene nanoribbon (ASiNR) comprising 108 atoms. To assess the structural, electronic, and transport characteristics, we have configured it as a two-probe device, delineated into three distinct regions: the left electrode, the central scattering region, and the right electrode. The lattice constant of the optimized silicene is determined to be 3.85 angstroms (Å) [54]. The parameters for the silicon-silicon bond length and buckling height were selected as 2.28 and 0.44 Å, respectively, in adherence to the established standard values [24]. The length of two electrodes was considered to be 6.72Å. The integration of the ASiNR system with electrodes was undertaken to vanquish the current quantization effects induced by contact regions. To assess the potential adsorption of volatile organic compounds (VOCs) on the surface of the ASiNR model, a thorough analysis was conducted through Density Functional Theory (DFT) based first principles computations utilizing the Quantum Atomistix Toolkit (ATK) software [55]. Current calculations have been executed utilizing the Landauer–Buttiker formula [56], conjoined with Non-Equilibrium Greens Function (NEGF) formalism, as articulated by the following expression:

$$I = \frac{2e}{h} \int_{-\infty}^{\infty} T(E, V_b) [f(E - \mu_L) - f(E - \mu_R)] dE, \quad (1)$$

where $T(E, V_b)$ represents the transmission function at a given energy E and voltage V_b , while, $(E - \mu_L)$ and $(E - \mu_R)$ denote the Fermi distribution functions of the left and right electrodes, respectively.

To evaluate the alterations in various sensing properties including the adsorption energy, interaction distance, IV curves, transmission spectra, projected device density of states (PDDOS), sensitivity (%), selectivity and recovery time (τ), both alcohol molecules were positioned proximate to the ASiNR surface. The models were simulated using density functional theory with an electrode temperature of 300 K and the density mesh cut-off was set at 75 Hartree. The maximum range for the interaction was taken as 10 Å and the Fourier 2D solver was approved as the poisson solver for the boundary conditions. The potential difference applied between the two electrodes ranged from 0 to 2 volts to scrutinize the current flowing across the models. Additionally, the exchange-correlation functional of Perdew, Burke, and Ernzerhof (PBE) type [57] coupled with the Double Zeta Polarized (DZP) basis set [58] has been employed to facilitate the relaxation of the geometrical structures of the ASiNR models adsorbed with two alcohol molecules, namely, methanol and ethanol. A vacuum space of 15 Å was taken into consideration, in the x and y directions where the structures lack periodicity, to abstain the mirrored interactions. In the pursuit geometry optimization, the Brillouin zone has been thoroughly sampled using a grid resolution of $1 \times 1 \times 21$ k-points [59, 60] and for calculating the total energy, and electron

transport properties, Monkhorst–Pack Scheme is used with a k-point grid of $1 \times 1 \times 100$ (z -direction along the ASiNR increasing direction) [59–62]. Preceding the computational analyses, exhaustive optimization procedures were applied to all structures, ensuring that both force tolerance and the corresponding lattice stress reached values below 0.05 eV/\AA and 0.0005 eV/\AA^3 respectively with the maximum step size of 0.2 \AA . The optimization process was executed by employing the limited memory Broyden–Fletcher–Goldfarb–Shanno (LBFGS) algorithm.

3. Results and discussion

Since ASiNRs having width $L = 3n$ or $L = 3n + 1$ (where n is an integer) are known to express semiconducting behaviour [63], we construct an ASiNR with a width of 7 atoms. To ensure the stability of the edges, the dangling bonds of the silicon atoms at the edges of the ASiNR are passivated on both sides with hydrogen atoms. Because of the incomplete sp^3 hybridization in silicene and the heightened reactivity of the edges compared to the surface, the surface is left unaltered [64–66]. As per reports, the paramagnetic semiconductor 7-ASiNR exhibits a band gap of 0.54 eV [62, 67]. The semiconducting ASiNR was selected based on the presumption that the adsorption of gas molecules has a significantly diminished impact on the electrical characteristics of metallic zigzag SiNRs (ZSiNRs). We design the ASiNR into a two-probe device with three regions: the left electrode, the central scattering region, and the right electrode for calculating the sensing properties. The design structure of our proposed ASiNR device is shown in Fig. 1, where, the bond lengths between Si–Si and Si–H, are outlined as 2.28 and 1.43 \AA , respectively, across the three regions.

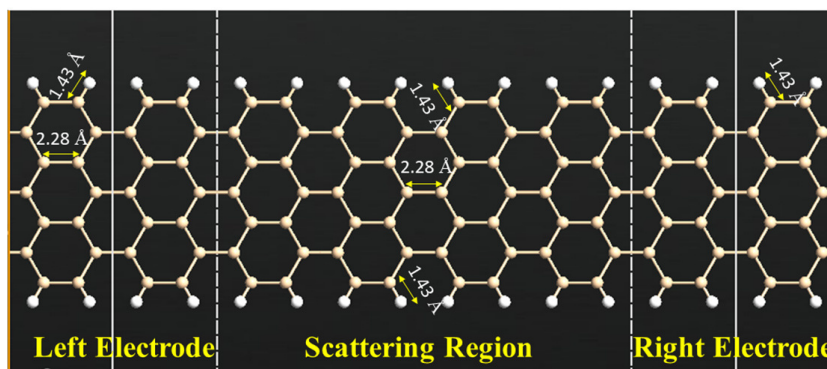


FIG. 1. The modeled ASiNR device comprising of the left electrode, the central scattering region & the right electrode. The upper and lower white balls represent the passivated H-atoms

3.1. Sensing profile

3.1.1. Structural configuration. After optimising the ASiNR models, it was found that the adsorption process induces a subtle deformation in both the base and target materials. The bond lengths and buckling heights of the ASiNR modelled devices were calculated before and after adsorption. It was determined that these values exhibited variation in the scattering region ranging from 2.28 to 2.30 \AA and 0.44 to 0.60 \AA , respectively, for methanol and from 2.28 to 2.29 \AA and 0.44 to 0.54 \AA , respectively, for ethanol. Additionally, the Si–H bond lengths were also found to vary in the scattering region ranging from 1.43 to 1.50 \AA . Moreover, we have also calculated the bond lengths of methanol, ethanol and water molecules, which demonstrate minimal deviation, with the exception being observed in the bond lengths between C–O and O–H, which increase from their standard values after adsorption on the ASiNR models. Specifically, in the case of methanol, the C–O and O–H bond lengths show a variation within the range of 1.39 to 1.45 \AA and 0.95 to 0.98 \AA , respectively, while, for ethanol, the C–O and O–H bond lengths demonstrate a variation within the range of 1.41 to 1.47 \AA and 0.95 to 0.98 \AA , respectively. The optimised structures of VOC based sensors are illustrated in Fig. 2, elucidating the most advantageous places of methanol and ethanol on the ASiNR surface after optimisation.

3.1.2. Adsorption response of the target molecules on silicene. To investigate the interactions between the target molecules and ASiNR, we put them 3.5 \AA from the ASiNR surface. After complete relaxation, the adsorption behaviour of molecules on the ASiNR device are analysed. It was found that the structural and electronic characteristics of the base-target materials appear to change after optimization. The adsorption energies and interaction distances of both modelled devices were determined in order to figure out the most stable configuration. Our simulated models revealed negative adsorption energy, signifying a substantial reduction in electron cloud repulsion compared to electrostatic contact between the three molecule and the ASiNR. This phenomenon resulted in the adsorption of proposed molecules on the ASiNR surface. The larger the negative value of adsorption energy is, the stronger the contact and consequently the greater is the charge transfer. The adsorption energy (E_{ad}) is computed using the following equation [67, 68]:

$$E_{ad} = E_{\text{ASiNR+Molecule}} - E_{\text{ASiNR}} - E_{\text{Molecule}} \quad (2)$$

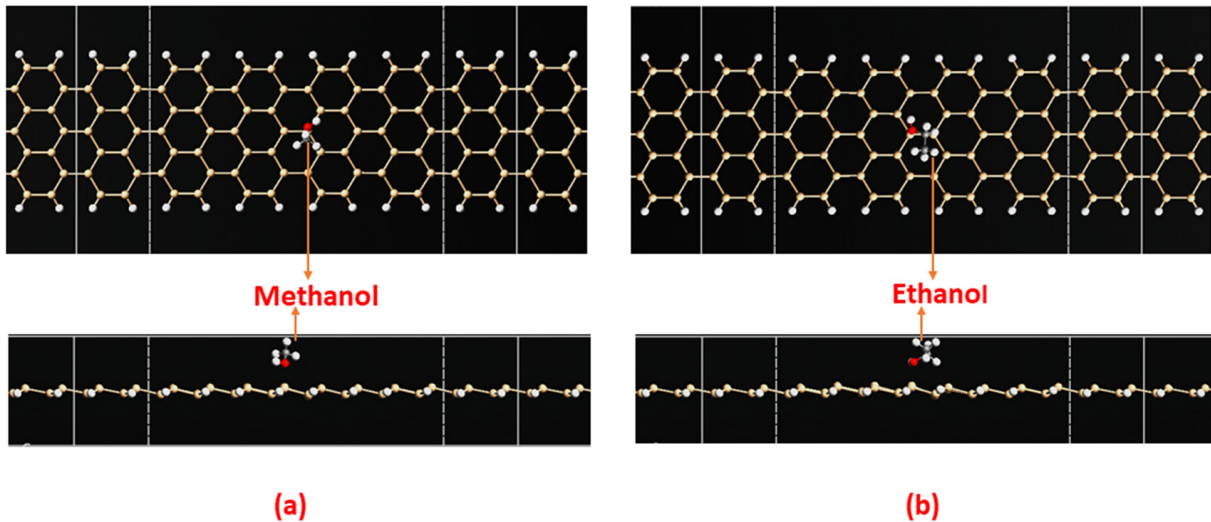


FIG. 2. Top and side views of optimised models of ASiNR with (a) methanol and (b) ethanol

The terms $E_{\text{ASiNR+Molecule}}$, E_{ASiNR} , and E_{Molecule} represent the total energies of the ASiNR-molecule system, pristine ASiNR, and the individual gas molecule, respectively. The interaction distance of 2.20 Å was found for ML and EL, while 2.9 Å in case of water molecule, confirming the Van der Waals type of interaction. It is noteworthy that chemical bonds do not exist in their fully relaxed structures based on the obtained interaction distances. The interaction distance reflects the binding strength, which is inversely proportional to distance [69]. In our computational work, methanol and ethanol were positioned at various places on the surface of ASiNR. The hydroxyl group (-OH) facing the surface of ASiNR models was shown to be the most suitable adsorption configuration of the molecules after optimisation. To have a clear understanding of our observations, we have shown the zoomed side views of the ASiNR modelled devices adsorbed with ML and EL in Fig. 3.

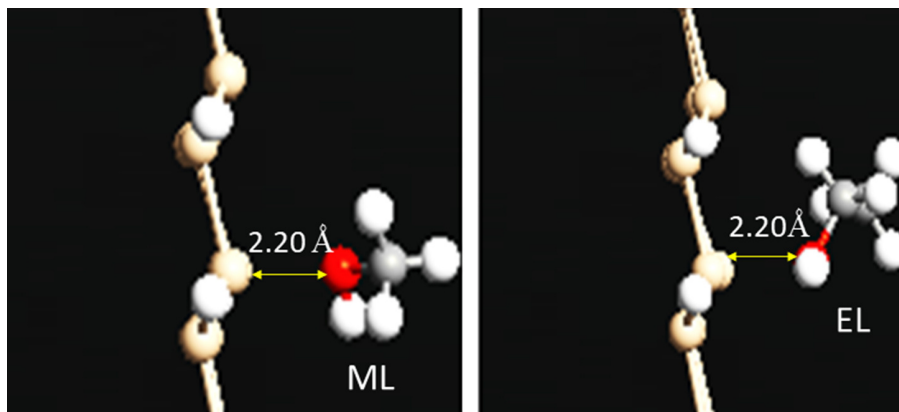


FIG. 3. Zoomed sideview representation of the ASiNR modelled devices with ML and EL at a distance of 2.20 Å respectively after optimisation

Furthermore, the obtained adsorption energy values of -1.56 eV for ML, -1.62 eV for EL and -1.43 eV for water molecule are higher as compared to the previously reported sensors [41–43]. The more negative value of adsorption energy for ethanol suggests a stronger adsorption, leading to a longer recovery time for ASiNR compared to methanol and water molecule (which will be discussed in section 3.1.6).

3.1.3. Transport characteristics:

3.1.3.1. IV Curve. In assessing the sensing capabilities of the ASiNR based device for the proposed gas molecules, a thorough evaluation of the current versus bias voltage was performed by employing a bias voltage range of 0 – 2 V. The findings, as depicted in Fig. 4, distinctly reveal that the threshold voltage for both pristine, and VOC adsorbed ASiNR is 0.63 V. It is noteworthy to note that methanol, ethanol and water molecules are characterized as polar molecules. Consequently, the adsorption process facilitates a direct charge transfer mechanism between the sensor surface and the proposed molecules. This intermolecular interaction leads to an augmentation in the concentration of majority charge carriers, thereby resulting in a discernible elevation in the overall current traversing through the device. This observation underscores the efficacy of the proposed device in detecting and responding to gas molecules through direct charge transfer mechanisms during the adsorption process. Apart from that, an elevation in current observed beyond the threshold bias voltage is a direct consequence of an augmented number of conduction states in close proximity to the Fermi level. In the case of ASiNR adsorbed with methanol, the current registers lower values in comparison to pristine and ASiNR adsorbed with ethanol and water molecules. This disparity can be attributed to lattice distortion, which in turn diminishes the mobility of the sensing device. Additionally, notable peak currents of 38.6, 22.3, 34.8 and 33.7 μA are discerned for pristine, ML-adsorbed, EL-adsorbed and water molecule-adsorbed ASiNR respectively. The low peak currents of ASiNR based sensors compared to pristine one could indeed be attributed to electron withdrawing effects of methanol, ethanol and water molecules. Their adsorption leads to a decrease in the availability of conducting electrons and thus, resulting in lower peak currents. Furthermore, our observations align with existing literature, providing a contextual framework for understanding the implications of these findings. [47, 62, 68].

3.1.3.2. Transmission Spectra. We have carried out a thorough analysis of the electronic transport characteristics, specifically focusing on the transmission spectrum, pertaining to the ASiNR model in the absence and in the presence of two alcohol molecules. Fig. 5 presents a comparative analysis of the transmission spectra, illustrating the distinctions between pristine ASiNR without any adsorption and ASiNR adsorbed with ML and EL. The comparison was conducted across various bias voltages, specifically at 1.2, 1.8, and 2 V, revealing distinctive electronic transport properties under these conditions. Our observations indicate a remarkable similarity in the transmission spectra of ASiNR models both before and after adsorption, with the notable distinction lying in the values of transmission peaks. As depicted in Fig. 5, it is evident that the transmission probability is at its maximum for ASiNR adsorbed with EL at a bias voltage of 1.2 V. Moreover, the transmission probability is at its minimum for ASiNR adsorbed with ML at a bias voltage of 1.8 V. Furthermore, under a bias voltage of 2 V, the pristine ASiNR, without any adsorption, exhibits the maximum transmission probability. The obtained results are consistent with the previously acquired IV characteristics. Therefore, the fluctuations observed in the transmission spectrum further confirm the device's responsiveness towards the specified alcohol molecules.

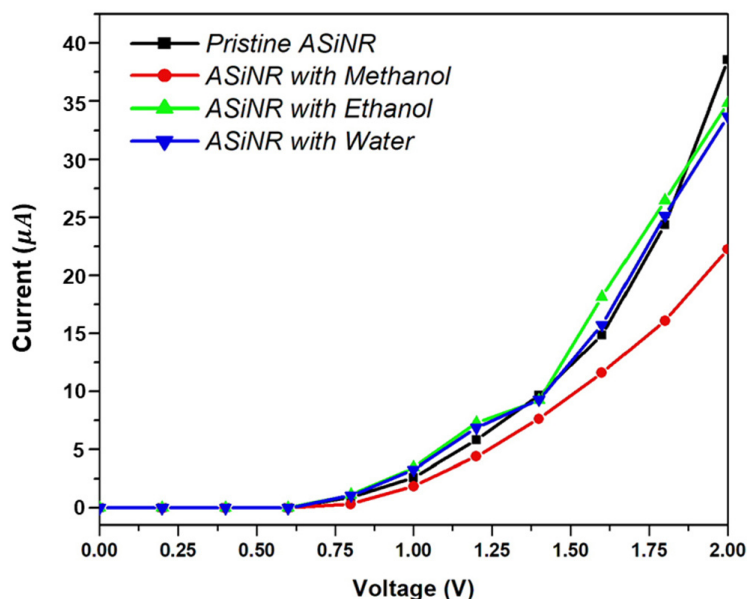


FIG. 4. IV characteristics of Pristine ASiNR and ASiNR adsorbed with methanol, ethanol and water molecules

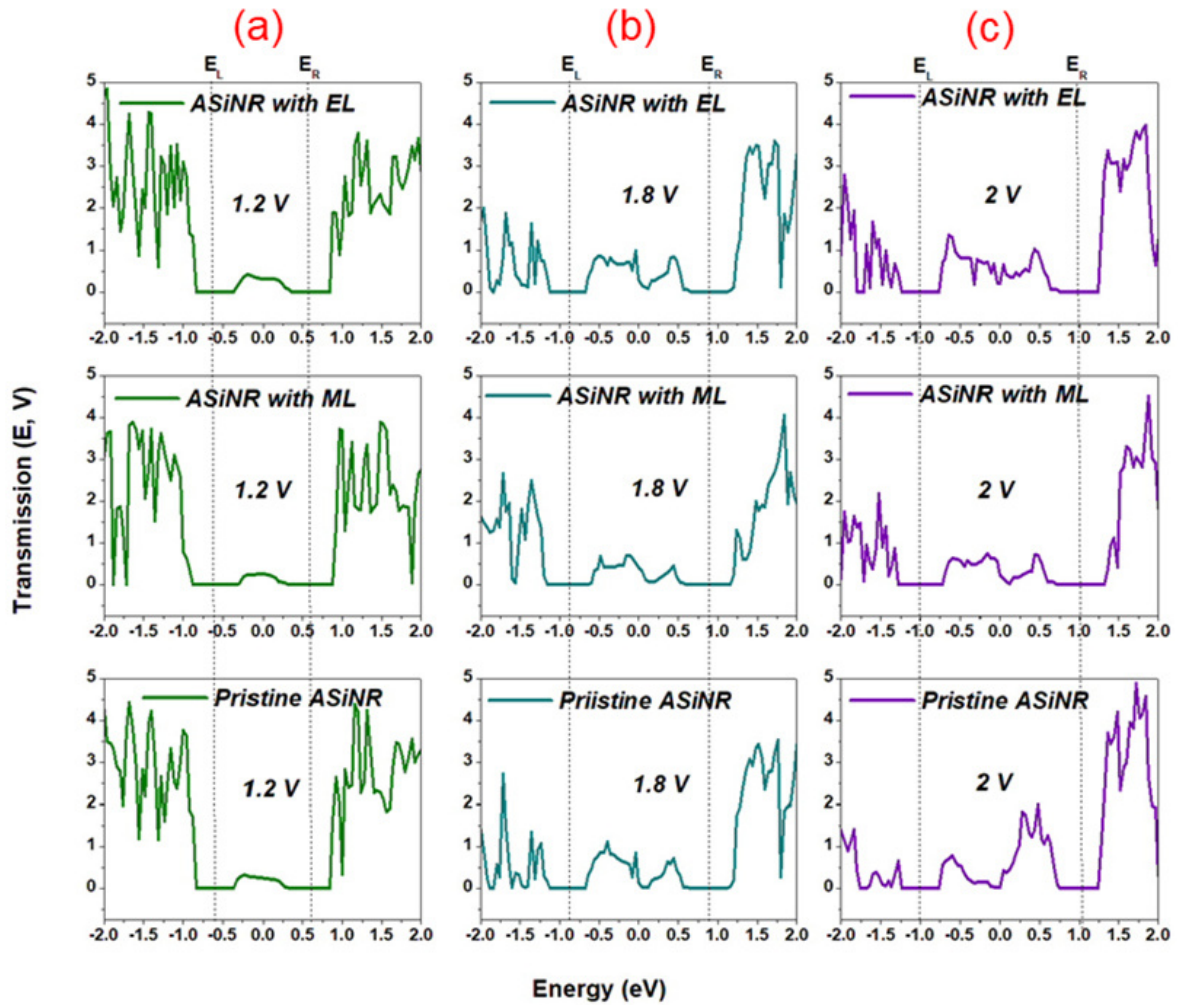


FIG. 5. Transmission Spectra of Pristine ASiNR and ASiNR with ML and EL at (a) 1.2 V, (b) 1.8 V and (c) 2 V

3.1.4. Density of states. The projected device density of states represents the contribution of each atomic orbital to the overall density of states at a specific energy level. In order to comprehend the impact of Volatile Organic Compounds (VOCs) on the electronic characteristics of ASiNR, we have computed the projected device density of states both before and after adsorption. From Fig. 6, it is evident that there are no peaks present around the Fermi level. This observation suggests that ASiNR maintains its semiconducting properties both before and after the adsorption of target molecules. The absence of peaks around the Fermi level additionally supports the conclusion that molecules undergo physisorption on the ASiNR surface. Moreover, these findings align with the adsorption energy and transport characteristics of the modelled device.

3.1.5. Sensitivity (%). To ensure a clear comprehension of the sensing capabilities of ASiNR, we calculated the sensitivity, which is defined as the change in conductance. Initially, we assessed the conductance (I/V) of the ASiNR modelled devices. The calculated conductance was then employed to conduct a focussed analysis on sensitivity, by utilizing the following equation [24].

$$S = \left| \frac{G_{\text{ASiNR+Molecule}} - G_{\text{ASiNR}}}{G_{\text{ASiNR}}} \right|. \quad (3)$$

The terms $G_{\text{ASiNR+Molecule}}$ and G_{ASiNR} represent the conductance of the ASiNR-molecule system and pristine ASiNR respectively. Table 1 lists the sensitivity (%) of the sensor towards the three proposed molecules at 1.2, 1.4, 1.6, 1.8 and 2.0 V.

Notably, at 1.8 and 2.0 V, the sensor exhibits high sensitivity, reaching 33 and 42 %, respectively, for methanol, while demonstrating low sensitivities for ethanol and water molecules. Thus, the obtained sensitivities are larger compared to the sensitivities in the previous literature [48, 49]. This suggests that the sensor can selectively detect methanol as compared to ethanol and water molecules. Furthermore, the graphical representation of these sensitivities at various voltages is illustrated in Fig. 7.

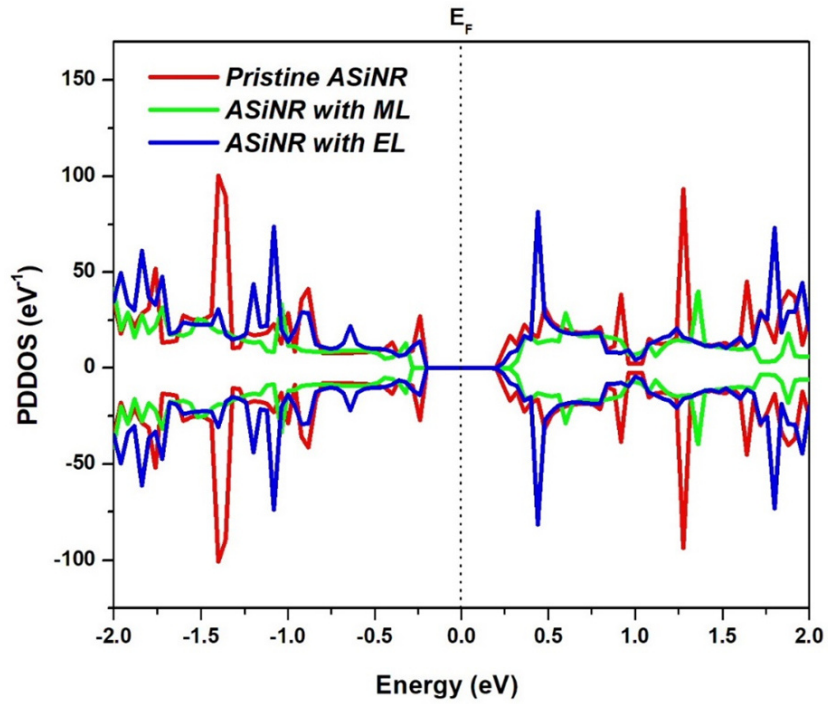


FIG. 6. Projected device density of states of ASiNR with and without adsorption of VOCs

TABLE 1. The calculated values of sensitivity (%) of the ASiNR sensor at bias voltages of (1.2, 1.4, 1.6, 1.8 and 2.0) V

Bias voltage	Target molecules		
	Methanol	Ethanol	Water
1.2 V	24	25	17
1.4 V	20	4.3	3.9
1.6 V	21	22	5.9
1.8 V	33	8.5	3.3
2.0 V	42	9.7	12.6

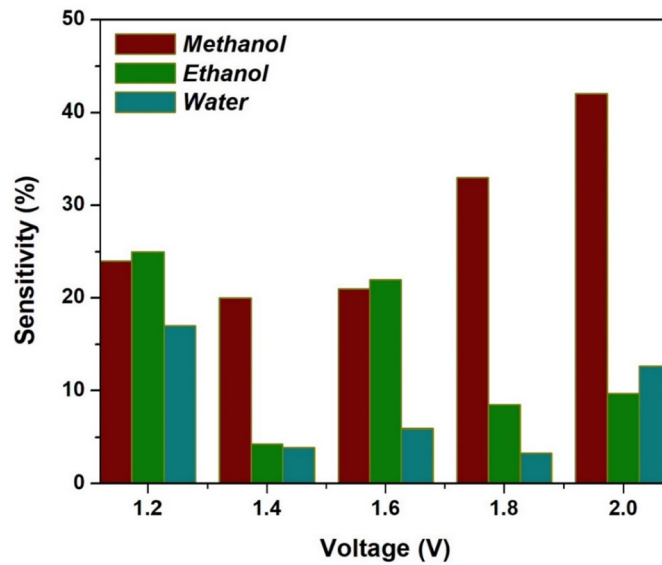


FIG. 7. Sensitivity of ASiNR sensor at different bias voltages

TABLE 2. Review of the proposed ASiNR sensor with other state of art sensors

2D Sensing Materials	Analytes	Adsorption Energy (eV)	Sensor's Performance	References
Graphene-like BC₆N	Acetone, Ethanol, Methanol, Formaldehyde, Toluene	-0.381, -0.378, -0.316, -0.228, -0.910	6.1 %, 14.7 %, 9.5 %, 14.7 %, 14.7 %	[9]
Defected-BC₆N	Acetone, Ethanol, Methanol, Formaldehyde, Toluene	-0.527, -0.754, -0.750, -0.647, -1.00	1.7 %, 61.0 %, 1.8 %, 15.4 %, 8.8 % (sensitivities) 740 s, 4.9 s, 4.2 s, 77 ms, 6800 s (recovery time)	[9]
Pristine-ASiNR	CH ₄ , CO ₂ , CO	-0.32, -0.59, -1.69	Not Given	[44]
Defective-ASiNR	CH ₄ , CO ₂ , CO	-0.45, -0.70, -1.94	Not Given	[44]
Silicene	Acetone, Toluene	Not Given	Not Given	[45]
Defected-Silicene	Isopropanol	Not Given	Not Given	[46]
C₃N Mono-layer	Methanol, Ethanol, Acetone, Isopropanol, Isobutanol	-0.2408, -0.2203, 0.2531, -0.1225, -0.4359	26.96 %, 8.7 %, 71 % 59.5 %, 24.15 % (sensitivities)	[48]
Pristine Phosphorene	Acetone, Methanol, Ethanol, Toluene, CO ₂ , H ₂ O	-0.74, -0.67, -0.73, -1.16, -0.44, -0.54	1.27 %, 0.82 %, NR, NR (sensitivities) 2.67 s, 0.18 s, 1.81 s, 3.03 · 10 ⁷ s, 2.45 · 10 ⁻⁵ s, 0.001 s (recovery time)	[49]
Pd-decorated Phosphorene	Acetone, Methanol, Ethanol, Toluene, CO ₂ , H ₂ O	-1.14, -0.84, -1.06, -1.53, -0.45, -0.79	15.1 %, 14.3 %, NR, NR (sensitivities) 1.39 · 10 ⁷ s, 127.94 s, 4.95 · 10 ¹⁵ s, 4.95 · 10 ¹³ s, 2.45 · 10 ⁻⁵ s, 18.5 s (recovery time)	[49]
Al-doped GeS	Methanol, Ethanol	-0.379, -0.450	Not Given	[50]
Graphyne Nanosheet	Methanol, Ethanol	-0.167 to -0.532	Not Given	[52]
MoSe₂	Methanol, Ethanol	-0.375 to -0.732	Not Given	[53]
Pristine-ASiNR	NH ₃	-0.49	Not Given	[67]
Silicene	Formaldehyde	-0.076	Not Given	[69]
ASiNR	Methanol, Ethanol, H₂O	-1.56, -1.62, -1.43	42 %, 9.7 %, 12.6 % (sensitivities) 2.4 · 10 ¹⁴ s, 2.5 · 10 ¹⁵ s, 1.5 · 10 ¹² s (recovery time)	This Work

3.1.6. *Recovery time* (τ). Another important parameter for a sensor is its reusability, which is related to the recovery time (τ) and relies on the adsorption energy (E_{ad}). In accordance with the conventional transition state theory, the recovery time τ can be described as [9, 68]:

$$\tau = \nu_0^{-1} \exp\left(-\frac{E_{ad}}{K_B T}\right), \quad (4)$$

where ν_0 is the attempt frequency, K_B is the Boltzmann constant and T is the operational temperature of sensor. In visible light ($\nu_0 = 10^{12}$ Hz) and at room temperature ($T = 298$ K), the stronger binding of ethanol ($E_{ad} = -1.62$ eV) compared to methanol ($E_{ad} = -1.56$ eV) and water ($E_{ad} = -1.43$ eV) implies that removing ethanol from the ASiNR sensor may be more challenging. By incorporating these parameters in Eq. (4), the obtained τ values are 2.4×10^{14} s for methanol, 2.5×10^{15} s for ethanol and 1.5×10^{12} s for water molecule. Consequently, it is basically impossible for the three molecules to desorb from the surface of ASiNR based device, it can be considered that the three molecules can stably exist in the ASiNR based device and are difficult to escape. The long desorption time shows that ASiNR based device has strong adsorption performance for the three molecules. Once the target molecules are captured by ASiNR, they will be hard to break free. Therefore, it can be used as an ideal adsorption material to remove the target molecules, showing great potential in the area of toxic gas scavenger.

The performance of the proposed sensor with that of other DFT based similar sensors mentioned in the literature is contrasted in Table 2. The table indicates that the interactions between VOCs and ASiNR are stronger than those with other 2D materials discussed in the literature such as graphene-like BC₆N [9], C₃N monolayer [48], pristine and Pd-decorated phosphorene [49], Al-doped GeS [50], graphyne nanosheet [52], MOSe₂ [53]. However, the proposed ASiNR sensor suffers an extremely longer recovery, which renders its application to be used as a reusable sensor.

4. Conclusion

In this study, we delved into the adsorption mechanism of human breath exhaled VOCs on the ASiNR based device. Our examination involves a meticulous exploration of the structural, electronic, and transport attributes of silicene. This study is performed by employing the advanced methodologies such as density functional theory and non-equilibrium Green's function (NEGF) formalism. The calculated adsorption energy (E_{ad}) follows the trend: ethanol > methanol > water. Additionally, we have identified substantial alterations in the transport properties resulting from the application of bias within the range of 0 to 2 V. Apart from that, we have also calculated the sensitivity (%), which confirms that methanol was highly sensitive as compared to the other molecules. Moreover, our analysis of the density of states demonstrates that ASiNR remains semiconducting both before and after adsorption, affirming the physisorption of the target molecules. Furthermore, although physisorption occurs, the ASiNR-based sensor exhibits a notably prolonged recovery time, suggesting challenges in desorbing molecules from the material's surface. This material positively influences the elimination of toxic gas molecules, highlighting ASiNR's significant potential in both detecting and removing toxic gases, making it suitable for disposable sensors and scavengers.

References

- [1] Sun X., Shao K., Wang T. Detection of volatile organic compounds (VOCs) from exhaled breath as noninvasive methods for cancer diagnosis. *Analytical and Bioanalytical Chemistry*, 2016, **408**, P. 2759–2780.
- [2] Mehdi Aghaei S., Aasi A., Panchapakesan B. Experimental and theoretical advances in MXene-based gas sensors. *ACS Omega*, 2021, **6** (4), P. 2450–2461.
- [3] Aasi A., Mehdi Aghaei S., Panchapakesan B. Outstanding performance of transition-metal-decorated single-layer graphene-like BC₆N nanosheets for disease biomarker detection in human breath. *ACS Omega*, 2021, **6** (7), P. 4696–4707.
- [4] Das S., Pal M. Non-invasive monitoring of human health by exhaled breath analysis: A comprehensive review. *J. of The Electrochemical Society*, 2020, **167** (3), 037562.
- [5] Hakim M., Broza Y.Y., Barash O., Peled N., Phillips M., Amann A., Haick H. Volatile Organic Compounds of Lung Cancer and Possible Biochemical Pathways. *Chem. Rev.*, 2012, **112**, P. 5949–5966.
- [6] Kim J.S., Yoo H.W., Choi H.O., Jung H.T. Tunable volatile organic compounds sensor by using thiolated ligand conjugation on MoS₂. *Nano Letters*, 2014, **14** (10), P. 5941–5947.
- [7] Chatterjee S., Castro M., Feller J.F. An e-nose made of carbon nanotube-based quantum resistive sensors for the detection of eighteen polar/nonpolar VOC biomarkers of lung cancer. *J. of Materials Chemistry B*, 2013, **1** (36), P. 4563–4575.
- [8] Deng C., Zhang J., Yu X., Zhang W., Zhang X. Determination of acetone in human breath by gas chromatography–mass spectrometry and solid-phase microextraction with on-fiber derivatization. *J. of Chromatography B*, 2004, **810** (2), P. 269–275.
- [9] Aghaei S.M., Aasi A., Farhangdoust S., Panchapakesan B. Graphene-like BC₆N nanosheets are potential candidates for detection of volatile organic compounds (VOCs) in human breath: A DFT study. *Applied Surface Science*, 2021, **536**, 147756.
- [10] Boots A.W., van Berkel J.J., Dallinga J.W., Smolinska A., Wouters E.F., van Schooten F.J. The versatile use of exhaled volatile organic compounds in human health and disease. *J. of breath research*, 2012, **6** (2), 027108.
- [11] Atkinson R. Atmospheric chemistry of VOCs and NO_x. *Atmospheric environment*, 2000, **34** (12–14), P. 2063–2101.
- [12] Nagarajan V., Chandiramouli R.. First-Principles Investigation on Interaction of NH₃ Gas on a Silicene Nanosheet Molecular Device. *IEEE Trans. Nanotechnology*, 2017, **16**, P. 445–452.
- [13] Jariwala D., Sangwan V.K., Lauhon L.J., Marks T.J., Hersam M.C. Emerging Device Applications for Semiconducting Two-Dimensional Transition Metal Dichalcogenides. *ACS Nano*, 2014, **8**, P. 1102–1120.
- [14] Nagarajan V., Chandiramouli R. CO and NO monitoring using pristine germanene nanosheets: DFT study. *J. Mol. Liq.*, 2017, **234**, P. 355–363.

- [15] Nagarajan V., Chandiramouli R. Investigation of electronic properties and spin-orbit coupling effects on passivated stanene nanosheet: A first-principles study. *Superlattices Microstruct.*, 2017, **107**, P. 118–126.
- [16] Ni Z., Liu Q., Tang K., Zheng J., Zhou J., Qin R., Gao Z., Yu D., Lu J. Tunable bandgap in silicene and germanene. *Nano Letters*, 2012, **12**, P. 113–118.
- [17] Tao L., Cinquanta E., Chiappe D., Grazianetti C., Fanciulli M., Dubey M., Molle A., Akinwande D. Silicene field-effect transistors operating at room temperature. *Nature Nanotechnology*, 2015, **10**, P. 227–231.
- [18] Tsai W.F., Huang C.-Y., Chang T.-R., Lin H., Jeng H.-T., Bansil A. Gated silicene as a tunable source of nearly 100 % spin-polarized electron. *Nat. Commun.*, 2013, **4** P. 1–6.
- [19] Sadeghi H., Bailey S., Lambert C.J. Silicene-based DNA nucleobase sensing. *Applied Physics Letters*, 2014, **104**, 103104.
- [20] Gao N., Zheng W.T., Jiang Q. Density functional theory calculations for two-dimensional silicene with halogen functionalization. *Physical Chemistry Chemical Physics*, 2012, **14**, P. 257–261.
- [21] Lopez-Bezanilla A. Substitutional doping widens silicene gap. *J. Phys. Chem. C*, 2014, **118**, P. 18788–18792.
- [22] Gao N., Li J.C., Jiang Q. Bandgap opening in silicene: Effect of substrates. *Chem. Phys. Lett.*, 2014, **592**, P. 222–226.
- [23] Pan F., Wang Y., Jiang K., Ni Z., Ma J., Zheng J., Quhe R., Shi J., Yang J., Chen C., Lu J. Silicene nanomesh. *Scientific Reports*, 2015, **5**, 9075.
- [24] Aghaei S.M., Monshi M.M., Torres I., Calizo I. Edge functionalization and doping effects on the stability, electronic and magnetic properties of silicene nanoribbons. *RSC advances*, 2016, **6**, P. 17046–17058.
- [25] Aghaei S.M., Calizo I. Band gap tuning of armchair silicene nanoribbons using periodic hexagonal holes. *J. Appl. Phys.*, 2015, **118**, 104304.
- [26] Kharadi M.A., Malik G.F., Shah K.A., Khanday F.A. Performance analysis of functionalized silicene nanoribbon-based photodetector. *Int. J. of Numerical Modelling: Electronic Networks, Devices and Fields*, 2021, **34**, e2809.
- [27] Masson L., Prévot G. Epitaxial growth and structural properties of silicene and other 2D allotropes of Si. *Nanoscale Advances*, 2023, **5** (6), P. 1574–1599.
- [28] Meng L., Wang Y., Zhang L., Du S., Wu R., Li L., Zhang Y., Li G., Zhou H., Hofer W.A., Gao M.J. Buckled silicene formation on Ir (111). *Nano Letters*, 2013, **13** (2), P. 685–690.
- [29] Fleurence A., Friedlein R., Ozaki T., Kawai H., Wang Y., Takamura Y. Experimental evidence for epitaxial silicene on diboride thin films *Phys. Rev. Letters*, 2012, **108** (24), 24550.
- [30] Aizawa T., Suehara S., Otani S. Silicene on zirconium carbide (111). *J. Phys. Chem. C*, 2014, **118** (40), 23049.
- [31] Wang X.Q., Li H.D., Wang J.T. Induced ferromagnetism in one-side semi-hydrogenated silicene and germanene. *Phys. Chem. Chem. Phys.*, 2012, **14** (9), P. 3031–3036.
- [32] Zheng F.B., Zhang C.W. The electronic and magnetic properties of functionalized silicene: a first-principles study. *Nanoscale Res. Letters*, 2012, **7**, P. 1–5.
- [33] Liu C., Feng W., Yao Y. Quantum spin Hall effect in silicene and two-dimensional germanium. *Phys. Rev. Letters*, 2011, **107** (7), 076802.
- [34] Xu C., Luo G., Liu Q., Zheng J., Zhang Z., Nagase S., Gao Z., Lu J. Giant magnetoresistance in silicene nanoribbons. *Nanoscale*, 2012, **4**, P. 3111–3317.
- [35] Chen L., Feng B., Wu K. Observation of a possible superconducting gap in silicene on Ag (111), surface. *Appl. Phys. Letters*, 2013, **102** (8), 081602.
- [36] Aufray B., Kara A., Vizzini S., Oughaddou H., Leandri C., Ealet B., Le Lay G. Graphene-like silicon nanoribbons on Ag (110): A possible formation of silicene. *Applied Physics Letters*, 2010, **96** (18), 183102.
- [37] De Padova P., Quaresima C., Ottaviani C., Sheverdyaeva P.M., Moras P., Carbone C., Topwal D., Olivieri B., Kara A., Oughaddou H., Aufray B., Le Lay G. Evidence of graphene-like electronic signature in silicene nanoribbons. *Applied Physics Letters*, 2010, **96** (26), 261905.
- [38] De Padova P., Kubo O., Olivieri B., Quaresima C., Nakayama T., Aono M., Le Lay G. Multilayer silicene nanoribbons. *Nano Letters*, 2012, **12** (11), P. 5500–5503.
- [39] Tchalala M.R., Enriquez H., Mayne A.J., Kara A., Roth S., Silly M.G., Bendounan A., Sirotti F., Greber T., Aufray B., Dujardin G., Ali M.A., Oughaddou H. Formation of one-dimensional self-assembled silicon nanoribbons on Au (110),-(2× 1). *Applied Physics Letters*, 2013, **102** (8), 083107.
- [40] Zha D., Chen C., Wu J. Electronic transport through a silicene-based zigzag and armchair junction. *Solid State Communications*, 2015, **219**, P. 21–24.
- [41] Houssa M., van den Broek B., Scalise E., Pourtois G., Afanasev V.V., Stesmans A. An electric field tunable energy band gap at silicene/ (0001), ZnS interfaces. *Physical Chemistry Chemical Physics*, 2013, **15** (11), P. 3702–3705.
- [42] Prasongkit J., Amorim R.G., Chakraborty S., Ahuja R., Scheicher R.H., Amornkitbamrung V. Highly Sensitive and Selective Gas Detection Based on Silicene. *J. Phys. Chem. C*, 2015, **119**, P. 16934–16940.
- [43] Nagarajan V., Chandiramouli R. First-Principles Investigation on Interaction of NH₃ Gas on a Silicene Nanosheet Molecular Device. *IEEE Trans. Nanotechnology*, 2017, **16**, P. 445–452.
- [44] Walia G.K., Randhawa D.K.K. Gas-sensing properties of armchair silicene nanoribbons towards carbon-based gases with single-molecule resolution. *Struct. Chem.*, 2018, **29**, P. 1893–1902.
- [45] Pham T.L., Ta T.L., Vo V.O., Dinh V.A. DFT Study on Adsorption of Acetone and Toluene on Silicene. *VNU J. of Science: Mathematics-Physics*, 2020, **36**, P. 95–102.
- [46] Vo V.O., Pham T.L., Dinh V.A. Absorption of Isopropanol on Surface of Defect Silicene. *VNU J. of Science: Mathematics-Physics*, 2020, **36**, P. 92–99.
- [47] Showket S., Shah K.A., Dar G.N. Pristine and Modified Silicene based Volatile Organic Compound Toxic Gas Sensor: A First Principles Study. *Physica Scripta*, 2023, **98**, 085937.
- [48] Agrawal S., Kaushal G., Srivastava A. Electron transport in C₃N monolayer: DFT analysis of volatile organic compound sensing. *Chemical Physics Letters*, 2021, **762**, 138121.
- [49] Aasi A., Aghaei S.M., Bajjani S.E., Panchapakesan B. Computational Study on Sensing Properties of Pd-Decorated Phosphorene for Detecting Acetone, Ethanol, Methanol, and Toluene: A Density Functional Theory Investigation. *Advanced Theory and Simulations*, 2021, **4**, 2100256.
- [50] Pu K., Dai X., Bu Y., Guo R., Tao W., Jia D., Song J., Zhao T., Feng L. Al-doped GeS nanosheet as a promising sensing material for O-contained volatile organic compounds detection. *Applied Surface Science*, 2020, **527**, 146797.
- [51] Singen S., Watwiangkham A., Ngamwongwan L., Fongkaew I., Jungthawan S., Suthirakun S. Defect Engineering of Green Phosphorene Nanosheets for Detecting Volatile Organic Compounds: A Computational Approach. *ACS Applied Nano Materials*, 2023, **6**, P. 1496–1506.
- [52] Nagarajan V., Dharani S., Chandiramouli R. Density functional studies on the binding of methanol and ethanol molecules to graphyne nanosheet. *Comput. Theor. Chem.*, 2018, **1125**, P. 86–94.

- [53] Nagarajan V., Chandiramouli R. MoSe₂ nanosheets for detection of methanol and ethanol vapors: a DFT study. *J. of Molecular Graphics and Modelling*, 2018, **81**, P. 97–105.
- [54] Gani M., Shah K.A., Parah S.A. Realization of a sub-10 nm silicene magnetic tunnel junction and its application for magnetic random access memory and digital logic. *IEEE Transactions on Nanotechnology*, 2021, **20**, P. 466–473.
- [55] URL: <https://synopsys.com/silicon/quantumatk.html> Synopsys Quantum ATK, P-2019.03, 2019.
- [56] Zeng M., Feng Y., Liang G. Graphene-based spin caloritronics. *Nano Letters*, 2011, **11**, P. 1369–1373.
- [57] Perdew J.P., Burke K., Ernzerhof M. Generalised gradient approximation made simple. *Phys. Rev. Lett.*, 1996, **77**, P. 3865–3868.
- [58] Abadir G.B., Walus K., Pulfrey D.L. Basis-set choice for DFT/ NEGF simulations of carbon nanotubes. *J. Comp. Electron.*, 2009, **8**, P. 1–9.
- [59] Yamacli S. Comparison of the electronic transport properties of metallic graphene and silicene nanoribbons. *J. Nanopart. Res.*, 2014, **16**, 2576.
- [60] Srivastava P., Jaiswal N.K., Tripathi G.K. Chlorine sensing properties of zigzag boron nitride nanoribbons. *Solid State Commun.*, 2014, **185**, P. 41–46.
- [61] Wei X.L., Chen Y.P., Liu W.L., Zhong J.X. Enhanced gas sensor based on nitrogen-vacancy graphene nanoribbons. *Phys. Lett. A*, 2012, **376**, P. 559–562.
- [62] Aghaei S.M., Monshi M.M., Calizo I. A theoretical study of gas adsorption on silicene nanoribbons and its application in a highly sensitive molecule sensor. *RSC*, 2016, **6**, P. 94417–94428.
- [63] Ding Y., Ni J. Electronic structures of silicon nanoribbons. *Applied Physics Letters*, 2009, **95**, 083115.
- [64] Davila M.E., Marele A., De Padova P., Montero L., Hennes F., Pietzsch A., Shariati M.N., Gomez Rodriguez J.M., Le Lay G. Comparative structural and electronic studies of hydrogen interaction with isolated versus ordered silicon nanoribbons grown on Ag (110). *Nanotechnology*, 2012, **23**, 385703.
- [65] Osborn T.H., Farajian A.A., Puyesheva O.V., Aga R.S., Voon L.L.Y. Ab initio simulations of silicene hydrogenation. *Chem. Phys. Lett.*, 2011, **511**, P. 101–105.
- [66] Naqash A.N., Shah K.A., Sheikh J.A., Kumbhani B., Andrabi S.M. Transport properties of GaAs Co-doped H-passivated low-buckled and high-buckled zigzag silicene nanoribbon two probe devices. *Nanosystems: Physics, Chemistry, Mathematics*, 2023, **14** (4), P. 438–446.
- [67] Walia G.K., Randhawa D.K.K. Electronic and transport properties of silicene-based ammonia nanosensors: an ab initio study. *Structural Chemistry*, 2018, **29**, P. 257–265.
- [68] Walia G.K., Randhawa D.K.K. Gas sensing properties of armchair silicene nanoribbons towards carbon-based gases with single molecule resolution. *Structural Chemistry*, 2018, **29**, 1893.
- [69] Wang X., Liu H., Tu S.T. Study of formaldehyde adsorption on silicene with point defects by DFT method. *RSC Advances*, 2015, **80**, P. 65255–65263.

Submitted 5 January 2024; revised 21 February 2024; accepted 7 April 2024

Information about the authors:

Shazia Showket – Department of Physics, University of Kashmir, Srinagar, J&K – 190006, India; ORCID 0009-0009-7438-2260; shaziashowket.phscholar@kashmiruniversity.net

Khurshed A. Shah – Postgraduate Department of Physics, Sri Pratap College, Cluster University Srinagar, J&K – 190001, India; ORCID 0000-0002-2694-4515; drkhursheda@gmail.com

Ghulam Nabi Dar – Department of Physics, University of Kashmir, Srinagar, J&K – 190006, India; ORCID 0000-0002-5066-0141; gndphy@kashmiruniversity.ac.in

Muzaffar Ali Andrabi – Department of Applied Sciences, Institute of Technology, University of Kashmir, Srinagar, J&K – 190006, India; ORCID 0009-0001-9584-3398; muzaffar2000@gmail.com

Conflict of interest: the authors declare no conflict of interest.



NANOSYSTEMS:

PHYSICS, CHEMISTRY, MATHEMATICS

INFORMATION FOR AUTHORS

The journal publishes research articles and reviews, and also short scientific papers (letters) which are unpublished and have not been accepted for publication in other magazines. Articles should be submitted in English. All articles are reviewed, then if necessary come back to the author to completion.

The journal is indexed in Web of Science Core Collection (Emerging Sources Citation Index), Chemical Abstract Service of the American Chemical Society, Zentralblatt MATH and in Russian Scientific Citation Index.

Author should submit the following materials:

1. Article file in English, containing article title, the initials and the surname of the authors, Institute (University), postal address, the electronic address, the summary, keywords, MSC or PACS index, article text, the list of references.
2. Files with illustrations, files with tables.
3. The covering letter in English containing the article information (article name, MSC or PACS index, keywords, the summary, the literature) and about all authors (the surname, names, the full name of places of work, the mailing address with the postal code, contact phone number with a city code, the electronic address).
4. The expert judgement on possibility of publication of the article in open press (for authors from Russia).

Authors can submit a paper and the corresponding files to the following addresses: nanojournal.ifmo@gmail.com, popov1955@gmail.com.

Text requirements

Articles should be prepared with using of text editors MS Word or LaTeX (preferable). It is necessary to submit source file (LaTeX) and a pdf copy. In the name of files the English alphabet is used. The recommended size of short communications (letters) is 4-6 pages, research articles– 6-15 pages, reviews – 30 pages.

Recommendations for text in MS Word:

Formulas should be written using Math Type. Figures and tables with captions should be inserted in the text. Additionally, authors present separate files for all figures and Word files of tables.

Recommendations for text in LaTeX:

Please, use standard LaTeX without macros and additional style files. The list of references should be included in the main LaTeX file. Source LaTeX file of the paper with the corresponding pdf file and files of figures should be submitted.

References in the article text are given in square brackets. The list of references should be prepared in accordance with the following samples:

- [1] Surname N. *Book Title*. Nauka Publishing House, Saint Petersburg, 2000, 281 pp.
- [2] Surname N., Surname N. Paper title. *Journal Name*, 2010, **1** (5), P. 17-23.
- [3] Surname N., Surname N. Lecture title. In: Abstracts/Proceedings of the Conference, Place and Date, 2000, P. 17-23.
- [4] Surname N., Surname N. Paper title, 2000, URL: <http://books.ifmo.ru/ntv>.
- [5] Surname N., Surname N. Patent Name. Patent No. 11111, 2010, Bul. No. 33, 5 pp.
- [6] Surname N., Surname N. Thesis Title. Thesis for full doctor degree in math. and physics, Saint Petersburg, 2000, 105 pp.

Requirements to illustrations

Illustrations should be submitted as separate black-and-white files. Formats of files – jpeg, eps, tiff.



NANOSYSTEMS:

PHYSICS, CHEMISTRY, MATHEMATICS

Журнал зарегистрирован

Федеральной службой по надзору в сфере связи, информационных технологий и массовых коммуникаций

(свидетельство ПИ № ФС 77 - 49048 от 22.03.2012 г.)

ISSN 2220-8054

Учредитель: федеральное государственное автономное образовательное учреждение высшего образования

«Национальный исследовательский университет ИТМО»

Издатель: федеральное государственное автономное образовательное учреждение высшего образования

«Национальный исследовательский университет ИТМО»

Отпечатано в Учреждении «Университетские телекоммуникации»

Адрес: 197101, Санкт-Петербург, Кронверкский пр., 49

Подписка на журнал НФХМ

На второе полугодие 2024 года подписка осуществляется через

ОАО «АРЗИ», подписной индекс Э57385